DISS. ETH NO. 26211

INTERPLAY BETWEEN STRUCTURAL, ELECTRONIC, AND MAGNETIC PROPERTIES IN RARE-EARTH NICKELATES

A thesis submitted to attain the degree of

Doctor of Sciences of ETH Zurich
(Dr. sc. ETH Zürich)

presented by

ALEXANDER HAMPEL

M.Sc. in Physics,
University of Hamburg

born on 14.08.1989

citizen of Germany

accepted on the recommendation of

Prof. Dr. Claude Ederer, examiner
Prof. Dr. Markus Aichhorn, co-examiner
Prof. Dr. Manfred Sigrist, co-examiner
Dr. Marisa Medarde, co-examiner

2019

Alexander Hampel
Interplay between structural, electronic, and magnetic properties in rare-earth nickelates
July 2019

ABSTRACT

Rare-earth nickelates are a series of functional materials that crystallize in the perovskite structure with the chemical formula $RNiO_3$, and are in particular known for their rich phase diagram. All nickelates with rare-earth ion, R, from Pr to Lu exhibit a metal-insulator transition (MIT) accompanied by a structural transition. Furthermore, all compounds of the series (except $LaNiO_3$) display antiferromagnetic ordering at low-temperatures. Notably, both the MIT and the magnetic ordering temperature depend on the size of the R site ion.

The MIT found in the nickelate series is driven by strong electronic correlations, and is inherently coupled to a so called "breathing mode" structural distortion, which together results in a charge-ordered insulating state. This strong coupling of structural and electronic degrees of freedom in nickelates allows for a systematic tuning from itinerant to localized behavior, e.g. by changing the rare-earth cation, by applying strain, pressure, or electromagnetic fields, making the compounds very interesting for technical applications. However, until today the emerging phase diagram is only partially understood. Especially, the nature and exact mechanism of the coupled electronic-structural transition is still debated and is the central topic of this thesis. Considering the fact that the compounds are difficult to synthesize, and that experimental data is therefore sparse, it is particularly valuable to gain insights into the materials properties by means of first-principles calculations. However, the theoretical description of such materials, in which electronic, magnetic, and structural degrees of freedom couple, is extremely challenging.

In this thesis I utilize state of the art first-principles methods to obtain a parameter-free description of electronic and structural properties across the rare-earth nickelate series. To do so, I combine density functional theory (DFT) with more sophisticated methods, such as dynamical mean field theory (DMFT), to describe the correlated electron system and its coupling to structural degrees of freedom completely *ab inito*. This allows to describe the different phases of the series on a quantitative level, and to shine light on the underlying mechanism of the coupled structural-electronic MIT. Thereby, I aim to push the boundaries of the applied methodology, making its application to materials that also exhibit complex coupling of structural and electronic degrees of freedom more feasible.

In the first part of this thesis I present a comprehensive DFT+U study across the whole nickelate series, where I extract structural parameters within the magnetic phase found at low temperatures. This will lay a foundation for the application of the more sophisticated

DMFT method. Moreover, I obtain a qualitative correct description of structural trends within DFT+U. However, the study will also reveal deficiencies of the method, demonstrating the need of more sophisticated approaches to capture the correlated electron physics more accurately.

Next, I examine the coupled transition by combining DFT and DMFT. Here, I determine structural parameters on a quantitative level across the series for the correlated insulating state. Furthermore, the analysis of the breathing mode distortion energetics reveals a first-order character of the coupled MIT, in agreement with experimental data. The transition is driven by an electronic instability related to the charge-ordering phenomena. In a further study, I construct a model Hamiltonian, reducing the complex problem, only keeping the key ingredients to investigate the mechanism and control parameters of the coupled MIT of the nickelate series. This study reveals that the the bandwidth, which in turn is controlled by the octahedral rotations, critically influences how close the system is to the electronic instability, and hence determine trends across the series. Thus, these results lead to a comprehensive understanding of the paramagnetic part of the rare-earth nickelates phase diagram.

In the last part of this thesis I perform combined DFT and DMFT calculations for the magnetically ordered state, to elucidate the transition from the insulating paramagnetic to insulating antiferromagnetic phase. First, I demonstrate that these demanding calculations capture the magnetically ordered state correctly. Then, the obtained results are compared with the results obtained from the magnetic DFT+U calculations. Thereby, I point out current limitations of the method that need to be addressed to understand the coupling to the magnetically ordered state in nickelates in greater depth. This is a missing link to obtain a full understanding of the phase diagram. Furthermore, I give an outlook for future directions of research both in the field of rare earth nickelates, and using the combined DFT+DMFT approach for realistic materials modeling.

ZUSAMMENFASSUNG

Nickelate sind eine Serie von funktionellen Materialien, die in der Perowskitstruktur mit der chemischen Formel $RNiO_3$ kristallisieren und insbesondere für ihr aussergewöhnliches Phasendiagramm bekannt sind. R kann ein beliebiges Ion der seltenen Erden sein. Alle Nickelate mit R Ion zwischen Pr und Lu zeigen einen Metall-Isolator-Übergang, der mit einem strukturellen Übergang einhergeht. Darüber hinaus ordnen alle Verbindungen der Nickelat-Serie (außer $LaNiO_3$) antiferromagnetisch bei niedrigen Temperaturen. Bemerkenswerterweise, hängt sowohl die Metall-Isolator, als auch die magnetische Übergangstemperatur, von der Grösse des R Ions ab.

Dieser Metall-Isolator-Übergang wird durch starke Elektronenkorrelationseffekte getrieben und ist mit einer strukturellen Verzerrung des Gitters gekoppelt, der sogenannten *Breathing Mode*, was zu einem ladungsgeordneten isolierendem Zustand führt. Diese besondere Kopplung von strukturellen und elektronischen Freiheitsgraden in Nickelaten ermöglicht ein systematisches Variation von metallischem zu isolierendem Zustand, z.B. durch Änderung des Seltene Erden-Ions, durch Gitter-Dehnungen, Anwenden von Druck oder elektromagnetischen Feldern. Dies macht die Nickelate für technische Anwendungen sehr interessant. Allerdings ist das daraus resultierende Phasendiagramm nur teilweise verstanden. Insbesondere der genaue Mechanismus des gekoppelten elektronisch-strukturellen Übergangs wird diskutiert und ist das zentrale Thema dieser Arbeit. Aufgrund der Tatsache, dass die Herstellung von Nickelaten schwierig ist, und daher nur wenige experimentelle Daten vorliegen, können Simulationen wertvolle Erkenntnisse über deren Eigenschaften liefern. Allerdings ist die theoretische Beschreibung von Materialien, in denen elektronische, magnetische und strukturelle Freiheitsgrade gekoppelt sind, äusserst schwierig.

In dieser Arbeit verwende ich modernste *ab inito* Simulationsmethoden, um eine theoretische Beschreibung der elektronischen und strukturellen Eigenschaften der Nickelate zu ermöglichen. Um das korrelierte Elektronensystem und die Kopplung zur Struktur zu beschreiben, kombiniere ich die Dichtefunktionaltheorie (DFT) mit der dynamischen Molekularfeldtheorie (DMFT). Dies ermöglicht, die verschiedenen Phasen der Nickelate auf einem quantitativen Level zu beschreiben, und den Mechanismus des gekoppelten Übergangs zu untersuchen. Des Weiteren, erweitert dies die Möglichkeiten der DFT+DMFT Methode, Materialien mit einer komplexen Kopplung von strukturellen und elektronischen Freiheitsgraden zu beschreiben.

Im ersten Teil dieser Arbeit präsentiere ich eine DFT+U Studie für die gesamte Nickelat-Serie. Dabei bestimme ich strukturelle Parameter innerhalb der magnetischen Phase bei niedrigen Temperaturen. Diese Resultate werden dann als Ausgangspunkt für die Anwendung der DMFT Methode benutzt. Die DFT+U Studie liefert dabei auch eine qualitativ korrekte Beschreibung der strukturellen Trends in der Serie. Ausserdem werden Unzulänglichkeiten der DFT deutlich, so dass klar wird, dass weiterführende Methoden zur Beschreibung des korrelierten Elektronensystems notwendig sind.

Als nächstes untersuche ich den gekoppelten Übergang durch die Kombination von DFT und DMFT. Dabei gelingt es, quantitative strukturelle Parameter für die gesamte Serie im isolierendem paramagnetischem Zustand zu berechnen. Ausserdem zeigt eine Analyse der Energetik der strukturellen *Breathing Mode*, dass es sich eindeutig um einen Phasenübergang erster Ordnung handelt, was wiederum in Übereinstimmung mit experimentellen Daten ist. Weiterhin zeigt sich, dass der Übergang durch eine elektronische Instabilität getrieben wird. Um dies besser zu verstehen, konstruiere ich ein Modell, dass das komplexe Problem auf die wichtigsten Parameter zur Beschreibung des Übergangs reduziert. Bei der Untersuchung dieses Modells zeige ich, dass die Bandbreite, die wiederum durch die Rotationen der Sauerstoffoktaeder bestimmt wird, entscheidend beeinflusst, wie nah das System an dieser elektronischen Instabilität ist, und somit die Trends der Serie bestimmt. Die hier gewonnen Erkenntnisse ermöglichen ein umfassendes Verständnis des paramagnetischen Teils des Phasendiagramms der Nickelate.

Im letzten Teil dieser Arbeit verwende ich DFT+DMFT Berechnungen, um den magnetischem Zustand der Nickelate zu beschreiben und den Übergang von dem isolierendem paramagnetischem, zum isolierendem antiferromagnetischem Zustand besser zu verstehen. Als Erstes zeige ich, dass DFT+DMFT den magnetisch geordneten Zustand korrekt erfasst. Anschliessend werden die Ergebnisse mit den magnetischen DFT+U Resultaten verglichen. Hierbei wird deutlich, dass für aussagekräftige Ergebnisse weitere Rechnungen notwendig sind, die dann das Verständnis der Kopplung zum Magnetismus in den Nickelaten verbessern würden. Dies wiederum würde ein umfassendes Verständnis des kompletten Phasendiagramms ermöglichen. Am Ende der Arbeit gebe ich auch einen Ausblick auf zukünftige Entwicklungen auf dem Gebiet der Nickelate und für die Verwendung der kombinierten DFT+DMFT Methode zur Beschreibung von funktionellen Materialien.

There are only two days in the year that nothing can be done. One is called yesterday and the other is called tomorrow. Today is the right day to love, believe, do, and mostly live.

— Dalai Lama XIV

ACKNOWLEDGMENTS

I would like to express my deep gratitude to everyone who accompanied me on my path to my PhD. This work would have not been possible without all the love, team spirit, and commitment of the people who have surrounded me in recent years.

First of all I would like to give special thanks to my supervisor Prof. Claude Ederer. I could not have imagined a better supervisor to guide me through the last four years. Thank you so much for your time and dedication. I would also like to thank Prof. Nicola Spaldin for creating such a wonderful working environment with almost unlimited possibilities and of course for the helpful discussions. Working in this group became something very special.

Next, I am very grateful for all my colleagues of the Materials Theory group. It was a truly amazing time. I cannot remember a single day when I was not looking forward going to work and enjoying your company. Everyone was always friendly and helpful, thank you. And, I will always remember all the hours I spend with you in activities such as running, tennis, skiing, bouldering, or just hanging out in a bar. I would also like to thank our secretary Susanne Blatter for organizing *everything* in no time at all. Having you was an unforgettable experience.

Moreover, I would also like to thank all my collaborators. Special thanks go to Prof. Antoine Georges, Oleg E. Peil, Manuel Zingl, and to Prof. Cesare Franchini for helping me on the technical side, which enabled me to use all the different methods during my doctorate. I would also like to thank Marisa Medarde for all the helpful discussions on nickelate experiments.

Last but not least, I would like to thank all my friends and my family. Especially for their patience and support during these years. Special thanks to my former colleagues Raphael and Lars, and to my friend Tobias, for bringing so much joy in my life. In particular I am very grateful that I had Sophie by my side during these years, who supported me so much both in private and at work. I would also like to thank Lina, who encouraged me and enabled me to begin my work at ETH Zurich. Moreover, I like to express my deep gratitude to my parents Claudia and Torsten, who have always been there for me during my studies and who have constantly supported me over the years.

CONTENTS

ACRONYMS

MIT metal-insulator transition

TMO transition metal oxides

AFM antiferromagnetic

CT charge-transfer

DFT density functional theory

DMFT dynamical mean field theory

DC double counting

DOS density of states

CSC charge self-consistent

CDI charge disproportionated insulator

LB long bond

SB short bond

KS Kohn-Sham

QMC quantum Monte Carlo

CT-QMC continuous-time QMC

GGA generalized gradient approximation

cRPA constrained random phase approximation

MLWF maximally localized Wannier functions

PLOs projection onto localized orbitals

AIM Anderson impurity model

AMF around mean-field

FLL fully localized limit

1 INTRODUCTION

Many of the advances in technology of the recent decades in areas such as more efficient semiconductors, better data storage, superconductors, construction materials, more durable and lighter composite materials, to name but a few, have been made possible by fundamental materials research. It is this very part of research that deals with finding completely new materials, developing approaches to design these materials, and to understand the underlying principles how they function. Although usually far away from a ready-to-deploy industry product, one can argue that the deep understanding of materials is the key to keeping progress alive, by paving the way for the next step of research or engineering, namely the realization and implementation of these insights into real products.

Complex transition metal oxides (TMO) are one of the pillars of modern materials research. These materials are often found in an ABO_3 perovskite structure, where B can be any of the transition metals. This family of materials exhibits a variety of phenomena that are of high interest for future technological applications [1–3], such as, e.g., multiferroicity [4], non-Fermi liquid behavior [5], high-temperature superconductivity [6], or metal insulator transitions (MIT's) [7]. Moreover, the progress in synthesis of these materials, especially thin film growth and heterostructuring, which allows to fine-tune their properties, boosted the research interest in this class of materials enormously [8, 9].

Perovskite transitional metal oxides are characterized by different competing phases, which change the material properties significantly and thus rich phase diagrams emerge. A prominent example are the family of cuprates that show different phases under chemical doping e.g. a metallic, a pseudogap phase, a superconducting state, and an antiferromagnetic (AFM) insulating phase [6]. Another example are the family of manganites, which show also under doping a rich variety of different magnetic orderings [10]. Moreover, various heterostructure compounds, build of TMOs, show phase transitions upon strain, or thickness dependent transitions [11].

Materials for which it is easy to control the above mentioned effects, for example tuning a MIT by applying external fields, are promising candidates to store or process data in information technology [11, 12]. Thereby, it is desirable to achieve fast switching times between metal and insulator, or other phases, which means that the material needs to be very close to the transition. Thus, multiple phases compete with each other on a very small energy scale. Then, modeling and

simulating these materials becomes a challenge, because the different interactions and mechanisms at play have the same magnitude, and need to be considered on the same footing. Such materials are nowadays called *quantum materials*, because their macroscopic properties are determined by quantum effects on a very small energy scale, and thus their properties are defined by the electronic structure close to the Fermi level [13]. If the electron interaction in the states close to the Fermi level is additionally strong, it often has a tremendous effect on the properties of the material. Such systems, where the electronic interaction is highly entangled with other properties of the system, are called strongly correlated electron systems [7].

The quantitative description of these correlation effects, due to electron many body physics is incredibly difficult. However, the theoretical approaches to capture these effects in *ab initio* electronic structure calculations made tremendous progress in recent years. Especially, the advances in combining density functional theory (DFT) with more advanced methods like dynamical mean field theory (DMFT) were significant, and now allow for treating electronic correlations in realistic material calculations on a very sophisticated level [14, 15]. However, these calculations are computationally very demanding, and one needs to carefully examine which degrees of freedom one can neglect to make calculations more feasible. Usually, the coupling of the electronic correlations to other effects, e.g. lattice (phonons) or magnetic ordering is neglected to make calculations more practicable.

The DFT+DMFT method has become the method of choice, to calculate spectroscopic properties of correlated systems from first principles over the past years. However, the prediction of structural properties has only been achieved very recently [16, 17]. First results show, that DFT+DMFT can indeed be used to predict structural properties of strongly correlated compounds, achieving better agreement with experiment compared to DFT [18]. Still, calculating the structural energetics within DFT+DMFT is computationally very demanding.

Rare-earth nickelates are a family of compounds that are a very prominent example for quantum materials exhibiting strong electronic correlations. They are located at the border between itinerant and localized electron behavior, and exhibit a MIT inherently coupled to a structural transition [19–21]. The MIT displays the characteristics of a Mott transition [22, 23]. Moreover, rare-earth nickelates display a distinct magnetic transition at lower temperatures, which is also coupled to electronic and structural properties. This interplay is sketched in Fig. 1. Thus, it becomes apparent that one has to model all three, structural, electron correlation, and magnetic effects on the same footing to render a coherent picture of the physics found in these compounds.

Since the synthesis of rare-earth nickelates is quite complicated, experimental data, especially temperature dependent structural data, is

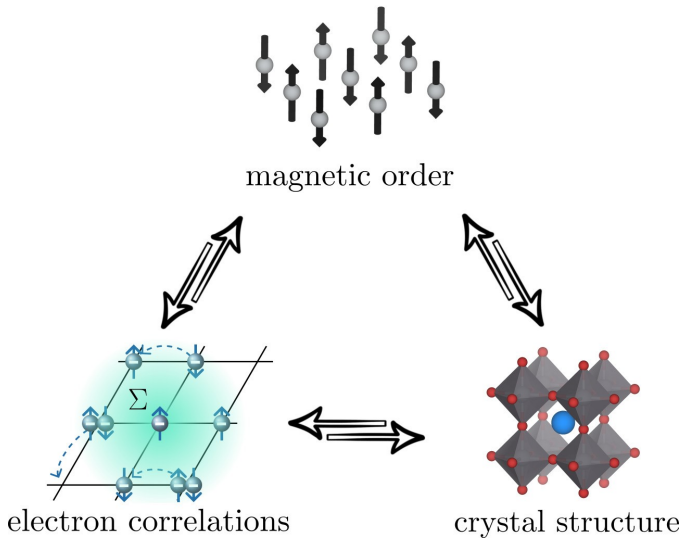

Figure 1: Schematic diagram of the interplay of the crystal structure, the magnetic order, and strong electronic correlations found in rare-earth nickelates.

quite sparse. Therefore, theoretical insights are highly valuable to better understand the coupling of structural and electronic degrees of freedom.

Pioneering work of Park *et al.* [24] showed that the DFT+DMFT method correctly describes the paramagnetic insulating state driven by electronic correlations in these compounds. Furthermore, the authors of Ref. [24] demonstrated that structural parameters can be obtained in agreement with experiment. On the other hand, early DFT calculations were also able to capture certain structural and magnetic aspects qualitatively correctly [24–26]. This was achieved, by introducing magnetic order in the calculations and accounting with an additional $+U$ term for static correlation effects. Although, these were important pieces of a puzzle, it was left unclear how a comprehensive coherent picture for the whole series can be drawn from these results. Especially, the nature of the coupled transition itself was not revealed, and no mechanisms were identified driving the trends across the series. Moreover, the connection of the MIT to the magnetic ordering has not been investigated.

1.1 GOAL AND STRUCTURE OF THIS THESIS

In this work I explore the possibilities of modeling the compounds of the rare-earth nickelates series by means of first principles methods. Thereby, I elucidate the interplay of the crystal structure, magnetic ordering, and strong electronic correlations found in these compounds,

giving rise to complex ordering phenomena. Special focus lies on the understanding of the combined electronic-structural transition, what key parameters drive trends across the series, and the complex magnetic ordering found in these compounds. To do so, I utilize DFT in combination with more advanced methods, e.g. DFT+U and DFT+DMFT, to capture the strong electronic correlations.

To achieve this, it is first necessary to understand in detail what results can be obtained from DFT alone. This includes mainly structural properties, and determining their trends across the series. Then, I utilize the DFT+U method, to investigate the influence of static correlation effects. Here, the goal is to systematically try different interaction parameter strengths and different magnetic orderings, to find out if and how correct structural trends can be obtained across the whole series. This ideally should also allow to draw a coherent picture of previous DFT+U results acquired for certain compounds of the series. Finally, the aim is to understand what properties and trends can be obtained correctly from the DFT+U method, and for which the more advanced description within DFT+DMFT is necessary.

This leads to the next part of this work utilizing the DFT+DMFT method. First, I derive a suitable low-energy model from DFT, which is capable to describe the paramagnetic insulating phase found in experiment. The goal is then to calculate structural parameters, and gain insights into the coupled electronic-structural transition by performing systematic calculations across the series. Thereby, trends across the series are obtained and analyzed, which are compared with experiments and DFT calculations. This further establishes the usage of the DFT+DMFT method to describe both electronic and structural degrees of freedom.

Finally, I try to gain insights into the magnetically ordered phase using DFT+DMFT to better understand its coupling to the MIT, which also allows for a direct comparison with DFT+U results. Furthermore, this pushes the boundaries of the DFT+DMFT method to allow the treatment of lattice, magnetic, and electronic degrees of freedom on the same footing, and thereby get a better fundamental understanding of the complex phase-diagram of rare-earth nickelates.

Besides, I will investigate certain technical aspects of the DFT+DMFT method that can have potential influence on results. Namely, the charge self-consistency between DFT and DMFT, the choice of interaction parameters in low-energy models, and also the crucial double counting (DC) correction between DFT and DMFT. This is of importance for future studies investigating other correlated materials where structural and electronic properties are coupled [18].

The thesis is structured as follows. In chapter 2, I give an introduction to rare-earth nickelates, thereby also introducing some general aspects of TMOs. Chapter 3 is dedicated to the theoretical framework used in this work. It covers all basics necessary to understand the

methods applied in this work. Furthermore, I pay specific attention to parts of the theory that are of special importance in the context of this work, such as the interface between DFT and DMFT, Coulomb interaction in low-energy Hamiltonians, and calculation of total energies in DFT+DMFT. Afterwards, the results obtained during my research are presented.

The results are presented in the form of my published research articles. For each of the published articles I first give an introduction, and motivation in the context of this thesis. Including a discussion of relevant literature. Furthermore, I provide additional information and results that have not been included in the corresponding articles, either necessary to understand it, or providing further insights. This is followed by a brief summary of the research article, and a conclusion in the context of this thesis. Finally, the article itself is included.

In chapter 4 I present a comprehensive DFT study on the interplay of magnetism and structural degrees of freedom across the nickelate series. Next, in chapter 5 I utilize DFT+DMFT to analyze the energetics of the breathing mode distortion in the paramagnetic state across the series, comparing also with results obtained in DFT. This is followed by a model study in chapter 6 analyzing the MIT itself, which has been carried out with Oleg E. Peil and Antoine Georges. Here, the mechanisms and control parameters of this coupled transition are identified. In chapter 7, I analyze the influence of charge self-consistency in DFT+DMFT, and thereby also of the DC correction, in charge ordered and orbitally polarized systems. Finally, I examine in chapter 8 the possibilities of the DFT+DMFT method to model the magnetic ordering of rare-earth nickelates. This is still ongoing work, without a published research article, and I present my preliminary results.

Chapter 9 concludes the work, and gives also an outlook for future directions of the applied method and nickelate research.

2

RARE EARTH NICKELATES

In this chapter I give a general introduction to the family of rare-earth nickelates. This includes general aspects of perovskite structures, as well as a review of results obtained by experiment. Moreover, I introduce basic theoretical concepts of d orbital physics typically found in perovskite structures, and discuss in this context also its relevance for nickelates.

2.1 THE PEROVSKITE STRUCTURE

Perovskites have the chemical composition ABX_3, where the cations A, B, and X can be a occupied by a variety of different atomic species. The ideal perovskite structure is cubic with space group $Pm\bar{3}m$, where the B cation sits in the center of the unit cell, the A site occupies the corner, and the X ions build an octahedra around the B site ion. See Fig. 2a for an example. The most often studied perovskite compounds are TMOs, where the B site is occupied by any 3d, 4d, or 5d transition metal. Furthermore, the X site is occupied by oxygen, and the A site is usually occupied by a rare-earth metal or an alkaline earth cation for a correct stoichiometry of the compound.

The stability of TMOs depends critically on the size difference of the A and B site cations. If A and B have the ideal size ratio, the ionic packing works perfectly, the A site cation fits perfectly in the empty spots in between the oxygen octahedra surrounding the B site cation, and a perfectly cubic lattice structure forms. The so-called Goldschmidt tolerance factor quantifies the size ratio as:

$$t = \frac{r_A + r_O}{\sqrt{2}(r_B + r_O)} \quad , \tag{1}$$

where r_A is the ionic radius of the A site cation, r_B is the radius of the B site cation, and r_O of the oxygen. If the ratio is close to one, a cubic lattice structure forms. If A is too big, or B too small, $t > 1$, either a different hexagonal crystal structure or a tetragonally distorted perovskite structure forms. If A is too small or B too large, $t < 0.9$, a orthorhombically or rhombohedrally distorted structure forms.

The change from the cubic structure to one of the above mentioned lower symmetries is caused by rotations of the oxygen octahedra to optimize the ionic packing. As an example the perfect cubic structure of $SrVO_3$ is shown in Fig. 2a, and in contrast in Fig. 2b the orthorhombic structure of $GdFeO_3$ is displayed, which has a tolerance factor of

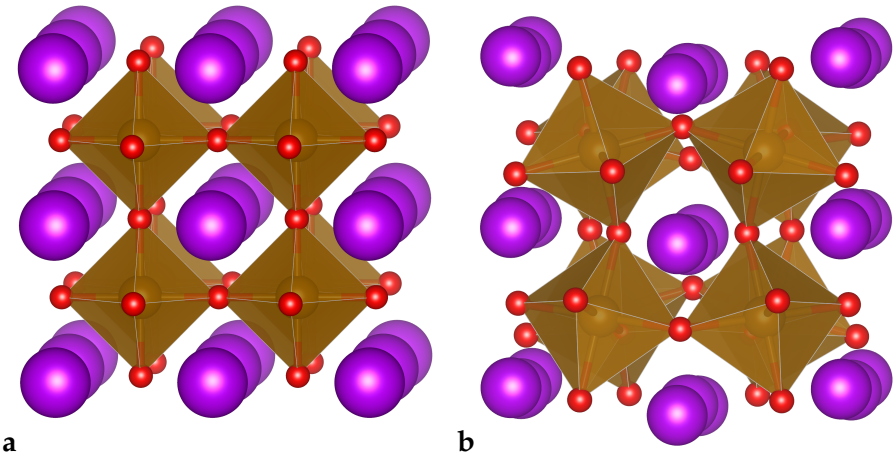

a **b**

Figure 2: Examples of perovskite structures. The A site cations are displayed in purple, oxygen atoms in red, and the B site cations located in the center of the oxygen octahedra in gray. **a** Cubic perovskite structure of $SrVO_3$. **b** Orthorhombic structure of $GdFeO_3$. The rotations of the oxygen octahedra, and the displacements of the Gd ions to best accommodate the space in between the oxygen octahedra can be seen.

$t = 0.81$. One can clearly see the rotations of the oxygen octahedra, and additionally the position adjustments of the A site cations, to fit best into the structure.

2.2 STRUCTURAL ASPECTS OF NICKELATES

The family of rare-earth nickelates compounds, $RNiO_3$, crystallizes in the perovskite structure. Here, R can be any rare-earth metal ion from La to Lu, and the resulting structures have a tolerance factor ranging from $LaNiO_3$ with $t = 0.94$ to $LuNiO_3$ with $t = 0.85$ [19]. Consequently, all compounds have lower than cubic symmetry, and crystallize in the orthorhombic space-group $Pbnm$ at high temperatures, except $LaNiO_3$, which is found to be in the rhombohedral space-group $R\bar{3}c$. It is therefore convenient to characterize the series by their tolerance factor, or by the resulting octahedral rotation angle Ni-O-Ni.

The phase diagram of the rare-earth nickelates series is depicted in Fig. 3 as a function of temperature and Ni-O-Ni rotation angle, with data extracted from various experiments. It can be seen, that depending on the choice of the R cation, the compounds show a MIT at varying temperatures. The MIT gradually decreases in temperature from Lu to La, where $LaNiO_3$ exhibits no MIT at all, and for $LuNiO_3$ the MIT occurs at ~ 600 K. This allows to study in a almost continuous fashion the crossover between itinerant and localized behavior, by changing the chemical composition. The MIT is rather unique, as it goes hand in hand with a structural transition lowering the space

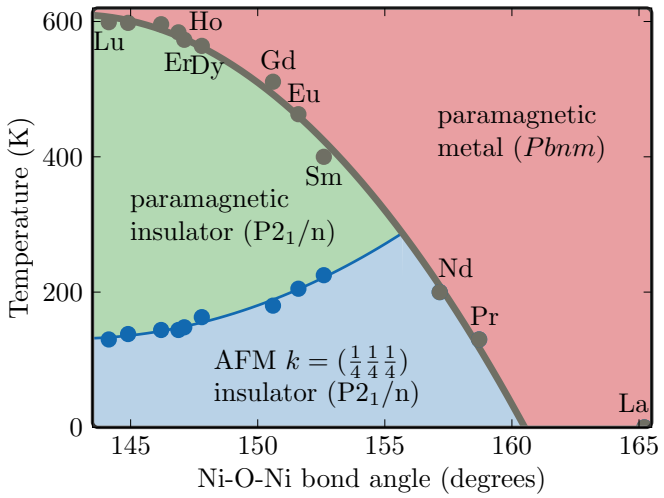

Figure 3: Phase diagram of the rare-earth nickelates. Transition temperatures are shown as function of the average Ni-O-Ni bond angle. Three different phases can be distinguished: i) paramagnetic metal with Pbnm symmetry (red), ii) paramagnetic insulator with $P2_1/n$ symmetry (green), and iii) AFM insulator with $P2_1/n$ symmetry (blue). Based on experimental data taken from Refs. [20, 27–32].

group symmetry from Pbnm to $P2_1/n$. Moreover, for the compounds with R=Lu to Sm the MIT occurs in the paramagnetic regime of the phase diagram. This combined structural and metal-insulator transition is of high interest, because of the strong coupling between electronic and lattice degrees of freedom. Furthermore, nickelates have a variety of potential applications, because the MIT can be tuned by pressure, strain, electromagnetic fields, and doping. [19–21, 34–36]

It can be seen from the phase-diagram in Fig. 3 that all nickelates compounds, except $LaNiO_3$, order antiferromagnetically at low temperatures. For compounds with R larger than Sm, the MIT temperature (T_{MIT}) and magnetic transition temperature (T_N) coincide. Thus, for compounds with R from Lu to Sm the AFM transition occurs at lower temperatures than the MIT. Initially, for $LaNiO_3$ no insulating or AFM phase has been found. However, recently AFM order has been reported in this compound [37], and is still under discussion [38]. It is therefore reasonable to assume, that $LaNiO_3$ is very close to the magnetic transition, which would also potentially make it insulating. It is quite interesting to note, that T_N as function of R is increasing, whereas T_{MIT} is decreasing. Moreover, it was pointed out in Ref. [25], that the magnetic transition breaks in principle the symmetry of the lattice even further making the nickelates potentially multi-ferroic [25]. However, in experiment no such lowering of symmetry has been observed yet.

Due to challenges in synthesis, experimental data on the bulk materials is relatively sparse, and especially large amount of powder samples are not easy to produce. Therefore, high precision neutron

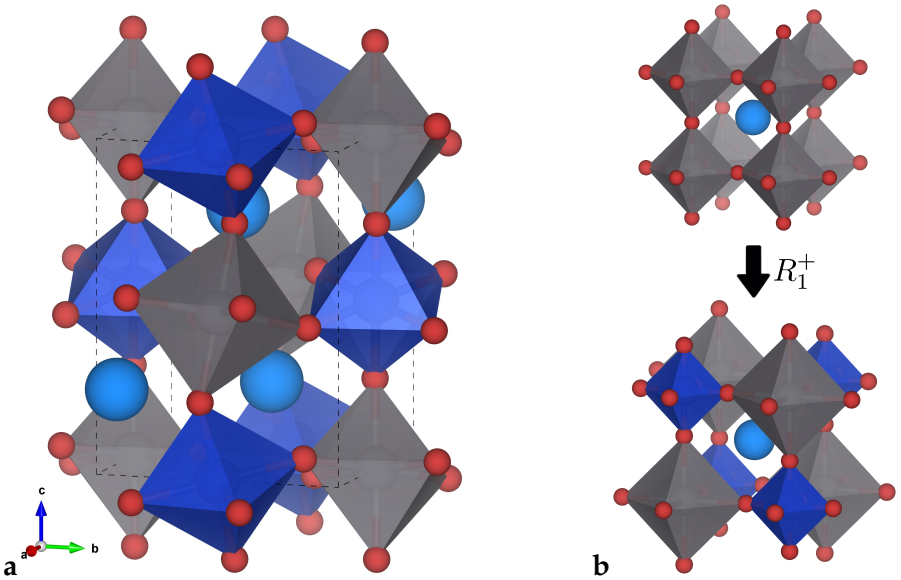

Figure 4: **a** Experimentally observed $P2_1/n$ crystal structure of $LuNiO_3$ at 60 K below the MIT [29]. LB octahedra around the Ni sites are shaded in gray, SB octahedra are shaded in blue, light blue spheres represent Lu, and red spheres represent O. The volumes of the bond-disproportionated NiO_6 octahedra differ by ~12 %. The crystal structure is visualized using VESTA [33]. **b** illustration of the breathing mode distortion (R_1^+ mode) in an idealized cubic structure.

experiments are hard to perform, and accurate data is not available for all systems. Although the first bulk nickelate sample has been synthesized and characterized in 1971 [39], the structural symmetry lowering from $Pbnm$ to $P2_1/n$ during the MIT was first observed almost 30 years later [30]. During the transition the formerly symmetry-equivalent NiO_6 octahedra in the $Pbnm$ phase become non equivalent within $P2_1/n$. One half of the NiO_6 octahedra expand their volume, while the other half reduces their volume by changing the Ni-O bond lengths accordingly. Eventually, a three-dimensional checkerboard-like arrangement of alternating long bond (LB) and short bond (SB) octahedra emerges in the insulating phase [28, 29], which is referred to as breathing mode distortion. The $P2_1/n$ structure of $LuNiO_3$ below the MIT is depicted in Fig. 4a [29]. The difference in volume between LB and SB octahedra for this structure is roughly ~ 12 %. To visualize the breathing mode distortion more clearly, Fig. 4b shows, in a schematic fashion, the arising checkerboard pattern of LB and SB octahedra without octahedral rotations.

The nature and exact mechanism of the coupled electronic-structural transition is still debated and is the central topic of this thesis. Considering the fact that the compounds are hard to synthesize, and therefore experimental data is sparse, it becomes

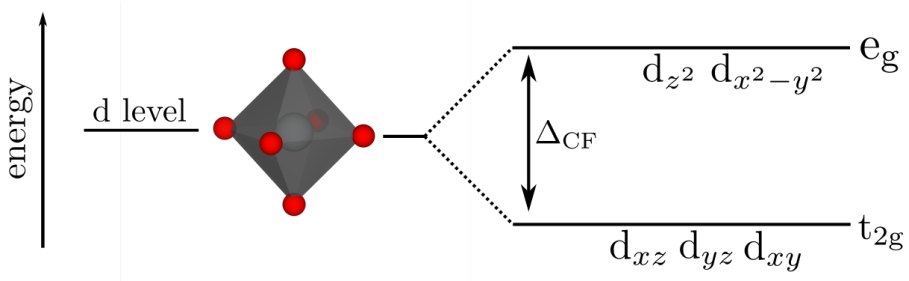

Figure 5: Splitting of d orbital levels, due to the octahedral crystal field splitting induced by the octahedral coordination. The degeneracy of the d orbital manifold is lifted and the three t_{2g} levels are split by Δ_{CF} from the two e_g states.

evident that theoretical insights into the materials properties are highly valuable.

2.3 d ORBITAL PHYSICS

To understand the properties of rare-earth nickelates it is crucial to understand their low-energy physics. In general, perovskite transition metal oxides show rich physics that arise due to the d electron valence states of the B site cations located at the Fermi level. Furthermore, these d states hybridize with the oxygen p states, with the hybridization strength depending on the orbital overlap of p and d states and their energy difference. This hybridization is tunable by external parameters depending on the distance between B site and oxygen. Furthermore, these intrinsic properties depend crucially on the rotation angles of the oxygen octahedra, since both p and d orbitals are highly directional. It is the complex interplay of both of these effects that determines the properties of TMOs, and thus gives rise to the rich physics found in TMOs. In the following, I introduce the basic mechanisms of this d orbital physics, important to understand the physics found in rare-earth nickelates.

The six oxygen atoms surrounding the B site cation in perovskites produce an octahedral crystal field, which lifts the degeneracy of the five d orbitals of the B site cation. For a perfectly cubic symmetric compound the d levels are split into three degenerate t_{2g} and two degenerate e_g states. For compounds with an orthorhombic space group, e.g. nickelates, the t_{2g} states are lowered in energy compared to the e_g states. Fig. 5 illustrates this phenomenon by showing a schematic level diagram. The degeneracy of the t_{2g} and e_g orbitals can further be lifted by distorting the oxygen octahedra.

In TMOs the bandwidth of the states close to the Fermi level, and thus the kinetic energy, is often small due to very confined electronic orbitals. Since, these states are determining the material properties, other effects on a similar energy scale, e.g. charge, orbital, and mag-

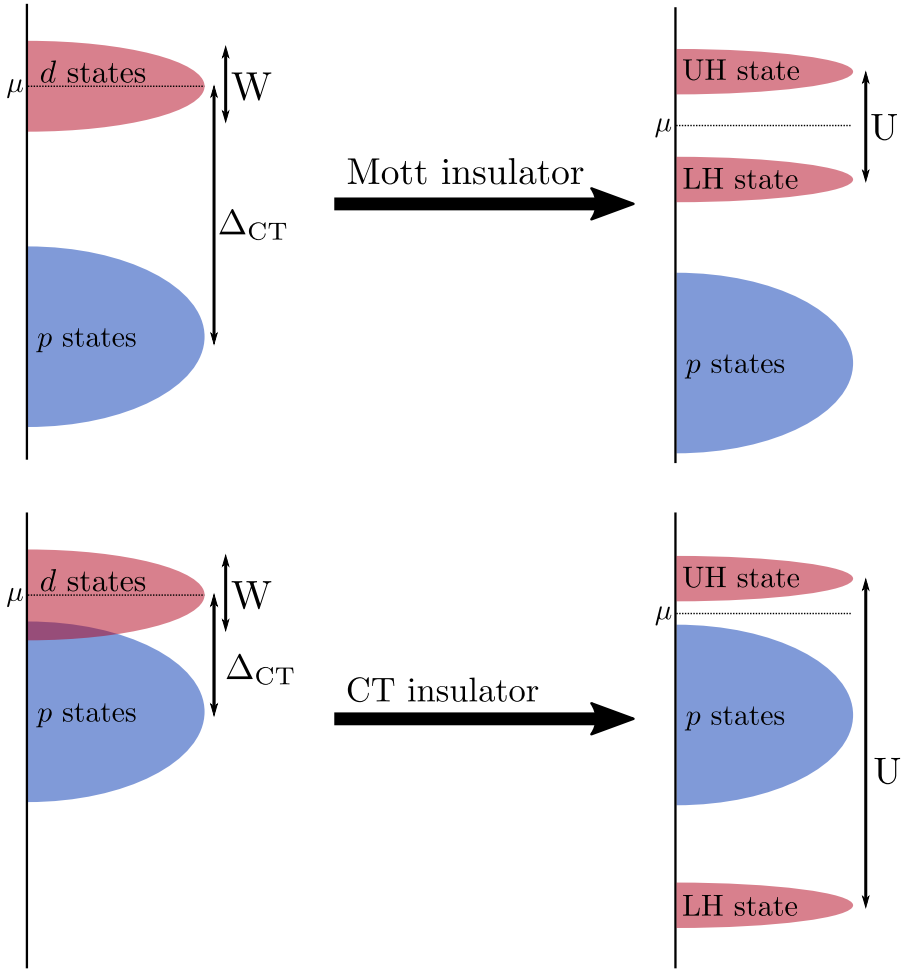

Figure 6: Top: transition from half filled d shell metal to Mott insulator. The d states are separated from the p states by the charge transfer energy Δ_{CT}. The local Coulomb interaction U overcomes the bandwidth W, hindering the electrons to move, and splits the d states into a lower Hubbard band (LH) and an unoccupied upper Hubbard band (UH). Bottom: transition from half filled d shell metal to charge transfer (CT) insulator, where $U > \Delta_{CT} > W$ and the LH bands are pushed below the p bands. The gap is openend between p and UH states.

netic ordering, can have a huge influence on the material properties. This becomes even more evident in situations, where multiple electronic states (bands) are degenerate, and these levels are not completely filled. If there exists now a mechanism that breaks the symmetry, and lowers the energy of some of these degenerate states, the system could potentially lower its energy by not occupying the states higher in energy. Furthermore, if the gain in energy is comparable with the kinetic energy, the system exhibits an instability for this mechanism, which lifts the degeneracy. One of the most prominent examples, especially in d^4, d^7, or d^9 systems, is the Jahn-Teller effect elongating the octahedra in one direction by lifting the e_g degeneracy.

Such a lifting of degeneracy often goes hand in hand with a MIT. In many cases this MIT cannot be understood in an effective, non-interacting, single particle picture, but is a so-called Mott transition [7]. The Mott transition occurs in localized electron states, when the local Coulomb interaction U overcomes the band-width W, hence the kinetic energy of the electrons. This prevents the electrons to hop from one atomic site to another, due to the high Coulomb energy U, which they would have to overcome. The transition is characterized by the occurrence of new electronic states, the so-called upper and lower Hubbard bands, above and below the Fermi level. Note, that the transition does not involve any long range magnetic order, and does not have to necessarily require a symmetry lowering distortion.

Therefore, the strong electron interaction in TMOs with very confined d electrons, can drive the system from itinerant to localized behavior. This effect is particularly pronounced if the valence states are half-filled, as for every hopping process the Coulomb interaction U has to be paid. If U is larger than W, the system undergoes the MIT. This is depicted in the top of Fig. 6. For a traditional Mott transition the oxygen p states are rather low in energy compared to the d states of the B site cation.

Another scenario would emerge if U is larger than the difference in energy between p and d states. This energy splitting is called charge-transfer (CT) energy Δ_{CT}, and according to Zaanen *et al.* [40] the Mott transition results in a different state of the systems. Here, the hybridization between d and p orbitals is very strong, and one cannot describe the transition in atomic d states solely. The gap opens between the hybridized oxygen p states (the ligand states) and the upper Hubbard band of the transition metal d state. Thus, in this case it is the CT energy that determines the size of the gap. This transition is depicted in the bottom of Fig. 6. One can classify these different systems by Δ_{CT} and U. If $U < \Delta_{CT}$ the system is a classic Mott-Hubbard insulator, whereas for $U > \Delta_{CT}$ the system is a CT insulator. Typical systems that belong to the Mott-Hubbard insulator class, are titanates, vanadates and some ruthenates, and examples for CT insulators are MnO, cuprates, or NiO.

Interestingly, rare-earth nickelates behave differently than the above mentioned systems. Although, according to the scheme of Zaanen *et al.* [40] nickelates should be metallic since they have a very small U, and a small Δ_{CT} compared to W, in experiment a paramagnetic MIT is observed. They can neither be characterized as normal Mott-Hubbard insulator, nor like a CT insulator. The Ni cations are in a d^7 configuration, where all t_{2g} states are completely filled. One electron occupies the degenerate e_g states, which are well separated from the t_{2g} states. Even though, this configuration should in principle be susceptible to a Jahn-Teller distortion that lifts

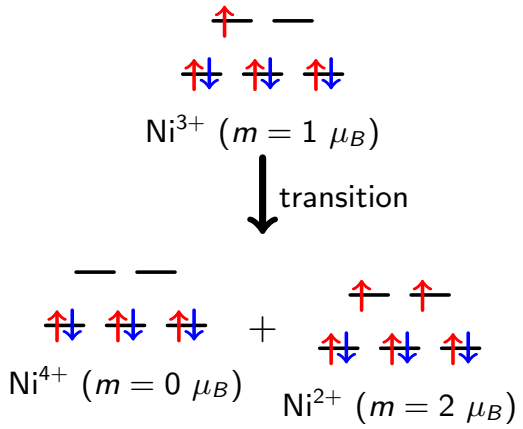

Figure 7: Charge disproportionation as alternative to Jahn-Teller Distortion as suggested by Mazin *et al.* [22]. Before the transition, in the high-temperature metallic phase, all Ni cations are in a Ni^{3+} configuration. During the transition one Ni cation gives away an electron going to a Ni^{4+} configuration, and hence becoming insulating. The nearest neighbor Ni cation takes this electron becoming Ni^{2+}. This half filled e_g state then undergoes a Mott-Hubbard insulator transition.

the degeneracy, as for example in the manganites [41], no signs of such a distortion are observed in experiment [21].

2.4 CHARGE DISPROPORTIONATED INSULATOR

Mazin *et al.* [22] proposed that instead of lifting the degeneracy of the e_g states on each Ni site by the JT effect, the system undergoes a transition into a charge ordered state. Thereby, it gets rid of the degeneracy by moving one electron from one Ni site to a nearest neighbor. This transition is depicted in Fig. 7 and is described as:

$$2Ni^{3+} \rightarrow Ni^{4+} + Ni^{2+} \quad . \tag{2}$$

Now, on one Ni site the e_g states are completely empty, leaving a gap to the completely filled t_{2g} states at lower energy, and on the other Ni site the e_g orbitals are half-filled. The half-filled Ni site can now undergo a Mott-Hubbard transition, resulting in a paramagnetic insulating state. This transition has been characterized as a site-selective Mott insulator [23].

This mechanism is favorable, because of the strong hybridization of Ni e_g and oxygen p states. Therefore, the Coulomb interaction in the Ni e_g orbitals is highly screened in rare-earth nickelates. Such a reduction is especially strong in systems with a small or negative Δ_{CT}. On the other hand, the Hund's rule coupling J_H is hardly sensitive to screening, and is therefore large compared to the screened U. J_H favors configurations that maximize the spin, thus making it energetically favorable to occupy a single Ni site with both electrons,

and thus a larger local moment. If J_H is sufficiently large compared to U the system can overcome the additional cost of U, which needs to be paid if both electrons occupy the same Ni site, and the charge ordered state is favored. The charge disproportionation goes hand in hand with the SB / LB Ni-O octahedra arrangement, with the Ni_{LB} site having more electrons.

So far, I described the transition with atomic-like orbitals. However, recent calculations and experiments showed that the transition does not necessarily goes along with a strong charge disproportionation [23, 42–45]. Because, of the strong hybridization between p and d states, hence small Δ_{CT}, a purely atomic point of view of the transition might in some cases be misleading. Therefore, one can describe the transition also in a ligand picture, where the configuration is described including the oxygen p ligands. In this picture the lowest excitation of an electron is for example $d^n \rightarrow d^{n+1}L$, leaving a hole in the oxygen p states, denoted by L. The transition can be then described as [46]:

$$(d^8L)_i + (d^8L)_j \rightarrow (d^8L^2)_{SB} + (d^8)_{LB} \quad . \tag{3}$$

Contrary, one can also make use of Wannier functions built from the low-energy states around the Fermi level (see also section 3.3 for more details). These orbitals involve both, d and p states, and one can thus understand these as effective orbitals containing also partially the ligand states. This has the advantage that occupation changes are easy to understand, because they correspond directly to band occupations. However, both approaches are equally valid as shown in Ref. [44], as long as one keeps in mind in which picture one interprets the physics.

Consistent with both pictures a strong modulation of the magnetic moments in the antiferromagnetically ordered phase is found in experiment [31, 47]. In the ligand hole picture the ligand holes screen the magnetic moment of the Ni_{SB} site, whereas the Ni_{LB} site have a spin configuration of $S = 1$ [22]. Interestingly, the AFM transition is of second order for all compounds $T_{Neel} \neq T_{MIT}$, but also first order for the compounds $T_{Neel} = T_{MIT}$ [48].

The exact nature of the transition is still debated in literature. Experiments show that all members of the series exhibit a hysteresis across the paramagnetic MIT transition, which is almost completely smeared out by temperature effects for some of the compounds [19]. Such hysteresis indicates a first order phase transition. However, whether both structural and electronic transition work cooperatively, or if the electronic or the structural transition are triggering the transition, is still subject of research. This was only addressed in the recent two to three years [49–51].

The understanding of this coupled transition is one of the main aspects of this thesis. Before my PhD research, different theoretical

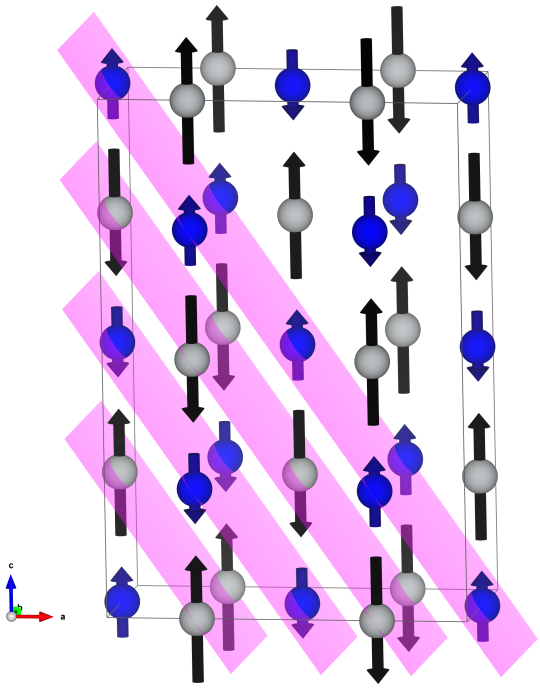

Figure 8: Sketch of a possible magnetic ordering of rare-earth nickelates corresponding to the $(1/4\ 1/4\ 1/4)_{pc}$ wavevector. The ordering is characterized by an $\uparrow\uparrow\downarrow\downarrow$ ordering in all directions of the lattice, where large Ni_{LB} site (gray spheres) magnetic moments (black arrows) and small Ni_{SB} site (blue spheres) magnetic moments (blue arrows) alternate. The structure is also characterized by ferro-magnetically coupled planes along the $(111)_{pc}$ direction.

and computational approaches have highlighted different aspects of the coupled structural-electronic transition in the nickelates, thereby focusing either on structural or electronic aspects [23, 24, 43, 52], but lacking a complete picture of all aspects.

The physics observed in rare-earth nickelates can also be found in other highly covalent TMO compounds, with B site cations like Cu^{3+}, Ni^{3+}, or Fe^{4+}. They exhibit also a small or even negative Δ_{CT}, and depending on the band-width W and Coulomb interaction U show similar behavior. For example, $NaCuO_2$, $LiNiO_2$, and $CaFeO_3$, are also found to be insulating at low temperatures [19, 46, 53].

2.5 MAGNETIC ORDER

As described above all nickelates compounds, except $LaNiO_3$, order antiferromagnetically at low temperatures. The existence of the ordering was probed and confirmed by neutron and resonant soft x-ray diffraction measurements. The order is characterized by the wavevector of $k = (1/4\ 1/4\ 1/4)_{pc}$ in pseudocubic notation, or by $k = (1/2\ 0\ 1/2)_{or}$ in orthorhombic notation [54–56]. Therefore, the AFM pattern has a periodicity of four Ni sites in all lattice directions.

However, besides the ordering wavevector it is still debated whether the ordering is collinear or not, and also how large the SB Ni site moments are. It is evident, that the moments are different in size, but some neutron data even suggests that the SB Ni moments vanish completely, whereas X-ray experiments on thin-films suggest a non-vanishing SB moment with a non-collinear ordering [31, 47, 57]. The progress in experiment is hindered for the bulk phase by the lack of sufficient samples. More experimental data is available for thin films. However, since this work deals with the investigation of the bulk phase diagram, I do not specifically introduce the rich topic of rare-earth nickelate thin-films. An overview over recent progress can be found in the review article of Catalano *et al.* [19].

A magnetic ordering compatible with the found wave vector $k = (1/4\ 1/4\ 1/4)_{pc}$ is shown in Fig. 8. Here, a collinear ordering with $\uparrow\uparrow\downarrow\downarrow$ ordering in all directions of the lattice is shown, where the large LB and small SB Ni moments alternate. This ordering forms ferromagnetically coupled planes perpendicular to the $(111)_{pc}$ direction. The rare-earth moments (not displayed in the figure) order at very low temperatures below ~10 K, and Ref. [31] suggests the same periodicity of Ni and Dy moments in $DyNiO_3$. Contrary, in Ref. [47] a different magnetic periodicity of the rare earth moments relative to the Ni moments is reported in $HoNiO_3$. However, due to the low ordering temperature compared to T_N, the ordering of the rare-earth magnetic moments is most probably not critical to the mechanism of the MIT.

Already from the phase diagram in Fig. 3 it can be seen, that the interplay of the AFM ordering and the MIT is quite complex. For example, T_N increases for increasing R cation size, whereas T_{MIT} gets lower in temperature. Furthermore, for $NdNiO_3$ and $PrNiO_3$ both transition coincide. Ruppen *et al.* [58] and Girardot *et al.* [59] investigated the magnetic transition of $SmNiO_3$ and $NdNiO_3$, and found clear differences between the magnetic transition in compounds with $T_N = T_{MIT}$ and $T_N \neq T_{MIT}$. They suggest a structural and electronic change at T_N for $SmNiO_3$, which means there exists clearly a coupling of structural and electronic degrees of freedom to the magnetic ordering. Furthermore, the magnetic ordering itself lowers the symmetry of the compound making it potentially multi-ferroic [25].

From theoretical calculations, the complex AFM order can be obtained as well, and it is one of the topics in this thesis to better understand the interplay of the magnetic ordering with the other degrees of freedom. Of course, various other studies exist that shine light on these properties as well, which is highlighted and discussed at the appropriate point in this work.

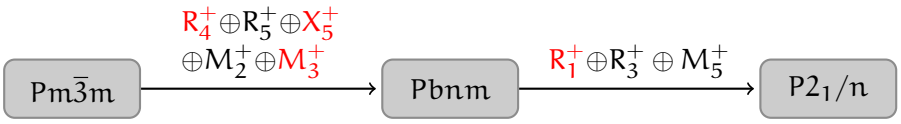

Figure 9: Subsequent symmetry lowering of the cubic perovskite structure due to lattice distortions. Starting from cubic undistorted $Pm\bar{3}m$ the symmetry gets first lowered to $Pbnm$, which is the nickelate high temperature metallic structure. During the MIT the symmetry gets further lowered to $P2_1/n$ in the low temperature regime of nickelates. The important non-negligible distortion amplitudes are highlighted in red.

2.6 DISTORTION MODE DECOMPOSITION

As it can be seen from the phase diagram in Fig. 3, the degree of octahedral rotations in the nickelate series changes quite drastically from R=La to Lu, due to the changes in the rare-earth ion radii. Moreover, experimental data from different compounds hints to the fact that the amplitude of the breathing mode changes as well when the rare-earth ion is changed [29, 31, 60, 61]. Hence, it becomes evident that the transition temperature and breathing mode strength depend critically on the other structural aspects, e.g., the lattice distortions deviating from the high-symmetry cubic structure. Therefore, it appears necessary to describe the lattice distortions in a quantified and well-defined manner, which ideally should also be intuitive.

A very systematic way of describing structural distortions is presented in the paper of Perez-Mato *et al.* [62], where the structural distortions found in a low-symmetry structure are decomposed in a basis of symmetry-adapted distortion modes. Thereby, the distorted atom positions $\vec{r}_i^{\,dist}$ are described by the undistorted positions $\vec{r}_i^{\,0}$ in the corresponding high symmetry reference structure plus all distortions described by normalized displacement vectors $\vec{d}_{im}$ with a certain amplitude A_m:

$$\vec{r}_i^{\,dist} = \vec{r}_i^{\,0} + \sum_m A_m \, \vec{d}_{im} \quad . \tag{4}$$

In this way it is possible to describe all tilts of the octahedra and other changes of atomic positions by distortion mode amplitudes. For nickelates this was first done in detail in the work of Balachandran & Rondinelli [63] for the experimental structures with the following rare earth ions: Lu, Ho, Y, Er, Nd, Pr and Dy.

For the high temperature $Pbnm$ structure, there are the following 5 possible distortion modes:

- R_4^+: out-of-phase rotation of oxygen octahedra
- R_5^+: bending/buckling mode of oxygen octahedra

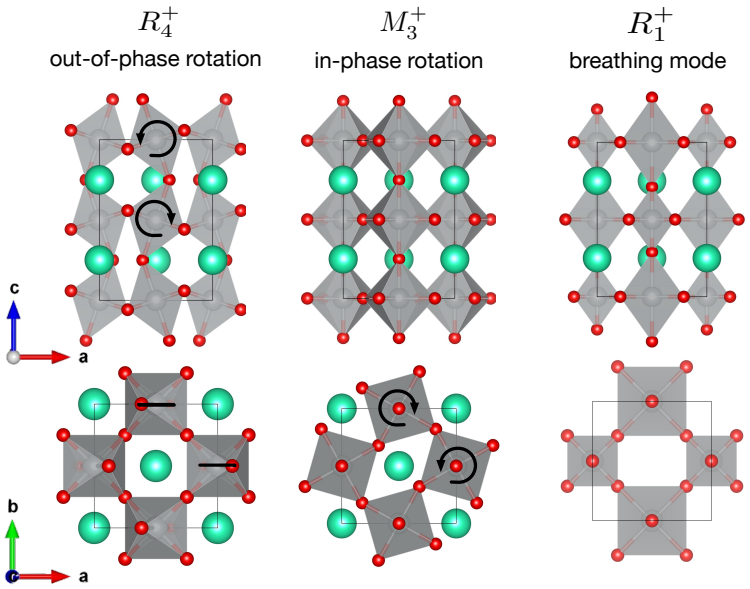

Figure 10: Depiction of the three most important distortion modes found in nickelate compounds. NiO_6 octahedra are shown in gray. The R_4^+ $Pbnm$ mode that corresponds to an out-of-phase rotation of NiO_6 octahedra around the orthorhombic b axis, the M_3^+ $Pbnm$ mode that corresponds to an in-phase rotation of NiO_6 octahedra around the c axis, and the R_1^+ $P2_1/n$ mode that corresponds exactly to the bond-disproportionation of NiO_6 octahedra in the low temperature phase of the nickelates.

- X_5^+: in-phase tilting of Ni-O-Ni bond
- M_2^+: Jahn-Teller type
- M_3^+: in-phase rotation of oxygen octahedra

and for the low symmetry $P2_1/n$ phase there are 3 additional modes:

- R_1^+: breathing mode of oxygen octahedra
- R_3^+: Jahn-Teller type
- M_5^+: out-of-phase tilting of Ni-O-Ni bond

The symmetry label is given by the change and symmetry of the atomic positions, where this notation is taken from [63]. In this reference one can find additionally a depiction (fig. 5 in [63]) of the distortion modes for the nickelate structures. Note, that the exact labeling depends on the choice of the origin of the unit cell. The process of subsequent symmetry lowering is schematically displayed in Fig. 9. While all of the above mentioned modes can in principle be present in the $Pbnm$ respectively $P2_1/n$ structures, according to the available experimental data (and confirmed by my calculations), only the following modes have non-negligible amplitudes R_4^+, X_5^+, M_3^+, and R_1^+. Fig. 10 depicts the R_4^+, M_3^+, and R_1^+ distortion modes.

With this description of the distortion modes it is possibility to describe and compare the nickelate structures by means of symmetry adapted distortion mode amplitudes. Hereby, one can clearly separate the different distortions in a more intuitive form than comparing Wyckoff positions. The actual computation of these distortion mode amplitudes in this work is done with the software ISODISTORT [64] from Campbell *et al.* [64].

This concludes the review of rare-earth nickelates within the context of this thesis. Of course this only highlights specific aspects, necessary to understand the broader picture of this research. For further reading, and a more profound overview of nickelate research I like to refer the reader to the recent review of Catalano *et al.* [19], or the Ph.D. thesis of Scherwitzl [65].

3

DESCRIPTION OF CORRELATED MATERIALS FROM FIRST PRINCIPLES

The goal of this work is a parameter-free description of rare-earth nickelates, by means of first-principles calculations. This means, that the only input for the calculation is a first guess for the unit-cell and atomic positions of the system. The calculation scheme should allow to investigate the coupling of structural, magnetic, and electronic degrees of freedom, to understand the phase-diagram of the nickelates series.

To achieve this, the Schrodinger equation of the quantum system of a solid:

$$\mathcal{H}\,|\Psi\rangle = E\,|\Psi\rangle \tag{5}$$

needs to be solved. In the non-relativistic limit, the Hamiltonian $\mathcal{H}$ for this many body system has the general form:

$$\begin{aligned}\mathcal{H} = &\sum_{j=1}^{M} \frac{-\hbar^2}{2M_j}\nabla^2_{R_j} + \sum_{i=1}^{N} \frac{-\hbar^2}{2m_e}\nabla^2_{r_i} \\ &+ \frac{1}{2}\sum_{i\neq j}^{M} \frac{e^2 Z_i Z_j}{4\pi\epsilon_0 |R_i - R_j|} - \sum_{i=1}^{N}\sum_{j=1}^{M} \frac{e^2 Z_j}{4\pi\epsilon_0 |r_i - R_j|} \\ &+ \frac{1}{2}\sum_{i\neq j}^{N} \frac{e^2}{4\pi\epsilon_0 |r_i - r_j|} \quad ,\end{aligned} \tag{6}$$

where M are nuclei at positions R_j with masses M_j and charges $Z_j e$, plus N electrons at positions r_i with masses m_e. In this case the many body wave function $|\Psi\rangle$ depends on the position and spin configurations of all $N + M$ particles in the system

$$|\Psi\rangle = |\Psi(\{\mathbf{R}, \sigma\}, \{\mathbf{r}, \sigma\})\rangle \quad . \tag{7}$$

It is clear that such a problem cannot be solved directly, because the many-particle problem and its wave function depend on the position and spin configuration of all particles in the solid, a number exceeding all computational limits. Therefore, the eigenvalue problem can only be solved under certain approximations. This chapter introduces the methods and tools for solving the Hamiltonian using suitable approaches.

The first simplification is the so-called "adiabatic" or "Born-Oppenheimer approximation". Since the mass of the nuclei is several orders higher than that of the electrons and therefore their movement

is much slower, one can factorize these two parts within the wave function. Therefore, one only considers the electronic system, and the nuclear degrees of freedom enter only has an potential $V(\mathbf{r})$ produced by the nuclei. The Hamiltonian for the electrons thus reads:

$$\mathcal{H} = \sum_{i=1}^{N} \left[\frac{-\hbar^2}{2m_e} + V(\mathbf{r}_i) \right] + \frac{1}{2} \sum_{i \neq j}^{N} \frac{e^2}{4\pi\epsilon_0 |\mathbf{r}_i - \mathbf{r}_j|} \quad . \tag{8}$$

However, the Hilbert space still growths exponentially with the number of electrons, and a general solution is not yet within reach.

In 1964, Hohenberg & Kohn [66] proposed a theorem that has proven to be of tremendous importance to make the solution of the above Hamiltonian feasible. They showed that all ground-state properties of the interacting electron gas are uniquely determined by the ground-state electron density $\rho(r)$ alone, without the need to calculate the many body wave function. In contrast to the wave function, the electron density depends only on three spatial coordinates, and is therefore easier to handle.

This theory proposed by Hohenberg & Kohn [66] and Kohn & Sham [67] known as density functional theory, has been further developed to solve the electron problem of a solid. The method was very successful in recent decades describing many material properties that were not accessible before. Nowadays, it is *the* method of choice for describing solid state material properties from first principles calculations. Truly speaking, there is no other alternative for solids. Quantum chemistry methods and model Hamiltonians are both powerful methods, but they are either limited to finite size systems, or, not fully *ab-inito*.

3.1 DENSITY FUNCTIONAL THEORY

The idea of Hohenberg & Kohn [66] was to use the electron density as the main quantity to describe the quantum mechanic system:

$$\rho(\mathbf{r}_1) = N \cdot \int d\mathbf{r}_2 \cdots \int d\mathbf{r}_N \, |\Psi(\mathbf{r}_1, \ldots, \mathbf{r}_N)|^2 \quad , \tag{9}$$

which depends only on 3 spatial variables. Importantly, it was shown in Ref. [66] that the full many particle ground state is a unique functional of the ground state electron density $\rho_0(\mathbf{r})$. Additionally, Hohenberg & Kohn [66] proved that a well constructed energy functional of $\rho(\mathbf{r})$ will be minimal if, and only if, the electron density $\rho(\mathbf{r})$ is the ground state electron density $\rho_0(\mathbf{r})$:

$$E[\rho] \geqslant E[\rho_0] \quad . \tag{10}$$

By minimizing the energy as a functional of the electron density $\rho(\mathbf{r})$ one obtains the ground state density. Then, in principle, all ground state properties can be determined from the density.

In Ref. [67] these two so-called Hohenberg-Kohn theorems are applied to solve a general many body problem, by mapping the interacting problem onto an effective one-particle model:

$$\left[-\frac{\hbar^2}{2m}\Delta + V_{\text{eff}}(\mathbf{r})\right]\Psi_i(\mathbf{r}) = \epsilon_i\Psi_i(\mathbf{r}) \quad . \tag{11}$$

This effective model is constructed in a way that it has the same ground state electron density as the original interacting problem. The effective, Kohn-Sham (KS), potential reads

$$V_{\text{eff}}(\mathbf{r}) = V_{\text{ext}}(\mathbf{r}) + \underbrace{e^2\int d\mathbf{r}'\frac{\rho(\mathbf{r}')}{|\mathbf{r}-\mathbf{r}'|}}_{V_H} + V_{xc}[\rho] \quad . \tag{12}$$

The effective potential consists of the external potential of the nuclei, the classical Coulomb interaction (Hartree interaction), and the exchange-correlation potential $V_{xc}[\rho]$, which includes all many body effects that go beyond classical Hartree interaction. As both V_H and V_{xc} depend on the electron density of all electrons, they act as a static mean field in which each of the electrons move.

The corresponding KS energy functional reads:

$$E_{KS}[\rho] = T_s[\rho] + \int \rho(r)V(r) + \frac{1}{2}e^2\int\int d\mathbf{r}'\,d\mathbf{r}\frac{\rho(\mathbf{r})\rho(\mathbf{r}')}{|\mathbf{r}-\mathbf{r}'|} + E_{xc}[\rho] \quad . \tag{13}$$

Here, $T_s[\rho]$ represents the kinetic energy functional of the non interacting KS system in Eq. 11. The exchange correlation functional as the general form:

$$E_{xc}[\rho] = (T[\rho] - T_s[\rho]) + E_x[\rho] + E_c[\rho] \quad , \tag{14}$$

where the fist term is the kinetic energy difference between the interacting and non-interacting problem, E_x is the exchange energy, and E_c the correlation energy. At the moment the exchange-correlation functional is just a construct, which should map the real system exactly, and its form is not known.

After solving Eq. 11, the effective one-particle wave functions of the system are obtained and the electron density can be obtained as

$$\rho(\mathbf{r}) = \sum_i^{\text{occ}} |\Psi_i(\mathbf{r})|^2 \quad . \tag{15}$$

This set of equations allows to solve in an iterative fashion the original interacting problem, by starting with an initial guess for $\rho^{(0)}(r)$, which can be taken as the sum of the densities of the individual atoms comprising the system. To calculate then the ground state density of the system one follows this self-consistent scheme:

$$\rho^{(0)}(\mathbf{r}) \xrightarrow{\text{Eq. 12}} V_{\text{eff}}^{(0)}(\mathbf{r}) \rightarrow \text{solve KS equation 11} \rightarrow \Psi_i^{(0)}(\mathbf{r})$$
$$\rightarrow \rho^{(1)}(\mathbf{r}) \rightarrow \text{check if self-consistent} \xrightarrow{\text{no}} V_{\text{eff}}^{(1)}(\mathbf{r}) \rightarrow \ldots$$

To minimize the energy in Eq. 13 a suitable minimization (or mixing) procedure is applied for $E_{KS}[\rho]$ each time a new ρ is determined before a new V_{eff} is constructed.

Besides the ground state density, this method also yields as a solution the ground state energy, and the eigenvalues and eigenstates of the KS system. Therefore, also forces to relax the atomic positions can be calculated. Moreover, the scheme can be easily extended to systems involving spin-polarization [68], by making the potential, and electron density, spin-dependent. Hence, allowing the calculation of magnetic properties.

Even though the ground state density is exactly the one of the real system, one should always keep in mind that the calculated eigenvalues, and hence possible excitation energies or other related observables, belong to the auxiliary KS system, and have no true physical meaning per se. However, the density of states (DOS) and band structure of the KS system have been proven to be astonishingly representative for the real system, and hence from now on I use these calculated properties as first approximation for the real system.

Importantly, no approximations were made so far, which means, if the exact exchange correlation functional would be known, the interacting many body problem would be solved exactly.

3.1.1 *Exchange correlation functionals*

Unfortunately, the exact form of the exchange correlation functional is not known, and therefore approximations have to be devised.

The by far most successful and most universal exchange correlation functional is the "Local Density Approximation" (LDA) functional [67], which is constructed from the homogeneous electron density limit. Here, one describes E_{xc} as an integral over $\mathbf{r}$ with an integrand that depends only on the local value of $\rho(\mathbf{r})$. The exchange correlation energy under the integral is taken from a homogeneous electron gas ϵ_{xc} with the electron density ρ:

$$E_{xc} \approx E_{xc}^{LDA}[\rho(r)] := \int d^3\mathbf{r}\ \epsilon_{xc}[\rho(\mathbf{r})]\rho(\mathbf{r}) \quad . \tag{16}$$

ϵ_{xc} can be obtained with great accuracy from quantum Monte Carlo (QMC) calculations [69], and can be easily extended to describe spin-polarized systems. The approximation can be motivated by the fact, that for example in simple metallic systems the electron density should be very homogeneous, and hence close to a uniform electron gas. The LDA proved to be very successful in practical applications, also for systems with strongly varying electron densities, due to very robust and consistent error cancellation, which makes it a very reliable approximation for various systems [70, 71].

Another important E_{xc} functional in the scope of this work is the generalized gradient approximation (GGA) proposed by Perdew *et al.*

[72]. This family of functionals considers also the gradient of the electron density:

$$E_{xc}^{GGA}[\rho_\uparrow, \rho_\downarrow] := \int d^3r \; f_{xc}[\rho(\rho_\uparrow, \rho_\downarrow, \nabla\rho_\uparrow, \nabla\rho_\downarrow)]\rho(\mathbf{r}) \quad . \tag{17}$$

If properly constructed, fulfilling exact condition and limits of the E_{xc} of the system, GGA produces generally very good results. One of the most used flavors of the GGA is the PBE functional introduced by Perdew *et al.* [73]. However, in contrast to LDA, which often underestimates bond lengths, GGA tends to overestimate them.

In recent decades, many more exchange correlation functionals have been developed. A overview over the available functionals is given in the book of Martin [74] in chapter 8.

3.1.2 *Projector augmented wave method*

To practically solve the KS equations, Eq. 12, for any system, one has to chose a suitable basis set in which the wave function of the effective Hamiltonian is represented.

In periodic systems, Bloch's theorem holds [75]. Therefore, any solution of the KS equation $\Psi(\mathbf{r})$ can be characterized by a wave-vector $\mathbf{k}$ within the first Brillouin zone, and can be represented naturally in a plane wave basis:

$$\Psi_{\mathbf{k}\nu}(\mathbf{r}) = \sum_{\mathbf{G}} c_{\nu,\mathbf{k}+\mathbf{G}} \; exp(i(\mathbf{k}+\mathbf{G})\cdot\mathbf{r}) \; . \tag{18}$$

Here, $\mathbf{G}$ is a Bravais vector of the reciprocal lattice, and $\mathbf{k}$ a vector in the first Brillouin zone.

Numerically, one is bound to a finite set of plane waves. The number of plane waves is determined by a energy cut-off E_{cut} for the kinetic energy:

$$\frac{\hbar^2|\mathbf{k}+\mathbf{G}_{cut}|^2}{2m} \; < \; E_{cut} \quad . \tag{19}$$

Using plane waves has the advantage that the solution behaves very systematic with respect to the energy cut-off. In some cases a large number of plane waves is needed for convergence, but the eigenvalues and eigenstates will converge smoothly with an increasing cut-off energy.

These advantages of plane-waves are also their biggest drawback. Since they are localized in $\mathbf{k}$ space they are completely delocalized in real space, and hence, a large number of plane waves is needed to describe the rapidly varying wave function close to the core of the nuclei. To overcome this problem, a possible solution is to replace the wave function close to the core by a smoothly varying function, such as the projector augmented wave (PAW) method developed by

Blöchl [76]. This formalism is implemented in the DFT code "Vienna Ab initio Simulation Package"(VASP) [77–79] used for my research.

The key idea of the PAW formalism is to replace the true all-electron wave function $|\Psi\rangle$ by a pseudo wave function $|\tilde{\Psi}\rangle$. To get from $|\tilde{\Psi}\rangle$ to the real $|\Psi\rangle$ one has to replace (augment) it inside the core regions. Inside the core regions a so-called "partial wave expansion" is used; an expansion in a well localized real space basis set, and the interstitial region away from the core is described by plane waves. The original $|\Psi\rangle$ is then connected to $|\tilde{\Psi}\rangle$ by a linear transformation $\hat{T}$:

$$|\Psi\rangle = \hat{T}\ |\tilde{\Psi}\rangle = \left(1 + \sum_{\mu} \hat{t}_{\mu}\right) |\tilde{\Psi}\rangle \quad . \tag{20}$$

$\hat{T}$ is required to be unity in the interstitial region, away from the nuclei, where the normal plane wave basis can be used. Thus, the transformation consists of multiple contributions $\hat{t}_{\mu}$ that vanish outside of spheres around each nucleus at position R_{μ}. In each sphere μ an expansion in partial waves $|\phi_{\alpha}\rangle$ is performed. Furthermore, for each $|\phi_{\alpha}\rangle$ a smooth pseudo partial wave $|\tilde{\phi}_{\alpha}\rangle$ is constructed, which matches $|\phi_{\alpha}\rangle$ at the boundary R:

$$|\phi_{\alpha}\rangle = (1 + \hat{t}_{\mu})\,|\tilde{\phi}_{\alpha}\rangle \tag{21}$$

$$\Leftrightarrow \hat{t}_{\mu}\,|\tilde{\phi}_{\alpha}\rangle = |\phi_{\alpha}\rangle - |\tilde{\phi}_{\alpha}\rangle \quad . \tag{22}$$

Here, the index α is a multi-index for the atomic position $\mathbf{R}$, the angular momentum l,m and n labeling the radial quantum number. For $|\phi_{\alpha}\rangle$ on can use for example solutions of the Schrodinger equation for the atom at hand, and for $|\tilde{\phi}_{\alpha}\rangle$ eigenfunctions of the radial Schrodinger equation using a smooth pseudo potential can be used [76]. Note, that $|\phi_{\alpha}\rangle$ needs to form in principle a complete basis set inside the spheres to make the transformation $\hat{T}$ exact. The PAW decomposition is visualized in Fig. 11 for the Cl_2 molecule.

To find now a closed expression for $|\Psi\rangle$, one has to find a representation of $|\tilde{\Psi}\rangle$ in the basis of $|\tilde{\phi}\rangle$ inside the sphere. Therefore, we define projector functions $\langle\tilde{p}_{\alpha}|$:

$$|\tilde{\Psi}\rangle = \sum_{\alpha} |\tilde{\phi}_{\alpha}\rangle\,\langle\tilde{p}_{\alpha}|\tilde{\Psi}\rangle \qquad , \langle\tilde{p}_{\alpha}|\tilde{\phi}_{\beta}\rangle = \delta_{\alpha\beta} \quad . \tag{23}$$

The projector functions are the dual basis to the partial waves. Inserting now everything in equation Eq. 20 gives the final expression for the all electron wave function:

$$\begin{aligned} |\Psi\rangle &= |\tilde{\Psi}\rangle + \sum_{\mu} \hat{t}_{\mu}\,|\tilde{\Psi}\rangle = |\tilde{\Psi}\rangle + \sum_{\mu}\sum_{\alpha} \hat{t}_{\mu}\,|\tilde{\phi}_{\alpha}\rangle\,\langle\tilde{p}_{\alpha}|\tilde{\Psi}\rangle \\ \Rightarrow |\Psi\rangle &= |\tilde{\Psi}\rangle + \sum_{i} \left(|\phi_{\alpha}\rangle - |\tilde{\phi}_{\alpha}\rangle\right)\langle\tilde{p}_{\alpha}|\tilde{\Psi}\rangle \quad . \end{aligned} \tag{24}$$

Importantly, the transformation is in principle exact, but the basis expansion in α is in practice truncated. Therefore, the power of

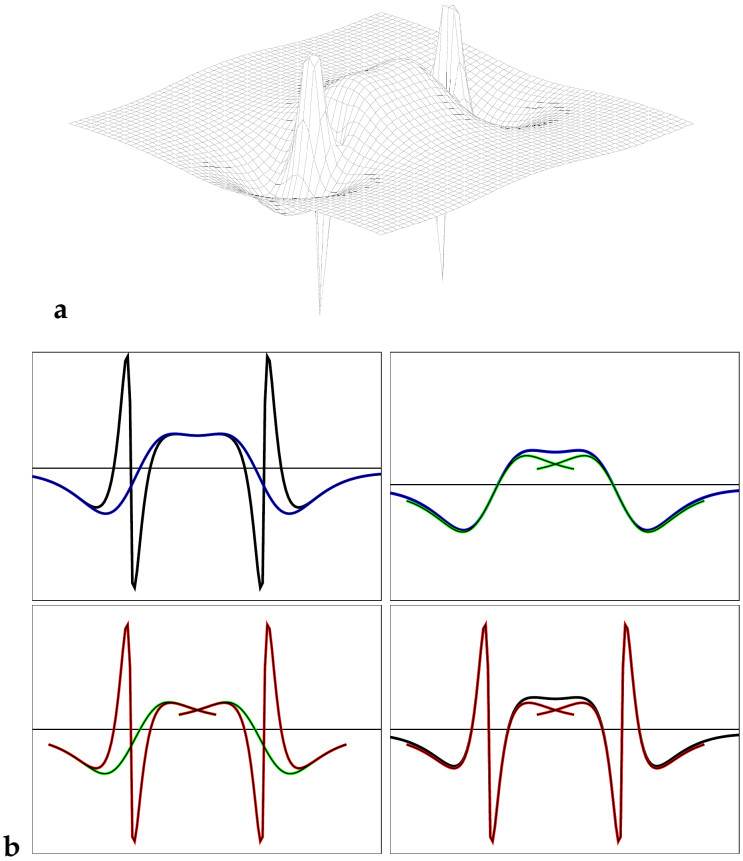

Figure 11: **a** Bonding $p - \sigma$ orbital of the chlorine Cl_2 molecule. The Cl ions are located in the deep wells. **b** Wave function corresponding to the orbital in **a**, and its decomposition into auxiliary wave function and partial waves. Top-left: True wave function Ψ (black), and the auxiliary wave function $\tilde{\Psi}$ (blue). One can see how $\tilde{\Psi}$ is perfectly smooth at the Cl ion positions. Top-right: auxiliary wave function $\tilde{\Psi}$ (blue) and its partial wave expansion in pseudo partial waves $\tilde{\phi}_\alpha$ (green). Bottom-left: comparison of the true partial wave ϕ_i (red) and the pseudo partial wave $\tilde{\phi}_\alpha$ (green). Bottom-right: Ψ (black) and its partial wave expansion in ϕ_α (red). Taken from Ref. [80].

the method depends crucially on the given basis functions, which are defined for each atomic species and have to be chosen carefully. Moreover, not all electrons of the atom are treated explicitly. Usually, only the important valence electrons have partial wave definitions, whereas other electrons are approximated in the core, with an new effective pseudo potential. This approximation is called frozen core approximation, with a significant gain in computational efficiency [79].

The calculation of observables is possible in this formalism even without the explicit back transformation from $|\tilde{\Psi}\rangle$ to $|\Psi\rangle$. The expec-

tation value of an operator $\hat{A}$ can be calculated from $|\tilde{\Psi}\rangle$, $\langle \tilde{p}_\alpha|\tilde{\Psi}\rangle$, and the partial waves:

$$\begin{aligned}\langle \hat{A}\rangle &:= \langle \Psi|\,\hat{A}\,|\Psi\rangle \\ &= \langle \tilde{\Psi}|\,\hat{A}\,|\tilde{\Psi}\rangle + \sum_{\alpha,\beta} \rho_{\alpha\beta}\left(\langle \phi_\beta|\,\hat{A}\,|\phi_\alpha\rangle - \langle \tilde{\phi}_\beta|\,\hat{A}\,|\tilde{\phi}_\alpha\rangle\right) \quad ,\end{aligned} \tag{25}$$

where one defines the one-center density matrix $\rho_{\alpha\beta}$ as follows:

$$\rho_{\alpha\beta} := \sum_{\nu\mathbf{k}} f_{\nu\mathbf{k}} \langle \tilde{\Psi}_{\nu\mathbf{k}}|\tilde{p}_\alpha\rangle \langle \tilde{p}_\beta|\tilde{\Psi}_{\nu\mathbf{k}}\rangle \quad . \tag{26}$$

Here, I reintroduced the band index ν and the $\mathbf{k}$ point index. $f_{\mathbf{k}\nu}$ is equal to one for occupied and zero for unoccupied electron orbitals. Importantly, for a complete set of projectors, this one-center density matrix is exactly identical to the charge density inside of the augmentation spheres. This shows that the PAW formalism provides a straightforward way to calculate local properties, e.g. charges per atom per orbital, or magnetic moments per atom per orbital, without evaluating the full wave function. This is due to the fact, that the main contribution to these quantities stems from the wave function part inside the spheres R, and thus can be evaluated from the one-center density matrix $\rho_{\alpha\beta}$.

I would also like to mention, that the PAW method is very closely related to the formalism of ultra-soft pseudo potentials [81], which is also based on the idea of replacing the effective potential close to the nuclei with a pseudo potential, generating a smooth wave function. This method allows to use a plane-wave basis for the whole space, since the effective pseudo potential does not produce rapidly oscillating wave functions. Formally this method is very similar to the PAW formalism due to non-local pseudo potentials involving projectors, and has been development before the PAW formalism.

This rounds up the description for the basic functionality of the DFT code VASP used for my work. DFT has been proven to be a very powerful tool for performing electronic structure calculations. However, it has some deficiencies that occur especially when describing systems with localized electronic states that exhibit strong electron interactions. These problems can be for example related to the mapping to an effective one particle problem in DFT, which means that no physical state can be described, which is not representable by a single Slater determinant. An example for such a state is a Mott insulating state. This means, that even if one has access to the exact exchange-correlation functional, that accounts for all electron interaction correctly, the one-particle KS spectrum cannot describe such a many body state. There are developments to circumvent these problems by modeling super cells, or averaging over different electronic configurations, e.g. averaging multiple Slater determinants [82]. However, those methods will not be further discussed. Moreover, one should

keep in mind the fact that DFT is a ground state formalism performed at 0 K, and in principle not designed to describe excited states.

3.2 DFT++ METHODS FOR CORRELATED MATERIALS

Problems in DFT occur often for systems where the interactions between electrons in rather localized d or f valence states are important, especially for systems with partially filled orbitals. Here, the properties of the system are dominated by these interactions, as described in chapter 1. Different methods were proposed to incorporate strong electron interactions of such localized valence electrons manually into the KS equations. In general, it would be ideal to find a way to keep the benefits of DFT, and to patch the deficiencies due to the local interaction effects. Therefore, this section is devoted to so-called *DFT++* methods [83], which extend DFT to incorporate the strong local Coulomb interactions found in partially filled d or f orbitals.

The general idea of these methods is to identify a correlated subset of orbitals that lacks a proper description in DFT, when using the commonly available local or semi-local E_{xc} functionals. Then, an improved description of the Coulomb interaction for these correlated states is added, and finally the interaction in these orbitals that already has been accounted for in DFT is subtracted:

$$\hat{H}_{\text{DFT+}} = \hat{H}_{\text{KS}} + \hat{H}_{\text{U}} - \hat{H}_{\text{DC}} \quad . \tag{27}$$

Here, $\hat{H}_{\text{KS}}$ is the full KS Hamiltonian, $\hat{H}_{\text{U}}$ is the added Coulomb interaction in the correlated orbitals, and $\hat{H}_{\text{DC}}$ is the so-called double counting, to subtract the Coulomb interaction already accounted for in DFT.

The rest of the chapter is dedicated to explain how to perform such DFT++ calculations. First, Wannier functions are introduced as a tool to construct suitable basis sets for the correlated subspace. Then, I introduce $\hat{H}_{\text{U}}$, in its various flavors and emphasize the question of choosing an appropriate basis in which the Hamiltonian is represented. Moreover, I outline the constrained random phase approximation (cRPA) method to calculate the screened Coulomb interaction from DFT, which can then be used in DFT++ methods. Finally, I present two actual implementations of the DFT++ formalism: the DFT+U method [84, 85], and the DFT+DMFT method [86], which are both used during my research.

3.3 WANNIER FUNCTIONS

To apply a local Coulomb interaction in a chosen subset of bands, C, it is necessary to write $\hat{H}_{\text{U}}$ in a well localized basis set. Unfortunately, the Bloch states of a solid are very delocalized in real space. Therefore, it is not practical to select the KS states (bands) close to the Fermi

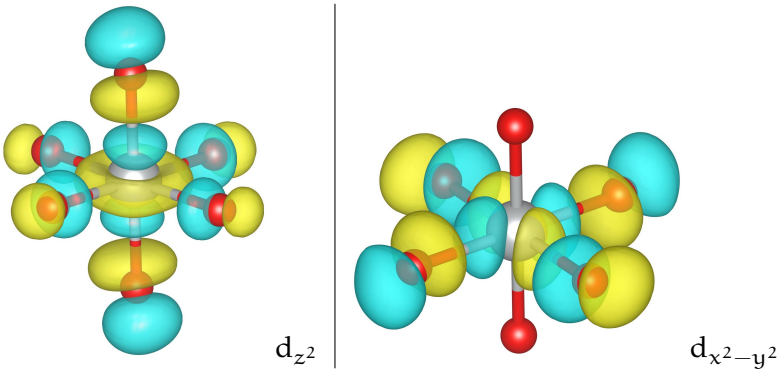

Figure 12: Constructed MLWFs for the two e_g orbitals of $LuNiO_3$, from the bands close to the Fermi level, without including the oxygen p bands. Therefore, clear oxygen p tails can be observed, which stem from the strong hybridization with Ni d states.

level and apply U. Here, I introduce Wannier functions, which are the Fourier transforms of Bloch states, that can serve as suitable basis states for $\hat{H}_U$.

3.3.1 *Maximally localized Wannier functions*

In general, Wannier functions can be obtained directly by a Fourier transformation of the KS states $|\Psi_{\mathbf{k}\nu}\rangle$ of the correlated subset of bands C:

$$|w_{\mathbf{R},m}\rangle = \frac{V}{(2\pi)^3}\int_{BZ} dk\, e^{-i\mathbf{k}\mathbf{R}} \sum_{\nu\in C} U_{m\nu}^{(k)} |\Psi_{\mathbf{k}\nu}\rangle \quad . \tag{28}$$

Here, V is the real space unit cell volume, and $U_{m\nu}^{(k)}$ is a unitary matrix, which in the case of a single Bloch function corresponds to the arbitrary phase factor of the Bloch wave function. If multiple Bloch states are involved this matrix is not necessarily diagonal, but there is the possibility to mix the Bloch states at each **k**-point. Therefore, it is clear that the resulting Wannier functions are not uniquely defined, and to obtain uniquely defined Wannier functions one has to fix the unitary matrix $U_{m\nu}^{(\mathbf{k})}$ by additional constraints.

The idea of maximally localized Wannier functions (MLWF) [87, 88] is to determine $U_{m\nu}^{(\mathbf{k})}$ in a certain way, that maximizes the localization of the resulting Wannier functions in real space. Therefore, one obtains $U_{m\nu}^{(\mathbf{k})}$ by minimizing the following functional:

$$J[U_{m\nu}^{(\mathbf{k})}] := \sum_m (\langle r^2\rangle_m - \langle r\rangle_m^2) \qquad \text{with } \langle o\rangle_m = \int dr\, o\, |w_m(r)|^2 \quad . \tag{29}$$

This procedure is implemented in the *Wannier90* code [89], which is interfaced with many DFT codes including VASP. Importantly, if no

overlap between the bands in the chosen energy window with other bands exists, the band structure is exactly represented. From this procedure one obtains the real space Wannier functions $|w_\alpha\rangle$, which has an example are depicted for $LuNIO_3$ in Fig. 12. Moreover, one obtains the hopping amplitudes between these Wannier orbitals:

$$t_{\alpha\beta} = \langle w_\alpha | \hat{H}_C^{kin} | w_\beta \rangle \quad , \tag{30}$$

where $\hat{H}_C^{kin}$ is tight-binding like description of H_{KS} in the chosen energy window. Note, that the resulting Wannier functions will be more localized for larger energy windows, hence if using more bands C during the construction of the Wannier functions.

3.3.2 *Projections onto localized orbitals*

There is an alternative framework to MLWFs to construct localized Wannier functions, the projection onto localized orbitals (PLOs) [90, 91].

The idea of the PLO formalism is to project the Bloch states $|\Psi_{\mathbf{k}\nu}\rangle$ onto a set of localized orbitals $|\chi_\alpha\rangle$, where $\alpha = \{\mathbf{R}, l, m, \sigma\}$. One can define a projection matrix as

$$\tilde{P}_{\alpha\nu}(\mathbf{k}) \equiv \langle \chi_\alpha | \Psi_{\nu\mathbf{k}} \rangle \ , \tag{31}$$

which projects the Bloch states within a energy window $\mathcal{W}$ onto localized orbitals:

$$|\tilde{\chi}_\alpha(\mathbf{k})\rangle = \sum_{\nu \in C} \tilde{P}^\dagger_{\alpha\nu}(\mathbf{k}) \, |\Psi_{\nu\mathbf{k}}\rangle \ . \tag{32}$$

Often, the number of localized orbitals to project on is smaller than the number of bands within the energy window $\mathcal{W}$. This means, that $\hat{P}_{\alpha\nu}(\mathbf{k})$ can be a non-square matrix. As the projection is usually performed for a subset of bands $\mathcal{W}$, the $|\tilde{\chi}_\alpha(\mathbf{k})\rangle$ do not form an orthonormal basis set. Orthonormalizing them gives:

$$|w_\alpha(\mathbf{k})\rangle = \sum_\beta O^{-1/2}_{\alpha\beta} \, |\tilde{\chi}_\beta(\mathbf{k})\rangle \ , \tag{33}$$

where I introduced the overlap matrices:

$$O_{\alpha\beta} = \sum_{\nu\mathbf{k}} \hat{P}_{\alpha\nu}(\mathbf{k}) \hat{P}^\dagger_{\beta\nu}(\mathbf{k}) \ . \tag{34}$$

The Fourier transformation of $|w_\alpha(\mathbf{k})\rangle$ will give a localized Wannier function. Therefore, the PLO formalism provides a well defined basis of localized orbitals by connecting the Wannier functions to the Bloch bands by the projection operator:

$$\hat{P}_{\alpha\nu}(\mathbf{k}) = \langle w_\alpha(\mathbf{k}) | \Psi_{\nu\mathbf{k}} \rangle \quad . \tag{35}$$

Note, that this is a projection scheme and the projection matrices are in general not unitary. Therefore, due to the orthonormalization $\sum_\nu \hat{P}_{\alpha\nu}(\mathbf{k})\hat{P}^\dagger_{\nu\beta}(\mathbf{k}) = \mathbb{1}$ holds, but not $\sum_\nu \hat{P}^\dagger_{\alpha\nu}(\mathbf{k})\hat{P}_{\beta\nu}(\mathbf{k}) \neq \mathbb{1}$. Only if the projection matrices are quadratic they perform a unitary transformation, see for a proof Ref. [92] p.101-104.

The projection operator can be used for down-folding any KS property. For example, one can extract the kinetic Hamiltonian for the correlated subspace as

$$\hat{H}^{\text{kin}}_C = \sum_{\nu\in C} \hat{P}_{\alpha\nu}(\mathbf{k})\hat{H}_{\text{KS}}\hat{P}^\dagger_{\beta\nu}(\mathbf{k}) \quad . \tag{36}$$

I would like to emphasize the importance of the chosen energy window $\mathcal{W}$ for the construction, as it critically determines how localized the resulting Wannier functions are. In general a larger energy window will produce more localized Wannier functions, which then also can have projection weight on other bands.

With this I presented two different approaches to extract a set of localized orbitals, defining a basis for the correlated target subspace C.

3.4 COULOMB INTERACTION TENSOR

For all DFT++ methods one needs to add the Coulomb interaction in the localized basis set for the correlated subspace, which were introduced in the previous section. However, it is important to understand how crystal symmetries and different basis sets affect the form of the Coulomb interaction tensor. Therefore, this section is devoted to a derivation of the Coulomb interaction tensor, based on Ref. [93].

A first assumption is that the Coulomb interaction, which is added for the correlated states, is purely local. This assumption is based one the fact that other electrons will screen the Coulomb interaction, often leading to an exponential decay of the Coulomb interaction with the distance $\mathbf{r}$ between two electrons. This is further elucidated in section 3.5. Moreover, one assumes that all long-range interactions and mean-field exchange correlations are well captured already in DFT.

The local Coulomb interaction on each atomic site $\mathbf{R}$ can be written in second quantization as

$$\hat{H}_U = \frac{1}{2}\sum_{\sigma\sigma'}\sum_{mm'm''m'''} U_{mm'm''m'''}\, c^\dagger_{m\sigma}c^\dagger_{m'\sigma'}c_{m'''\sigma'}c_{m''\sigma} \quad . \tag{37}$$

Here, $c^{\dagger}_{m\sigma}$ and $c_{m\sigma}$ are creation and annihilation operators for the localized Wannier states $|w_\alpha\rangle = |w_{\mathbf{R},l,m,\sigma}\rangle$, and $U_{mm'm''m'''}$ is the Coulomb interaction tensor:

$$\begin{aligned} U_{mm'm''m'''} &= \langle mm'|\, U \,|m''m'''\rangle \\ &= \int d\mathbf{r}_1 \int d\mathbf{r}_2 \; w^*_m(\mathbf{r}_1) w^*_{m'}(\mathbf{r}_2) \frac{1}{|\mathbf{r}_1 - \mathbf{r}_2|} w_{m'''}(\mathbf{r}_2) w_{m''}(\mathbf{r}_1) \quad . \end{aligned} \tag{38}$$

Next, I reduce the complexity of the Coulomb tensor by considering crystal symmetries that are typical for perovskites.

3.4.1 *Slater integral parameterization*

This parameterization makes use of the specific form of atomic orbitals, and is therefore applicable if the basis functions $w_\alpha(\mathbf{r})$ are atomic orbitals with spherical symmetry. Strictly speaking this is only valid for isolated ions, but often d-orbitals in a solid are very close to spherical symmetry [91].

Slater [94] showed that the full Coulomb interaction tensor $U_{mm'm''m'''}$ in Eq. 38, represented in the spherical harmonic basis:

$$\phi_{nlm}(\mathbf{r}) = R_{nl}(\mathbf{r}) Y_{lm}(\theta, \phi) \quad , \tag{39}$$

can be decomposed into an angular part described by the Racah-Wigner numbers α, and a radial part, which is then expressed in terms of Slater integrals F^k:

$$U_{mm'm''m'''} = \sum_{k=0}^{2l} \alpha_k(mm'm''m''') F^k \quad . \tag{40}$$

For the d-shell one can show that only three Slater integrals F^0, F^2, and F^4 are needed to construct the full Coulomb interaction tensor due to the spherical symmetry of the isolated ion [95].

The most important Coulomb integrals are the matrix elements that differ only in up to two different indices m. These are the direct and the exchange integrals:

$$U^{\sigma\bar{\sigma}}_{mm'} = \sum_{k=0}^{2l} \alpha_k(m, m', m, m') F^k \tag{41}$$

$$J_{mm'} = \sum_{k=0}^{2l} \alpha_k(m, m', m', m) F^k \quad . \tag{42}$$

Often one only considers these contributions, as they can be expressed by density-density terms only [93]. Moreover, one averages the interaction over all orbitals to obtain:

$$U_{avg} = \frac{1}{(2l+1)^2} \sum_{mm'} U^{\sigma\bar{\sigma}}_{mm'} = F_0 \tag{43}$$

$$U_{avg} - J_{avg} = \frac{1}{2l(2l+1)} \sum_{m \neq m'} J_{mm'} \quad . \tag{44}$$

For a d-shell of an isolated ion one can show that

$$J_{avg} = \frac{F^2 + F^4}{14} \tag{45}$$

holds. Typically, one fixes the ratio F^4/F^2 and hence, U_{avg} and J_{avg} are the only input parameters needed for the construction of the Coulomb interaction tensor. The ratio F^4/F^2 is obtained empirically and for transition metals it is reported to be $F^4/F^2 \approx 0.625$. The ratio usually varies only slightly between different atoms [96–98].

3.4.2 *Hubbard-Kanamori parameterization*

In systems with cubic symmetry with an octhedral crystal field splitting, the d orbital manifold is split into t_{2g} and e_g states. By choosing now real spherical harmonics (cubic harmonics) as a basis for $U_{mm'm''m'''}$ the Coulomb interaction tensor becomes block diagonal, hence we can exactly rewrite the interaction tensor for the t_{2g} or e_g subspace [99, 100]. Moreover, $U_{mm'm''m'''}$ is nonzero only if at maximum two different orbital indices occur in each summand of Eq. 37.

There are four different Coulomb matrix elements that one is left with after applying this restriction:

$$\begin{aligned} U_{mmmm} &= \langle mm|\, U \,|mm\rangle \\ U_{mm'mm'} &= \langle mm'|\, U \,|mm'\rangle \\ U_{mm'm'm} &= \langle mm'|\, U \,|m'm\rangle \\ U_{mmm'm'} &= \langle mm|\, U \,|m'm'\rangle \quad . \end{aligned} \tag{46}$$

Therefore, it follows for the full Coulomb interaction operator in Eq. 37 with use of the density operator $\hat{n}_{m\sigma} = c^\dagger_{m\sigma} c_{m\sigma}$:

$$\begin{aligned} \hat{H}_U = &\frac{1}{2} \sum_{\sigma\sigma'} \sum_{m} U_{mmmm}\, \hat{n}_{m\sigma} \hat{n}_{m\sigma'} \\ &+ \frac{1}{2} \sum_{\sigma\sigma'} \sum_{m \neq m'} U_{mm'mm'}\, \hat{n}_{m\sigma} \hat{n}_{m'\sigma'} \\ &+ \frac{1}{2} \sum_{\sigma\sigma'} \sum_{m \neq m'} U_{mm'm'm}\, c^\dagger_{m\sigma} c^\dagger_{m'\sigma'} c_{m\sigma'} c_{m'\sigma} \\ &+ \frac{1}{2} \sum_{\sigma\sigma'} \sum_{m \neq m'} U_{mmm'm'}\, c^\dagger_{m\sigma} c^\dagger_{m\sigma'} c_{m'\sigma'} c_{m'\sigma} \quad . \end{aligned} \tag{47}$$

Introducing now $\bar{\sigma}$ as the opposite spin of σ, and with some rearrangement one obtains:

$$\begin{aligned}
\hat{H}_U = &\frac{1}{2}\sum_{\sigma}\sum_{m} U_{mmmm}\ \hat{n}_{m\sigma}\hat{n}_{m\bar{\sigma}} \\
&+\frac{1}{2}\sum_{\sigma}\sum_{m\neq m'} U_{mm'mm'}\ \hat{n}_{m\sigma}\hat{n}_{m'\bar{\sigma}} \\
&+\frac{1}{2}\sum_{\sigma}\sum_{m\neq m'} (U_{mm'mm'} - U_{mm'm'm})\hat{n}_{m\sigma}\hat{n}_{m'\sigma} \\
&+\frac{1}{2}\sum_{\sigma}\sum_{m\neq m'} U_{mm'm'm}\ c^{\dagger}_{m\sigma}c^{\dagger}_{m'\bar{\sigma}}c_{m\bar{\sigma}}c_{m'\sigma} \\
&+\frac{1}{2}\sum_{\sigma}\sum_{m\neq m'} U_{mmm'm'}\ c^{\dagger}_{m\sigma}c^{\dagger}_{m\bar{\sigma}}c_{m'\bar{\sigma}}c_{m'\sigma} \quad .
\end{aligned} \tag{48}$$

The two-index matrices can be re-labeled:

$$\begin{aligned}
U^{\sigma\bar{\sigma}}_{mm'} &\equiv U_{mm'mm'} \\
J_{mm'} &\equiv U_{mm'm'm} \\
U^{\sigma\sigma}_{mm'} &\equiv U_{mm'mm'} - J_{mm'}
\end{aligned} \tag{49}$$

and are commonly referred as U matrix, exchange matrix J, and U' matrix. For the Kanamori parameterization of the interaction of a t_{2g} or e_g subset it is assumed that the differences in different orbitals within the two-index matrices are small. Therefore, we can introduce averaged parameters for the two-index matrices:

$$\begin{aligned}
\mathcal{U} &\equiv \frac{1}{N}\sum_{m} U_{mmmm} \\
\mathcal{U}' &\equiv \frac{1}{N(N-1)}\sum_{m\neq m'} U_{mm'mm'} \\
\mathcal{J} &\equiv \frac{1}{N(N-1)}\sum_{m\neq m'} U_{mm'm'm} \\
\mathcal{J}_C &\equiv \frac{1}{N(N-1)}\sum_{m\neq m'} U_{mmm'm'} \quad ,
\end{aligned} \tag{50}$$

which are the so-called Hubbard-Kanamori parameters. With this one obtains the Kanamori parameterization with four parameters:

$$\begin{aligned}
\hat{H}_U = &\frac{1}{2}\sum_{\sigma}\sum_{m} \mathcal{U}\ \hat{n}_{m\sigma}\hat{n}_{m\bar{\sigma}} \\
&+\frac{1}{2}\sum_{\sigma}\sum_{m\neq m'} \left[\mathcal{U}'\ \hat{n}_{m\sigma}\hat{n}_{m'\bar{\sigma}} + (\mathcal{U}' - \mathcal{J})\hat{n}_{m\sigma}\hat{n}_{m'\sigma}\right] \\
&+\frac{1}{2}\sum_{\sigma}\sum_{m\neq m'} \left[\mathcal{J}\ c^{\dagger}_{m\sigma}c^{\dagger}_{m'\bar{\sigma}}c_{m\bar{\sigma}}c_{m'\sigma} + \mathcal{J}_C\ c^{\dagger}_{m\sigma}c^{\dagger}_{m\bar{\sigma}}c_{m'\bar{\sigma}}c_{m'\sigma}\right] \quad .
\end{aligned} \tag{51}$$

In perfect cubic symmetry one can verify that $U' = U - 2J$ and $J = J_C$ holds [99], which is true for the t_{2g} or e_g subset. The resulting interaction operator has the following form:

$$\begin{aligned}\hat{H}_U^{kan} = &\frac{1}{2}\sum_{\sigma}\sum_{m} U\ \hat{n}_{m\sigma}\hat{n}_{m\bar{\sigma}} \\ &+ \frac{1}{2}\sum_{\sigma}\sum_{m\neq m'} [(U-2J)\ \hat{n}_{m\sigma}\hat{n}_{m'\bar{\sigma}} + (U-3J)\hat{n}_{m\sigma}\hat{n}_{m'\sigma}] \\ &+ \frac{1}{2}\sum_{\sigma}\sum_{m\neq m'} J(\underbrace{c^{\dagger}_{m\sigma}c^{\dagger}_{m'\bar{\sigma}}c_{m\bar{\sigma}}c_{m'\sigma}}_{spin-flip} + \underbrace{c^{\dagger}_{m\sigma}c^{\dagger}_{m\bar{\sigma}}c_{m'\bar{\sigma}}c_{m'\sigma}}_{pair-hopping}) \ .\end{aligned} \tag{52}$$

Importantly, this form of the interaction is rotationally invariant, which means that within the subset of orbitals, arbitrary unitary transformations can be applied to the Hamiltonian without the need to transform the Kanamori parameters.

If the system has cubic symmetry there is a one to one correspondence for the t_{2g} or the e_g subset between the Slater interaction matrix and the Kanamori interaction matrix [93]. However, the Kanamori parameterization is not generally valid for the full d shell, only if the system has spherical symmetry $U' = U - 2J$ holds. Then, a direct relation to the Slater integrals is given also for the full d shell [101]. Note, that in many real materials these symmetries are not completely satisfied, as for example in rare-earth nickelates, and one makes a further simplification by assuming that the interaction still fulfills the symmetry conditions and deviations are small.

3.5 CONSTRAINED RANDOM PHASE APPROXIMATION

Now, that the form of the Coulomb interaction for the correlated subspace of d electrons, or the t_{2g} or e_g subset, in real solids is properly defined the question of how to choose appropriate values for the interaction parameters remains. One can, in principle, calculate the Coulomb interaction in single atoms directly, but the interaction of d electrons in ions typically has a strength of about ~20 eV. However, this value is a magnitude larger than the kinetic energy of any electron in a solid, thus there would be no metallic systems in nature.

In solids the effective Coulomb interaction is reduced by screening effects, due to the presence of other electrons in the systems. Consider an extra electron in the system as perturbing potential for the other electrons. They will avoid the area directly around this extra electron, effectively creating screening holes that are positively charged, which screen the "bare" Coulomb potential acting on other electrons. Of course, one does not need to specifically add an extra electron; this holds for any electron in the system. Hence, the effective interaction between any two electrons in a solid is screened by all other electrons.

One should also note, that this picture also holds for excited electron-hole pairs making the screening dynamic i.e. frequency dependent.

To calculate the screened Coulomb interaction, I utilize in this thesis the constrained Random Phase Approximation (cRPA) [102], as implemented in VASP [103]. This method allows to calculate the dynamic screening from a KS band structure completely *ab initio*. The following brief introduction to cRPA follows Ref. [104].

Consider applying a time-dependent perturbation $\delta\phi$ to a system of electrons, that induces a change in the electron density, which in turn changes the Hartree potential V_H of the system. Therefore, the total potential change under the influence of the perturbation is given as:

$$\delta W = \delta\phi + \delta V_H \, . \tag{53}$$

Thus, the induced Hartree potential screens the applied perturbation resulting in a screened potential δW, where the ratio between perturbation and resulting screened potential is defined as the inverse of the dielectric function:

$$\epsilon^{-1}(1,2) = \frac{\delta W(1)}{\delta\phi(2)} \quad . \tag{54}$$

Here, I used short-hand notations for space time coordinates $1 = (\mathbf{r}_1, \sigma_1, t_1)$.

The bare Coulomb interaction V between two particles can also be interpreted as perturbation to the system as a Coulomb potential V arising at 1 due to another electron at position 2, resulting in a screened Coulomb potential W:

$$W(1,2) = \int d4\epsilon^{-1}(1,4)V(4,2) \tag{55}$$

or in matrix notation:

$$W = \epsilon^{-1}V \, . \tag{56}$$

A central quantity in the cRPA method it the polarization function P, which expresses the polarization of the system due to the perturbation. The polarization function is within the cRPA method approximated in RPA, by neglecting all beyond Hartree contributions. The polarization in RPA can be directly calculated from DFT [102]:

$$\begin{aligned} P(\mathbf{r},\mathbf{r}',\omega) = \sum_{\nu\mathbf{k}}^{\text{occ}} \sum_{\nu'\mathbf{k}'}^{\text{unocc}} \Bigg[& \frac{\Psi^\dagger_{\nu\mathbf{k}}(\mathbf{r})\Psi_{\nu'\mathbf{k}'}(\mathbf{r})\Psi^\dagger_{\nu'\mathbf{k}'}(\mathbf{r}')\Psi_{\nu\mathbf{k}}(\mathbf{r}')}{\omega - \epsilon_{\nu'\mathbf{k}'} + \epsilon_{\nu\mathbf{k}} + i\delta} \\ & - \frac{\Psi_{\nu\mathbf{k}}(\mathbf{r})\Psi^\dagger_{\nu'\mathbf{k}'}(\mathbf{r})\Psi_{\nu'\mathbf{k}'}(\mathbf{r}')\Psi^\dagger_{\nu\mathbf{k}}(\mathbf{r}')}{\omega + \epsilon_{\nu'\mathbf{k}'} - \epsilon_{\nu\mathbf{k}} - i\delta} \Bigg] \, , \end{aligned} \tag{57}$$

where $\Psi_{\nu\mathbf{k}}$ and $\epsilon_{\nu\mathbf{k}}$ mark KS eigenstates and eigenvalues. Moreover, it can be shown that the dielectric function can be calculated from the polarization P as [102]:

$$\epsilon = 1 - VP \, . \tag{58}$$

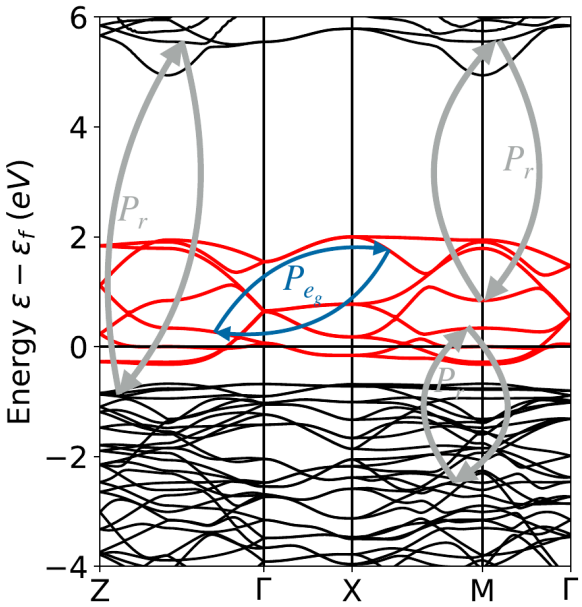

Figure 13: Band structure of $LuNiO_3$, with constructed Wannier functions for the Ni e_g bands (red). The decomposition in the polarization channels P_{e_g} within the correlated subspace, and the polarization channels P_r outside, from, and to the e_g subspace are schematically depicted as blue and grey arrows.

To calculate now the effective screened Coulomb interaction U in a correlated subspace, I consider the example depicted in Fig. 13 of $LuNiO_3$. The effective screened Coulomb interaction is calculated by first splitting the polarization of the system in two parts:

$$P = P_{e_g} + P_r \quad . \tag{59}$$

Namely, the polarization restricted only to the e_g-e_g transitions P_{e_g}, e.g. the e_g screening channels, and P_r, which takes into account all other transitions. Now one can deduce the partially screened interaction W_r from P_r as:

$$W_r = \epsilon_r^{-1} V = [1 - V\, P_r]^{-1} V \,, \tag{60}$$

which includes all screening effects except the one from the e_g-e_g channels. Indeed, W_r can be interpreted as the screened Coulomb interaction tensor $U_{mm'm''m'''}$ for the e_g orbitals, because adding the polarization P_{e_g} to P_r, one would recover the fully screened interaction [102]. Hence, it follows:

$$U = [1 - V\, P_r]^{-1} V \quad . \tag{61}$$

The name constrained stems from the fact, that we constrained the screening to all transitions except the ones inside the correlated subspace. Note, that due to the energy dependency of the polarization, the Coulomb interaction is naturally frequency dependent. However,

in this work I use the static limit $U_{mm'm''m'''}(\omega \to 0)$, which is a widely used approximation [91, 96, 105]. However, the effect of dynamic screening should not be underestimated as shown for example in the work of Ref.[103, 105].

In principle $U_{mm'm''m'''}$ can be calculated in any basis and can then directly used as input for $\hat{H}_U$. Therefore, $U_{mm'm''m'''}$ is usually calculated directly in the correlated subspace Wannier basis $|w_\alpha(r)\rangle$. However, often one still parameterizes the interaction matrix from the obtained W_r, either in the Slater parameterization, or the Kanamori parameterization, depending on the chosen subspace. This is done, because these parameters are often required as input for DFT++ methods. Furthermore, I would also like to mention that cRPA is not the only method to calculate interaction parameters *ab initio*. The constrained LDA method [106] provides another formalism based on DFT to calculate the Coulomb interaction. Moreover, Ref. [107] shows that under certain conditions cRPA does not give correct results, and hence the obtained values should be considered as a guideline.

3.6 DFT+U

Next, I present the actual implementations of the DFT++ methods used in this thesis.

In the DFT+U formalism one modifies directly the effective potential of the KS Hamiltonian by adding an orbital dependent potential in the spirit of Eq. 27. This additional potential has the form of a Coulomb interaction for the atomic orbitals, which are not treated on a satisfactory level in plain DFT. This has the clear advantage, that all normal DFT observables are accessible, and the calculation of atomic forces etc. is possible. A good overview about DFT+U is given in the review article of Himmetoglu *et al.* [108].

Anisimov *et al.* [84] were the first who added a Hubbard type local interaction of the general form

$$\hat{H}_U^R = \frac{U}{2} \sum_{\substack{m\sigma, m'\sigma' \\ m\sigma \neq m'\sigma'}} n_m^\sigma n_{m'}^{\sigma'} \tag{62}$$

to certain orbitals in the KS formalism, where n_m is the DFT occupation of an orbital m of an specific atomic species at site $\mathbf{R}$. The occupations are calculated in the PAW formalism from the one-center density matrix (Eq. 26). More precisely, in VASP the Coulomb interaction is applied to well localized PAW projectors with a certain l character. Therefore, the obtained occupations are very close to the formal charges of the cations, which would correspond to Wannier functions calculated for a large energy window.

In fact, the interaction term that I use in this work is of the form as introduced by Liechtenstein *et al.* [109]:

$$\hat{H}_U^R = \frac{1}{2} \sum_{\{m\}\sigma} [\, U_{mm''m'm'''}\; n^{\sigma}_{mm'} n^{\bar{\sigma}}_{m''m'''} + (U_{mm''m'm'''} - U_{mm''m'''m'})\; n^{\sigma}_{mm'} n^{\sigma}_{m''m'''}] \quad . \tag{63}$$

which accounts for spin-dependent interactions (index σ), effective on-site Coulomb-interactions, and exchange-interactions. Importantly, this form is rotationally invariant allowing to make use of the Slater paramaterization of interaction parameters for d electrons as introduced in section 3.4. Therefore, the Coulomb interaction parameter is defined as $U_{avg} = F_0$, and the exchange-interaction parameter as $J_{avg} = \frac{F^2+F^4}{14}$

As already mentioned the GGA or LDA approximation already accounts for some of the interactions of these electrons in orbital i of the chosen atom. Therefore, one would incorporate "too much" interaction for those electrons. This problem is called DC and therefore, by adding the term E^{DC}, one tries to subtract the interaction energy that is "too much". The spin-dependent full energy functional in this formalism reads

$$E^{DFT+U}[\rho^{\sigma}] = E^{DFT}[\rho^{\sigma}] + \sum_{\alpha} E^{U}[n_{\alpha}] - E^{DC}[n_{\alpha}] \quad . \tag{64}$$

The specific form of the DC correction is discussed in section 3.7.6, because for the DFT+DMFT method the same DC correction schemes are used.

The DFT+U method results in a tendency to avoid fractional occupations in the correlated orbitals and tends to empty orbitals less than half filled, and fills orbitals more than half filled. The difference in potential energy for empty and full states is approximately equal to U_{avg}. Together with a spin-dependent treatment of the system, this allows to open a gap between up and down spin channels, within the orbital in question. Moreover, this cures the tendency to over-delocalize electrons in normal exchange-correlation functionals. However, there is an inherent problem arising due to the DC term. Since, the exchange-correlation functional and $\hat{H}_U$ are formulated on a different, formally incompatible, footing, the correct double-counting is not known. From the exchange-correlation functional it cannot be extracted how much contribution to the Coulomb interaction stems from a certain local orbital and what parts come from other contributions, because it depends on the average particle density in a non-linear way.

Even though, one can in principle calculate U_{avg} for the local orbitals using the cRPA method, the question what a suitable value of U_{avg} is, often still remains. This is due to several reasons. As described, the DC is ill-defined. Moreover, the cRPA method is an

approximative scheme [107], and moreover most current implementation do not allow to input a full Coulomb interaction tensor directly obtained from cRPA. Therefore, U_{avg} is usually treated as parameter, and fitted to experimental results until satisfactory results are achieved. However, I demonstrate in this thesis that the cRPA method is a powerful tool to obtain a first guess for the Coulomb interaction strength.

Throughout this thesis I extensively use the DFT+U method to study structural properties and magnetic order in rare-earth nickelates. However, the DFT+U method is still a static mean field method, and thus does not account for dynamic fluctuations, that are necessary to model a Mott insulating state. Hence, to get access to the site-selective Mott insulating state in the paramagnetic regime found in rare-earth nickelates, one needs to go beyond static mean field theory, and access the true many body state of the system.

3.7 DFT+DMFT FRAMEWORK

A completely different approach to tackle the problem of correlated electron systems is developed in the context of the Dynamical Mean Field Theory (DMFT). This method was developed to solve the so-called Hubbard Hamiltonian proposed by Hubbard [110], which is a very important model showing a rich phase diagram describing many different physical phases, e.g. Fermi-liquids, bad metals, Mott insulators, superconductivity, and Kondo physics, to name a few examples.

The Hamiltonian is described for a simple one band case by electrons on a lattice, that can hop from from site to site with a certain amplitude t, which will interact with each other by a Coulomb interaction U if they meet at the same lattice site:

$$\mathcal{H}^{\text{Hubbard}} = \underbrace{-\sum_{ij\sigma} t_{ij} c^{\dagger}_{i\sigma} c_{j\sigma}}_{\hat{H}^{\text{kin}}} + \underbrace{U \sum_{ij} \hat{n}_{i,\uparrow} \hat{n}_{j,\downarrow}}_{\hat{H}^{U}} . \tag{65}$$

Here, the indices i and j mark the lattice sites, $c^{\dagger}_{i\sigma}$ is an operator creating, and $c_{i\sigma}$ an operator destroying an electron with spin σ on site i. U is a local Coulomb interaction, and $\hat{n}_i$ is the density operator for site i. The model is depicted in Fig. 14. The Hubbard Hamiltonian can be straightforwardly extended to multi-orbital systems by introducing the multi indices $\alpha = \{R, l, m, \sigma\}$, where R marks now an atomic site, rather than its position.

Although, the Hubbard Hamiltonian is a model Hamiltonian, it can be utilized in the context of realistic materials modeling, and combined with DFT to allow for a description of the correlated electron physics in d-orbitals. In general, the idea follows the same Ansatz as for DFT+U: one identifies the correlated subspace, constructs localized Wannier functions, extracts the hopping amplitudes $t_{\alpha\beta}$, and

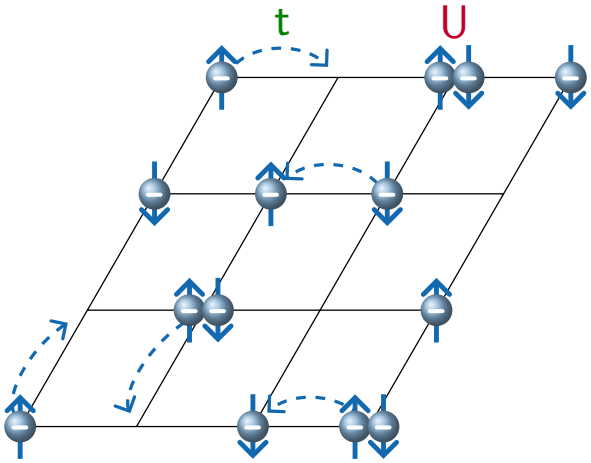

Figure 14: Visualization of the Hubbard Hamiltonian on a two dimensional lattice. Electrons hop with an amplitude t from site to site, and whenever two electrons meet on the same lattice site, they interact with the interaction energy U with each other. Adapted from Ref. [111] with permission from the author.

uses them as input for the Hubbard Hamiltonian in Eq. 65 extended to multi-orbitals. This maps the correlated subspace from the KS Hamiltonian to the kinetic part of the Hubbard Hamiltonian. By adding the local Coulomb interaction one has an appropriate description of the interaction within the low energy subspace.

The Hubbard Hamiltonian appears to be very simplistic, but it is not solvable, except for a few special cases, without approximations. Next, I present DMFT as an approximation to solve the Hubbard Hamiltonian in a beyond static mean field fashion, to describe properly electronic correlations. Afterwards, I show that DFT and DMFT, can be combined in a formal way. Here, I follow the review article of Ref. [15], and the lecture notes of Ref. [112] to give first a brief introduction to DMFT, and then a more detailed overview how DFT and DMFT are deployed together.

3.7.1 *Green's function formalism*

At this point it convenient to introduce the concept of Green's functions. A Green's function can be best described as a propagator for a particle or multiple particles (here I only consider electrons) in a system, possibly disturbing the system (interactions). Sometimes they are also described as correlation functions. Within this work I am only interested in one-particle Green's functions, which allow to store very efficiently information about the interacting many body system. A formal introduction to the formalism of Green's functions can be found in Refs. [93, 113].

The formal definition of the Green's function is given by:

$$iG_{\alpha\beta}(t,t') = \langle T[c_\alpha(t)c^\dagger_\beta(t')]\rangle \quad , \tag{66}$$

where $c_\alpha(t)$ are Heisenberg operators with the multi-index α, and the time dependence t:

$$c_\alpha(t) = e^{i\hat{H}t}c_\alpha e^{-i\hat{H}t} \ . \tag{67}$$

T represents the time ordering operator. Hence, the Green's function describes the probability, that an electron created at t' in state β propagates to t in state α. In general the Green's function is a function of two distinct times t and t'. If the Hamiltonian $\hat{H}$ is explicitly time independent, than $G_{\alpha\beta}(t,t')$ depends only on the time difference:

$$G_{\alpha\beta}(t,t') = G_{\alpha\beta}(t-t',0) \quad . \tag{68}$$

In the context of this work I am interested in a special type of one-particle Green's functions, the so-called Matsubara Green's functions at finite temperatures. The propagator is then defined by the imaginary times $i\tau$, $0 < \tau < \beta$, where

$$\beta = \frac{1}{k_B T} \tag{69}$$

is the inverse temperature, and the Green's function is anti-periodic in τ. For time-independent Hamiltonians, the Matsubara Green's function is defined as:

$$G_{\alpha\beta}(\tau) = -\langle T[c_\alpha(\tau)c^\dagger_\beta(0)]\rangle \quad . \tag{70}$$

and can be Fourier transformed to obtain:

$$G_{\alpha\beta}(i\omega_n) = \int_0^\beta d\tau e^{i\omega_n\tau}G_{\alpha\beta}(\tau) \quad , \tag{71}$$

where ω_n are the fermionic Matsubara frequencies $\omega_n = \frac{\pi}{\beta}(2n+1)$.

In the case of the Hubbard Hamiltonian, the Matsubara lattice Green's function is given by:

$$G_{\alpha\beta}(i\omega_n, \mathbf{k}) = \frac{1}{i\omega_n - \hat{H}^{\text{kin}}_{\alpha\beta}(\mathbf{k}) + \mu + \Sigma_{\alpha\beta}(i\omega_n, \mathbf{k})} \quad . \tag{72}$$

Here, μ is the chemical potential, and $\Sigma_{\alpha\beta}(i\omega_n, \mathbf{k})$ is the so-called self-energy. The self-energy is defined as the difference between the inverse of the full interacting Green's function G and the non-interacting Green's function G_0:

$$\Sigma_{\alpha\beta}(i\omega_n, \mathbf{k}) = \left[G_0^{-1}(i\omega_n, \mathbf{k})\right]_{\alpha\beta} - \left[G^{-1}(i\omega_n, \mathbf{k})\right]_{\alpha\beta} \quad . \tag{73}$$

This equation is known as Dyson's equation. The non-interacting Green's function G_0 is defined as:

$$[G_0(i\omega_n, \mathbf{k})]_{\alpha\beta} = \frac{1}{i\omega_n - \hat{H}^{kin}_{\alpha\beta}(\mathbf{k}) + \mu} \quad . \tag{74}$$

Importantly, the one-particle Green's function holds relevant information about the many body state of the system, and one can calculate the expectation value of any single particle operator $\hat{A}_{\alpha\beta}$ from $G_{\alpha\beta}(\tau)$:

$$\langle \hat{A}_{\alpha\beta} \rangle = \lim_{\tau \to 0^-} \sum_{\alpha\beta} A_{\alpha\beta} G_{\beta\alpha}(\tau) \tag{75}$$

or Fourier transformed:

$$\langle \hat{A}_{\alpha\beta} \rangle = \frac{1}{\beta} \sum_{\alpha\beta n} A_{\alpha\beta} G_{\beta\alpha}(i\omega_n) \quad , \tag{76}$$

where I dropped the $\mathbf{k}$ index for simplicity. Therefore, one can for example extract the ground state expectation value of the density matrix of the system by evaluating:

$$\hat{\rho}_{\alpha\beta} = \langle \Psi_0 | \, c^\dagger_\beta(t) c_\alpha(t) \, | \Psi_0 \rangle \tag{77}$$

$$= - \lim_{t \to 0^+} \langle \Psi_0 | \, T[c_\alpha(0) c^\dagger_\beta(t)] \, | \Psi_0 \rangle \tag{78}$$

$$= -iG_{\alpha\beta}(0, 0^+) \, . \tag{79}$$

One can see that the density matrix is obtained from the Green's function at equal time. This is why the Green's function is sometimes called time dependent extension of $\hat{\rho}$. This result can be translated to Matsubara Green's functions as well to calculate the thermal equilibrium value of $\hat{\rho}$:

$$\hat{\rho}_{\alpha\beta} = \frac{1}{\beta} \sum_{n} G_{\alpha\beta}(i\omega_n) \quad . \tag{80}$$

Moreover, the Green's function is directly connected to the spectral function of the system:

$$A_{\alpha\beta}(\omega) = -\frac{1}{\pi} \mathrm{Im} G_{\alpha\beta}(\omega, \mathbf{k}) \quad , \tag{81}$$

which can be directly related to experimentally measured photo emission spectra. Note, that here $G_{\alpha\beta}(\omega, \mathbf{k})$ is the retarded real frequency Green's function, which is obtained by analytic continuation, i.e. taking $i\omega \to \omega + i\delta$ from the Matsubara Green's function.

An important representation of the Matsubara Green's function in the context of this thesis is the Legendre representation [114]. Here, $G(\tau)$ is expanded in terms of Legendre polynomials $P_l(x)$ defined on the interval $[-1, 1]$:

$$G(\tau) = \sum_{l \geqslant 0} \frac{\sqrt{2l+1}}{\beta} P_l[x(\tau)] G_l \, , \tag{82}$$

where $x(\tau) = 2\tau/\beta - 1$ and G_l are the Legendre coefficients. It can be shown, that the coefficients G_l decay faster than $1/l^x$ for any x, and hence, the Legendre representation allows for a very compact representation of the Matsubara Green's function.

The formalism of Green's functions is a powerful tool to express the solution of the Hubbard Hamiltonian (or in any other physical system) in a compact, but yet general form at finite temperatures with arbitrary Coulomb interaction, where the non-trivial part of the solution is stored in the self-energy Σ.

3.7.2 *Dynamical mean field theory*

To make the solution of the Hubbard Hamiltonian feasible, Metzner & Vollhardt [115] found that at infinite coordination numbers of the lattice, $z \to \infty$, i.e., an infinite number of nearest neighbors per site, the self-energy of the Hubbard Hamiltonian in Eq. 65 becomes $\mathbf{k}$ independent:

$$\lim_{z\to\infty} \Sigma_{\alpha\beta}(i\omega_n, \mathbf{k}) \to \Sigma_{\alpha\beta}(i\omega_n) \, . \tag{83}$$

Importantly, already for a three dimensional cubic lattice, with coordination number $z = 6$, and only a local interaction, approximating the self-energy k-independent is almost indistinguishable from the full solution [116]

This locality of the self-energy is the starting point of the development of the DMFT method, where an auxiliary impurity problem is introduced with the same local interaction as the lattice problem (Hubbard Hamiltonian). This impurity is connected to a non-interacting bath, where the connection between bath and impurity is described by a local non-interacting Green's function $\mathcal{G}^0_{\alpha\beta}(i\omega_n)$. Due to the similarity to other mean field theories $\mathcal{G}^0$ is often called *Weiss field*. The mapping from lattice to impurity model is depicted in Fig. 15.

Next, one approximates the lattice self-energy by the impurity self-energy, and one requests that the Green's function of the impurity is identical to the local Green's function of the lattice Problem:

$$G^{\text{imp}}_{\alpha\beta} \stackrel{!}{=} G^{\text{loc}}_{\alpha\beta} \tag{84}$$

This gives the self-consistency condition for DMFT in the form of a Dyson equation:

$$\mathcal{G}^0_{\alpha\beta}(i\omega_n)^{-1} = G^{\text{loc}}_{\alpha\beta}(i\omega_n)^{-1} + \Sigma^{\text{imp}}_{\alpha\beta}(i\omega_n) \quad . \tag{85}$$

This mapping was first introduced by Georges & Kotliar [117], by showing that DMFT maps the Hubbard model exactly to an Anderson impurity model (AIM):

$$\hat{H}^{\text{AIM}} = \hat{H}^{\text{loc}} + \hat{H}^{\text{bath}} + \hat{H}^{\text{hyb}} \, . \tag{86}$$

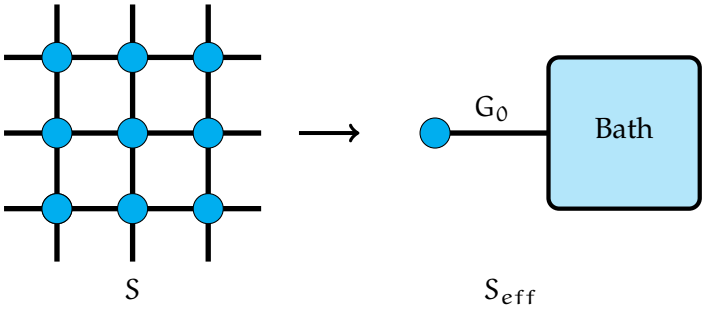

Figure 15: lattice problem S and associated auxiliary impurity problem S_{eff} that is numerically exactly solvable.

Here, $\hat{H}^{loc}$ contains all local parts, i.e. the impurity energy levels and the local Coulomb interaction $\hat{H}_U$. The bath is defined via non-interacting bath states b_γ as:

$$\hat{H}^{bath} = \sum_\gamma \tilde{\epsilon}_\gamma b^\dagger_\gamma b_\gamma \quad , \tag{87}$$

where $\tilde{\epsilon}_\gamma$ are the bath energy levels. The hybridization part describes the coupling between impurity and bath as:

$$\hat{H}^{hyb} = \sum_{\gamma\alpha} V_{\gamma\alpha}(c^\dagger_\alpha b_\gamma + b^\dagger_\gamma c_\alpha) \quad . \tag{88}$$

Importantly, Georges & Kotliar [117] showed that the Weiss Field $\mathcal{G}^0_{\alpha\beta}(i\omega_n)$ is directly connected to the hybridization function of the Anderson impurity model:

$$\Delta_{\alpha\beta}(i\omega_n) = \sum_\gamma \frac{V^*_{\gamma\alpha} V_{\gamma\beta}}{i\omega_n - \tilde{\epsilon}_\gamma} \quad , \tag{89}$$

as follows:

$$\mathcal{G}^0_{\alpha\beta}(i\omega_n) = \left[i\omega_n - \mu - \Delta_{\alpha\beta}(i\omega_n)\right]^{-1} \quad . \tag{90}$$

This is an important step in the practical solution of the Hubbard Hamiltonian, since to solve the Anderson impurity problem various approaches have been developed decades before DMFT even was formulated, allowing to calculate the partition function of the AIM [116]:

$$Z = \mathrm{Tr}\left[e^{-\beta \hat{H}^{AIM}}\right] \tag{91}$$

and hence, the calculation of the impurity Green's function:

$$G^{imp}_{\alpha\beta}(\tau) = \frac{1}{Z}\mathrm{Tr}\left[e^{-(\beta-\tau)\hat{H}^{AIM}} c_\alpha e^{-\tau \hat{H}^{AIM}} c^\dagger_\beta\right] \quad . \tag{92}$$

The approaches to solve this impurity problem are discussed in the next section 3.7.3.

The resulting DMFT self-consistency cycle to calculate the lattice Green's function of the Hubbard Hamiltonian in Eq. 65 is:

1. start with an arbitrary impurity self-energy $\Sigma^{\text{imp}}_{\alpha\beta}(i\omega_n)$
2. construct a lattice Green's function $G_{\alpha\beta}(i\omega_n, \mathbf{k})$ (Eq. 72) by setting:
$$\Sigma_{\alpha\beta}(i\omega_n, \mathbf{k}) \equiv \Sigma^{\text{imp}}_{\alpha\beta}(i\omega_n) \tag{93}$$
3. extract its local part by $\mathbf{k}$ summation:
$$G^{\text{loc}}_{\alpha\beta}(i\omega_n) = \sum_{\mathbf{k}} G_{\alpha\beta}(i\omega_n, \mathbf{k}) \tag{94}$$
4. Apply the DMFT self-consistency condition Eq. 84, by identifying the local Green's function with the impurity Green's, to define the dynamic Weiss field:
$$\mathcal{G}^0_{\alpha\beta}(i\omega_n)^{-1} = G^{\text{loc}}_{\alpha\beta}(i\omega_n)^{-1} + \Sigma^{\text{imp}}_{\alpha\beta}(i\omega_n) \tag{95}$$
5. solve the impurity problem, to obtain the impurity Green's function $G^{\text{imp}}_{\alpha\beta}(i\omega_n)$
6. construct a new impurity self-energy:
$$\Sigma^{\text{imp}}_{\alpha\beta}(i\omega_n) = \mathcal{G}^0_{\alpha\beta}(i\omega_n)^{-1} - G^{\text{imp}}_{\alpha\beta}(i\omega_n)^{-1} \tag{96}$$
7. start again with point 2, until self-consistency is reached

The computational heavy part in DMFT is solving the impurity problem, and obtaining the partition function Z.

3.7.3 *Impurity solvers*

To solve the impurity problem many different schemes exist, and an overview can be found in the review article of Ref. [118]. Here, I would like to focus on Quantum Monte Carlo (QMC) methods to obtain the partition function of the system. More specifically, on the continuous-time QMC (CT-QMC) methods, which allow for a numerically exact solution of the Anderson impurity problem [119, 120]. The basic idea of CT-QMC is to split the Hamiltonian $\hat{H}^{\text{AIM}}$ into an exactly solvable part $\hat{H}_1$, and a part $\hat{H}_2$, which is harder to solve. Then, one defines the time dependent operators of the system in the interaction picture as:

$$O(\tau) = e^{\tau H_1} O e^{-\tau H_1} \quad . \tag{97}$$

If divided into two parts, the solution to the AIM is found in a perturbative way using a power expansion in $\hat{H}_2$:

$$\begin{aligned} Z &= \text{Tr}\left[e^{-\beta \hat{H}_1} T e^{-\int_0^\beta d\tau \hat{H}_2(\tau)}\right] \\ &= \sum_{n=0}^{\infty} \int_0^\beta d\tau_1 \cdots \int_{\tau_{n-1}}^\beta d\tau_n \text{Tr}\left[e^{-\beta \hat{H}_1} H_2(\tau_n) \cdots H_2(\tau_1)\right] \quad . \end{aligned} \tag{98}$$

There are two common flavors of this expansion. The first one chooses for H_2 the $\hat{H}_{loc}$ part, containing the local Coulomb interaction $\hat{H}_U$. This expansion is the so-called interaction expansion (CT-INT) [119]. In this work I use the other common expansion, called hybridization expansion (CT-HYB) [120], which became widely used. Here, the expansion is performed in the hybridization $\hat{H}_2 = \hat{H}^{hyb}$, and $\hat{H}_1$ contains all other terms of the AIM $\hat{H}^{L+B} = \hat{H}^{loc} + \hat{H}^{bath}$:

$$\begin{aligned} Z = \mathrm{Tr}\, e^{-\beta \hat{H}^{AIM}} &= \mathrm{Tr}\left[e^{-\beta \hat{H}^{L+B}}\, T_\tau\, \exp\left(\int_0^\beta d\tau\, H^{hyb}(\tau) \right) \right] \\ &= \sum_{n=0}^{\infty} \int_0^\beta d\tau_1 \cdots \int_{\tau_{n-1}}^\beta d\tau_n \mathrm{Tr}\, \left(e^{-\beta \hat{H}^{L+B}} H^{hyb}(\tau_n) \cdots H^{hyb}(\tau_1) \right) . \end{aligned} \tag{99}$$

Now one uses the fact, that $\hat{H}^{L+B}$ does not mixes impurity and bath degrees of freedom and hence, $\hat{H}^{loc}$ can be separated from $\hat{H}^{bath}$. The non-interacting bath partition function Z^{bath} can be calculated analytically, and it can be shown that the rest of the Hamiltonian can be recast in the determinant of the hybridization function $\Delta_{\alpha\beta}(i\omega_n)$. This gives for the full partition function Z [118]:

$$\begin{aligned} Z = Z^{bath} \sum_{n=0}^{\infty} \int_0^\beta d\tau_1 \cdots \int_{\tau_{n-1}}^\beta d\tau_n \int_0^\beta d\tau'_1 \cdots \int_{\tau'_{n-1}}^\beta d\tau'_n \times \\ \sum_{i_1 \cdots i_n} \sum_{i'_1 \cdots i'_n} \mathrm{Tr}\, \left[e^{-\beta \hat{H}^{loc}}\, T_\tau\, c_{i_n}(\tau_n) c^\dagger_{i'_n}(\tau'_n) \cdots c_{i_1}(\tau_1) c^\dagger_{i'_1}(\tau'_1) \right] \times \\ \det \Delta_{\alpha\beta}(\tau) \quad , \end{aligned} \tag{100}$$

where the operators c_i are impurity states.

Instead of summing all possible contributions to the partition function, Z is evaluated by importance sampling. Here, certain configurations are proposed to be added to the sum and integral of Z, which consist of creation and annihilation operators. This results than in a Markov chain Monte Carlo process with detailed balance, in which new configurations are proposed and accepted or rejected, depending on their acceptance probability, and the corresponding terms are then added to the partition function. While doing this, the Green's function can also be directly measured by adding two additional creation / annihilation operators [118].

Like all QMC methods dealing with fermionic systems also the CT-HYB method suffers from the so-called sign problem, which occurs depending on the chosen basis and the complexity of $\hat{H}_{loc}$ [121]. The problem is, that in fermionic systems exchanging two fermions causes a sign change in the term added to the partition function. Hence, it cannot be ensured that each contribution to Z is positive,

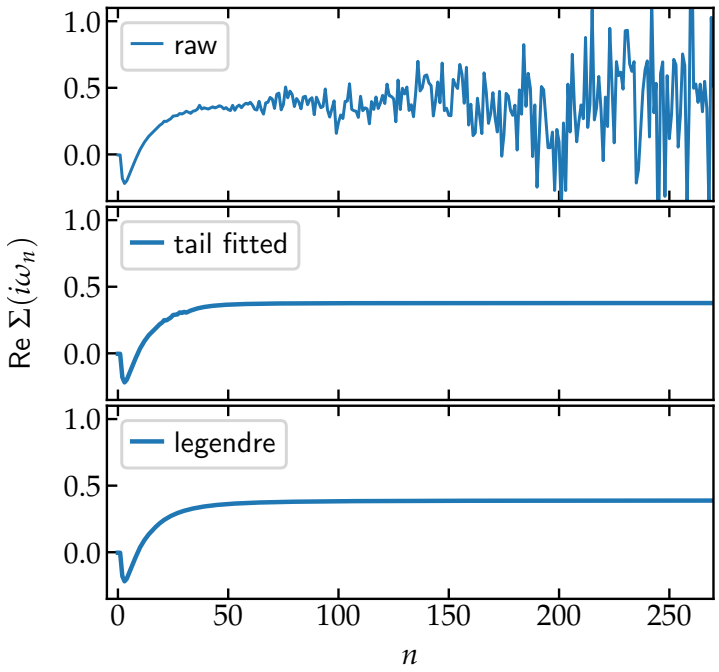

Figure 16: High frequency behavior of the self-energy $\Sigma(i\omega_n)$ calculated from the impurity Matsubara Green's function, comparing different schemes to obtain smooth high-frequency tails. Top: Raw output from the CT-HYB QMC solver, with very noisy data for $n > 50$. Middle: $\Sigma(i\omega_n)$ with the moments of the Green's function fitted by a least-square fit. Bottom: $\Sigma(i\omega_n)$ obtained by a impurity Green's function sampled directly in Legendre coefficients

and eventually different contributions can cancel each other out in the summation. Then, the sampling of Z becomes ineffective, which reduces the accuracy of QMC. Furthermore, this problem grows exponentially with the size of the configuration space of $\hat{H}_{loc}$, and the inverse temperature β of the simulation [118]. However, by choosing an appropriate basis for $\hat{H}_{loc}$ one can make the problem less severe. Popular choices are the crystal field basis, hence diagonalizing the impurity energy levels, or the basis that diagonalizes the impurity occupations.

To solve the impurity problem I utilize the TRIQS/CTHYB solver [122] in this thesis.

3.7.4 *Taking care of the high frequency tail*

As discussed in the previous section, the CT-HYB QMC solver measures the impurity Green's function by a stochastic process. The self-energy is then obtained by the Dyson equation, Eq. 96, by inverting G^{imp} and $\mathcal{G}_0$, and subtracting them from each other. Problematically, the error in Σ^{imp} due to the statistical noise of G^{imp} amplifies itself

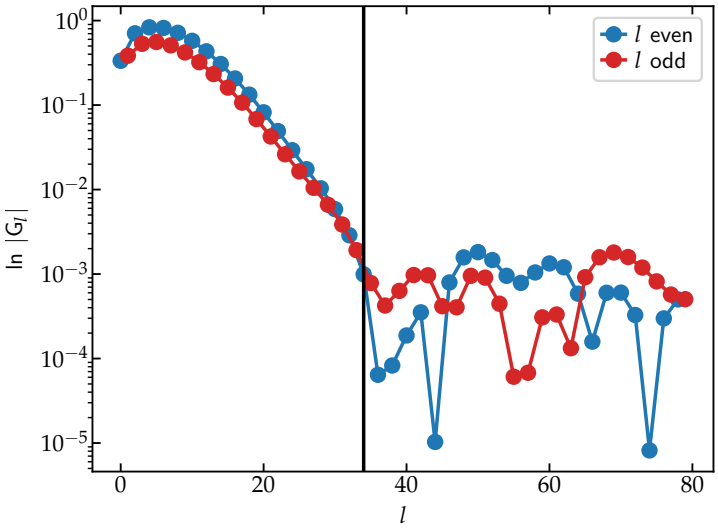

Figure 17: Logarithmic plot of the absolute values of the Legendre coefficients G_l for $SrVO_3$ (one of the three degenerate t_{2g} orbitals), to demonstrate the exponential decay of G_l. For $l > 34$ QMC noise becomes visible and G_l should be truncated at this value. Even (blue) and odd (red) l are plotted separately.

by this inversion. It is found that especially for high-frequencies ω_n, called the *tail*, the error becomes very large, because here $\mathcal{G}_0$ and G^{imp} have similar values [123]. This is critical, since the calculation of any observable from the Green's function involves the summation over all Matsubara frequencies (see eq. 76). Especially the calculation of the interaction energy depends on both G and Σ (see section 3.7.5). Taking care of this high frequency behavior of the Green's function is essential to perform accurate DFT+DMFT calculations. In this section I present two different approaches to minimize the statistical noise in measuring G^{imp}.

The high frequency tail can be described by the moments c_i of the high frequency expansion of the Green's function:

$$G(i\omega_n) = \frac{c_1}{i\omega_n} + \frac{c_2}{(i\omega_n)^2} + \frac{c_2}{(i\omega_n)^3} + \dots \quad . \tag{101}$$

The most straightforward way to minimize the statistical noise, is to perform a least-square fit of the moments of $G(i\omega_n)$ in a window of Matsubara frequencies where the error is still small. Thus, the coefficients c_i can be determined, and a physical high-frequency tail is obtained. An example is shown in Fig. 16. Here, the real part of the impurity self energy $\mathrm{Re}\Sigma(i\omega_n)$ is shown, where the top panel shows the obtained Σ calculated directly from the raw $G(i\omega_n)$ as measured by the QMC solver. In the middle pane a tail fit is performed and a smooth tail is obtained with asymptotic behavior.

Another way to filter the QMC noise is to directly measure the impurity Green's function in the Legendre representation (see eq. 82) in

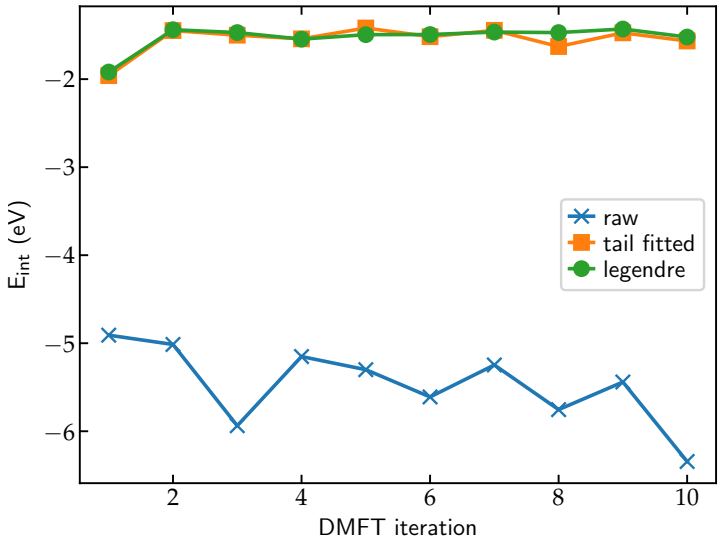

Figure 18: Comparison of the DMFT interaction energy obtained from the raw sampled Matsubara Green's function, the tail fitted Green's function, and the Green's function sampled directly in Legendre coefficients.

DMFT as described in detail in Ref. [114]. Here, one uses the fact that the Legendre coefficients decay very fast as described in section 3.7.1. Of course, the QMC measurement of G_l carries in principle the same noise as the measurement of $G(i\omega_n)$, and higher l will show more statistical noise, as they directly correlate with the higher Matsubara frequencies [114]. However, in Ref. [114] it is shown that the physical properties of the system are carried by the low order coefficients, and a basis truncation will act as an effective QMC noise filter. The result is demonstrated in the bottom panel of Fig. 16, showing as well a smooth high-frequency behavior, without performing a tail fit.

The choice, when the basis is truncated has to be handled with care, since the actual decay of G_l can vary, for example at different temperatures, or in insulating and metallic phases. Therefore, one has to identify the highest G_l that is essentially free of statistical noise. Theoretically G_l decays exponentially fast and the truncation can be performed when the exponential decay stops [114]. This is demonstrated in Fig. 17. Here, G_l is shown the computed for $SrVO_3$ in the insulating phase. To demonstrate the exponential decay, G_l is plotted on a logarithmic scale, for even and odd l. The exponential decay is visible up to $l \sim 34$. Above, the statistical noise becomes visible and the basis can be truncated, which amounts to setting all G_l with $l > l_{max}$ to zero.

Furthermore, the importance of a accurate treatment of the high-frequency tail is demonstrated in Fig. 18. Here, the interaction energy as function of the DMFT iteration is shown. The calculation of the interaction energy is defined later in Eq. 120. The energy is cal-

culated from three differently obtained Green's functions. First, with the raw $G(\tau)$ (blue). Second, with a least-square tail fit performed in $G^{imp}(i\omega_n)$ (orange), and third, by sampling directly Legendre coefficients of G^{imp} (green). Importantly, the tail fit and Legendre sampling result in similar energy values, which are quite constant throughout the DMFT iterations. Contrary, the interaction energy calculated from the raw $G(\tau)$ shows a large offset of ~ 4 eV, and very large oscillations between the iterations. This large shift is due to the fact, that the interaction energy is critically determined by the high-frequency value of Re $\Sigma(i\omega_n)$, which is the so-called Hartree shift of the self-energy.

For all calculations presented in this thesis, I utilized the direct measurement of G_l in the TRIQS/CTHYB solver [122], as this resulted in very fast convergence and accurate observables, without adjusting fit parameters.

3.7.5 *DFT+DMFT functional*

The spectral density functional theory, which formally connects DFT and DMFT, allows to tackle the correlated electron problem for realistic materials starting from DFT [124]. The spectral density functional theory defines a functional of the free energy, which under approximations leads to the DMFT self-consistency equations, and to a consistent connection between DFT and DMFT via the charge density $\rho(\mathbf{r})$. Here, I give a brief summary based on the review article [14] and the lecture notes [112].

In spectral density functional theory, one chooses variables to perform a Legendre transformation of the partition function Z, or the free energy, of the system, to obtain a functional solely in terms of a chosen variable. The general Baym-Kadanoff functional Γ is such a functional, which uses the one-particle Green's function as variable, and gives at the stationary point the free energy of the system. It has the following form [125]:

$$\Gamma[G] = \mathrm{Tr}\ \ln G - \mathrm{Tr}\ \left[(G_0^{-1} - G^{-1})G)\right] + \Phi[G] \quad , \tag{102}$$

and is decomposed into the single particle kinetic part, a correction to the kinetic energy due to the interaction, and the correlated i.e. interaction part of the functional, $\Phi[G]$, the so-called Luttinger-Ward part. Here, G is the full Green's function of the whole system without explicit matrix notation, and G_0 is the corresponding non-interactig Green's function. Extremizing $\Phi[G]$ with respect to G defines the interaction part of the electron self-energy [124]:

$$\Sigma = \frac{\delta\Phi}{\delta G} \tag{103}$$

In general $\Phi[G]$ is not known, but provides a starting point to develop approximations.

For the DFT+DMFT approximation the Luttinger-Ward part of the functional is approximated by the interacting part of the DFT functional in Eq. 13, and the DMFT functional of the correlated subspace [124]:

$$\Phi[G] \approx E_H[\rho(\mathbf{r})] + E_{XC}[\rho(\mathbf{r})] + \Phi^{DMFT}[G^{loc}_{\alpha\beta}] - \Phi^{DC}[n_{\alpha\beta}] \quad . \tag{104}$$

Here, Φ^{DC} is the double-counting correction to correct for the correlation effects already accounted in DFT, which is determined by the local occupation $n_{\alpha\beta}$. Crucially, there exists no diagrammatic representation of Φ^{DC}, because $E_{XC}[\rho(\mathbf{r})]$ includes already energy contributions from all orbitals in some form, and the contributions from the correlated subspace cannot be separated easily. Note, that the full Green's function of the system is connected with the charge-density by:

$$\rho(r) = \frac{1}{\beta}\sum_n G(\mathbf{r}, i\omega_n) \quad . \tag{105}$$

The full DFT+DMFT functional is now given by:

$$\begin{aligned} &\Gamma_{DFT+DMFT}[G] \\ &= \mathrm{Tr}\,\ln[G] - \mathrm{Tr}\,\left[(G_0^{-1} - G^{-1})G)\right] + E_H[\rho] + E_{XC}[\rho] \\ &+ \Phi^{DMFT}[G^{loc}_{\alpha\beta}] - \Phi^{DC}[n_{\alpha\beta}] \quad . \end{aligned} \tag{106}$$

The free energy is obtained by extremizing the functional with respect to G, obtaining the conditions for stationarity:

$$\frac{\delta\Gamma_{DFT+DMFT}}{\delta G} = 0 \quad , \tag{107}$$

which gives the Dyson equation of the system:

$$G_0^{-1} - G^{-1} = V_H + V_{XC} + \frac{\delta\Phi^{DMFT}}{\delta G} - \frac{\delta\Phi^{DC}}{\delta G} \quad . \tag{108}$$

Since Φ^{DMFT} only depends on G^{loc}, because in DMFT G is approximated with its local counterpart, one obtains for the derivative of Φ^{DMFT}:

$$\frac{\delta\Phi^{DMFT}}{\delta G} = \frac{\delta\Phi^{DMFT}}{\delta G^{loc}_{\alpha\beta}} = \Sigma^{DMFT}_{\alpha\beta} \quad . \tag{109}$$

Here, the DMFT self-energy is defined for the full lattice system. The self-energy is then given by the impurity self-energy, because at DMFT self-consistency the lattice self-energy can be identified with the impurity self-energy. Accordingly, the derivative of Φ^{DC} gives:

$$\frac{\delta\Phi^{DC}}{\delta G} = \Sigma^{DC} \quad . \tag{110}$$

The down- and up-folding from the correlated subspace to the KS basis, to connect the full system Green's function, G, with the impurity self-energy Σ^{imp}, is done via the projection operators defined in Eq. 35. The full lattice self-energy for the DMFT part, including the DC, can then be defined as:

$$\Sigma^{\text{DMFT}}(\mathbf{k}, i\omega_n) = \sum_{\alpha\beta} \hat{P}^{\dagger}_{\alpha\nu}(\mathbf{k}) \left(\Sigma^{\text{imp}}_{\alpha\beta}(i\omega_n) - \Sigma^{\text{DC}}_{\alpha\beta}\right) \hat{P}_{\beta\nu'}(\mathbf{k}) \quad . \tag{111}$$

For bands outside of the projection window C, the self-energy is set to zero, so that Σ^{DMFT} is defined for all bands ν. Therefore, we can now rearrange Eq. 108:

$$G_0^{-1} - G^{-1} = V_H + V_{XC} + \Sigma^{\text{DMFT}}(\mathbf{r}, i\omega_n) \quad . \tag{112}$$

Here, the self-energy as been Fourier transformed. Moreover, one should note that the system can contain multiple correlated atomic sites, that each give a separate impurity problem, coupled through the DMFT self-consistency loop. Hence, $\Sigma^{\text{imp}}_{\alpha\beta}(i\omega_n)$, and Σ^{DC} being block diagonal in R.

Now, from Eq. 112, the full Green's function of the system can be defined as:

$$G(\mathbf{r}, i\omega_n) = \left[i\omega_n + \mu + \frac{1}{2m}\Delta - V_{KS}(\mathbf{r}) - \Sigma^{\text{DMFT}}(\mathbf{r}, i\omega_n) \right]^{-1} \quad . \tag{113}$$

Since ρ is obtained from $G(\mathbf{r}, i\omega_n)$, this equation shows that ρ and Σ^{DMFT} are indeed coupled, and stationarity of $\Gamma_{\text{DFT+DMFT}}$ is only reached if both charge-density, and Green's function are self-consistently calculated. A DFT+DMFT calculation performed in this way is called charge self-consistent (CSC). This is done in two self-consistency loops. One inner loop for DMFT, converging G for a given ρ respectively $\Psi_{\nu\mathbf{k}}$, resulting in a new charge density, and one outer loop to convergence ρ each time a new charge density is obtained from DMFT. To obtain stationarity one also needs to satisfy $\delta\hat{P}/\delta G = 0$, since the up- and down-folding depends on $\hat{P}$. In practice this can cause problems, because the projectors change as the DFT wave functions change whenever a new ρ is calculated [126].

Inserting both Eq. 112 and Eq. 113 into the DFT+DMFT functional Eq. 106, gives the free energy functional of the system at the stationary G and ρ:

$$\begin{aligned}
&\Gamma_{\text{DFT+DMFT}}[\rho, G^{\text{imp}}] \\
&= -\operatorname{Tr} \ln \left[i\omega_n + \mu + \frac{1}{2m}\Delta - V_{\text{KS}}(\mathbf{r}) - \Sigma(\mathbf{r}, i\omega_n) \right] \\
&\quad - \int d\mathbf{r} \left[V_{\text{KS}}(\mathbf{r}) - V_{\text{ext}}(\mathbf{r}) \right] \rho(\mathbf{r}) - \operatorname{Tr} \left[\Sigma^{\text{DMFT}}(\mathbf{r}, i\omega_n)\, G(\mathbf{r}, i\omega_n) \right] \\
&\quad + E_{\text{H}}[\rho(\mathbf{r})] + E_{\text{XC}}[\rho(\mathbf{r})] + \Phi^{\text{DMFT}}[G^{\text{imp}}] - \Phi^{\text{DC}}[n^{\text{imp}}_{\alpha\beta}] \,,
\end{aligned} \tag{114}$$

This shows that approximating the Luttinger-Ward part of the Baym-Kadanoff functional with both the DFT and the DMFT approximations, motivates a combined DFT+DMFT scheme, which, if all stationarity conditions are fulfilled, gives the equilibrium free-energy of the system.

The KS Green's function of the system is given as:

$$G_{\text{KS}}(\mathbf{k}, i\omega_n) = \frac{1}{i\omega_n + \mu - \epsilon^{\text{KS}}_{\mathbf{k}}} \quad , \tag{115}$$

which allows to rewrite the free energy of the system in Eq. 114:

$$\begin{aligned}
\Gamma_{\text{DFT+DMFT}}[\rho, G^{\text{imp}}] = \Gamma_{\text{DFT}}[\rho] &\\
+ \operatorname{Tr} \ln G^{-1}_{\text{KS}}(\mathbf{k}, i\omega_n) + \operatorname{Tr} \ln G(\mathbf{r}, i\omega_n) &\\
- \operatorname{Tr} \left[\Sigma^{\text{DMFT}}(\mathbf{r}, i\omega_n)\, G(\mathbf{r}, i\omega_n) \right] &\\
+ \Phi^{\text{DMFT}}[G^{\text{imp}}] - \Phi^{\text{DC}}[n^{\text{imp}}_{\alpha\beta}] \quad .&
\end{aligned} \tag{116}$$

Here, $\Gamma_{\text{DFT}}[\rho]$ is the free energy of the DFT system, which at $T \to 0$ K is $E_{\text{DFT}}[\rho]$. The functional Φ^{DMFT} is not known, but one can construct the free energy functional for the DMFT impurity problem [126]:

$$\begin{aligned}
\Gamma_{\text{imp}}[G^{\text{imp}}] = \operatorname{Tr} \ln G^{\text{imp}}_{\alpha\beta}(i\omega_n) - \operatorname{Tr} \left[\Sigma^{\text{imp}}_{\alpha\beta}(i\omega_n) G^{\text{imp}}_{\alpha\beta}(i\omega_n) \right] &\\
+ \Phi^{\text{DMFT}}[G^{\text{imp}}] \quad ,&
\end{aligned} \tag{117}$$

and use the fact that the impurity problem has the same Luttinger-Ward part as $\Gamma_{\text{DFT+DMFT}}$. Therefore, inserting Eq. 117 into Eq. 116 gives:

$$\begin{aligned}
\Gamma_{\text{DFT+DMFT}}[\rho, G^{\text{imp}}] = \Gamma_{\text{DFT}}[\rho] &\\
+ \operatorname{Tr} \ln G^{-1}_{\text{KS}}(\mathbf{k}, i\omega_n) + \operatorname{Tr} \ln G(\mathbf{r}, i\omega_n) &\\
+ \Gamma_{\text{imp}}[G^{\text{imp}}] - \operatorname{Tr} \ln G^{\text{imp}}_{\alpha\beta}(i\omega_n) &\\
- \Phi^{\text{DC}}[n^{\text{imp}}_{\alpha\beta}] \quad .&
\end{aligned} \tag{118}$$

This form of the free energy can be computed, with an expression of the free energy of the impurity [126]. Moreover, one approximates the DC term with one of the DC schemes presented in section 3.7.6. However, calculating these expressions including all entropy terms is rather tedious and has only been achieved very recently [126].

In the context of this work I am interested in calculating the energetics of structural distortions, hence the calculation of the DFT+DMFT energy is necessary. To do so, I use the total energy, which corresponds to the $T \to 0$ K limit of the free energy. This is obtained by replacing the DFT and impurity free energy by the corresponding total energy expressions, and by separating energy from entropy terms [124]:

$$E_{\text{DFT+DMFT}} = E_{\text{DFT}}[\rho] - \frac{1}{N_k} \sum_{\lambda,\vec{k}} w_{\vec{k}}\, \epsilon^{\text{KS}}_{\lambda,\vec{k}}\, f_{\lambda\vec{k}} + \text{Tr}\langle H_{\text{KS}} G(\mathbf{k}, i\omega_n)\rangle + E^{\text{imp}}_{\text{int}}[G^{\text{imp}}_{\alpha\beta}(i\omega_n)] - E_{\text{DC}}[n^{\text{imp}}_{\alpha\beta}] \quad . \tag{119}$$

Here, $\epsilon^{\text{KS}}_{\lambda,\vec{k}}$ are the KS energies in the correlated subspace, hence the kinetic energy part of the KS system for C. The third term then adds the kinetic energy of the correlated system. The interaction part of DMFT, $E^{\text{imp}}_{\text{int}}$, is calculated using the Galitskii-Migdal formula [127]:

$$E^{\text{imp}}_{\text{int}} = \langle H_U \rangle = \frac{1}{2} \sum_{\alpha\beta n} \left[\Sigma^{\text{imp}}_{\alpha\beta}(i\omega_n) G^{\text{imp}}_{\beta\alpha}(i\omega_n) \right] \quad . \tag{120}$$

In principle, one would assume that for the calculation of the expectation value of a two particle operator, such as $\hat{H}_U$, one needs to evaluate a two particle Green's function. However, as shown in Ref. [127], for the expectation value of H_{int} a single particle Green's function is sufficient. Note, that this form is only exact for 0 K. Therefore, whenever the impurity energy is calculated in the context of this work I approximate the energy by the Galitskii-Migdal formula. The corresponding derivation for the ground state can be found in the Appendix A.

It should be mentioned that this form of the interaction energy is only correct if the functional in Eq. 114 is fully stationary and the calculation is performed at $T = 0$ K. Besides the temperature effects, this is problematic, since the double-counting term is not known exactly, which is necessary to fulfill the stationary conditions. Therefore, the calculated energies are only approximative, and dependent on the chosen double-counting correction scheme.

3.7.6 *double-counting correction*

The problem of double-counting inherent in DFT+DMFT, and also in DFT+U (section 3.6), is a ill-defined problem. There exist several expressions for E_{DC}, where the two most prominent ones are the

around mean-field (AMF) approximation [84], and the fully localized limit (FLL) [128, 129]. In AMF one assumes that DFT corresponds to a mean-field solution of the many body problem, in which the occupation matrix of the local orbitals in the correlated subspace in DFT are orbital independent, and one uses the orbital averaged occupation matrix of the local orbitals as DC correction. However, the method led to unsatisfactory results in many cases. Often the assumption made is not correct, as it can be observed that the crystal field splittings, and hence orbital dependent occupations, are usually quite well captured in DFT.

This led to the formulation of the FLL method, which takes the converse approach coming from the atomic limit. This results in an energy correction of the following form:

$$E_{DC}^{FLL}[n_R] = \frac{U_{avg}}{2} n_R(n_R - 1) - \sum_{\sigma} \frac{J_{avg}}{2} n_R^{\sigma}(n_R^{\sigma} - 1) \quad , \tag{121}$$

where n_R is the total occupation of the correlated orbitals of the atomic site R, n_R^{σ} the corresponding occupation of one of the spin channels. The corresponding double-counting potential is then:

$$\Sigma^{DC}[n_R] = \frac{\delta E_{DC}^{FLL}}{\delta n_R} = U_{avg}\left(n_R - \frac{1}{2}\right) - J_{avg}\left(n_R^{\sigma} - \frac{1}{2}\right) \quad . \tag{122}$$

A similar approach, which is closely related to the FLL approximation was derived by Ref. [15, 130], which I will label "ANI". It is specifically formulated for systems with cubic symmetry containing octahedral crystal field splittings, and is thus suitable for t_{2g} or e_g correlated subspaces. The energy correction has the form:

$$E_{DC}^{ANI}[n_R] = \frac{1}{2}\bar{U} n_i(n_i - 1) \quad , \tag{123}$$

where $\bar{U}$ is the averaged Coulomb interaction:

$$\bar{U} = \frac{\mathcal{U} + (M-1)(\mathcal{U} - 2\mathcal{J}) + (M-1)(\mathcal{U} - 3\mathcal{J})}{2M - 1} \, . \tag{124}$$

Here, M is the number of orbitals, and $\mathcal{U}$ and $\mathcal{J}$ correspond to the interaction parameters of the Hubbard-Kanamori interaction Hamiltonian in Eq. 52. Hence, this DC scheme is directly tailored for the use with the Hubbard-Kanamori interaction [15]. The resulting DC potential reads:

$$\Sigma_{DC}[n_R] = \bar{U}(n_R - \frac{1}{2}) \, . \tag{125}$$

It is quite obvious that the FLL scheme and the ANI scheme are quite similar, where in the latter the exchange part J is condensed into the averaged interaction parameter $\bar{U}$. In fact, it can be shown that for $M = 5$ and half-filling both schemes give the same DC potential [131].

An interesting question arises when it comes to the evaluation of the occupations n_R in any of the DC schemes. These occupations for the DC potential can either be directly calculated from the Wannier functions constructed from DFT, or from the impurity Green's function G^{imp} calculated by the QMC solver within DMFT. It can be misleading to assume that these quantities are always the same. Indeed, when the system is in a charge-ordered phase, such as found, e.g., in heterostructures or nickelates with multiple impurities, it often occurs that the occupations of the different atomic sites are quite different in DMFT compared to the DFT result. Then, this results in differences in the DC potential shift between the sites, compared to the DC potential calculated with the DFT Wannier function occupations. One should note, that in a charge self-consistent DFT+DMFT calculation the DFT obtained occupations lose their physical meaning, since the DFT calculation is non-self-consistent. This question is further elucidated in chapter 7.

3.7.7 *DFT+DMFT in practice*

Finally, I would like to condense the theory of the last sections to sketch the working scheme for doing DFT+DMFT calculations. This scheme is well known by now, and several different implementations exist [132–134].

First, a normal self-consistent DFT calculation is performed for the chosen crystal structure. From the band structure or the orbital-resolved DOS, the correlated subspace C can be identified. As an example, one can use as a correlated subspace the e_g orbitals, which are the frontier orbitals found around the Fermi level of all nickelate compounds. Of course one could also identify all d-orbitals as correlated subspace, or even all oxygen p- and d-orbitals.

Next, Wannier functions are constructed for these KS eigenstates, as described in section 3.3. In principle, either of the two described schemes, MLWFs or PLOS, can be applied. I mostly utilize the projection onto localized orbitals, which has been very recently implemented in the VASP code [135]. In a first step, the projection of the KS eigenstates onto localized orbitals $|\tilde{\chi}_\alpha(\mathbf{k})\rangle$ is performed within VASP. This is done for all d-states in the chosen energy window of C, as described in Eq. 31. In the PAW framework, the resulting projection operator, can be expressed as [90, 136]:

$$\hat{P}_{\alpha\nu}(\mathbf{k}) = \sum_i \langle \chi_\alpha | \phi_{\alpha,n} \rangle \langle \widetilde{p}_{\alpha,n} | \widetilde{\Psi}_{\nu,\mathbf{k}} \rangle \quad , \tag{126}$$

where $\phi_{\alpha,n}$ is an all-electron partial wave, as introduced in Eq. 22, with n labeling the radial quantum number explicitly, i.e. the PAW channel. $\widetilde{p}_{\alpha,n}$ is a PAW projector, and $\widetilde{\Psi}_{\nu,\mathbf{k}}$ is the pseudo-KS state.

One is left with the choice of the localized state χ_α, which defines the basis of the correlated subspace. In the PAW formalism the partial

waves are solutions to the radial Schrodinger equation for an atom and thus, can in principle be used as convenient choice for the localized states, i.e. $|\chi_\alpha\rangle \equiv |\phi_{\alpha,n}\rangle$. Still, one needs to choose an appropriate augmentation channel n. To achieve an optimal projection, I apply the scheme introduced in Ref. [135], choosing a linear combination of the augmentation channels, to maximize the overlap between the projector and the KS state in a chosen energy window, which matches that of the correlated subspace. Then, the projectors need to be orthonormalized in the chosen energy window according to Eq. 33, which is done within the TRIQS/DFTTools software package [137, 138].

I would like to emphasize the importance of the chosen energy window $\mathcal{W}$ for the construction. If only the bands are chosen close to the Fermi level, which have dominant d or f character, the possible hybridization to oxygen p orbitals shows itself as tails, extending the Wannier functions to the oxygen atoms. As an example the constructed e_g orbitals for $LuNiO_3$ are shown in Fig. 12. On the other hand, if one would include the oxygen p bands in the construction, and hence increasing the energy window, the resulting MLWFs would be drastically more localized, appearing to be more atomic like.

With the obtained projector functions $\hat{P}_{\alpha\nu}(\mathbf{k})$ it is now possible to extract the local Green's function from the full lattice Green's function (Eq. 113):

$$\begin{aligned} G^{loc}_{\alpha\beta}(i\omega_n) &= \sum_{\mathbf{k}} \hat{P}_{\alpha\nu}(\mathbf{k}) G(\mathbf{k}, i\omega_n) \hat{P}^\dagger_{\nu'\beta}(\mathbf{k}) \\ &= \sum_{\mathbf{k}} \left[\hat{P}_{\alpha\nu}(\mathbf{k}) \left(i\omega_n + \mu - \hat{H}_{KS}(\mathbf{k}) - \Sigma^{DMFT}(\mathbf{k}, i\omega_n) \right) \hat{P}^\dagger_{\nu'\beta}(\mathbf{k}) \right]^{-1} \\ &= \sum_{\mathbf{k}} \left[i\omega_n + \mu - \hat{P}_{\alpha\nu}(\mathbf{k}) \hat{H}_{KS}(\mathbf{k}) \hat{P}^\dagger_{\nu'\beta}(\mathbf{k}) - \Sigma^{imp}_{\alpha\beta}(i\omega_n) + \Sigma^{DC}_{\alpha\beta} \right]^{-1} \\ &= \sum_{\mathbf{k}} \left[i\omega_n + \mu - \epsilon^C_{\alpha\beta}(\mathbf{k}) - \Sigma^{imp}_{\alpha\beta}(i\omega_n) + \Sigma^{DC}_{\alpha\beta} \right]^{-1} . \end{aligned} \tag{127}$$

Here, $\epsilon^C_{\alpha\beta}(\mathbf{k})$ is diagonal containing the KS eigenvalues in the correlated subspace. Importantly, $\epsilon^C_{\alpha\beta}(\mathbf{k})$ contains the local orbital energy levels $\epsilon_{\alpha\beta}$, e.g. the crystal field splittings, which are $\mathbf{k}$-independent. Therefore, by performing the $\mathbf{k}$ summation, the crystal field splittings enter DMFT directly:

$$\epsilon_{\alpha\beta} = \frac{1}{N_k} \sum_{\mathbf{k}} \epsilon^C_{\alpha\beta}(\mathbf{k}) \tag{128}$$

Note that in the first iteration $\Sigma^{imp}_{\alpha\beta}(i\omega_n)$ is set to zero. Now, one can construct the Weiss field $\mathcal{G}^0_{\alpha\beta}(i\omega_n)$ from $G^{loc}_{\alpha\beta}(i\omega_n)$, which serves as part of the input for the DMFT impurity solver. The handling of the

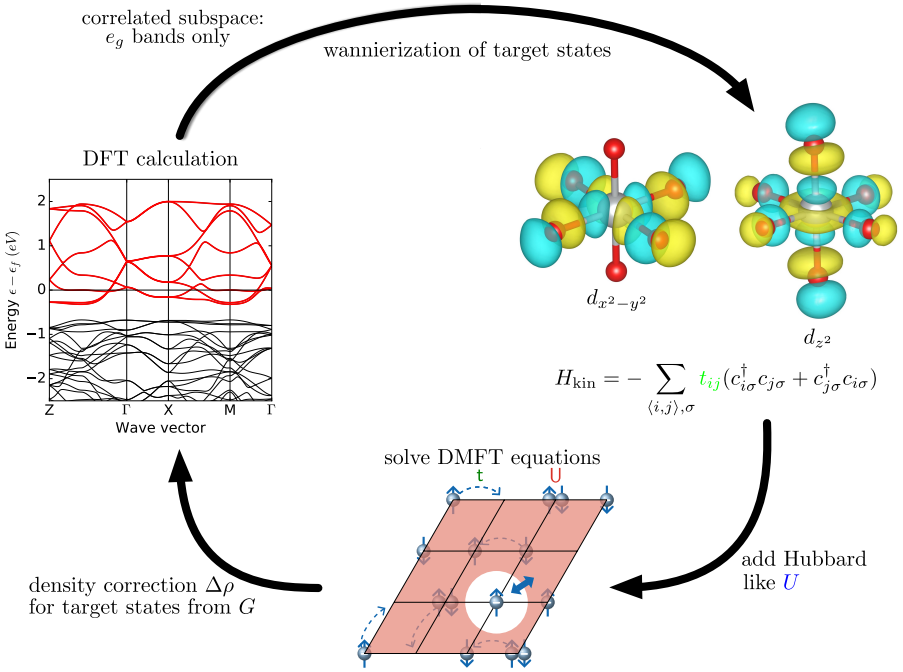

Figure 19: Full DFT+DMFT scheme for practical calculations. Starting from a DFT calculation (left) one identifies a correlated subspace, for which Wannier functions are constructed (right). From here, hopping parameters $t_{\alpha\beta}$ are extracted, e.g. the band dispersion $\epsilon^C_{\alpha\beta}(\mathbf{k})$. By adding $\hat{H}_U$ one obtains a Hubbard like Hamiltonian, which is solved self-consistently in the DMFT approximation (bottom). From the resulting impurity Green's function a new DFT charge density is constructed. The correction $\Delta\rho$ is handed back to DFT. From here, the cycle repeats itself by obtaining new KS eigenstates.

Green's function objects is done within the TRIQS software library [138].

Next, a Hubbard like interaction $\hat{U}$ is defined for the local Hamiltonian for each impurity problem. As already mentioned, the choice of C influences the form of the Wannier orbitals, and hence also how to construct a suitable interaction matrix $\hat{U}$, see section 3.4. The Coulomb interaction tensor can be calculated using the cRPA method as presented in section 3.5, or treated as a parameter, using either the Slater, or the Hubbard-Kanamori parameterization. The resulting impurity problem is then solved with the TRIQS/CTHYB solver [122]. The DMFT cycle is iterated until self-consistency is reached. Here, the difference in orbital occupations from the impurity Green's function between two consecutive DMFT iterations can be used to check whether self-consistency is reached. However, there exist no clear metric in the community how self-consistency is quantified, and it should always be communicated how convergence is defined.

From the resulting $G^{imp}(i\omega_n)$ an updated charge density for DFT is constructed:

$$\begin{aligned}\rho(\mathbf{r}) = &\sum_{\mathbf{k}} \sum_{\nu \notin C} f_{\nu\mathbf{k}} \langle \mathbf{r}|\Psi_{\nu,\mathbf{k}}\rangle \langle \Psi_{\nu,\mathbf{k}}|\mathbf{r}\rangle \\ &+ \sum_{\mathbf{k}} \sum_{\nu\nu' \in C} \langle \mathbf{r}|\Psi_{\nu,\mathbf{k}}\rangle \, \rho_{\nu\nu'}(\mathbf{k}) \, \langle \Psi_{\nu',\mathbf{k}}|\mathbf{r}\rangle \ ,\end{aligned} \tag{129}$$

where $\rho_{\nu\nu'}(\mathbf{k})$ is the up-folded impurity occupation. Per definition, the change in the charge density due to $\rho_{\nu\nu'}(\mathbf{k})$ summed over $\mathbf{k}$ must be zero, to ensure charge neutrality. The updated charge density is now handed back to the DFT code (VASP), which in turn calculates new KS eigenstates, and the circle is closed by calculating new projectors. Note that in practice the DFT calculation is performed in a non self-consistent mode during the DFT+DMFT iterations. This means, that the charge density is only updated from the DMFT output. Once, the charge density does not change anymore convergence between DFT and DMFT is reached.

This calculational scheme allows to perform fully charge self-consistent DFT+DMFT calculations completely *ab initio*. The full scheme is sketched in Fig. 19. It should be noted, that one can also do a so-called one-shot (OS) calculation, by not updating the charge density. This reduces the computational effort, and can be justified for systems where the charge density is only insignificantly influenced by the DMFT result. A detailed comparison between CSC and OS calculations is performed in chapter 7.

From a technical point of view, TRIQS is a software library, which means, that the actual program that controls the DFT code, performs the DMFT self-consistency loop, handles the up- and down-folding, and extracts physical observables, needs to be written.

The development of a DFT+DMFT software, that can also used by other members of the community, was also part of my PhD thesis. I worked closely together with the developers of the VASP / TRIQS interface, namely Oleg E. Peil, Matle Schüler, and Gernot Kraberger. The resulting code, which I used for the DFT+DMFT calculations, was developed mainly by myself and partially by Sophie Beck, and is openly available on github [139].

This concludes the description of the methodological background. In what follows, I use the DFT++ methods presented here, to investigate the rare-earth nickelates series.

4

ESTABLISHING TRENDS OF THE SERIES BY USING DFT+U

In this chapter I present the work of the first part of my research, in which I used DFT+U to establish structural trends across the nickelate series. Moreover, I examined the influence of the choice of interaction parameters, and different magnetic orderings on structural properties. These calculations are important to establish a well-defined starting point for the following DFT+DMFT calculations. As described in chapter 1, I motivate the work by discussing already appeared literature, which is then followed by a summary of the project. This includes also further results obtained, which are not in the published research article.

The work was published as *"Interplay between breathing mode distortion and magnetic order in rare-earth nickelates $RNiO_3$ within DFT+U"* in Physical Review B, see Ref. [140]. Copyright (2017) by the American Physical Society. I performed all calculations, and wrote the first draft, which has been then discussed, and corrected together with my supervisor C. Ederer.

4.1 MOTIVATION

Motivated by the work of Balachandran & Rondinelli [63], I first analyzed present experimental data of nickelate compounds in terms of their distortion mode amplitudes as described in section 2.6. From this analysis it becomes evident, that the structural data from experiment for the metallic high-temperature $Pbnm$ phase of nickelates is quite consistent and complete. Only experimental data for $R = Gd$, and Sm is still missing. However, for the low-temperature $P2_1/n$ phase, the existing structural data, especially for the most relevant breathing mode distortion amplitude, does not result in clear trends across the series (see Fig. 9 of the presented paper [140]). Problematically, the experiments for the different compounds are performed at different temperatures, partially in the paramagnetic, and partially in the anti-ferromagnetic phase. Furthermore, temperature-dependent structural parameters are rarely available. This makes it difficult to recognize systematic trends across the series. Especially, data for $R =$ Dy [31], and Ho [28, 29] is puzzling, with breathing mode distortions considerably larger than for the other compounds. Hence, it becomes apparent that structural data from *ab initio* calculations are highly valuable to better understand the properties of the nickelate series.

ab initio studies employing DFT and its extensions to obtain structural parameters of the rare-earth nickelates are all relatively recent [23, 24, 26, 34, 44, 49]. Before I started my research only the works of Ref. [23, 26, 34] had been published. In Ref. [26] a DFT+U study on $NdNiO_3$ is performed, analyzing the effect of U_{avg} on the breathing mode distortion. They find, that without +U, and magnetic order, the high-temperature $Pbnm$ structure of $NdNiO_3$ is well captured. When +U calculations are performed and magnetic ordering is induced, a finite breathing mode amplitude is stabilized in relaxations, capturing the low-temperature structure of $NdNiO_3$. Moreover, they show that the breathing mode distortion amplitude is quite sensitive to U_{avg}, with increasing size for larger U_{avg}. At large values U_{avg} the breathing mode distortion eventually destabilizes.

In Ref. [34] the influence of strain on bulk $LuNiO_3$ is investigated. In the study of Ref [23] also $LuNiO_3$ is investigated with DFT+U using $U_{avg} = 5$ eV and ferromagnetic order. Here, the electronic structure is mainly investigated, comparing also to a possible occurring Jahn-Teller distortion in DFT+U. From these findings it becomes clear, that even though a description of the low-temperature phase with DFT+U is possible, this was only shown for certain members of the series and the possible influence of different magnetic orderings is not yet clear. Also a detailed comparison with experiment across the series has not been done.

These results were taken as starting point for my first research project. Here, I am addressing the question of how well structural parameters are described across the nickelate series within DFT+U, both for the high-temperature and the low-temperature phase. Furthermore, I investigated how the magnetic order couples to the breathing mode distortion. Moreover, I analyzed critically the influence of the interaction parameters in DFT+U. These calculations allow to better understand the capabilities and limitations of DFT+U do describe the complex phases in nickelates. This will in turn show for which properties more advanced, beyond static mean field methods, are needed.

4.2 PROJECT SUMMARY

We first performed calculations for the experimental structure of $LuNiO_3$ in the low-temperature $P2_1/n$ phase [29]. Here, we analyze the stability of different magnetic orderings as function of U_{avg} and J_{avg}. We show for the first time, that the AFM ordering observed in experiment is only energetically favored in for small values of U_{avg} (see Fig. 6 of Ref. [140]). The ferromagnetic ordering, which is not observed in experiment, is favored for all other chosen interaction parameter settings. Moreover, we energetically compare various AFM orderings, and it is shown that the experimentally compatible ordering, T-AFM, is favored for a wide parameter range compared

to other AFM orderings. Therefore, we conclude that the magnetic order is correctly captured by DFT calculations, if a rather small value of $U_{avg} \leqslant 2$ eV is used.

Next, the response upon changes to the breathing mode amplitude R_1^+ is investigated (see Fig. 7 of Ref. [140]). Starting from the experimental structure of $LuNiO_3$ [29] in the low-temperature phase, the R_1^+ amplitude is varied manually to obtain the energetics of the breathing mode distortion. Here, we observe that even though the ferromagnetic ordering is lower in energy, the response $E(R_1^+)$ is considerably increased in the AFM calculations. Moreover, we find that the Ni_{LB} and Ni_{SB} magnetic moments differ considerably more in the AFM calculations. The minimum of $E(R_1^+)$ is found to be in best agreement with the experimental value of the R_1^+ amplitude with the ferromagnetic ordering by using $U_{avg} = 5$ eV. When performing AFM calculations, $U_{avg} = 2$ eV gives best agreement to the experimental R_1^+ amplitude, where for $U_{avg} = 5$ eV the AFM calculation overestimates the R_1^+ amplitude. Therefore, we find that the breathing mode amplitude is strongly influenced by the choice of magnetic order, and with respect to experiment the small $U_{avg} = 2$ eV value is preferable.

Next, non-magnetic relaxations are performed to address the question how well non-magnetic DFT calculations can reproduce the structural trends found in experiment for the high-temperature $Pbnm$ phase. Therefore, structural relaxations for the compounds with R =Lu, Er, Ho, Y, Dy, Gd, Sm, Nd, Pr, and La are performed (see Fig. 8 of Ref. [140]). We find very good agreement with experimental data for all distortion mode amplitudes. As expected, the degree of octahedral rotation decreases continuously across the series from Lu to La.

Next, we perform the same calculations with magnetic ordering and +U correction to describe the breathing mode distortion trends across the series (see Fig. 9 of Ref. [140]). Here, we find that the R_1^+ amplitude decreases across the series. However, the size of the amplitude is crucially influenced by the choice of U_{avg} and the magnetic ordering. The AFM ordering gives overall larger R_1^+ amplitudes. From the results, an overall good description of structural properties for all compounds of the series can be found using a small $U_{avg} = 2$ eV, and $J_{avg} = 1$ eV. In principle, one could also apply different values of U_{avg} across the series, but at this point we limited the calculations to a single value for all compounds.

Finally, the size of the R_1^+ amplitude as function U_{avg} is analyzed for R = Lu, and Pr, comparing the two end members of the series that exhibit a stable breathing mode distortion at low-temperatures (see Fig. 10 of Ref. [140]). From the results it can be observed that in $LuNiO_3$ the R_1^+ mode is more sensitive to U_{avg}, with overall larger values. Furthermore, we find that for very large U_{avg} values the breathing mode distortion becomes unstable, and the system

becomes again metallic, relaxing to Pbnm symmetry, which was also found in Ref. [26]. We observe, that for large $U_{avg} > 7$ eV values, the e_g states are pushed lower in energy than the oxygen p states. At this point the breathing mode distortion is destabilized.

We also find that the energy difference between the ferromagnetic and antiferromagnetic state is larger in $PrNiO_3$ compared to $LuNiO_3$. Therefore, the AFM ordering is more stable for larger R site cations. Interestingly, the AFM ordering, including a small but yet finite breathing mode distortion, can be stabilized also for $U = 0$ eV.

4.3 CONCLUSION

The results presented in this work draw a clear picture of the predictive capabilities of the DFT+U approach. We find, that non-magnetic DFT calculations allow very good structural predictions for the high-temperature Pbnm phase of the whole nickelate series. This allows to use these structures as starting point for further DFT+DMFT studies. Moreover, we show that for a small $U_{avg} = 2$ eV, and $J_{avg} = 1$ eV the breathing mode distortion can be qualitatively correctly described. For $LuNiO_3$ even on a quantitative level, but the decrease of the breathing mode distortion is smaller compared to experimental data. A similar trend is obtained using the ferromagnetic ordering using a larger U_{avg} value. However, with respect to the correct magnetic order, we suggest the use of a smaller $U_{avg} = 2$ eV value, which is in contrast to what was suggested in Ref. [26]. Additionally, the deficiencies in the present experimental data are revealed, where especially temperature dependent structural data is missing.

We also demonstrate that the stability of the ferromagnetic state seems to be overestimated in DFT+U, especially for the smaller rare-earth ions, and for larger U_{avg} values. Moreover, the different magnetic orderings result in quite different structural parameters, and the influence of U_{avg}, and J_{avg} differs in the different magnetic orderings. This is also important in view of results of Ref. [24], where it is found for $U_{avg} = 5$ eV and ferromagnetic order, that DFT+U overestimates the breathing mode distortion. We show that other interaction parameters used with the correct magnetic order provide more satisfactory results.

In the work of Ref. [44] and [49], which appeared at a similar time, some of these questions are also addressed. Here, DFT+U calculations have been performed for several compounds of the series, potentially explaining trends of structural parameters across the series, and mechanisms of the transition itself. However, none of these studies contains a complete, systematic study of structural parameters across the whole series. That said, these works are highly valuable to explain certain aspects of the physics found in nickelates. In Ref. [44] also trends across the series are calculated with DFT+U in agreement

with my findings. Here, the authors focus on a single value of interaction parameters. In Ref. [49] the mechanism of the coupled transition itself is investigated by using DFT+U. Thereby, also structural trends are obtained, which agree well with my results.

4.4 PEER REVIEWED WORK

PHYSICAL REVIEW B **96**, 165130 (2017)

Interplay between breathing mode distortion and magnetic order in rare-earth nickelates $R\mathrm{NiO_3}$ within DFT + U

Alexander Hampel* and Claude Ederer†
Materials Theory, ETH Zürich, Wolfgang-Pauli-Strasse 27, 8093 Zürich, Switzerland
(Received 13 July 2017; revised manuscript received 25 September 2017; published 16 October 2017)

We present a systematic density functional theory (DFT) plus Hubbard U study of structural trends and the stability of different magnetically ordered states across the rare-earth nickelate series, $R\mathrm{NiO_3}$, with R from Lu to La. In particular, we investigate how the magnetic order, the change of the rare-earth ion, and the Hubbard interaction U are affecting the bond-length disproportionation between the nickel sites. Our results show that structural parameters can be obtained that are in very good agreement with present experimental data and that DFT+U is in principle able to capture the most important structural trends across the nickelate series. However, the amplitude of the bond-length disproportionation depends very strongly on the specific value used for the Hubbard U parameter and also on the type of magnetic order imposed in the calculation. Regarding the relative stability of different magnetic orderings, a realistic antiferromagnetic order, consistent with the experimental observations, is favored for small U values and becomes more and more favorable compared to the ferromagnetic state towards the end of the series (i.e., towards R = Pr). Nevertheless, it seems that the stability of the ferromagnetic state is generally overestimated within the DFT+U calculations. Our work provides a profound starting point for more detailed experimental investigations and also for future studies using more advanced computational techniques such as, e.g., DFT combined with dynamical mean-field theory.

DOI: 10.1103/PhysRevB.96.165130

I. INTRODUCTION

Materials that are located at the crossover between itinerant and localized electronic behavior often exhibit rich phase diagrams, including different forms of electronic order (charge, orbital, magnetic) and metal-insulator transitions [1,2]. Moreover, exotic properties such as non-Fermi liquid behavior [3], high-temperature superconductivity [4], or colossal magnetoresistance [5] can typically be found in this regime, and in many cases a strong coupling between electronic and lattice degrees of freedom, such as, e.g., the Jahn-Teller effect [5,6], can be observed.

An interesting example to study the crossover between localized and itinerant electronic behavior is found in the series of perovskite-structure rare-earth nickelates, $R\mathrm{NiO_3}$, where R can be any rare-earth ion ranging from Lu to La [7,8]. All members of this series (except $\mathrm{LaNiO_3}$) exhibit a metal-insulator transition (MIT) as a function of temperature, which is accompanied by a structural distortion that lowers the space group symmetry of the crystal structure from orthorhombic $Pbnm$ in the high temperature metallic phase to monoclinic $P2_1/n$ in the low temperature insulating phase [9–12]. In addition, all systems (except $\mathrm{LaNiO_3}$) order antiferromagnetically at low temperatures [7,13]. The corresponding phase diagram (based on experimental data taken from Refs. [7,10–12,14–16]) is depicted in Fig. 1, where the temperature dependence of the phase boundaries is shown as a function of the average ⟨Ni-O-Ni⟩ bond angle. It can be seen that the transition temperature for the MIT, T_{MIT}, decreases monotonously with increasing ⟨Ni-O-Ni⟩ bond angle, whereas the antiferromagnetic (AFM) transition temperature, T_{N}, increases up to R = Sm but then becomes identical to T_{MIT}. Thus, for R from Lu to Sm, the AFM transition occurs at lower temperatures than the MIT, whereas for R = Nd and Pr, T_{N} coincides with T_{MIT}. In contrast, $\mathrm{LaNiO_3}$ is a paramagnetic metal at all temperatures and exhibits a slightly different, rhombohedrally-distorted perovskite structure with $R\bar{3}c$ symmetry [17].

The rare-earth nickelates allow us to study the transition from itinerant paramagnetic behavior to a localized AFM state in a quasicontinuous fashion using simple stoichiometric bulk systems, i.e., without the need to introduce dopants or substitutional atoms. Moreover, the nickelates are also highly tunable by pressure, strain, electromagnetic fields, or doping, and are potentially multiferroic (see, e.g., Refs. [8,19,20]). Consequently, the perovskite rare-earth nickelates have received considerable attention during recent decades [7,8,21,22].

The strong coupling between electronic and structural degrees of freedom in the rare-earth nickelates is apparent from the observation that the MIT is accompanied by a structural transition from $Pbnm$ to $P2_1/n$. Hereby, formerly symmetry-equivalent $\mathrm{NiO_6}$ octahedra become inequivalent. One half of the $\mathrm{NiO_6}$ octahedra expand their volumes while the other half reduce their volumes by changing the Ni-O bond lengths accordingly. This results in a three-dimensional checkerboardlike arrangement of alternating long bond (LB) and short bond (SB) octahedra [11,12]. The $P2_1/n$ structure of $\mathrm{LuNiO_3}$ below the MIT [12] is depicted in Fig. 2. The checkerboardlike arrangement of LB and SB octahedra around the Ni cations within a [001]-type plane (in pseudocubic notation) is also schematically shown in Fig. 3.

The exact mechanism that drives this unusual MIT is still under debate. In the simplest picture, the nominal $\mathrm{Ni^{3+}}$ cations are split into $\mathrm{Ni^{2+}}$ and $\mathrm{Ni^{4+}}$, corresponding to LB and SB octahedra, respectively. Such charge disproportionation has been suggested as alternative to a Jahn-Teller distortion for cases where the Hund's coupling J overcomes the on-site Coulomb repulsion U [24]. This can occur in systems such

*Corresponding author: alexander.hampel@mat.ethz.ch
†Corresponding author: claude.ederer@mat.ethz.ch

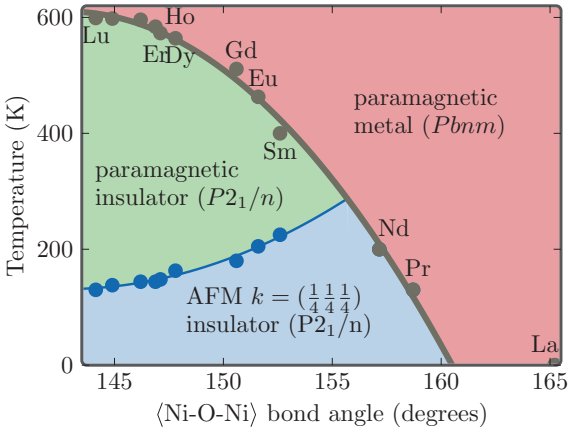

FIG. 1. Phase diagram of the rare-earth nickelates. Transition temperatures are shown as a function of the average ⟨Ni-O-Ni⟩ bond angle. Three different phases can be distinguished: (i) paramagnetic metal with $Pbnm$ symmetry (red), (ii) paramagnetic insulator with $P2_1/n$ symmetry (green), and (iii) antiferromagnetic (AFM) insulator with $P2_1/n$ symmetry (blue) [18].

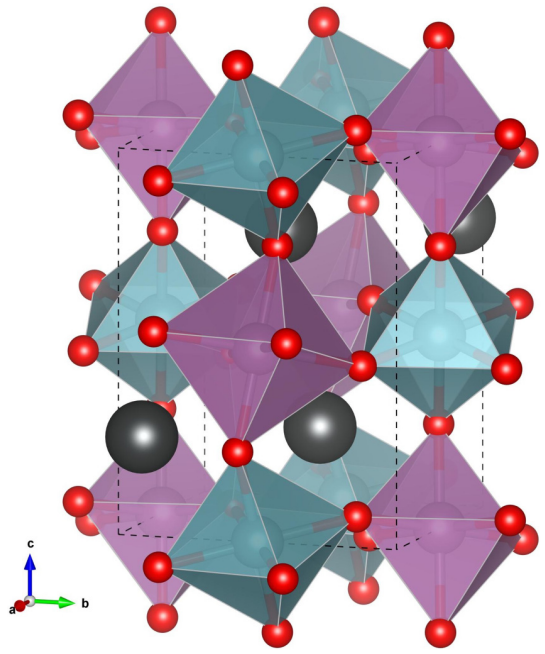

FIG. 2. Experimentally observed $P2_1/n$ crystal structure of $LuNiO_3$ at 60 K below the MIT [12]. LB octahedra around the Ni sites are shaded in purple, SB octahedra are shaded in green, black spheres represent Lu, and red spheres represent O. The volumes of the bond-disproportionated NiO_6 octahedra differ by ∼12%. The crystal structure is visualized using VESTA [23].

as the nickelates, with a small or negative charge transfer energy and strong hybridization between Ni e_g orbitals and O p states, resulting in strong screening of the local Coulomb repulsion and thus a rather small effective U [25]. Indeed, no Jahn-Teller distortion has been observed in the nickelates [26], even though the nominal $t_{2g}^6 e_g^1$ electron configuration of the Ni^{3+} cations should in principle be susceptible to this type of distortion. However, it has also been questioned whether a picture of charge disproportionation on the Ni sites is really adequate [27,28]. Instead, it was shown that a description in terms of ligand holes, delocalized over the O octahedra, can account for the observed bond disproportionation without the need for charge transfer between the Ni sites [27,28].

Very recently, Varignon et al. suggested that both pictures could be consolidated through the use of Wannier functions centered at the Ni sites, and thus representing the formal valence states of the Ni cations, but also with significant orbital weight on the surrounding O ligands [29]. Indeed, the minimal low energy description employed by Subedi et al. is based on such Ni-centered e_g Wannier functions that are spatially more extended than simple atomic orbitals [25]. We note that all proposed mechanisms have in common that they result in a strong modulation of the magnetic moment on the two inequivalent Ni sites, in the limiting case with a spin $S = 1$ on the LB site and $S = 0$ on the SB site.

Apart from the exact mechanism underlying the MIT, the magnetic order observed in the nickelates is also not yet fully resolved and poses numerous open questions. All systems from $R =$ Lu to Pr exhibit the same antiferromagnetic wave vector $k = [\frac{1}{4}, \frac{1}{4}, \frac{1}{4}] \cdot \frac{\pi}{a_c}$ relative to the underlying simple cubic perovskite structure (with approximate cubic lattice constant a_c) [13,17,30]. Furthermore, it is known from experiment that the magnetic moments vary between the LB and SB Ni sites [15,31]. However, the exact magnetic structure is not yet established, due to the lack of sufficiently large single crystals. There are several possible arrangements that cannot be distinguished within the experimental resolution. As a result, it is still under debate whether the magnetic order is collinear or not. Moreover, below ∼10 K, the magnetic moments of the rare-earth ions also order. However, while Ref. [31] reports a different magnetic periodicity of the rare earth moments relative to the Ni moments in $HoNiO_3$, Ref. [15] suggests the same periodicity of Ni and Dy moments in $DyNiO_3$.

In order to gain further insights into the underlying mechanisms, and also to enable quantitative predictions about the physical properties of rare-earth nickelates, a first principles-based computational approach is very desirable. However, an accurate quantitative description of the complex interplay between the various factors that are believed to control the MIT in these materials, i.e., structural properties, electronic correlation effects, and hybridization between the Ni 3d states and the surrounding O ligands, is rather challenging.

Several previous studies have reported that both structural as well as electronic and magnetic properties of rare-earth nickelates can, at least to a certain extent, be described within the "plus Hubbard U" extension of density functional theory (DFT) [19,27,29,32,33]. Specifically, the correct bond-disproportionated crystal structure as well as the complex AFM order, compatible with experimental observations, can be obtained from such calculations. On the other hand, the small energy differences between the different possible magnetic structures are very difficult to resolve [32], and in most cases the ferromagnetic (FM) configuration appears to be energetically more favorable [27,33]. Moreover, it has recently been stated that DFT+U overestimates the tendency for bond disproportionation and that the more sophisticated DFT plus

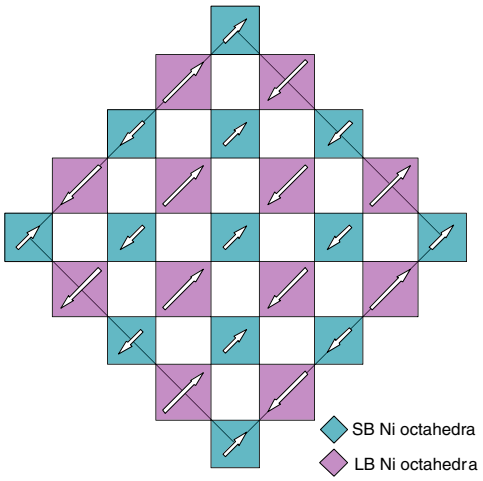

FIG. 3. Schematic depiction of a [001]-type layer of bond-disproportionated NiO_6 octahedra. Additionally, one of the experimentally suggested magnetic orderings (T-AFM) [7,13] is shown. The magnetic order is represented by short and long arrows that represent small respectively large magnetic moments of the two symmetry-inequivalent Ni cations.

dynamical mean-field theory (DMFT) (see, e.g., Ref. [34]) is required for a more accurate description [35].

However, all of these previous studies were either focused on only one (or few) specific member(s) of the series or have used specific values for the Hubbard interaction parameter U, ranging from $U = 2$ eV to $U = 8$ eV. It is therefore difficult to draw general conclusions regarding the predictive capabilities of the DFT+U approach for the whole series of rare-earth nickelates. In a very recent study, Varignon et al. have shown that for a small value of $U = 2$ eV the complex AFM configurations become energetically more favorable than FM order and that simultaneously good structural parameters are obtained for a large part of the series [29]. However, Ref. [29] has excluded the members of the series with the smallest rare earth cations (R = Lu to Ho), and the U dependence of the structural, electronic, and magnetic properties, as well as the effect of magnetic order on the bond disproportionation, has not been discussed.

Here, we present a systematic study of the whole nickelate series with rare-earth ions Lu, Er, Ho, Y, Dy, Gd, Sm, Nd, Pr, and La, using the DFT+U formalism. In particular we address the interplay between the strength of the Hubbard U, different magnetic orders, the size of the rare-earth cation R, and the resulting structural parameters. Our results thus fill an important gap and further clarify the capabilities of the DFT+U approach for quantitative predictions of the physical properties of rare-earth nickelates. Our work can also serve as a starting point for further studies using more advanced electronic structure methods such as, e.g., DFT+DMFT.

Our findings show that the amplitude of the bond-disproportionation distortion is strongly influenced by the size of U and also by the specific magnetic order but that in principle good agreement with available experimental data can be obtained for $U \approx 2$ eV. Moreover, the trends across the series agree well with experiment. Furthermore, our calculations show that a magnetic order with the experimentally observed wave vector is energetically favored for relatively small U values (also around $U \approx 2$ eV) and that the energy gain relative to ferromagnetic order increases from Lu to Pr, consistent with the observed trend of the magnetic ordering temperature.

The remainder of this paper is organized as follows. First, in Sec. II, we introduce the symmetry-based decomposition of distortion modes and discuss its application to the experimental structure of $LuNiO_3$ [12]. In Sec. III we then briefly describe our computational setup and list all relevant parameters used in the DFT+U calculations. The presentation of our main results is divided into two parts. We start in Sec. IV by discussing calculations for $LuNiO_3$ based on the experimental structure taken from Ref. [12]. Hereby, we investigate the stability of different magnetic phases for different interaction parameters U and J without relaxing the structural degrees of freedom. We then start to incorporate structural effects by varying the amplitude of the breathing mode distortion while keeping all other structural parameters fixed to the experimental values. Finally, our results of the full structural relaxations across the nickelate series are presented in Sec. V, and in Sec. VI we summarize our main results and discuss their implications.

II. DESCRIPTION OF STRUCTURAL DISTORTIONS USING SYMMETRY-BASED MODE DECOMPOSITION

For a systematic and quantitative discussion of the various structural distortions that are present in the $Pbnm$ and $P2_1/n$ crystal structures of the rare-earth nickelates, we use a symmetry-based mode decomposition as described by Perez-Mato et al. [36]. Thereby, the atomic positions within a distorted crystal structure (low-symmetry structure), $\vec{r}_i^{\,\mathrm{dist}}$, are written in terms of the positions in a corresponding nondistorted reference structure (high-symmetry structure), $\vec{r}_i^{\,0}$, plus a certain number of independent distortions described by orthonormal displacement vectors, $\vec{d}_{im}$, and corresponding amplitudes, A_m:

$$\vec{r}_i^{\,\mathrm{dist}} = \vec{r}_i^{\,0} + \sum_m A_m \, \vec{d}_{im} \quad . \tag{1}$$

The amplitudes A_m can thus be viewed as distinct order parameters for the different structural distortions present in the low symmetry structure. This allows us to clearly identify the most relevant structural degrees of freedom, and, in particular for the case of the rare-earth nickelates, to systematically distinguish between the various octahedral tilt distortions and the breathing mode related to the MIT.

The mode displacement vectors $\vec{d}_{im}$ are constructed such that each mode m has a well-defined symmetry, i.e., it corresponds to a specific irreducible representation (irrep) of the high symmetry space group. Here, we use the ideal cubic perovskite structure as high symmetry reference structure. Thus, all distortion modes are labeled according to the irreps of space group $Pm\bar{3}m$. Note that an irrep can involve distortion vectors with multiple degrees of freedom, e.g., corresponding to displacement patterns of different inequivalent atoms. All distortion modes corresponding to the same irrep can then be grouped together to define a total mode amplitude of that symmetry.

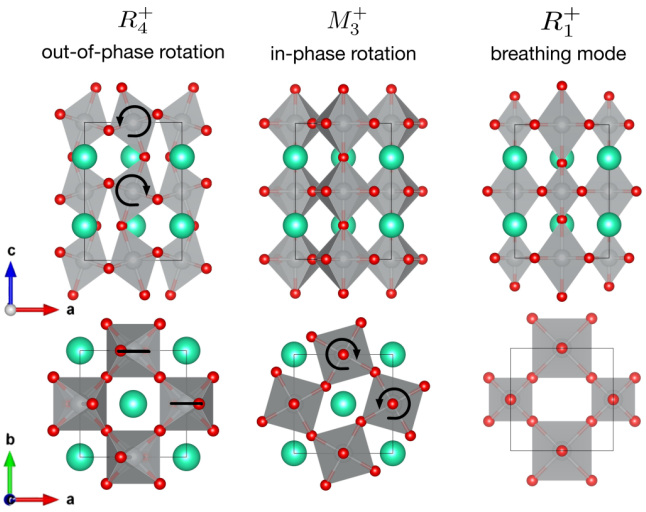

FIG. 4. Depiction of the three most important distortion modes found in nickelate compounds. NiO_6 octahedra are shown in gray. The R_4^+ $Pbnm$ mode that corresponds to an out-of-phase rotation of NiO_6 octahedra around the orthorhombic b axis, the M_3^+ $Pbnm$ mode that corresponds to an in-phase rotation of NiO_6 octahedra around the c axis, and the R_1^+ $P2_1/n$ mode that corresponds exactly to the bond disproportionation of NiO_6 octahedra in the low temperature phase of the nickelates.

Balachandran and Rondinelli have presented such a symmetry-based mode decomposition for the low temperature $P2_1/n$ structure of various nickelates, based on available experimental data [37]. Eight different irreps of the high symmetry $Pm\bar{3}m$ space group can occur within $P2_1/n$. Five of them, corresponding to symmetry labels R_4^+, M_3^+, X_5^+, R_5^+, and M_2^+, are already allowed within the high-temperature $Pbnm$ structure. The first two of these, R_4^+ and M_3^+, correspond to out-of-phase and in-phase tilts of the oxygen octahedra, and, as shown by Balachandran and Rondinelli [37], only the distortions corresponding to R_4^+, M_3^+, and X_5^+ have consistently non-negligible mode amplitudes throughout the nickelate series. In contrast, the amplitude of the M_2^+ mode, which corresponds to a staggered Jahn-Teller distortion of the oxygen octahedra that is found, e.g., in many manganites, is negligibly small.

The low-temperature $P2_1/n$ structure allows for three additional irreps, labeled R_1^+, R_3^+, and M_5^+. Here, only the R_1^+ mode, which describes the breathing mode distortion with alternating LB and SB octahedra, has a non-negligible amplitude [38]. The three most relevant distortion modes found in the rare-earth nickelates, i.e., the octahedral tilt modes R_4^+ and M_3^+ ($Pbnm$ symmetry), as well as the R_1^+ breathing mode (within $P2_1/n$) are visualized in Fig. 4.

In Table I, we list the distortion mode amplitudes for $LuNiO_3$ at the three different temperatures measured in Refs. [11,12]. We use ISODISTORT [39] for the calculation of the distortion mode amplitudes. All mode amplitudes are given in Å and are normalized to the cubic high-symmetry parent structure (not to the 20 atom $Pbnm$ unit cell). Note that the data at room temperature is identical (except for the different normalization) to the corresponding data in the paper of Balachandran and Rondinelli [37]. Table I also contains data from our structural relaxations which will be discussed in Sec. V.

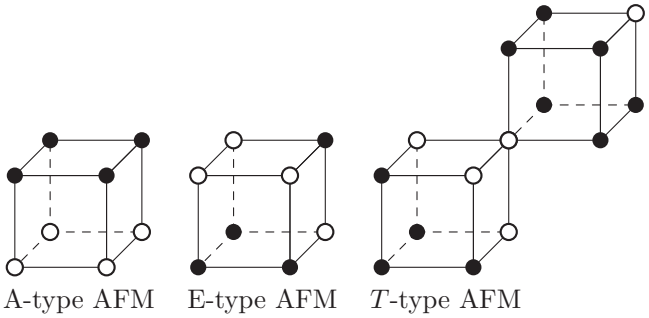

FIG. 5. Schematic depiction of the three different antiferromagnetic orderings that are investigated in this paper. White spheres correspond to spin-up and black spheres to spin-down moments on Ni sites. The special ordering along the [111] pseudocubic crystal axis is labeled T-AFM[32]. For the sake of simplicity we dropped all rare-earth atoms and oxygen atoms.

If one compares the experimental data from Ref. [12] obtained approximately 60 K above and below the MIT (first and second row of Table I), one can see that the largest $Pbnm$ mode amplitude, i.e., R_4^+, does almost not change during the MIT. The R_4^+ amplitude is 0.811 Å within the high temperature $Pbnm$ phase and 0.821 Å within the low-temperature $P2_1/n$ phase. This value corresponds to maximal displacements of individual oxygen atoms by 0.58 Å. Similar behavior can be observed for the other two main modes, M_3^+ and X_5^+. Finally, the bond-disproportionation mode in the low-temperature phase, R_1^+, exhibits an amplitude of 0.077 Å, which corresponds to a displacement of each oxygen atom by 0.044 Å.

III. COMPUTATIONAL METHOD

DFT calculations are performed using the projector augmented wave (PAW) method [40] implemented in the "Vienna *ab initio* simulation package" (VASP) [41–43]. We use the generalized gradient approximation (GGA) in the form proposed by Perdew, Burke, and Ernzerhof (PBE) [44] as exchange correlation functional. For an improved treatment of the strong local electron-electron interaction between the Ni $3d$ electrons, we add an effective on-site Coulomb interaction U and Hund's rule exchange interaction J in the form discussed by Liechtenstein et al. [45]. The values for U and J are varied throughout this paper as described in Secs. IV and V.

For Ni, the $3p$ semicore states are included as valence electrons in the PAW potential. For the rare-earth atoms, we use PAW potentials corresponding to a 3+ valence state with f electrons frozen into the core and, depending on the rare-earth cation, the corresponding $5p$ and $5s$ states are also included as valence electrons. Thus, we neglect the ordering of the rare-earth f magnetic moments, which only occurs at very low temperatures [15,31]. The kinetic energy cutoff for the plane-wave basis is set to 550 eV.

We consider four different types of magnetic order: FM and three different types of AFM order, which are depicted in Fig. 5. The rather common A-type AFM order (A-AFM)

corresponds to an alternating (↑↓) alignment of Ni magnetic moments along the Cartesian z direction and parallel alignment perpendicular to z. The E-type AFM order (E-AFM) corresponds to an ↑↑↓↓ alignment along both x and y directions and alternating moments, i.e., ↑↓↑↓, along the z direction. The T-type AFM order, which corresponds to the experimentally observed AFM wave vector, $k = [\frac{1}{4}, \frac{1}{4}, \frac{1}{4}] \cdot \frac{\pi}{a_c}$, exhibits an ↑↑↓↓ pattern along all three Cartesian directions. As shown by Giovannetti et al. [32] using DFT+U calculations, this T-type AFM order is energetically nearly indistinguishable from the other two magnetic order patterns (one collinear and one noncollinear) that are compatible with the experimental neutron data. In the following, we therefore use the (relatively simple) T-AFM structure as representative for the experimentally observed magnetic order. Both T-AFM and bond disproportionation are also illustrated in Fig. 3 within a [001]-type layer.

For the examination of the different magnetic order patterns, different unit cell sizes are used. For the FM and A-AFM order, we use a 20 atom unit cell consisting of $\sqrt{2} \times \sqrt{2} \times 2$ (pseudo)cubic perovskite units. This cell also corresponds to the primitive crystallographic unit cells for both the $Pbnm$ and $P2_1/n$ structures. For the E-AFM magnetic structure, this unit cell is doubled along the a direction (40 atoms), and for the special T-AFM order the cell is doubled once more, this time along the c direction (80 atoms). A k-point mesh with $10 \times 10 \times 8$ grid points along the three reciprocal lattice directions is used for the 20 atom $Pbnm$ and $P2_1/n$ unit cells to perform Brillouin zone integrations. For the 40 atom E-AFM cell we use an appropriately reduced $5 \times 10 \times 8$ k-point grid and for the 80 atom T-AFM cell a $5 \times 10 \times 4$ grid. For accurate structural relaxations, the forces acting on all atoms are minimized until all force components are smaller than 10^{-4} eV/Å. Local magnetic moments are obtained by integrating the spin density within the PAW spheres (LORBIT = 11).

IV. CALCULATIONS FOR $LuNiO_3$ BASED ON THE EXPERIMENTALLY OBSERVED STRUCTURE

We start by performing calculations for $LuNiO_3$ in the experimentally determined $P2_1/n$ structure at $T = 533$ K [12] and analyze the influence of the Hubbard and Hund's rule interaction parameters, U and J, on the relative stability of different magnetic configurations. We consider the FM case as well as three different AFM configurations (A-AFM, E-AFM, and T-AFM, see Sec. III for more details). Figure 6 shows the calculated total energies of the three AFM configurations relative to the FM state. All energies are normalized to a 20 atom unit cell. A negative value indicates that the corresponding AFM state is lower in energy, whereas a positive value indicates that the FM state is lower in energy.

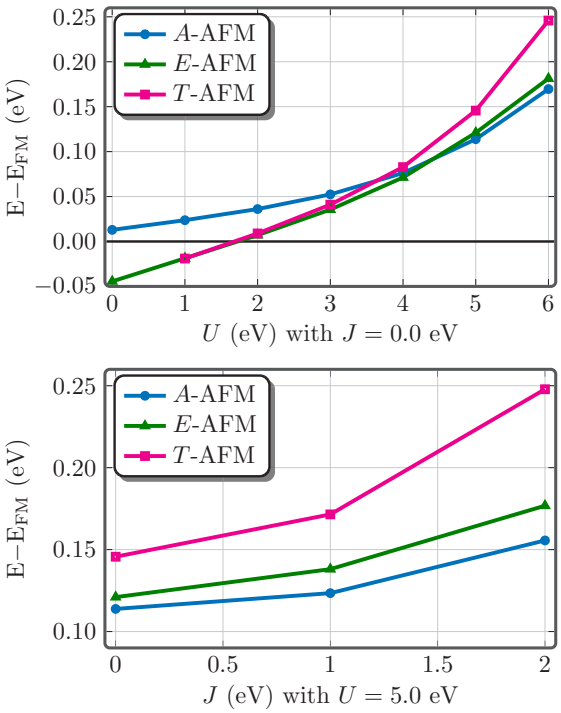

FIG. 6. Effect of U (top) and J (bottom) on the energy differences between different magnetically ordered states, calculated for $LuNiO_3$ using the experimentally observed $P2_1/n$ structure. For each U and J, the energies of three different AFM states are given relative to the FM state, normalized to a unit cell containing four Ni sites. The T-AFM order (magenta squares) is energetically favored only for rather small U values. Increasing J (bottom) also favors the FM state.

TABLE I. Mode decomposition of several structures obtained for $LuNiO_3$. The top three lines are based on available experimental data corresponding to different temperatures: $T = 643$ K ($Pbnm$) [12], $T = 533$ K ($P2_1/n$) [12], and $T = 295$ K ($P2_1/n$) [11]. The bottom five lines correspond to results of our structural relaxations for different magnetic orders (NM: nonmagnetic, FM: ferromagnetic, T-AFM: T-type antiferromagnetic) and using different values for the parameters U and J.

	$Pbnm$ modes					additional $P2_1/n$ modes		
	R_4^+	R_5^+	X_5^+	M_2^+	M_3^+	R_1^+	R_3^+	M_5^+
expt. 643 K ($Pbnm$)	0.811	0.117	0.449	0.018	0.626			
expt. 533 K ($P2_1/n$)	0.821	0.124	0.452	0.025	0.617	0.077	0.001	0.013
expt. 295 K ($P2_1/n$)	0.826	0.124	0.454	0.031	0.616	0.077	0.002	0.007
NM $U = 0$, $J = 0$ eV	0.845	0.129	0.487	0.023	0.625			
FM $U = 5$, $J = 1$ eV	0.875	0.126	0.476	0.027	0.623	0.094	0.006	0.023
T-AFM $U = 0$, $J = 0$ eV	0.861	0.130	0.480	0.026	0.622	0.037	0.001	0.002
T-AFM $U = 2$, $J = 1$ eV	0.870	0.129	0.480	0.034	0.625	0.081	0.008	0.019
T-AFM $U = 5$, $J = 1$ eV	0.879	0.124	0.475	0.037	0.623	0.124	0.009	0.029

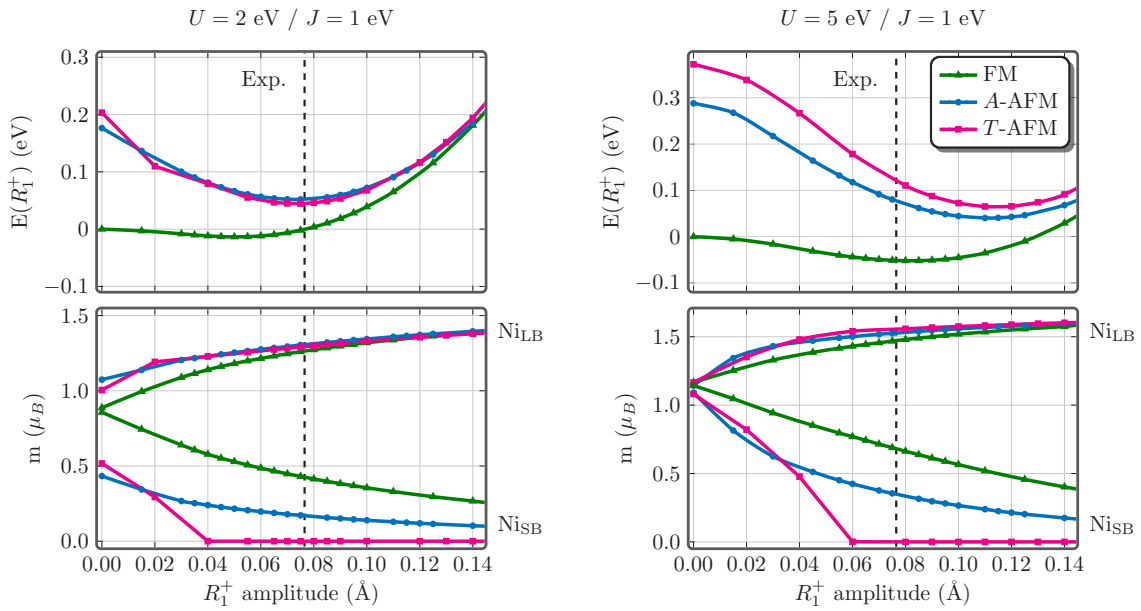

FIG. 7. Total energy (top) and Ni magnetic moments (bottom) as a function of the R_1^+ mode amplitude for different magnetic states and U values (left: $U = 2$ eV, right: $U = 5$ eV) and $J = 1$ eV. All other structural parameters (apart from the R_1^+ mode) are fixed to the experimental $P2_1/n$ structure, and the R_1^+ mode amplitude in the experimental structure is marked by the vertical dashed lines. In the bottom panels, the upper (lower) curves correspond to the Ni_{LB} (Ni_{SB}) site.

The top panel of Fig. 6 depicts the case with $J = 0$. It can be seen that for small values of U, the T-AFM and E-AFM states have very similar energies, and for $U < 2$ eV, both are lower in energy than the FM state. For values $U > 2$ eV the FM state is most favorable, while the simple A-AFM state is higher in energy over the whole range of U values. We also note that for $U = 0$ we were not able to stabilize the T-AFM state within our calculations.

The bottom panel of Fig. 6 shows the effect of varying the Hund's coupling parameter J for fixed $U = 5$ eV. Consistent with the results shown in the top panel, at this U value the FM state is favored for $J = 0$. If J is increased, the FM state becomes even more favorable compared to all three AFM orderings. The same trend can be observed for other values of U (not shown). Increasing J lowers the energy of the FM state relative to the various AFM orderings.

It appears that the T-AFM state, i.e., the state that is compatible with the experimental observations, is only favorable for small values of U and J. Furthermore, within this range of U and J, the energy difference between T-AFM and the closely related E-AFM state is rather small. On increasing both U and J, the FM states becomes lower in energy than all considered AFM orderings.

We note that nonmagnetic DFT calculations with $U = 0$ for $LuNiO_3$ in both the low temperature $P2_1/n$ and the high temperature $Pbnm$ structures (taken from Ref. [12]) result in a metallic system. By adding the local Coulomb interaction U we are able to stabilize the T-AFM order, which then results in an insulating ground state. FM order also results in an insulating ground state for $U > 0$ eV. Thus, magnetic order and a small value of U (around 1 eV or larger) is needed to obtain an insulating ground state in the experimental low temperature structure.

To investigate how sensitive the energy differences between different magnetic states depend on small variations in the crystal structure, in particular the R_1^+ breathing mode, we now use the mode decomposition of the experimental $P2_1/n$ structure and tune the amplitude of the R_1^+ mode while keeping all other structural degrees of freedom fixed to their experimental values. The result is shown in Fig. 7, which shows the total energy (top) and the magnetic moments on the Ni sites (bottom) as a function of the R_1^+ mode amplitude for different magnetic orderings and two different U values ($U = 2$ eV on the left and $U = 5$ eV on the right) together with $J = 1$ eV. In each case, the energy exhibits a minimum at a finite value of the R_1^+ amplitude, which indicates the value predicted by DFT+U for a given magnetic order (with all other structural parameters fixed to experimental values). The black vertical dashed line indicates the R_1^+ amplitude in the experimental structure, $R_1^+ = 0.077$ Å. Note that the experimental structure was determined in the paramagnetic insulating phase.

One observes that the energy of the FM state (green triangles) is always lower than that of the AFM states (magenta squares and blue circles). However, the energy difference between FM and AFM order is smaller for $U = 2$ eV than for $U = 5$ eV, consistent with the results shown in Fig. 6 (note that the top panel in Fig. 6 corresponds to $J = 0$, whereas Fig. 7 is obtained using $J = 1$ eV, and that increasing J favors the FM state). Furthermore, it is apparent that the AFM states couple much stronger to the R_1^+ breathing mode than the FM state, with a much deeper energy minimum relative to zero mode amplitude and a position of the energy minimum at significantly larger R_1^+ amplitude.

The predicted mode amplitude for T-AFM and $U = 2$ eV ($R_1^+ = 0.076$ Å) agrees very well with the experimental value, whereas the FM state results in an amplitude ($R_1^+ = 0.050$ Å)

that is much smaller than what is observed experimentally. Increasing U increases the predicted mode amplitudes for both FM and AFM order, and for $U = 5$ eV the amplitude obtained for FM order ($R_1^+ = 0.082$ Å) is close to the experimental value, whereas both AFM states exhibit significantly larger amplitudes ($R_1^+ \approx 0.11$ Å). There is only a small difference between the two different AFM orderings, and in particular the positions of the energy minima are very similar. For $U = 2$ eV, T-AFM is slightly lower in energy than A-AFM, whereas for $U = 5$ eV, A-AFM is lower.

The bottom panels of Fig. 7 show the local magnetic moments of the Ni cations for the different magnetic orderings as a function of the R_1^+ amplitude. For $U = 5$ eV, all moments have the same value of $\sim$1.1 μ_B at zero R_1^+ amplitude. In contrast, for $U = 2$ eV, the SB and LB moments differ already for $R_1^+ = 0$ in the two AFM cases, while they are both equal to $\sim$0.9 μ_B in the FM case. It thus appears that for $U = 2$ eV, the magnetic moments are much more susceptible to the small symmetry breaking resulting from the presence (albeit with very small amplitude) of the two other $P2_1/n$ modes, i.e., R_3^+ and M_5^+. We note that if these additional modes as well as the small monoclinic tilt of the unit cell are also removed, i.e., if the underlying crystal structure has exact $Pbnm$ symmetry, then the difference between the LB and SB moments also vanishes in the case of A-AFM order. However, this is not the case for the T-AFM ordering, since T-AFM order by itself breaks the $Pbnm$ symmetry, leading to two symmetry-inequivalent Ni sites.

With increasing R_1^+ amplitude, the moments of the SB sites decrease and the moments of the LB sites increase. Thereby, the size of the Ni_{LB} moments is rather independent of the magnetic order and seems to converge to a value of around 1.4 μ_B (1.6 μ_B) for $U = 2$ eV ($U = 5$ eV). In contrast, the decrease of the Ni_{SB} moments depends more strongly on the magnetic order. For T-AFM order, the Ni_{SB} moments vanish completely for R_1^+ amplitudes larger than $R_1^+ = 0.04$ Å ($R_1^+ = 0.06$ Å) for $U = 2$ eV ($U = 5$ eV). This means that, for both U values, the Ni_{SB} moments in the T-AFM state are zero at the experimental R_1^+ amplitude. For the A-AFM and FM cases, the SB moments seem to only asymptotically converge to zero, with the residual moment in the FM case about twice as large as in the A-AFM case. These results are consistent with earlier studies that also found nonvanishing magnetic moments on the SB sites for $LuNiO_3$ with FM order [27] and vanishing Ni_{SB} moments for $NdNiO_3$ with T-AFM order (for not too large U) [33].

We note that the behavior of the SB moments for larger R_1^+ amplitudes is consistent with a picture where the Ni_{SB} moment is simply induced by the effective field created by the magnetic moments on the neighboring Ni_{LB} sites. In the FM case, each SB site is surrounded by six LB nearest neighbors with parallel alignment of their magnetic moments. In the A-AFM case, only four of the six neighboring LB moments are parallel to each other, and thus the effective field at the SB site is reduced. For the T-AFM case, exactly half of the neighboring LB moments are aligned parallel to each other, while the other half is aligned antiparallel, leading to a cancellation of the effective field on the SB site. We also performed some calculations where we initiated the magnetic moments according to G-type AFM order. In this case, all LB moments are parallel to each other and thus the effective field at the SB site is the same as for FM order. As a result, the calculations converge to the FM solution even if the SB moments are initiated antiparallel to the LB moments.

It appears that DFT+U is able to correctly describe the bond-disproportionated state in $LuNiO_3$, resulting in R_1^+ amplitudes that are consistent with the experimentally obtained structure. However, the precise value of the R_1^+ amplitude depends strongly on the type of magnetic order that is imposed in the calculation and also on the value used for the Hubbard interaction parameter U. The complex T-AFM state, which is consistent with the available experimental data and is also stable within the calculations, is lower in energy than the FM and A-AFM states for small values of U (and J). However, the calculations seem to favor the FM solution for U values larger than $U = 2$ eV. Furthermore, the R_1^+ breathing mode results in a strong energy lowering of the AFM states and also leads to a strong disproportionation between the magnetic moments on the two different Ni sites (for all magnetic orderings). For T-AFM, the local magnetic moments on the Ni_{SB} sites vanish completely at the experimental R_1^+ amplitude.

We note that while different magnetic structures assumed in the refinements of the available experimental data generally lead to different values for the local magnetic moments, most studies indeed report a significant difference between Ni_{LB} and Ni_{SB} moments (see, e.g., Refs. [15,31]). Furthermore, our T-AFM calculations show that the Ni_{SB} moments can be zero, in spite of the fact that the integrated charges inside the PAW spheres differ only very little between the two different Ni sites (consistent with previous DFT-based studies). Thus, the SB moments can vanish completely even though the integrated charges do not correspond to a naive picture of full charge disproportionation within atomic spheres. The results presented in this section are also in good agreement with a recent DFT+U study by Varignon et al. [29] focusing on the members of the nickelate series with large R cations, which suggests that a value of $U = 2$ eV gives the best overall agreement with experimental observations, both regarding magnetic order and the magnitude of the bond disproportionation.

V. STRUCTURAL RELAXATIONS FOR THE WHOLE NICKELATE SERIES

Next, we perform full structural relaxations within the low-temperature $P2_1/n$ symmetry across the whole series of nickelates with R from Lu to La. We again compare different values of U and J and different magnetic orderings. However, we will focus mainly on the FM and T-AFM cases, since other AFM orderings give results similar to T-AFM. In addition, we also perform nonmagnetic (NM) structural relaxations with $U = 0$. Note that in this case the R_1^+ breathing mode is not stable and the system relaxes back to the higher symmetry $Pbnm$ structure, even if we initialize the system with a finite R_1^+ amplitude and $P2_1/n$ symmetry. To allow for a systematic comparison across the whole series, we also relax $LaNiO_3$ within both $Pbnm$ and $P2_1/n$ symmetries (i.e., similar to all other compounds), even though $LaNiO_3$ is experimentally found to exhibit a slightly different structure with $R\bar{3}c$ space group symmetry [17].

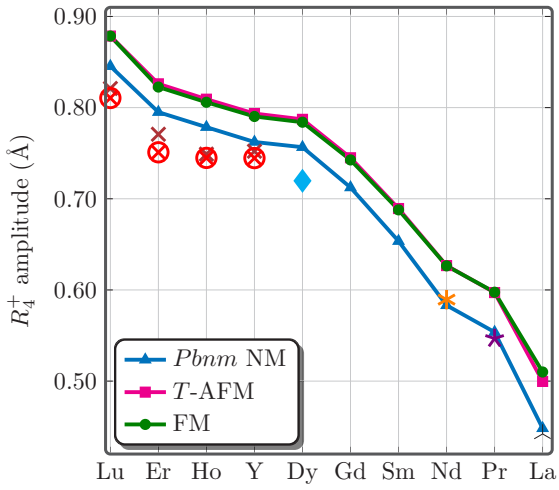

FIG. 8. R_4^+ mode amplitudes obtained from full structural relaxations across the nickelate series. The T-AFM (magenta squares) and the FM calculations (green circles) are performed using $U = 5$ eV and $J = 1$ eV and compared to nonmagnetic (NM) calculations (blue triangles) within $Pbnm$ symmetry and using $U = 0$. The larger symbols not connected by lines indicate various experimental results: Lu-Y from Ref. [12] (brown crosses obtained at 60 K below T_{MIT}, red crosses with circle at 60 K above T_{MIT}), Dy (blue diamond) from Ref. [15], Nd (orange asterisk) from Ref. [46], Pr (purple star) from Ref. [47], and La (black three-pointed star) from Ref. [17].

Generally, our calculated lattice parameters agree very well with available experimental data across the whole series, with maximal deviations of the unit cell volume of a few percent or less. For example, for $LuNiO_3$ the NM calculation results in a unit cell volume that deviates by -1.5% from the experimental high temperature structure [12], whereas the volume obtained in the FM calculation with $U = 5$ eV and $J = 1$ eV differs by only $+0.2\%$ from that of the experimental $P2_1/n$ structure at $\sim$60 K below T_{MIT} [12].

In Table I we list the amplitudes of all distortion modes obtained for $LuNiO_3$ in different settings. It can be seen that the R_1^+ mode is the only mode which depends very strongly on U, J, and the type of magnetic order. All other relevant mode amplitudes agree well with the experimental data, except maybe for a slight overestimation of the R_4^+ mode (and perhaps also X_5^+), in particular for the FM/AFM cases and increasing U.

As discussed in Sec. II, the R_4^+ mode is the most prominent distortion mode in the nickelate series and describes the out-of-phase octahedral tilts around the in-plane a direction (Glazer tilt $a^-a^-c^0$, see Fig. 4). The evolution of the R_4^+ amplitude across the nickelate series, calculated for different settings and compared to experimental data, is depicted in Fig. 8. Experimental data for $R =$ Lu, Er, Ho, and Y is taken from the two papers by Alonso et al. [10,12], for $R =$ Dy from Muñoz et al. [15], for $R =$ Nd from García-Muñoz et al. [46], and for $R =$ Pr from Medarde et al. [47]. Note, that the structural data is generally measured at different temperatures and that Alonso et al. [10,12] have obtained data both above and below the MIT transition, i.e., both within the metallic high temperature $Pbnm$ phase and the insulating low temperature $P2_1/n$ phase. However, we note that in all these cases, there is only a rather small difference in the R_4^+ amplitude between the two phases (see also Table I for the case with $R =$ Lu).

The amplitude of the R_4^+ mode is monotonously decreasing across the series from Lu to La, consistent with the increasing radius of the R cation. Furthermore, the R_4^+ amplitude is slightly smaller for the NM calculation with $U = 0$, compared to both FM and T-AFM calculations with $U = 5$ eV and $J = 1$ eV, while there is only a negligible difference between FM and T-AFM. Overall, there is rather good agreement, both qualitatively and quantitatively, between the calculated and experimentally measured mode amplitudes. The best agreement is obtained for the NM case with $U = 0$, whereas the magnetic relaxations with $U = 5$ eV lead to a slight overestimation of the octahedral tilt distortion compared to the experimental data.

Next, we discuss the R_1^+ breathing mode amplitude. We first note that, in contrast to the calculations for the fixed experimental structure presented in the previous section, the T-AFM magnetic order is stable within the fully relaxed structure even in the case with $U = 0$ eV. Moreover, in contrast to the FM and A-AFM (and NM) cases, in the T-AFM case all compounds from $R =$ Lu to La develop a finite R_1^+ amplitude already for $U = 0$. Although the resulting amplitudes are about two to three times smaller than the experimentally observed R_1^+ amplitudes, this nevertheless indicates that T-AFM strongly supports the R_1^+ mode. For larger U values, a finite R_1^+ amplitude emerges from the relaxations for all considered magnetic orderings.

In the following, we compare results for two different values of U, a smaller value of $U = 2$ eV and a larger value of $U = 5$ eV, in both cases with $J = 1$ eV. The corresponding R_1^+ mode amplitudes for FM and T-AFM cases are shown in Fig. 9 (top: $U = 2$ eV; bottom: $U = 5$ eV) together with available experimental data. Furthermore, to assess whether the slight overestimation of the R_4^+ octahedral tilt mode in the magnetically ordered $+U$ calculations (cf. Fig. 8) affect the calculated R_1^+ amplitude, we also consider a third case. Here, we use the $Pbnm$ structure obtained for the NM case (with $U = 0$) and then relax only the R_1^+ amplitude using FM order and $U = 5$ eV (while keeping all other mode amplitudes fixed). In the following, this relaxation is referred to as "R_1^+ only." The corresponding data is also shown in Fig. 9.

It can be seen that there are significant differences in the calculated R_1^+ mode amplitudes for the various cases, similar to what has been found in the previous section for $LuNiO_3$. The calculated R_1^+ mode amplitudes are consistently larger for T-AFM (magenta) compared to the FM case (green), and the larger U value results in overall larger R_1^+ amplitude across the whole series. Furthermore, in all cases we obtain a decrease of the R_1^+ amplitude across the series from $R =$ Lu towards $R =$ La. This decrease is most pronounced for the FM case with $U = 5$ eV. The "R_1^+-only" relaxations (blue) result in reduced R_1^+ amplitudes compared to the full FM relaxations at $U = 5$ eV. As suggested above, this can be attributed to the reduced octahedral tilt distortion (R_4^+ mode) in the underlying NM structures.

Rather good agreement with the experimental data is obtained in the T-AFM case using $U = 2$ eV, in particular for the compounds at the beginning of the series. However,

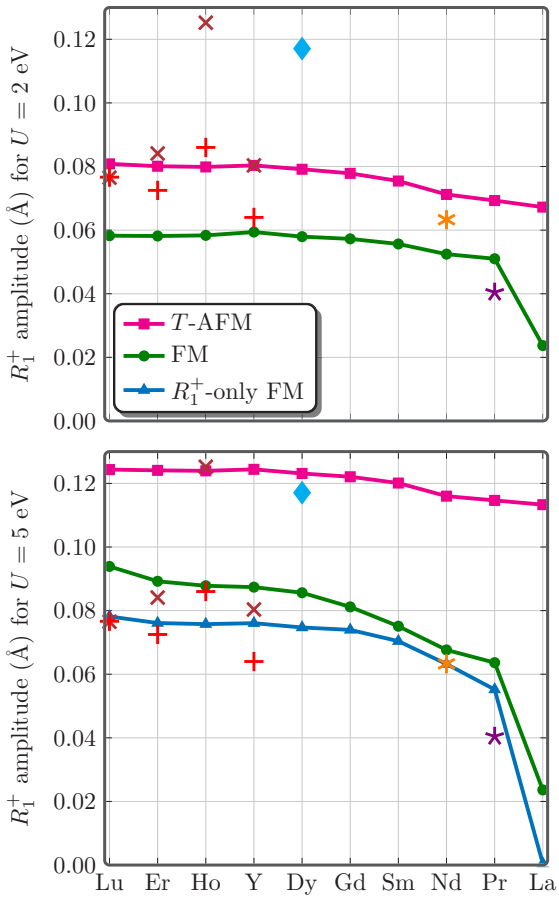

FIG. 9. R_1^+ mode amplitude for the relaxed structures with $U = 2$ eV (top) and $U = 5$ eV (bottom), in both cases using $J = 1$ eV. The relaxed mode amplitudes are given for the FM (green circles) and T-AFM (magenta squares) cases, as well as for the "R_1^+-only" relaxation with FM order (blue triangles). The large disconnected symbols (same in both panels) indicate different experimental values: brown crosses for Lu-Y from Ref. [12] at 60 K below T_{MIT}, red plus symbols for Lu-Y from Ref. [11] at $T = 290$ K, blue diamond for Dy from Ref. [15], orange asterisk for Nd from Ref. [46], and purple star for Pr from Ref. [47].

the decrease towards $R = \mathrm{Pr}$ appears weaker than for the experimental data. For FM order and $U = 5$ eV, the agreement is also good, including the decrease of the R_1^+ towards the end of the series. Note that a slightly smaller U value would also slightly reduce the R_1^+ amplitude and probably further improve the comparison of the FM case with the experimental data.

Another fact that becomes apparent from Fig. 9 is the rather large scattering of the experimental results for different members of the series, or even for the same compound measured at different temperatures (see, e.g., the data for $R = \mathrm{Ho}$ or Dy in Fig. 9). This can be attributed to difficulties in sample preparation, which is only possible under high pressure, leading to very small sample sizes and thus low experimental resolution [7,8]. Nevertheless, it seems that the decrease in R_1^+ amplitude for $R = \mathrm{Nd}$ and in particular $R = \mathrm{Pr}$ compared to the compounds at the beginning of the series can indeed be inferred from the experimental data.

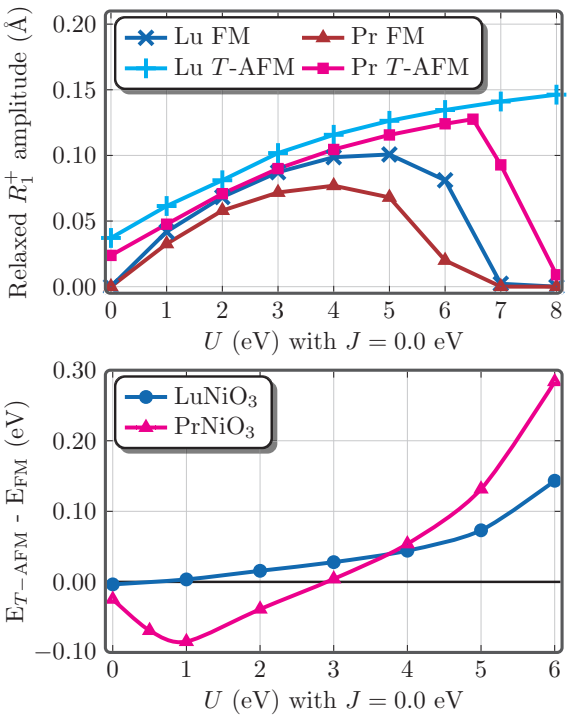

FIG. 10. Top: R_1^+ amplitudes calculated for $LuNiO_3$ (cyan plus symbols and blue crosses) and $PrNiO_3$ (brown triangles and magenta squares) as a function of U (with $J = 0$), in both cases with FM (crosses and triangles) as well as T-AFM ordering (plus symbols and squares). Bottom: energy difference between T-AFM and FM states for $PrNiO_3$ (magenta triangles) and $LuNiO_3$ (blue circles) for different U values (and $J = 0$).

We now have a closer look at the U dependence of the R_1^+ amplitude across the series. For this, we focus on the two "end members" of the nickelate series, $LuNiO_3$ and $PrNiO_3$, and perform full structural relaxations for various U values and both FM and T-AFM magnetic orders. Here, we use $J = 0$, so that the limiting case with $U = 0$ can be continuously incorporated. The results are depicted in the top panel of Fig. 10. We note that while the R_1^+ amplitude is very sensitive to the choice of U, the influence of J is much weaker, and therefore we present only results for varying U.

In agreement with the results shown in Fig. 9, the T-AFM state leads to an overall larger R_1^+ amplitude compared to the FM state. Furthermore, the R_1^+ amplitude is consistently larger for $LuNiO_3$ than for $PrNiO_3$ (with the same magnetic order). In all cases, the R_1^+ amplitude is monotonously increasing with U up to about 3–4 eV. For larger U, the R_1^+ amplitude starts to decrease and can even vanish completely at large U. The value of U where the turnaround from increasing to decreasing R_1^+ amplitude occurs, depends both on the R cation and the magnetic order. It is lowest for Pr and FM order and highest for Lu and T-AFM order (in fact, in this latter case the turnaround does not occur up to $U = 8$ eV).

The collapse of the breathing mode at large U has also been observed in earlier DFT calculations for $NdNiO_3$ by Prosandeev et al. [33]. It can be related to a qualitative change in the electronic structure beyond a certain U value. This

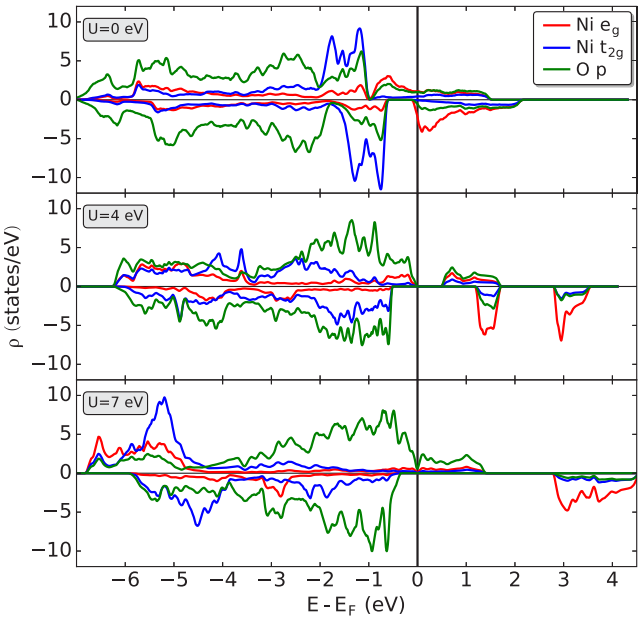

FIG. 11. Projected densities of states of fully relaxed $LuNiO_3$ with FM order for different U values (and fixed $J = 0$ eV). Only the Ni d (separated in t_{2g} and e_g orbital character) and O p projections are shown (summed over all Ni and O sites within the unit cell). Minority spin states are depicted with negative sign and the Fermi level defines zero energy. One can see that with increasing U the occupied Ni d states, i.e., t_{2g} (blue) and majority spin e_g (red), are shifted down in energy relative to the oxygen p states (green). For $U = 7$ eV the occupied Ni d states are lower in energy than the oxygen p states and the system becomes metallic.

is illustrated in Fig. 11, which shows projected densities of states (DOS) for relaxed $LuNiO_3$ with FM order for $U = 0$, $U = 4$ eV, and $U = 7$ eV (in all cases with $J = 0$). Here, the element-resolved DOS are summed over all atoms of a given type, i.e., the Ni DOS contains the contributions from both LB and SB sites.

For $U = 0$, the Ni d states (red and blue) are situated just above the oxygen p states (green). The system is slightly metallic and no breathing mode appears in the relaxed structure. With increasing U, the occupied Ni d states are pushed down in energy relative to the oxygen p states, and a gap opens between the top of the valence band with predominant O p character and the conduction bands with strong Ni d character. This is indicative of a charge transfer insulator with strong hybridization between the ligand p and transition metal d states. This is also the regime that supports the breathing mode in the relaxed structure. The site splitting between the two nickel sites can be observed as two distinct peaks (at energies of approximately 1.5 eV and 3 eV) in the unoccupied minority spin Ni e_g DOS for $U = 4$ eV (middle panel of Fig. 10).

However, for $U = 7$ eV, the occupied Ni d states are pushed completely below the oxygen p states, i.e., the system has entered a negative charge transfer regime. This leads to reduced hybridization between O p and Ni d states, and the unoccupied part of the majority spin states has now essentially pure O p character, i.e., it now clearly corresponds to two ligand holes. Interestingly, this regime does not support the breathing mode distortion, as seen from the top panel of Fig. 10. Thus, it appears that the bond disproportionation in the nickelates depends strongly on the degree of hybridization between the Ni d and O p states and requires a mixed character of the nominal Ni e_g bands. On the other hand, if the "ligand hole" character of the unoccupied states becomes too dominant, the bond disproportionation becomes unfavorable. This is very much in line with the interpretation of "charge order" in terms of hybridized Ni-centered e_g-like Wannier functions, as discussed by Varignon et al. [29].

Finally, in the bottom panel of Fig. 10, we compare the relative stability of the FM and T-AFM states for the two "end-members" $LuNiO_3$ and $PrNiO_3$ in the fully relaxed structures as a function of U (and using $J = 0$). Here, a negative (positive) value indicates that the T-AFM (FM) state is energetically favored. One can see that, while for $LuNiO_3$ the FM state is more favorable than T-AFM over essentially the whole range of U (with a nearly vanishing energy difference for $U = 0$), for the case of $PrNiO_3$ the energy difference $E_{T\text{-AFM}} - E_{\text{FM}}$ exhibits a nonmonotonous behavior with a minimum at around $U = 1$ eV. Most strikingly, the T-AFM state is favored in $PrNiO_3$ for U values up to $U \approx 3$ eV. Thus, in the small U regime (below 3–4 eV) the T-AFM state becomes more favorable for increasing size of the R cation, i.e., when going from Lu to Pr. This is consistent with the experimentally observed trend for the magnetic ordering temperature. We point out that, even though here we show only data for the two end members of the series, we have verified that the corresponding trends evolve continuously throughout the series.

The results for the energy difference between T-AFM and FM for $LuNiO_3$ are similar to the ones presented in Fig. 6 for the experimental structure, although in the experimental structure the T-AFM state is lower in energy than FM for $U < 2$ eV. This is due to the small structural differences between the experimental and relaxed structures, which slightly shift the energetics of the different magnetic orderings. Additionally, we note that in our calculations the T-AFM ordering is found to be stable in $LaNiO_3$ within $Pbnm$ symmetry. This is in agreement with a very recent theoretical work by Subedi [48], where it is also shown that the stability of the T-AFM ordering disappears if the correct $R\bar{3}c$ symmetry is considered. This shows that also $LaNiO_3$ is very close to a transition between the breathing mode phase with AFM ordering and the metallic $R\bar{3}c$ phase. Together with the differences found for $LuNiO_3$ in the experimental and relaxed structures, it also demonstrates that the energy differences between different magnetic states are rather sensitive to small changes in the underlying crystal structure, indicating a subtle interplay between magnetism and structure in the rare-earth nickelates.

VI. SUMMARY

We have presented a systematic DFT+U study for the whole series of perovskite structure rare-earth nickelates. Our goal was to assess if and to what extent the structural and magnetic properties of these compounds can be described within the DFT+U approach. In order to distinguish different structural distortions, we have used a symmetry-based mode

decomposition. Based on this decomposition, the transition from the metallic $Pbnm$ structure at high temperatures to the insulating $P2_1/n$ structure at lower temperatures can mainly be related to a single octahedral "breathing mode" corresponding to irrep R_1^+ of the cubic reference structure.

We find that essentially all structural parameters apart from this R_1^+ mode amplitude are rather well described already within nonmagnetic DFT calculations with $U = 0$. In particular, this is the case for the important R_4^+ mode describing the degree of out-of-phase octahedral rotations around the orthorhombic a axis, which decreases strongly from $R =$ Lu towards $R =$ La. However, in order to obtain a nonzero R_1^+ mode amplitude in agreement with the experimentally observed $P2_1/n$ low temperature structures, both magnetic order and a nonzero value of U are required within the calculations. Thereby, the obtained amplitudes of the breathing mode strongly depend on the value of U and also on the magnetic order imposed in the calculation. For not too large U, the R_1^+ amplitude increases with increasing U and it is significantly larger for the more realistic T-AFM order than for the FM case. For the case with T-AFM order, very good overall agreement with the experimentally determined structures across the whole series is achieved for $U = 2$ eV and $J = 1$ eV. Similar good agreement can also be achieved for FM order using a larger U value of around 5 eV. However, if U is further increased, and once the occupied Ni d states are pushed energetically below the O $2p$ manifold, the R_1^+ mode vanishes again and the system becomes metallic.

Both our calculations as well as the available experimental data indicate a decrease of the R_1^+ amplitude across the series from $R =$ Lu towards $R =$ Pr. This decrease seems to be somewhat weaker in our computational results compared to experiment. Here, we note that, in order to simplify the analysis, we have always compared results obtained with the same values for U and J across the whole series. However, the use of a constant U value for the whole nickelate series might not be fully appropriate. Considering the strong effect of U on the R_1^+ amplitude, even a small decrease of U from $R =$ Lu towards $R =$ Pr would result in a noticeably stronger decrease of the R_1^+ amplitude across the series. Since the octahedral rotations (R_4^+ and M_3^+ modes) decrease towards $R =$ Pr, and thus the hybridization between the Ni d and O p states increases, potentially leading to enhanced screening, the correct U value for $R =$ Pr could indeed be slightly smaller compared to $R =$ Lu. Therefore, in order to clarify how large (or small) these effects really are, first principles calculations of U across the series would be of great interest.

On the other hand, it should also be noted that the available experimental data is quite sparse. In particular, data for the compounds in the middle of the series, i.e., for $R =$ Gd and Sm, is currently not available. Furthermore, an unexpectedly large breathing mode amplitude has been reported for $HoNiO_3$ at 60 K below the MIT [12] and for $DyNiO_3$ at 2 K [15] (see Fig. 9), and systematic measurements of the temperature dependence of the R_1^+ amplitude are also lacking. In particular, considering the strong influence of the magnetic state on the R_1^+ amplitude obtained in the calculation, it would be of interest whether there is a noticeable change in the R_1^+ amplitude (or some other structural parameters) when the nickelate compounds (with R from Lu to Sm) undergo the transition to the AFM phase. Indeed, some anomalies of the phonon frequencies at the magnetic transition temperature have already been observed in $SmNiO_3$ thin films using Raman scattering [49].

While the overall trends and orders of magnitude seem to be well captured within the DFT+U calculations, some deficiencies also become apparent. For example, the imposed T-AFM ordering, which is compatible with the experimental data, is only energetically favored (compared to the FM state) for a relatively small range of U values. For the case of $LuNiO_3$ it is even hardly favored at all (only for $U = 0$ in the fully relaxed structure). Nevertheless, in the small U regime, the T-AFM state becomes more and more energetically favored with increasing radius of the rare-earth cation (see bottom panel of Fig. 10), consistent with the experimentally observed trend of the magnetic ordering temperature. Our calculations also show that the T-AFM order generally couples much stronger to the breathing mode distortion than the FM order.

Overall, we find that the best agreement with experimental observations across the whole series, regarding both structure and magnetic order, is achieved if a relatively small value of $U \approx 2$ eV is used in the calculations. This is consistent with the work of Varignon et al. [29] and in contrast to what has been suggested by Prosandeev et al. [33]. However, one should note that even for $U = 2$ eV, the stability of the FM state seems to be overestimated, in particular for the small rare-earth cations such as Lu.

To conclude, our results give a clear picture of the predictive capabilities of the DFT+U approach in the rare-earth nickelate series and also provide a solid starting point for the use of more advanced computational methods, such as, e.g., DFT+DMFT. Furthermore, they can also be used as reference for future experimental investigations regarding the temperature dependence of the structural parameters and trends across the series.

ACKNOWLEDGMENTS

We are indebted to Marisa Medarde, Oleg Peil, Antoine Georges, Michael Fechner, and Gabriele Sclauzero for helpful discussions. This work was supported by ETH Zurich and the Swiss National Science Foundation through Grant No. 200021-143265 and through NCCR-MARVEL. Calculations have been performed on the PASC cluster "Mönch," the MARVEL cluster "Daint," both hosted by the Swiss National Supercomputing Centre, and the "Euler" cluster of ETH Zurich.

[1] M. Imada, A. Fujimori, and Y. Tokura, Rev. Mod. Phys. **70**, 1039 (1998).
[2] E. Dagotto and Y. Tokura, Mater. Res. Soc. Bull. **33**, 1037 (2008).
[3] G. R. Stewart, Rev. Mod. Phys. **73**, 797 (2001).
[4] E. Dagotto, Rev. Mod. Phys. **66**, 763 (1994).
[5] E. Dagotto, T. Hotta, and A. Moreo, Phys. Rep. **344**, 1 (2001).
[6] J. Kanamori, J. Appl. Phys. **31**, 14 (1960).

[7] M. L. Medarde, J. Phys.: Condens. Matter **9**, 1679 (1997).
[8] G. Catalan, Phase Transitions **81**, 729 (2008).
[9] J. A. Alonso, J. L. García-Muñoz, M. T. Fernández-Díaz, M. A. G. Aranda, M. J. Martínez-Lope, and M. T. Casais, Phys. Rev. Lett. **82**, 3871 (1999).
[10] J. A. Alonso, M. J. Martínez-Lope, M. T. Casais, M. A. G. Aranda, and M. T. Fernández-Díaz, J. Am. Chem. Soc. **121**, 4754 (1999).
[11] J. A. Alonso, M. J. Martínez-Lope, M. T. Casais, J. L. García-Muñoz, and M. T. Fernández-Díaz, Phys. Rev. B **61**, 1756 (2000).
[12] J. A. Alonso, M. J. Martínez-Lope, M. T. Casais, J. L. García-Muñoz, M. T. Fernández-Díaz, and M. A. G. Aranda, Phys. Rev. B **64**, 094102 (2001).
[13] J. L. García-Muñoz, J. Rodríguez-Carvajal, and P. Lacorre, Europhys. Lett. **20**, 241 (1992).
[14] J. A. Alonso, M. J. Martınez-Lope, and I. Rasines, J. Solid State Chem. **120**, 170 (1995).
[15] A. Muñoz, J. A. Alonso, M. J. Martínez-Lope, and M. T. Fernández-Díaz, J. Solid State Chem. **182**, 1982 (2009).
[16] J. A. Alonso, M. J. Martínez-Lope, I. A. Presniakov, A. V. Sobolev, V. S. Rusakov, A. M. Gapochka, G. Demazeau, and M. T. Fernández-Díaz, Phys. Rev. B **87**, 184111 (2013).
[17] J. L. García-Muñoz, J. Rodríguez-Carvajal, P. Lacorre, and J. B. Torrance, Phys. Rev. B **46**, 4414 (1992).
[18] We note that, strictly speaking, the AFM order with the given wave vector is not compatible with $P2_1/n$ space group symmetry, and thus the symmetry of the system is further lowered within the AFM phase. However, the resulting effect on the structure is very small and is not relevant in the present context.
[19] Z. He and A. J. Millis, Phys. Rev. B **91**, 195138 (2015).
[20] R. Scherwitzl, P. Zubko, I. G. Lezama, S. Ono, A. F. Morpurgo, G. Catalan, and J.-M. Triscone, Adv. Mater. **22**, 5517 (2010).
[21] J. W. Freeland, M. van Veenendaal, and J. Chakhalian, J. Electron Spectrosc. Relat. Phenom. **208**, 56 (2016).
[22] S. Middey, J. Chakhalian, P. Mahadevan, J. W. Freeland, A. J. Millis, and D. D. Sarma, Annu. Rev. Mater. Res. **46**, 305 (2016).
[23] K. Momma and F. Izumi, J. Appl. Crystallogr. **44**, 1272 (2011).
[24] I. I. Mazin, D. I. Khomskii, R. Lengsdorf, J. A. Alonso, W. G. Marshall, R. M. Ibberson, A. Podlesnyak, M. J. Martínez-Lope, and M. M. Abd-Elmeguid, Phys. Rev. Lett. **98**, 176406 (2007).
[25] A. Subedi, O. E. Peil, and A. Georges, Phys. Rev. B **91**, 075128 (2015).
[26] J.-S. Zhou and J. B. Goodenough, Phys. Rev. B **69**, 153105 (2004).
[27] H. Park, A. J. Millis, and C. A. Marianetti, Phys. Rev. Lett. **109**, 156402 (2012).
[28] S. Johnston, A. Mukherjee, I. Elfimov, M. Berciu, and G. A. Sawatzky, Phys. Rev. Lett. **112**, 106404 (2014).
[29] J. Varignon, M. N. Grisolia, J. Íñiguez, A. Barthélémy, and M. Bibes, Nature Partner Journals Quantum Materials **2**, 21 (2017).
[30] J. L. García-Muñoz, J. Rodríguez-Carvajal, and P. Lacorre, Phys. Rev. B **50**, 978 (1994).
[31] M. T. Fernández-Díaz, J. A. Alonso, M. J. Martínez-Lope, M. T. Casais, and J. L. García-Muñoz, Phys. Rev. B **64**, 144417 (2001).
[32] G. Giovannetti, S. Kumar, D. Khomskii, S. Picozzi, and J. van den Brink, Phys. Rev. Lett. **103**, 156401 (2009).
[33] S. Prosandeev, L. Bellaiche, and J. Íñiguez, Phys. Rev. B **85**, 214431 (2012).
[34] K. Held, Adv. Phys. **56**, 829 (2007).
[35] H. Park, A. J. Millis, and C. A. Marianetti, Phys. Rev. B **89**, 245133 (2014).
[36] J. M. Perez-Mato, D. Orobengoa, and M. I. Aroyo, Acta Crystallogr. A **66**, 558 (2010).
[37] P. V. Balachandran and J. M. Rondinelli, Phys. Rev. B **88**, 054101 (2013).
[38] This is true for all nickelates analyzed in Ref.[37] except for $NdNiO_3$, which exhibits a surprisingly large M_5^+ mode amplitude. This mode describes an out-of-phase tilting of oxygen octahedra. However, the relatively large M_5^+ amplitude found in $NdNiO_3$ could be an experimental artifact.
[39] B. J. Campbell, H. T. Stokes, D. E. Tanner, and D. M. Hatch, J. Appl. Crystallogr. **39**, 607 (2006).
[40] P. E. Blöchl, Phys. Rev. B **50**, 17953 (1994).
[41] G. Kresse and J. Hafner, Phys. Rev. B **47**, 558 (1993).
[42] G. Kresse and J. Furthmüller, Phys. Rev. B **54**, 11169 (1996).
[43] G. Kresse and D. Joubert, Phys. Rev. B **59**, 1758 (1999).
[44] J. P. Perdew, K. Burke, and M. Ernzerhof, Phys. Rev. Lett. **77**, 3865 (1996).
[45] A. I. Liechtenstein, V. I. Anisimov, and J. Zaanen, Phys. Rev. B **52**, R5467(R) (1995).
[46] J. L. García-Muñoz, M. A. G. Aranda, J. A. Alonso, and M. J. Martínez-Lope, Phys. Rev. B **79**, 134432 (2009).
[47] M. Medarde, M. T. Fernández-Díaz, and P. Lacorre, Phys. Rev. B **78**, 212101 (2008).
[48] A. Subedi, arXiv:1708.08899.
[49] C. Girardot, J. Kreisel, S. Pignard, N. Caillault, and F. Weiss, Phys. Rev. B **78**, 104101 (2008).

5

DESCRIBING THE COUPLED TRANSITION WITHIN DFT+DMFT

In this chapter I utilize the DFT+DMFT method to describe the paramagnetic insulating state found in rare-earth nickelates. The goal is to obtain a quantitative correct description of the breathing mode distortion amplitude in the paramagnetic state. This is also motivated by my previous findings, that in DFT+U the R_1^+ amplitude depends heavily on the magnetic order. Furthermore, a better understanding of the MIT can be obtained, by analyzing the energetics of the breathing mode distortion in DFT+DMFT.

I demonstrate, that the coupling to an electronic instability is crucial to stabilize the breathing mode distortion. Furthermore, I obtain quantitative correct structural parameters by performing CSC DFT+DMFT total energy calculations across the series, which are then also compared to the magnetic DFT+U results. In order to see how U and J vary across the series and to obtain a magnitude, I use the cRPA method to calculate the interaction parameters across the series. The cRPA calculations reveal an important change in the screened Coulomb repulsion strength across the series, requiring to adapt the Coulomb interaction parameters for the different compounds of the series.

The following work was published as *"Energetics of the coupled electronic–structural transition in the rare-earth nickelates"* in npj Quantum Materials, see Ref. [50]. I performed and analyzed all DFT and DMFT calculations. To perform the cRPA calculations I visited the group of C. Franchini in Vienna. The cRPA calculations where done by myself, with the help of P. Liu. The initial manuscript was written by me, corrected by my supervisor C. Ederer, and discussed at several stages with C. Franchini and P. Liu.

5.1 MOTIVATION

In the previous chapter I demonstrated that DFT+U correctly captures structural trends for the breathing mode amplitude across the nickelate series in the AFM phase. Moreover, I showed that all internal structural parameters not specifically related to the low-temperature phase are well captured in non-magnetic DFT calculations. Together with experimental data, which shows that during the MIT all structural parameters not related to the breathing mode distortion undergo only very small changes [29], the $Pbnm$-relaxed structures from non-magnetic DFT calculations represent

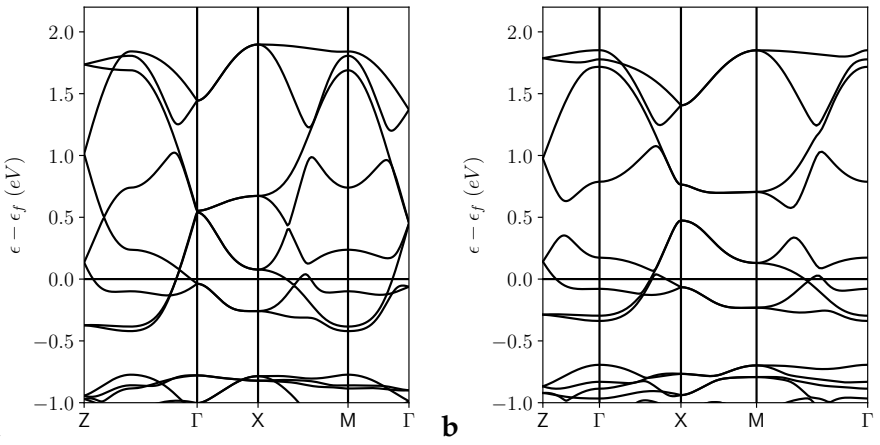

Figure 20: **a** DFT band structure for the relaxed Pbnm high-temperature phase of $LuNiO_3$. The relaxation and the band calculation is performed non-magnetic without any U correction. **b** DFT band structure for the relaxed $P2_1/n$ low-temperature structure. Here, the relaxation is performed with ferromagnetic ordering and $U_{avg} = 5$ eV and $J_{avg} = 1$ eV, resulting in a finite stable R_1^+ amplitude. The band calculation shown here is performed non-magnetic without +U. A gap opens at 0.5 eV above the Fermi level ϵ_f due to the Ni_{LB} / Ni_{SB} splitting, induced by the breathing mode distortion. Importantly, both results are clearly metallic, showing that the magnetic ordering is needed to open a gap at ϵ_f.

a good starting point for further studies analyzing the breathing mode distortion. The decomposition in distortion modes allows to explicitly add the breathing mode distortion on top of these relaxed structures to find the stable equilibrium breathing mode amplitude.

Within non-magnetic DFT calculations, all nickelate compounds are be metallic, even for the $P2_1/n$ structures with breathing mode distortion. This is due to the fact, that the Ni e_g states are quarter-filled, which means in a band picture that bands cross the Fermi level. This is illustrated in Fig. 20. Here, the band structures from non-magnetic DFT calculations are shown for both, the high-temperature Pbnm structure, and the low-temperature $P2_1/n$ structure with breathing mode distortion. The breathing mode distortion induces a splitting between the Ni_{LB} and Ni_{SB} sites, which opens a gap at 0.5 eV above the Fermi level. The lower Ni_{LB} site is still half-filled and bands cross the Fermi level. Hence, it becomes clear that a further mechanism is required to obtained an insulating state. In DFT+U calculations this is achieved by introducing long-range magnetic ordering. This lifts the spin degeneracy of the band crossing the Fermi level, and allows to open a gap at the Fermi level. The fact that magnetic order is needed in DFT+U to obtain an insulating state, makes it hard to distinguish between mechanisms responsible for the magnetic insulating state and the paramagnetic insulating state in

rare-earth nickelates. It becomes clear, that to directly investigate the coupled structural-electronic transition in the paramagnetic regime, DFT is not sufficient.

5.2 PREVIOUS WORK: CHARGE DISPROPORTIONATED INSULATOR IN DMFT

In the work of Ref. [23], it was demonstrated for the first time that the insulating paramagnetic state of rare-earth nickelates can be described by DFT+DMFT calculations. The strong electronic correlations result in a site selective Mott transition. Furthermore, it was shown in a following work by the same authors, that $E(R_1^+)$ obtained by DFT+DMFT calculations has a global minimum corresponding to a finite stable breathing mode distortion for $LuNiO_3$ [24]. Moreover, it was demonstrated, that for $LaNiO_3$ no such minimum exists in agreement with experiment. Therefore, it was concluded in Ref. [24] that DFT+DMFT is indeed able to correctly describe the electronic and structural properties of rare-earth nickelates across the series.

In Ref. [24], structures were interpolated between the high-temperature $Pbnm$ structure relaxed by non-magnetic DFT calculations, and the low-temperature $P2_1/n$ structure relaxed by ferromagnetic DFT+U calculations using $U_{avg} = 5$ eV. Then for these interpolated structures total energy calculations in DFT+DMFT were performed to find the equilibrium breathing mode distortion. I would like to note, that there exists a longer, more detailed paper by the same authors [52] providing more results. However, the way in Ref. [24] the structural optimization is performed can be problematic. The interpolation between the two structures induces multiple changes in structural parameters at once. In the previous chapter 4, I found that for example octahedral rotations are changing when calculations are performed with and without +U correction, whereas in experiment no such change is observed at T_{MIT} [29]. Moreover, the calculations presented in Ref. [24] seem to be influenced by the choice of U. Furthermore, it was stated that DFT+U overestimates the size of the breathing mode distortion amplitude compared to DFT+DMFT. However, as shown in chapter 4, the resulting breathing mode distortion amplitude is heavily influenced by the choice of the interaction parameters, and the magnetic order.

In Ref. [43] it was demonstrated that a minimal correlated subspace, built only from the Ni e_g states found at the Fermi level, is sufficient to capture the physics necessary to describe the paramagnetic insulating phase in rare-earth nickelates. I call such sub-space construction *frontier orbital* model. Subedi *et al.* [43] showed, that for a certain interaction parameter regime they find an insulating paramagnetic state by performing OS DFT+DMFT calculations. The insulating state is characterized by a strong charge disproportionation between the Ni_{LB}

and $_{LB}$ site. Hence, the insulating state is called charge disproportionated insulator (CDI), and is identified with the paramagnetic insulating state of the nickelates. In this state, the occupation of the Wannier functions of the different Ni sites changes drastically.

Wannier orbitals constructed for the frontier orbital model will be considerably more extended in space with oxygen p tails, than if built from all Ni d and oxygen-p states, as done in Ref. [24]. Here, the occupation of the Wannier orbitals is closer to the formal charge state of Ni, d^7, with one electron in the e_g orbitals per Ni site. In Ref. [43] it is assumed, that the Coulomb interaction U is highly screened in these orbitals, to values smaller than 2 eV. However, the frontier orbital model also results in a larger charge disproportionation effect compared to a full d and p model. As demonstrated in Ref. [44], both approaches to describe the system are valid, leading to the same physics, but require different interpretation of the resulting occupations.

In Ref. [43], it is shown that in agreement with Ref. [22] the breathing mode distortion induces a local potential shift Δ_s between the e_g orbitals on the Ni_{LB} and the Ni_{SB} site. Importantly, they find that the CDI state also occurs for the Pbnm structure without breathing mode distortion, hence $\Delta_s = 0$, for large Hund's coupling strengths. Thereby, they discuss that a strong Hund's coupling favors the CDI state, which will occur in the Hubbard-Kanamori Hamiltonian for $U - 3J \leqslant \Delta_s$.

The calculations in Ref. [43] were performed by constructing ML-WFs with wannier90 [87, 88] for the experimental high- and low-temperature $LuNiO_3$ structures. They were performed without DC correction and without CSC. They were a proof of concept, that a frontier orbital model is able to capture all necessary physics to describe rare-earth nickelates.

Here, I follow the ideas of Subedi *et al.* [43] to construct the correlated subspace only from the Ni e_g orbitals to perform DFT+DMFT calculations. Thereby, I go beyond this work by performing CSC calculations, with PLO formalism, and DC correction, for multiple members of the nickelate series by using the DFT relaxed Pbnm structures. Then, I utilize the distortion mode decomposition, rather than relying on the DFT+U relaxed structures, to obtain structural parameters by performing DFT+DMFT total energy calculations. Thereby, I overcome also the shortcomings of Ref. [24] and [52] relying on the interpolation of structures. Furthermore, I investigate the influence of the interaction parameters in detail, to be able to compare on a more quantitative level with previous DFT+U results.

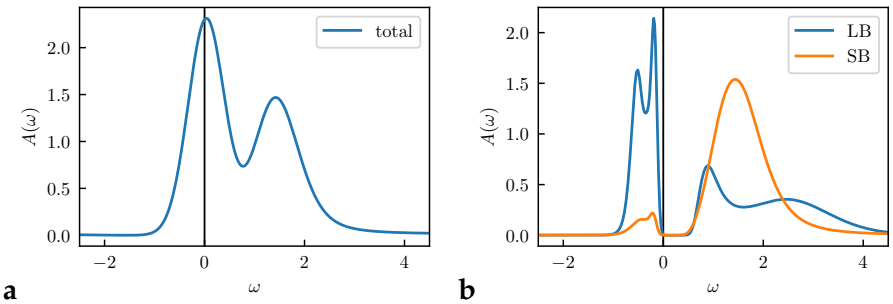

Figure 21: **a** Spectral function of the Ni e_g orbitals (summed) of $LuNiO_3$ in the metallic high-temperature phase without breathing mode distortion. **b** Spectral functions for the low-temperature insulating paramagnetic phase with experimental breathing mode distortion $R_1^+ = 0.075$ Å. The LB Ni e_g orbitals have considerably higher occupancy (blue), than the SB Ni e_g orbitals (orange). A clear gap of $\sim$ 0.5 eV can be observed at the Fermi level. Both spectral functions are obtained for $U = 2.04$ eV and $J = 0.47$ eV performing a full CSC DFT+DMFT calculation.

5.3 PROJECT SUMMARY

To compare with Ref. [43], We calculate in a first step interaction parameter phase diagrams for $LuNiO_3$ structures with, and without breathing mode distortion by performing OS DFT+DMFT calculations without DC correction. Thereby, we reproduce the results found in Ref. [43] that for $U - 3J \leqslant 0$ the CDI state emerges. Here, we use the Hubbard-Kanamori parameterization introduced in section 3.4.2. To characterize CDI state we calculate the spectral functions $A(\omega)$ for the insulating state of the $P2_1/n$ structure, and the metallic state in the $Pbnm$ structure. We performed the analytical continuation of the impurity Green's function to the real frequency axis, by using the maximum entropy method [141], utilizing the *triqs/maxent* software [142].

The results are shown in Fig. 21. For the $Pbnm$ structure, Fig. 21 **a**, the spectral function of all Ni e_g states is depicted showing a metallic state. A small splitting between the e_g states can be observed, similar to what is found with non-magnetic DFT calculations. In Fig. 21 **b** the spectral function for the low-temperature $P2_1/n$ structure is shown. The Ni LB and SB site are shown separately. The LB site has a larger occupation, whereas the SB site is almost empty. Moreover, a clear gap of 0.5 eV can be observed at the Fermi level. This is in agreement with Ref. [43].

We also performed calculations including a DC correction to check its influence in OS DFT+DMFT calculations. Here, we find that the DC correction can influence substantially the on-site potential shift Δ_s between Ni_{LB} and Ni_{SB} site, depending on the choice of how the DC correction is calculated. The effect of the DC will be further discussed

in chapter 7. In the following we use the DMFT impurity occupations for the DC correction.

In Fig. 1 of Ref [50] the U, J phase diagram for $LuNiO_3$ with $R_1^+ = 0.0$ Å preforming now CSC calculations is presented. Here, we find three distinctive phases in agreement with Ref. [43]. A metallic phase, a Mott insulating phase for large U values, and the CDI phase for larger J values. The Mott insulating phase is characterized by the Ni site occupation $n_{LB} \approx n_{SB} \approx 1.0$. In contrast, the CDI state is characterized by $n_{LB} \geqslant 1.5$ and $n_{SB} \leqslant 0.5$. Therefore, we find also in CSC calculations the spontaneous symmetry breaking into the CDI state due to an electronic instability. However, we find a strong shift in the strength of the Hund's coupling required for the CDI state to emerge. The required J is considerably smaller compared to OS DFT+DMFT calculations. Such a reduction has also been found in the work of Ref. [143] by including an inter-site Coulomb interaction in OS DFT+DMFT calculations. Hence, we suggest that CSC calculations include this effect, because the DFT charge density is updated in CSC calculations, accounting for the charge redistribution in the CDI state, and thus, at least on a Hartree level, are covered within DFT.

Next, we investigate how the electronic instability couples to the structural R_1^+ breathing mode distortion. We add the R_1^+ breathing mode distortion on top of the DFT relaxed $Pbnm$ structures from DFT to check systematically the influence of the breathing mode distortion. We observe a strong coupling to the R_1^+ amplitude, both in $LuNiO_3$ and $PrNiO_3$ in the corresponding U, J phase diagrams. The main effect is a strong reduction of the value of J required to stabilize the CDI state. Moreover, we find a small reduction of the value of U required to stabilize the CDI state for larger R_1^+ amplitudes, where this effect is more pronounced in $LuNiO_3$. This is shown in Fig. 2 of Ref. [50].

Next, we calculate the screened Coulomb interaction parameters, U and J, across the whole nickelate series. This is performed in a collaboration with C. Franchini and P. Liu from the University of Vienna by using the cRPA implementation in VASP [103]. We find a strong screening effect reducing the effective U values below 2 eV for nickelates, in agreement with previous work [143]. This is also consistent with the values required to obtain a stable CDI state. Furthermore, we find a reduction in U by 25% across the nickelate series from R =Lu to La (see Fig. 3 in Ref. [50]). This strongly suggests that the use of a single interaction parameter setting for the different members of the series is not appropriate. Furthermore, we show that this reduction is mainly due to stronger screening effects for larger R site cations, hence smaller octahedral rotations. Next, we compared the calculated U and J values for $LuNiO_3$ and $PrNiO_3$ with the U, J phase-diagrams. Here, we find that for $LuNiO_3$ the obtained values

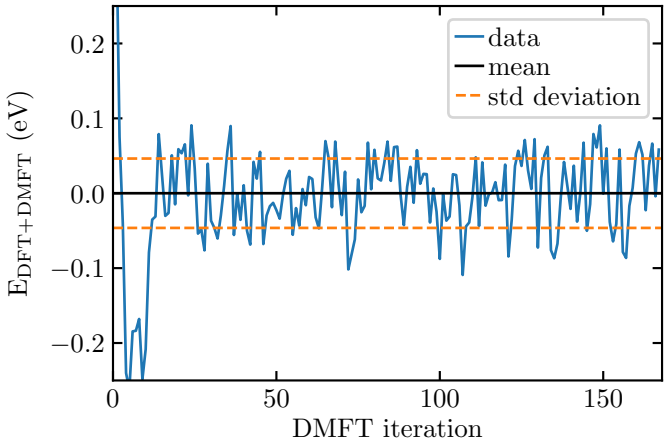

Figure 22: Example how the total energy can be determined to high accuracy by sampling converged DMFT iterations. The plot shows the total DFT+DMFT energy per iteration. After convergence is reached at iteration 25 the total energy values are sampled. Convergence was reached after the standard error of the impurity occupations in the past 10 DMFT iterations was smaller than 1.5×10^{-3}. The averaged mean value is shown by a black line. The standard deviation is shown to quantify the possible error.

of U and J give a stable CDI state for a broad range of R_1^+ amplitudes. For $PrNiO_3$ on the other hand the values obtained by cRPA for J are too small, and even a large R_1^+ amplitude does not produce a CDI state.

So far we limited the discussion to the stability of the electronic CDI state. In a next step, we addressed the stability of the structural R_1^+ distortion. To do so, we calculate the energy as function of the R_1^+ amplitude in DFT+DMFT, $E(R_1^+)$, to obtain the energetics of the breathing mode distortion. By performing such calculations systematically across the series, trends can be revealed.

The calculation of the total energy in DFT+DMFT is computationally demanding. Since DMFT is an iterative scheme, and furthermore each iteration involves solving the impurity problem by QMC, one has to deal with inaccuracies stemming from the iterative scheme itself and the QMC noise. To limit the QMC noise, we measure G^{imp} directly in the Legendre basis. Moreover, we sample the total energy over a minimum of additional 60 DMFT iterations after the CSC DFT+DMFT loop is in principle already converged. Typically, convergence is reached in my calculations, when the standard error of the Ni site occupation of the last 10 DFT+DMFT loops is smaller than 1.5×10^{-3}. In this way an accuracy in the total energy of $< 2\,\text{meV}$ per Ni site can be achieved. The extraction of the total energy is illustrated in Fig. 22. Here, the total energy as function of DMFT iterations is shown, and the calculated mean value, as well as the standard deviation.

For $LuNiO_3$, using the cRPA U, J values, we find a minimum in $E(R_1^+)$ close to the experimental R_1^+ amplitude. By increasing U, J slightly by 10% we find best agreement with experiment. By reducing U and J we demonstrate that the R_1^+ distortion is destabilized (see Fig. 4 in Ref. [50]). However, the electronic CDI state is still stable for $R_1^+ > 0.06$ Å, which demonstrates that the stability of the breathing mode distortion does not always goes hand in hand with the stability of the CDI state. Furthermore, we observe a kink in $E(R_1^+)$ when the MIT takes place. We find that this reshaping of $E(R_1^+)$ is critical for obtaining a stable breathing mode distortion, because it produces additional energy minima in $E(R_1^+)$ (see Fig. 4 in Ref. [50]). The resulting $E(R_1^+)$ shows typical characteristics of a first-order transition.

In the next step, we examine the energetics across the series by performing $E(R_1^+)$ calculations for R =Lu, Sm, and Pr for the U and J values obtained by cRPA increased by 10%. For $SmNiO_3$ we find a R_1^+ amplitude reduced by $\approx$ 20%, and for $PrNiO_3$ no R_1^+ distortion is obtained (see Fig. 5 bottom in Ref. [50]). This appears to be reasonable, as $PrNiO_3$ has only a stable breathing mode distortion within the AFM ordered phase [61]. Recently, it was also found for $NdNiO_3$ that the magnetic order is crucial to stabilize the breathing mode distortion [144]. This confirms our results, because $NdNiO_3$ also exhibits a finite R_1^+ amplitude only in the magnetically ordered state [60].

Finally, we analyze the influence of the octahedral rotations, by systematically reducing them in $LuNiO_3$ (see Fig. 5 top in Ref. [50]). Decreasing the rotations results in smaller equilibrium R_1^+ amplitudes, and shallower minima in energy. Eventually, for 70% of the original octahedral rotations amplitudes, the energy minimum at non-zero R_1^+ amplitudes is lost. This rotation amplitude is comparable to the one of $PrNiO_3$, which has no finite R_1^+ amplitude in the paramagnetic regime, thus demonstrating that the octahedral rotations play a crucial role in determining trends across the series.

5.4 CONCLUSION

In this chapter I demonstrated that DFT+DMFT can be utilized to describe the paramagnetic ground state, and the coupled structural and electronic phase transition, of rare-earth nickelates completely *ab initio* on a quantitative level. Performing these calculations allowed to elucidate the nature of the coupled electronic-structural transition. We reveal that the MIT, which is related to an electronic instability, leads to a significant restructuring of the energy landscape. This creates an energy minimum at finite R_1^+ amplitudes. Therefore, we concluded that the coupled electronic-structural transition is of first order, in agreement with experiment [19].

Moreover, I showed that the trends across the series are critically determined by the octahedral rotations, which in turn determines the strength of the electronic instability responsible for triggering the CDI state. It is found that the appearance of the electronic CDI state does not necessarily result in stable structural breathing mode distortion. Thus, demonstrating that it is inevitable to treat both electronic and structural degrees of freedom on the same footing, in order to arrive at a fully coherent picture. Furthermore, the screening of the Coulomb interaction is influenced by the octahedral rotation strength, or equivalently the R site cation, supporting the trends across the series by disfavoring the CDI for larger R site cations. The obtained structural parameters are in very good agreement with experiment, where we find a reduction of the R_1^+ amplitude from R =Lu to Sm of $\approx$ 20%. This reduction is much more pronounced compared to DFT+U calculations with $\approx$ 8%, and is in better agreement with experimental data. This discrepancy shows that a better understanding of the differences of the paramagnetic and magnetic phase is needed. The inclusion of magnetic order in DFT+DMFT will be further discussed in chapter 8.

In the work of Ref. [49], the MIT and the trends across the nickelate series are investigated as well. The authors of Ref. [49] construct a Landau model with parameters obtained by DFT+U calculations. The calculations are performed in the magnetically ordered phase and the resulting Landau model contains only structural degrees of freedom. In their work, the octahedral rotations are also identified as critical driving force for trends across the series, in agreement with our work. Moreover, they propose that the octahedral rotations trigger the stabilization of the breathing mode distortion. This is to some extent in agreement with our work, showing that the octahedral rotations critically influence the R_1^+ stability. However, from the constructed model the phase transition can only be classified as second order, hence not in agreement with experiment.

Finally, I would like to note that these results also demonstrate that the use of minimal correlated sub-space, the frontier orbital model, can indeed be used to obtain quantitatively correct results. Compared to a correlated subspace constructed for all Ni d and oxygen p orbitals, a frontier orbital model has a crucial advantage in computational effort, especially when calculating total energies. Moreover, the DC problem can be less severe, since one does not need to adjust the $d-p$ energy splitting by the DC potential [131].

5.5 PEER REVIEWED WORK

npj | Quantum Materials

www.nature.com/npjquantmats

ARTICLE OPEN

Energetics of the coupled electronic–structural transition in the rare-earth nickelates

Alexander Hampel[1], Peitao Liu[2], Cesare Franchini[2,3] and Claude Ederer[1]

Rare-earth nickelates exhibit a metal–insulator transition accompanied by a structural distortion that breaks the symmetry between formerly equivalent Ni sites. The quantitative theoretical description of this coupled electronic–structural instability is extremely challenging. Here, we address this issue by simultaneously taking into account both structural and electronic degrees of freedom using a charge self-consistent combination of density functional theory and dynamical mean-field theory, together with screened interaction parameters obtained from the constrained random phase approximation. Our total energy calculations show that the coupling to an electronic instability toward a charge disproportionated insulating state is crucial to stabilize the structural distortion, leading to a clear first order character of the coupled transition. The decreasing octahedral rotations across the series suppress this electronic instability and simultaneously increase the screening of the effective Coulomb interaction, thus weakening the correlation effects responsible for the metal–insulator transition. Our approach allows to obtain accurate values for the structural distortion and thus facilitates a comprehensive understanding, both qualitatively and quantitatively, of the complex interplay between structural properties and electronic correlation effects across the nickelate series.

npj Quantum Materials (2019)4:5 ; https://doi.org/10.1038/s41535-019-0145-4

INTRODUCTION

Complex transition metal oxides exhibit a variety of phenomena, such as, e.g., multiferroicity,[1] non-Fermi liquid behavior,[2] high-temperature superconductivity,[3] or metal–insulator transitions (MIT),[4] which are not only very intriguing, but are also of high interest for future technological applications.[5–7] However, the quantitative predictive description of these materials and their properties represents a major challenge for modern computational materials science, due to the importance of electronic correlation effects as well as due to the intimate coupling between electronic, magnetic, and structural degrees of freedom.[4,8]

An example, which has received considerable attention recently, is the family of rare-earth nickelates, $RNiO_3$, with $R =$ La–Lu and Y, which exhibit a rich phase diagram that is highly tunable by strain, doping, and electromagnetic fields.[9–14] All members of the nickelate series (except $LaNiO_3$) exhibit a MIT as a function of temperature, which is accompanied by a structural distortion that lowers the space group symmetry from orthorhombic *Pbnm*, where all Ni sites are symmetry-equivalent, to monoclinic $P2_1/n$, with two inequivalent types of Ni sites.[15–18] The structural distortion results in a three-dimensional checkerboard-like arrangement of long bond (LB) and short bond (SB) oxygen octahedra surrounding the two inequivalent Ni sites (see Fig. 2a), and corresponds to a zone-boundary breathing mode of the octahedral network with symmetry label R_1^+.[19] In addition, all systems exhibit antiferromagnetic (AFM) order at low temperatures.[9,20,21] For *R* from Lu to Sm, the AFM transition occurs at lower temperatures than the MIT, whereas for $R =$ Nd and Pr, the magnetic transition coincides with the MIT. AFM order in $LaNiO_3$ was only reported recently[21] and is still under discussion.[22] Due to challenges in synthesis, experimental data on the bulk materials is relatively sparse, and quantitative predictive calculations are therefore highly valuable to gain a better understanding of the underlying mechanisms.

Different theoretical and computational approaches have highlighted different aspects of the coupled structural–electronic transition in the nickelates, thereby focusing either on structural or electronic aspects.[23–30] Density functional theory plus Hubbard *U* (DFT + *U*) calculations have recently emphasized the coupling between the breathing mode and other structural distortions such as octahedral rotations, as well as the effect of magnetic order.[28–30] However, these calculations cannot properly describe the transition from the paramagnetic metal to the paramagnetic insulator observed in all nickelates with *R* cations smaller than Nd, and thus cannot correctly capture the important electronic instability. Using DFT plus dynamical mean-field theory (DFT + DMFT),[31] the MIT has been classified as site-selective Mott transition,[23] where an electronic instability drives the system toward a charge- (or bond-) disproportionated insulator.[26] However, the capability of DFT + DMFT to address structural properties is currently not well established, even though promising results have been achieved in previous work,[24,25,27] employing either simplified interpolation procedures between different structures, fixing lattice parameters to experimental data, or using ad hoc values for the interaction parameters.

Here, we combine a systematic analysis of the structural energetics, with an accurate DFT + DMFT-based description of the electronic structure, using screened interaction parameters obtained within the constrained random phase approximation (cRPA).[32] Our analysis thus incorporates both structural and electronic effects, and leads to a transparent and physically sound picture of the MIT in the nickelates, which also allows to obtain

[1]Materials Theory, ETH Zürich, Wolfgang-Pauli-Strasse 27, 8093 Zürich, Switzerland; [2]Faculty of Physics, Computational Materials Physics, University of Vienna, Vienna A-1090, Austria and [3]Dipartimento di Fisica e Astronomia, Università di Bologna, 40127 Bologna, Italy
Correspondence: Alexander Hampel (alexander.hampel@mat.ethz.ch) or Claude Ederer (claude.ederer@mat.ethz.ch)

Received: 14 November 2018 Accepted: 18 January 2019
Published online: 06 February 2019

Published in partnership with Nanjing University

accurate structural parameters across the whole series. We find that the electronic instability is crucial to stabilize the breathing mode distortion by essentially "renormalizing" the corresponding total energy surface, resulting in a coupled structural–electronic first order transition. Trends across the series are driven by the degree of octahedral rotations,[28] which control both the strength of the electronic instability as well as the magnitude of the screened interaction parameters.

RESULTS

Relaxation of *Pbnm* structures and definition of correlated subspace

All systems are fully relaxed within the high-temperature *Pbnm* space group using nonspinpolarized DFT calculations. We then use symmetry-based mode decomposition[33] to analyze the relaxed *Pbnm* structures and quantify the amplitudes of the various distortion modes. The mode decomposition allows for a clear conceptional distinction between different structural degrees of freedom, which enables us to obtain those structural degrees of freedom for which correlation effects are not crucial from standard DFT calculations, while the important breathing mode distortion is then obtained from DFT + DMFT total energy calculations. For further details on the DFT results and our distortion mode analysis we refer to our previous work.[30]

Next, we construct a suitable low-energy electronic subspace, for which the electron–electron interaction is treated within DMFT. Here, we follow the ideas of ref. [26], and construct Wannier functions only for a minimal set of bands with predominant Ni-e_g character around the Fermi level, which in all cases (except $LaNiO_3$) is well separated from other bands at lower and higher energies. The Wannier functions are then used as localized basis orbitals to construct the effective impurity problems for our fully charge self-consistent (CSC) DFT + DMFT calculations,[34] where the LB and SB Ni sites are treated as two separate impurity problems (even for zero R_1^+ amplitude) coupled through the DFT + DMFT self-consistency loop, and the system is constrained to remain paramagnetic. More details on the construction of the Wannier functions and the technical aspects of our CSC DFT + DMFT calculations can be found in the "Methods" section.

(*U*, *J*) Phase diagrams

We first establish the main overall effect of the interaction parameters *U* and *J* on the electronic properties of $LuNiO_3$ within the high-symmetry *Pbnm* structure, i.e., $R_1^+ = 0.0$ Å. The resulting phase diagram is presented in Fig. 1. Analogously to ref. [26], we can identify three distinct phases: First, a standard Mott-insulating phase for large *U* values, with vanishing spectral weight around the Fermi level, $A(\omega = 0) = 0$, and equal occupation of all Ni sites. Second, another insulating phase for moderate *U* values of around 2–3.5 eV and relatively large J ($\gtrsim 0.4$ eV), which is characterized by a strong difference in total occupation of the Wannier functions centered on LB and SB Ni sites, respectively ($n_{LB} \geq 1.5$ and $n_{SB} \leq 0.5$). We denote this phase as charge disproportionated insulating (CDI) phase.[35] Third, a metallic phase for small *U* values in between the two insulating regions, with equal occupation on all Ni sites, $n_{SB} \approx n_{LB} \approx 1.0$, and nonvanishing spectral weight at the Fermi level, $A(\omega = 0) > 0$.

The CDI phase has been identified as the insulating low-temperature phase of nickelates in ref. [26], where it has also been shown that the strong charge disproportionation is linked to the MIT (in ref. [26] this phase has been termed "bond disproportionated insulating"). We note that the Wannier basis within our low-energy subspace, while being centered on the Ni sites with strong e_g character, also exhibits strong tails on the O ligands, and thus the corresponding charge is distributed over the central Ni atom and the surrounding O atoms. The strong charge disproportionation found within our chosen basis set is thus fully consistent with the observation that the integrated charge around the two different Ni atoms differs only marginally.[23] Alternatively, within a negative charge transfer picture, the MIT can also be described, using a more atomic-like basis, as $(d^8\underline{L})_i(d^8\underline{L})_j \rightarrow (d^8\underline{L}^2)_{SB}(d^8)_{LB}$, where $\underline{L}$ denotes a ligand hole (c.f. refs. [23,29,36,37]).

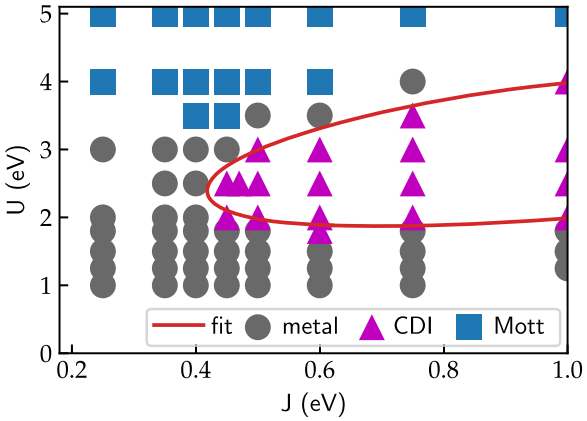

Fig. 1 Phase diagram as a function of interaction parameters *U* and *J* for the relaxed *Pbnm* structure of $LuNiO_3$, i.e., $R_1^+ = 0.0$ Å. Each calculation is represented by a marker. Three different phases can be identified, indicated by different symbols: metallic (gray circles), Mott-insulator (blue squares), and charge-disproportionated insulator (CDI, magenta triangles). The boundary of the CDI phase is fitted by the red line

One should also note that the CDI phase appears even though all Ni sites are structurally equivalent ($R_1^+ = 0$ in Fig. 1), which indicates an electronic instability toward spontaneous charge disproportionation. This has already been found in ref. [26], and indicates that a purely lattice-based description is incomplete. Moreover, within our CSC DFT + DMFT calculations, the CDI phase appears at significantly lower *J* and a more confined *U* range compared to the non-CSC calculations of ref. [26]. A similar reduction of *J* values necessary to stabilize the CDI phase has also been achieved in the non-CSC DFT + DMFT calculations of ref. [38], through the introduction of an (effective) inter-site Hartree interaction. This suggests that the latter can indeed mimic the main effect of a CSC calculation, where the charge density, and thus the local occupations, are updated and the Hartree energy is recalculated in each CSC step.

Next, we investigate how the electronic instability corresponding to the CDI phase couples to the structural R_1^+ breathing mode distortion. For this, we vary only the R_1^+ amplitude, while keeping all other structural parameters fixed to the fully relaxed (within nonmagnetic DFT) *Pbnm* structures, and calculate (*U*, *J*) phase diagrams for different values of the R_1^+ amplitude. We do this for both $LuNiO_3$ and $PrNiO_3$, i.e., for the two compounds with the smallest and largest rare earth cations within the series that exhibit the MIT. The (*U*, *J*) range of the CDI phase for a given R_1^+ amplitude is then extracted by interpolating the convex hull of the phase boundary (similar to the red line in Fig. 1). The results are summarized in Fig. 2b.

In both cases, R = Lu and R = Pr, the R_1^+ amplitude couples strongly to the CDI state, and increases the corresponding area within the (*U*, *J*) phase diagam. In particular, the minimal *J* required to stabilize the CDI phase is significantly lowered. Furthermore, also for R = Pr, there is a spontaneous instability toward the formation of a CDI state, but the corresponding (*U*, *J*) range is noticeably smaller than for R = Lu. In addition, the minimal *U* required to stabilize the CDI phase for a given R_1^+

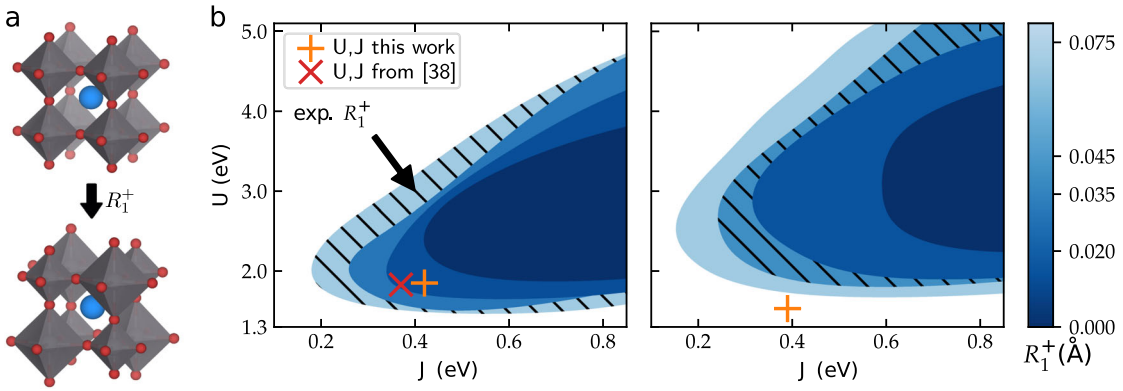

Fig. 2 **a** Illustration of the R_1^+ breathing mode distortion. **b** Extension of the CDI phase within the (*U*, *J*) phase diagram for varying R_1^+ breathing mode amplitude for $LuNiO_3$ (left) and $PrNiO_3$ (right). Each R_1^+ amplitude is represented by a different brightness level, according to the color scale on the right, starting from $R_1^+ = 0.0$ Å (darkest) to $R_1^+ = 0.075$ Å (brightest). The levels corresponding to the experimental R_1^+ amplitudes for $R = Lu$[18] and $R = Pr$,[66] respectively, are highlighted by diagonal stripes. The obtained cRPA values for *U* and *J* are marked by orange crosses and compared to the values from ref. [38] for $LuNiO_3$ (red diagonal cross)

amplitude is slighty higher for $R = Pr$ than for $R = Lu$. We note that, since the *R* ions do not contribute noticeably to any electronic states close to the Fermi level, the differences between the two materials are mainly due to the different underlying *Pbnm* structures, specifically the weaker octahedral tilts in $PrNiO_3$ compared to $LuNiO_3$. This increases the electronic bandwidth, which opposes the tendency toward charge disproportionation.

Calculation of interaction parameters

So far we have varied *U* and *J* in order to obtain the general structure of the phase diagram. Next, we calculate *U* and *J* corresponding to our correlated subspace for all systems across the series to see where in these phase diagrams the real materials are located. We use cRPA[32] to extract the partially screened interaction parameters (*U*, *J*) within the Hubbard–Kanamori parameterization, by separating off the screening channels related to electronic transitions within the correlated e_g subspace from all other transitions (see also Methods section).

The results of these cRPA calculations are shown in Fig. 3 as a function of the *R* cation and the corresponding R_4^+ amplitude, i.e., the main octahedral tilt mode in the *Pbnm* structure. The effective interaction parameters *U* corresponding to our e_g correlated subspace are strongly screened compared to the bare interaction parameters *V*. For $LuNiO_3$, we obtain $V = 13.91$ eV and $U = 1.85$ eV, while $J = 0.42$ eV with a corresponding bare value of 0.65 eV. This is in good agreement with ref. [38], which obtained $U = 1.83$ eV and $J = 0.37$ eV using the experimental $P2_1/n$ structure. Furthermore, both *U* and *J* decrease monotonically across the series (for decreasing R_4^+ amplitude), leading to an additional reduction of *U* by 25% in $LaNiO_3$ compared to $LuNiO_3$. This decrease is also observed in the ratio *U*/*V*, indicating that it is due to an even stronger screening for $R = La$ compared to $R = Lu$.

Our calculated (*U*, *J*) parameters for $R = Lu$ and $R = Pr$ are also marked in the corresponding phase diagrams in Fig. 2. It is apparent, that for $R = Lu$ the calculated cRPA values are well within the stability region of the CDI phase, even for a relatively small R_1^+ amplitude of 0.02 Å. In contrast, for $R = Pr$, the values are outside the CDI phase even for R_1^+ amplitudes larger than the one experimentally observed. Thus, at their respective experimental breathing mode amplitudes, our calculations predict a paramagnetic CDI state for $LuNiO_3$ but not for $PrNiO_3$.

Lattice energetics

Up to now, we have been addressing the stability of the CDI phase for a given (fixed) R_1^+ amplitude. Now, we will address the stability of the R_1^+ mode itself and calculate its amplitude across the series

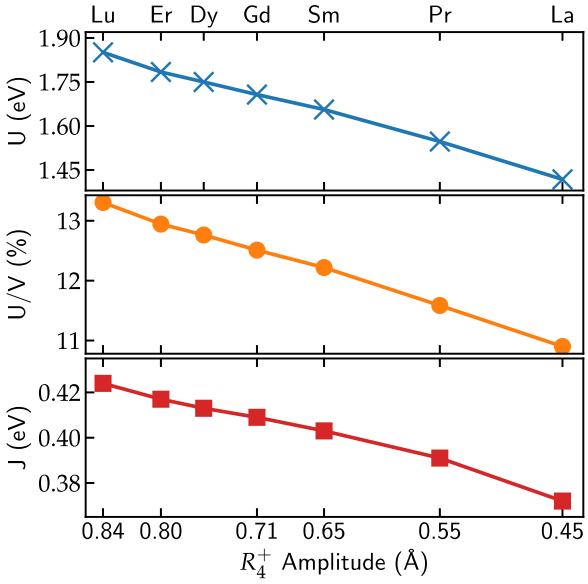

Fig. 3 Screened onsite Hubbard–Kanamori interaction parameters *U* (top) and *J* (bottom) for the e_g orbitals within our low-energy subspace across the nickelate series as a function of the octahedral tilt amplitude R_4^+. Additionally, the ratio between *U* and the corresponding bare (unscreened) interaction parameter *V* is shown (middle)

using total energy calculations within CSC DFT + DMFT. The symmetry-based mode decomposition allows us to systematically vary only the R_1^+ mode, while keeping all other structural parameters fixed to the values obtained from the nonmagnetic DFT calculations. Thus, in contrast to interpolation procedures as in refs. [25,27], our approach excludes any additional energy contributions related to simultaneous changes in other structural distortions, in particular the octahedral tilt modes.

Figure 4 shows the total energy and the spectral weight around the Fermi level, $\bar{A}(\omega = 0)$, as a function of the R_1^+ amplitude for $LuNiO_3$, calculated using different values for (*U*, *J*). First, we focus on the results obtained using our cRPA calculated values ($J = 0.42$ eV, $U = 1.85$ eV, orange crosses). It can be seen, that the energy indeed exhibits a minimum for an R_1^+ amplitude very close to the experimental value. Furthermore, as seen from $\bar{A}(\omega = 0)$, the system undergoes a MIT for increasing R_1^+ amplitude and is clearly insulating in the region around the energy minimum. Thus, our CSC DFT + DMFT calculations together with the calculated

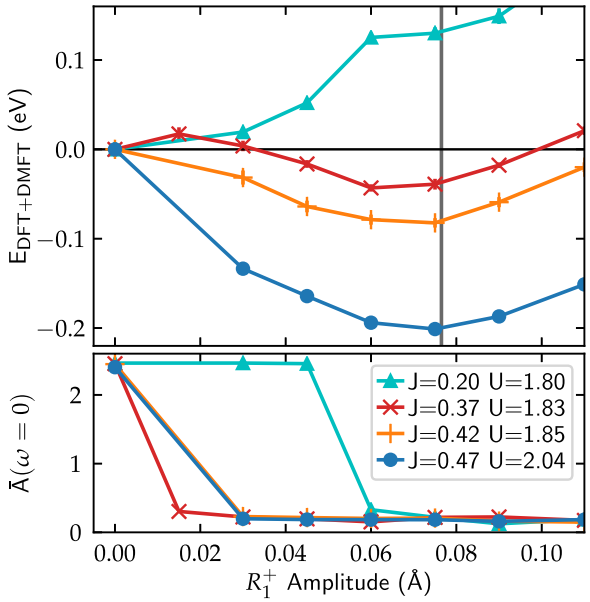

Fig. 4 Top: Total energy, $E_{DFT+DMFT}$, as a function of the R_1^+ breathing mode amplitude for $LuNiO_3$ using different values for the interaction parameters U and J. The experimental amplitude ($R_1^+ = 0.075$ Å[18]) is marked by the gray vertical line. Bottom: corresponding spectral weight at the Fermi level, indicating the MIT as a function of R_1^+ amplitude

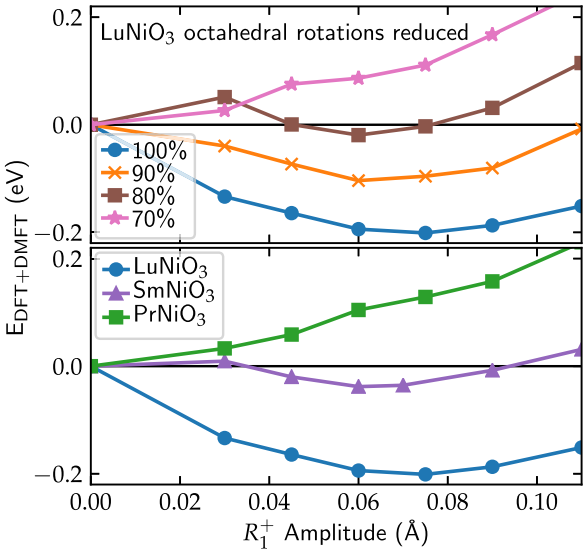

Fig. 5 Top: Total energy as a function of the R_1^+ breathing mode amplitude for $LuNiO_3$ with octahedral rotation amplitudes reduced to 90, 80, and 70% (for $U = 2.04$ eV and $J = 0.47$ eV). Bottom: corresponding data for various materials across the nickelate series. Here, (U, J) values are increased by 10% compared to the results of the cRPA calculations ($U = 2.04$ eV/$J = 0.47$ eV for $LuNiO_3$, $U = 1.82$ eV/$J = 0.44$ eV for $SmNiO_3$, and $U = 1.70$ eV/$J = 0.43$ eV for $PrNiO_3$)

cRPA interaction parameters correctly predict the CDI ground state for $LuNiO_3$, and furthermore result in a breathing mode amplitude that is in excellent agreement with experimental data.

To see how subtle changes in (U, J) influence the energetics of the system, we also perform calculations using the cRPA values obtained in ref. [38] ($J = 0.37$ eV, $U = 1.83$ eV, red diagonal crosses). In this case, we obtain a more shallow energy minimum at a slightly reduced amplitude of $R_1^+ = 0.06$ Å. This reduction is mainly caused by the slightly smaller J. Moving the values of (U, J) even closer to the boundary of the stability region of the CDI phase for the experimental R_1^+ amplitude, *cf.* Figure 2 (e.g., $J = 0.2$ eV, $U = 1.8$ eV, cyan triangles) results in a loss of the energy minimum for finite R_1^+ amplitude. Nevertheless, a kink in the total energy is clearly visible at the R_1^+ amplitude for which the system becomes insulating, indicating the strong coupling between the structural distortion and the MIT. A similar kink can also be recognized (for rather small R_1^+ amplitude) in the total energy obtained for $J = 0.37$ eV and $U = 1.83$ eV, resulting in an additional local energy minimum at $R_1^+ = 0$, a typical hallmark of a first order structural transition. In addition, we also perform calculations where (U, J) are increased by 10% compared to our cRPA values ($J = 0.47$ eV, $U = 2.04$ eV, red circles), which leads to a deeper energy minimum and an R_1^+ amplitude in near perfect agreement with experiment.

Next, we investigate the influence of the octahedral rotations on the energetics of the R_1^+ mode, where we perform a series of calculations for $LuNiO_3$ with artificially decreased octahedral rotations (see Methods section), fixed (U, J), and fixed volume. As can be seen from the data shown in the top panel of Fig. 5, decreasing the amplitude of the octahedral rotations to 70%, which corresponds roughly to the amplitudes found for $PrNiO_3$, leads to a vanishing of the minimum at nonzero R_1^+ amplitude. This confirms that the reduction of the octahedral rotation amplitudes plays a crucial role in the energetics of the breathing mode distortion and in determining the trend across the nickelate series.

Finally, we examine how the energetics of the R_1^+ mode varies across the series, by comparing the two end members $LuNiO_3$ and $PrNiO_3$, as well as $SmNiO_3$, which is the compound with the largest R cation in the series that still exhibits a paramagnetic CDI state. In each case we use (U, J) values that are increased by 10% relative to the corresponding cRPA values. The use of such slightly increased interaction parameters is motivated by the observation that the U values obtained from the static limit of the (frequency-dependent) screened cRPA interaction are often too small to reproduce experimental data for various materials.[31,39–41] The results are depicted in Fig. 5.

As discussed above, for $LuNiO_3$ (blue circles), we obtain an energy minimum exactly at the experimentally observed amplitude. For $SmNiO_3$ (purple triangles), we obtain a much more shallow minimum at $R_1^+ = 0.06$ Å, which corresponds to a reduction by ≈20% compared to $LuNiO_3$. Unfortunately, structural refinements for $SmNiO_3$ are only available within the *Pbnm* space group, and thus no information on the R_1^+ amplitude exists.[42] However, the reduction of the R_1^+ amplitude from R = Lu to R = Sm is much more pronounced compared to previous DFT + U calculations with AFM order,[30] where the reduction is only about 8%.

For $PrNiO_3$ (green squares), no stable R_1^+ amplitude is obtained within our paramagnetic DFT + DMFT calculations, but a kink marking the MIT is still visible at $R_1^+ = 0.06$ Å. This is also in agreement with the experimental observation that no paramagnetic CDI phase occurs in $PrNiO_3$.[9] Furthermore, it was recently demonstrated using DFT + DMFT calculations that for $NdNiO_3$ the CDI state becomes only favorable in the antiferromagnetically ordered state.[27] Our results indicate that this also holds for $PrNiO_3$, while in $SmNiO_3$ a stable R_1^+ amplitude can be found even in the paramagnetic case. Thus, the phase boundaries across the series are correctly described within the DFT + DMFT approach. We further note that, considering the (U, J) phase diagrams for $PrNiO_3$ in Fig. 2, a U of up to 2.5 or even 3 eV would be required to put $PrNiO_3$ well within the CDI phase region at its experimental R_1^+ amplitude, which appears necessary to obtain a stable R_1^+

amplitude. However, such a large U seems highly unrealistic considering the calculated cRPA values.

DISCUSSION

In summary, the successful application of CSC DFT + DMFT and symmetry-based mode analysis, without ad hoc assumptions regarding the strength of the Hubbard interaction or fixing structural parameters to experimental data, allows to elucidate the nature of the coupled electronic–structural transition across the nickelate series. Our analysis reveals that the MIT, which is related to an electronic instability towards spontaneous charge disproportionation, leads to a significant restructuring of the energy landscape, indicated by a kink in the calculated total energy. This creates a minimum at a finite R_1^+ amplitude (for appropriate U and J), and suggests a first order character of the coupled structural and electronic transition in the PM case, in agreement with experimental observations[11] for both $SmNiO_3$[43] and $YNiO_3$.[15] We note that, since a certain critical value of R_1^+ is necessary to induce the MIT (see, e.g., Fig. 4), a second order structural transition would imply the existence of an intermediate structurally distorted metallic phase, inconsistent with experimental observations.

The strength of the electronic instability towards spontaneous charge disproportionation and thus the stability range of the CDI phase, is strongly affected by the amplitude of the octahedral rotations, varying across the series. This is in agreement with ref. [28], but in addition we show that to arrive at a fully coherent picture, with correct phase boundaries, it is crucial to treat both electronic and structural degrees of freedom on equal footing. For example, even though a CDI state can be obtained for $PrNiO_3$ for fixed R_1^+ amplitude >0.06 Å, our calculations show that this is indeed energetically unstable. In addition, the octahedral rotations also influence the screening of the effective interaction parameters, disfavoring the CDI state for larger R cations. As a result, magnetic order appears to be crucial to stabilize the breathing mode distortion for both R = Nd and Pr.

Moreover, our calculations not only lead to a coherent picture of the MIT, but also allow to obtain accurate structural parameters across the nickelate series. Furthermore, this is achieved using only a minimal correlated subspace. We note that the use of such a reduced correlated subspace can be advantageous, since it not only allows to reduce the computational effort (due to less degrees of freedom), but also because the double-counting problem is typically less severe if the O-p dominated bands are not included in the energy window of the correlated subspace.[44,45] In the present case, the resulting more extended Wannier functions, which also incorporate the hybridization with the surrounding ligands, also provide a rather intuitive picture of the underlying charge disproportionation.

Finally, our study represents the successful application of a combination of several state-of-the-art methods that allows to tackle other open issues related to the entanglement of structural and electronic properties in correlated materials, such as Jahn–Teller and Peierls instabilities, charge density wave, or polarons.

METHODS

DFT calculations

All DFT calculations are performed using the projector augmented wave (PAW) method[46] implemented in the "Vienna Ab initio Simulation Package" (VASP)[47–49] and the exchange correlation functional according to Perdew, Burke, and Ernzerhof.[50] For Ni, the 3p semicore states are included as valence electrons in the PAW potential. For the rare-earth atoms, we use PAW potentials corresponding to a 3+ valence state with f-electrons frozen into the core and, depending on the rare-earth cation, the corresponding 5p and 5s states are also included as valence electrons. A k-point mesh with $10 \times 10 \times 8$ grid points along the three reciprocal lattice directions is used and a plane wave energy cut-off of 550 eV is chosen for the 20 atom $Pbnm$ unit cell. All structures are fully relaxed, both internal parameters and lattice parameters, until the forces acting on all atoms are smaller than 10^{-4} eV/Å. As in ref. [30], we perform calculations for $LaNiO_3$ within the $Pbnm$ and $P2_1/n$ space groups, to allow for a more consistent comparison with the rest of the series, even though $LaNiO_3$ is experimentally found in a different space group ($R\bar{3}c$). See also the discussion in ref. [22].

Distortion mode analysis

For the symmetry-based mode decomposition[33] we use the software ISODISTORT.[51] Thereby, the atomic positions within a distorted low-symmetry crystal structure, $\vec{r}_i^{\,\mathrm{dist}}$, are written in terms of the positions in a corresponding non-distorted high-symmetry reference structure, $\vec{r}_i^{\,0}$, plus a certain number of independent distortion modes, described by orthonormal displacement vectors, $\vec{d}_{im}$, and corresponding amplitudes, A_m:

$$\vec{r}_i^{\,\mathrm{dist}} = \vec{r}_i^{\,0} + \sum_m A_m \vec{d}_{im}. \tag{1}$$

The distortion modes of main interest here are the out-of-phase and in-phase tilts of the oxygen octahedra, R_4^+ and M_3^+, for characterization of the high-temperature $Pbnm$ structure, and the R_1^+ breathing mode distortion within the low-temperature $P2_1/n$ structure. A more detailed description for nickelates can be found, e.g., in refs. [19,30]. For the calculations with reduced octahedral rotation amplitudes shown in Fig. 5, both R_4^+ and M_3^+ modes, as well as the X_5^+ mode intimately coupled to these two modes, have been reduced by a common factor.

DMFT calculations

The Wannier functions for our CSC DFT + DMFT calculations are constructed via projections on local Ni e_g orbitals as described in ref. [52,53], using the TRIQS/DFTTools software package.[54,55] The effective impurity problems within the DMFT loop are solved with the TRIQS/cthyb continuous-time hybridization-expansion solver,[56] including all off-diagonal spin-flip and pair-hopping terms of the interacting Hubbard–Kanamori Hamiltonian.[57] The LB and SB Ni sites are treated as two separate impurity problems (even for zero R_1^+ amplitude), where the number of electrons per two Ni sites is fixed to 2, but the occupation of each individual Ni site can vary during the calculation (while the solution is constrained to remain paramagnetic).

The fully localized limit[58] is used to correct for the double-counting (DC) in the parametrization given in ref. [59]:

$$\Sigma_{dc,\alpha}^{imp} = \overline{U}\left(n_\alpha - \frac{1}{2}\right), \tag{2}$$

where n_α is the occupation of Ni site α, obtained in the DMFT loop, and the averaged Coulomb interaction is defined as $\overline{U} = (3U - 5J)/3$. Note, that in our Wannier basis the occupations change quite drastically from the original DFT occupations and the choice of the DC flavor can therefore influence the outcome. However, with respect to the lattice energetics we found no difference in the physics of the system when changing the DC scheme or using fixed DFT occupation numbers for the calculation of the DC correction. If the DFT occupations are used instead of the DMFT occupations, larger interaction parameters are required to obtain the same predicted R_1^+ amplitude. However, we note that the DFT occupations have no clear physical meaning within CSC DFT + DMFT.

The spectral weight around the Fermi level, $\overline{A}(\omega = 0)$, is obtained from the imaginary time Green's function[60]:

$$\overline{A}(\omega = 0) = -\frac{\beta}{\pi} G_{\mathrm{imp}}\left(\frac{\beta}{2}\right). \tag{3}$$

For $T = 0$ ($\beta \to \infty$), $\overline{A}$ is identical to the spectral function at $\omega = 0$. For finite temperatures, it represents a weighted average around $\omega = 0$ with a width of $\sim k_B T$[60].

The total energy is calculated as described in ref. [31]:

$$\begin{aligned} E_{\mathrm{DFT+DMFT}} = {} & E_{\mathrm{DFT}}[\rho] \\ & - \tfrac{1}{N_k} \sum_{\lambda,\vec{k}} \varepsilon_{\lambda,\vec{k}}^{\mathrm{KS}} f_{\lambda\vec{k}} + \langle H_{\mathrm{KS}} \rangle_{\mathrm{DMFT}} \\ & + \langle H_{\mathrm{int}} \rangle_{\mathrm{DMFT}} - E_{\mathrm{DC}}^{imp}. \end{aligned} \tag{4}$$

The first term is the DFT total energy, the second term subtracts the band energy of the Ni-e_g dominated bands (index λ), the third term evaluates the kinetic energy within the correlated subspace via the lattice

Green's function, the fourth term adds the interaction energy, where we use the Galitskii–Migdal formula,[61,62] and the last term subtracts the DC energy. To ensure good accuracy of the total energy, we represent both G_{imp} and Σ_{imp} in the Legendre basis[63] and obtain thus smooth high-frequency tails and consistent Hartree shifts. Moreover, we sample the total energy over a minimum of additional 60 converged DMFT iterations after the CSC DFT + DMFT loop is converged. Convergence is reached when the standard error of the Ni site occupation of the last 10 DFT + DMFT loops is smaller than 1.5×10^{-3}. That way we achieve an accuracy in the total energy of <5 meV. All DMFT calculation are performed for $\beta = 40\,\mathrm{eV}^{-1}$, which corresponds to a temperature of 290 K.

cRPA calculations

We use the cRPA method as implemented in the VASP code[64] to extract interaction parameters for our correlated subspace. These calculations are done for the relaxed *Pbnm* structures.[30] We follow the ideas given in the paper of ref. [26] and construct maximally localized Wannier functions (MLWFs) for the Ni-e_g dominated bands around the Fermi level using the wannier90 package.[65] Since the corresponding bands are isolated from other bands at higher and lower energies, no disentanglement procedure is needed, except for $LaNiO_3$, for which we ensured that the resulting Wannier functions are well converged and have a very similar spread as for all other compounds of the series.

We divide the total polarization, P, into a contribution involving only transitions within the effective "e_g" correlated subspace and the rest, $P = P_{e_g} + P_r$. The constrained polarization, P_r, and the static limit of the screened interaction matrix, $W_r(\omega = 0) = V[1 - VP_r(\omega = 0)]^{-1}$, where V is the bare interaction, are then calculated using a $5 \times 5 \times 3$ k-point mesh, a plane wave energy cut-off of $E_{cut} = 600$ eV, and 576 bands. Effective values for the Hubbard–Kanamori interaction parameters (U, J) are extracted from $W_r(\omega = 0)$ as described in ref. [57]. Our procedure is analogous to the calculation of effective interaction parameters for $LuNiO_3$ in ref. [38].

It should be noted that the MLWFs used for the cRPA calculations are not completely identical to the projected Wannier functions used as basis for the correlated subspace within our DMFT calculations. However, test calculations for the case of $LuNiO_3$ showed only minor differences between the hopping parameters corresponding to the MLWFs and the ones corresponding to the Wannier functions generated by the projection scheme implemented in VASP. Furthermore, we did not find a noticeable difference between the screened (U, J) values calculated for the MLWFs and the ones calculated for the initial guesses for these Wannier functions, i.e., before the spread minimization, which are also defined from orthogonalized projections on atomic-like orbitals. We thus conclude that the two sets of Wannier functions are indeed very similar, and that the cRPA values of (U, J) obtained for the MLWFs are also representative for the Wannier basis used in our DMFT calculations.

Additionally, we point out that, in contrast to what was found in ref. [38], we observe only negligible differences in the interaction parameters obtained for the relaxed *Pbnm* structure and the ones obtained for the experimental low-temperature $P2_1/n$ structure for $LuNiO_3$ (1.827 eV and 1.876 eV compared to 1.849 eV within *Pbnm*). In particular, the difference of the interaction parameters on the two inequivalent Ni sites in the $P2_1/n$ structure (±0.03 eV) are very small compared to the changes stemming from different degrees of octahedral rotations (i.e., different R cations), justifying the use of constant interaction parameters for different R_1^+ amplitudes. Furthermore, the differences in the intra-orbital U matrix elements between the d_{z^2} and the $d_{x^2-y^2}$ orbitals are negligible small, ~0.01 eV, in our calculations. Therefore, all the values of the interaction parameters are averaged over both e_g orbitals.

DATA AVAILABILITY

The data that support the findings of this study are available from the corresponding author upon reasonable request.

ACKNOWLEDGEMENTS

We are indebted to Oleg Peil and Antoine Georges for helpful discussions. This work was supported by ETH Zurich and the Swiss National Science Foundation through grant No. 200021-143265 and through NCCR-MARVEL. Calculations have been performed on the clusters "Mönch" and "Piz Daint", both hosted by the Swiss National Supercomputing Centre, and the "Euler" cluster of ETH Zurich.

AUTHOR CONTRIBUTIONS

A.H. performed and analyzed all DFT and DMFT calculations. The cRPA calculations were done by A.H. with the help of P.L. and supervised by C.F. The whole project was initiated by C.E. The initial manuscript was written by A.H. and C.E. All authors discussed the results at different stages of the work and contributed to the final manuscript.

ADDITIONAL INFORMATION

Competing interests: The authors declare no competing interests.

Publisher's note: Springer Nature remains neutral with regard to jurisdictional claims in published maps and institutional affiliations.

REFERENCES

1. Khomskii, D. Trend: classifying multiferroics: mechanisms and effects. *Physics* **2**, 20 (2009).
2. Stewart, G. R. Non-fermi-liquid behavior in *d*- and *f*-electron metals. *Rev. Mod. Phys.* **73**, 797–855 (2001).
3. Dagotto, E. Correlated electrons in high-temperature superconductors. *Rev. Mod. Phys.* **66**, 763–840 (1994).
4. Imada, M., Fujimori, A. & Tokura, Y. Metal-insulator transitions. *Rev. Mod. Phys.* **70**, 1039–1263 (1998).
5. Heber, J. Enter the oxides. *Nature* **459**, 28–30 (2009).
6. Takagi, H. & Hwang, H. Y. An emergent change of phase for electronics. *Science* **327**, 1601–1602 (2010).
7. Zhou, Y. & Ramanathan, S. Correlated electron materials and field effect transistors for logic: a review. *Crit. Rev. Solid State Mater. Sci.* **38**, 286–317 (2013).
8. Dagotto, E. & Tokura, Y. Strongly correlated electronic materials: present and future. *Mater. Res. Soc. Bull.* **33**, 1037–1045 (2008).
9. Medarde, M. L. Structural, magnetic and electronic properties of perovskites (R = rare earth). *J. Phys.: Condens. Matter* **9**, 1679–1707 (1997).
10. Catalan, G. Progress in perovskite nickelate research. *Phase Transit.* **81**, 729–749 (2008).
11. Catalano, S. et al. Rare-earth nickelates $RNiO_3$: thin films and heterostructures. *Rep. Progress. Phys.* **81**, 046501 (2018).
12. He, Z. & Millis, A. J. Strain control of electronic phase in rare-earth nickelates. *Phys. Rev. B* **91**, 195138 (2015).
13. Scherwitzl, R. et al. Electric-field control of the metal–insulator transition in ultrathin $NdNiO_3$ films. *Adv. Mater.* **22**, 5517–5520 (2010).
14. Middey, S. et al. Physics of ultrathin films and heterostructures of rare-earth nickelates. *Annu. Rev. Mater. Res.* **46**, 305–334 (2016).
15. Alonso, J. A. et al. Charge disproportionation in $RNiO_3$ perovskites: simultaneous metal–insulator andstructural transition in $YNiO_3$. *Phys. Rev. Lett.* **82**, 3871–3874 (1999).
16. Alonso, J. A., Martnez-Lope, M. J., Casais, M. T., Aranda, M. A. G. & Fernández-Daz, M. T. Metal–insulator transitions, structural and microstructural evolution of $RNiO_3$ (R = Sm, Eu, Gd, Dy, Ho, Y) perovskites: evidence for room-temperature charge disproportionation in monoclinic $HoNiO_3$ and $YNiO_3$. *J. Am. Chem. Soc.* **121**, 4754–4762 (1999).
17. Alonso, J. A., Martnez-Lope, M. J., Casais, M. T., Garca-Muñoz, J. L. & Fernández-Daz, M. T. Room-temperature monoclinic distortion due to charge disproportionation in $RNiO_3$ perovskites with small rare-earth cations (R = Ho, Y, Er, Tm, Yb, and Lu): a neutron diffraction study. *Phys. Rev. B* **61**, 1756–1763 (2000).
18. Alonso, J. A. et al. High-temperature structural evolution of $RNiO_3$ (R = Ho, Y, Er, Lu) perovskites: charge disproportionation and electronic localization. *Phys. Rev. B* **64**, 094102 (2001).
19. Balachandran, P. V. & Rondinelli, J. M. Interplay of octahedral rotations and breathing distortions in charge-ordering perovskite oxides. *Phys. Rev. B* **88**, 054101 (2013).
20. Garca-Muñoz, J. L., Rodrguez-Carvajal, J. & Lacorre, P. Sudden appearance of an unusual spin density wave at the metal-insulator transition in the perovskites $RNiO_3$ (R = Pr, Nd). *Europhys. Lett.* **20**, 241–247 (1992).
21. Guo, H. et al. Antiferromagnetic correlations in the metallic strongly correlated transition metal oxide $LaNiO_3$. *Nat. Commun.* **9**, 43 (2018).
22. Subedi, A. Breathing distortions in the metallic, antiferromagnetic phase of $LaNiO_3$. *ArXiv e-prints* (2017).
23. Park, H., Millis, A. J. & Marianetti, C. A. Site-selective mott transition in rare-earth-element nickelates. *Phys. Rev. Lett.* **109**, 156402 (2012).
24. Park, H., Millis, A. J. & Marianetti, C. A. Total energy calculations using DFT + DMFT: computing the pressure phase diagram of the rare earth nickelates. *Phys. Rev. B* **89**, 245133 (2014).

25. Park, H., Millis, A. J. & Marianetti, C. A. Computing total energies in complex materials using charge self-consistent DFT + DMFT. *Phys. Rev. B* **90**, 235103 (2014).
26. Subedi, A., Peil, O. E. & Georges, A. Low-energy description of the metal–insulator transition in the rare-earth nickelates. *Phys. Rev. B* **91**, 075128–16 (2015).
27. Haule, K. & Pascut, G. L. Mott transition and magnetism in rare earth nickelates and its fingerprint on the X-ray scattering. *Sci. Rep.* **7**, 10375 (2017).
28. Mercy, A., Bieder, J., Íñiguez, J. & Ghosez, P. Structurally triggered metal-insulator transition in rare-earth nickelates. *Nat. Commun.* **8**, 1677 (2017).
29. Varignon, J., Grisolia, M. N., Íñiguez, J., Barthélémy, A. & Bibes, M. Complete phase diagram of rare-earth nickelates from first-principles. *Nat. Partner J. Quantum Mater.* **2**, 1–8 (2017).
30. Hampel, A. & Ederer, C. Interplay between breathing mode distortion and magnetic order in rare-earth nickelates $R\mathrm{NiO_3}$ within DFT + *U*. *Phys. Rev. B* **96**, 165130 (2017).
31. Lechermann, F. et al. Dynamical mean-field theory using wannier functions: a flexible route to electronic structure calculations of strongly correlated materials. *Phys. Rev. B* **74**, 125120 (2006).
32. Aryasetiawan, F. et al. Frequency-dependent local interactions and low-energy effective models from electronic structure calculations. *Phys. Rev. B* **70**, 195104 (2004).
33. Perez-Mato, J. M., Orobengoa, D. & Aroyo, M. I. Mode crystallography of distorted structures. *Acta Crystallogr. A* **66**, 558–590 (2010).
34. Pourovskii, L. V., Amadon, B., Biermann, S. & Georges, A. Self-consistency over the charge density in dynamical mean-field theory: a linear muffin-tin implementation and some physical implications. *Phys. Rev. B* **76**, 235101 (2007).
35. Mazin, I. I. et al. Charge ordering as alternative to Jahn–Teller distortion. *Phys. Rev. Lett.* **98**, 176406 (2007).
36. Johnston, S., Mukherjee, A., Elfimov, I., Berciu, M. & Sawatzky, G. A. Charge disproportionation without charge transfer in the rare-earth-element nickelates as a possible mechanism for the metal–insulator transition. *Phys. Rev. Lett.* **112**, 106404 (2014).
37. Mandal, B. et al. The driving force for charge ordering in rare earth nickelates. *ArXiv e-prints* (2017).
38. Seth, P. et al. Renormalization of effective interactions in a negative charge transfer insulator. *Phys. Rev. B* **96**, 205139 (2017).
39. Casula, M. et al. Low-energy models for correlated materials: bandwidth renormalization from coulombic screening. *Phys. Rev. Lett.* **109**, 126408 (2012).
40. Anisimov, V. I. et al. Coulomb repulsion and correlation strength in LaFeAsO from density functional and dynamical mean-field theories. *J. Phys.* **21**, 075602 (2009).
41. van Roekeghem, A. et al. Dynamical correlations and screened exchange on the experimental bench: spectral properties of the cobalt pnictide $\mathrm{BaCo_2As_2}$. *Phys. Rev. Lett.* **113**, 266403 (2014).
42. Rodrguez-Carvajal, J. et al. Neutron-diffraction study of the magnetic and orbital ordering in $^{154}\mathrm{SmNiO_3}$ and $^{153}\mathrm{EuNiO_3}$. *Phys. Rev. B* **57**, 456–464 (1998).
43. Pérez-Cacho, J., Blasco, J., Garca, J., Castro, M. & Stankiewicz, J. Study of the phase transitions in $\mathrm{SmNiO_3}$. *J. Phys.* **11**, 405 (1999).
44. Janson, O. & Held, K. Finite-temperature phase diagram of (111) nickelate bilayers. *Phys. Rev. B* **98**, 115118 (2018).
45. Karolak, M. et al. Double counting in LDA + DMFT - the example of NiO. *J. Electron Spectrosc. Relat. Phenom.* **181**, 11–15 (2010).Proceedings of International Workshop on Strong Correlations and Angle-Resolved Photoemission Spectroscopy 2009.
46. Blöchl, P. E. Projector augmented-wave method. *Phys. Rev. B* **50**, 17953–17979 (1994).
47. Kresse, G. & Hafner, J. Ab initio molecular dynamics for liquid metals. *Phys. Rev. B* **47**, 558–561 (1993).
48. Kresse, G. & Furthmüller, J. Efficient iterative schemes for ab initio total-energy calculations using a plane-wave basis set. *Phys. Rev. B* **54**, 11169–11186 (1996).
49. Kresse, G. & Joubert, D. From ultrasoft pseudopotentials to the projector augmented-wave method. *Phys. Rev. B* **59**, 1758–1775 (1999).
50. Perdew, J. P., Burke, K. & Ernzerhof, M. Generalized gradient approximation made simple. *Phys. Rev. Lett.* **77**, 3865–3868 (1996).
51. Campbell, B. J., Stokes, H. T., Tanner, D. E. & Hatch, D. M. ISODISPLACE: a web-based tool for exploring structural distortions. *J. Appl. Crystallogr.* **39**, 607–614 (2006).
52. Schüler, M. et al. Charge self-consistent many-body corrections using optimized projected localized orbitals. *J. Phys.* **30**, 475901 (2018).
53. Amadon, B. et al. Plane-wave based electronic structure calculations for correlated materials using dynamical mean-field theory and projected local orbitals. *Phys. Rev. B* **77**, 205112 (2008).
54. Aichhorn, M. et al. TRIQS/DFTTools: a TRIQS application for ab initio calculations of correlated materials. *Comput. Phys. Commun.* **204**, 200–208 (2016).
55. Parcollet, O. et al. TRIQS: a toolbox for research on interacting quantum systems. *Comput. Phys. Commun.* **196**, 398–415 (2015).
56. Seth, P., Krivenko, I., Ferrero, M. & Parcollet, O. TRIQS/CTHYB: a continuous-time quantum monte carlo hybridisation expansion solver for quantum impurity problems. *Comput. Phys. Commun.* **200**, 274–284 (2016).
57. Vaugier, L., Jiang, H. & Biermann, S. Hubbard *U* and hund exchange *J* in transition metal oxides: Screening versus localization trends from constrained random phase approximation. *Phys. Rev. B* **86**, 165105 (2012).
58. Anisimov, V. I., Aryasetiawan, F. & Lichtenstein, A. I. First-principles calculations of the electronic structure and spectra of strongly correlated systems: the LDA + U method. *J. Phys.* **9**, 767 (1997).
59. Held, K. Electronic structure calculations using dynamical mean field theory. *Adv. Phys.* **56**, 829–926 (2007).
60. Fuchs, S., Gull, E., Troyer, M., Jarrell, M. & Pruschke, T. Spectral properties of the three-dimensional hubbard model. *Phys. Rev. B* **83**, 235113 (2011).
61. Abrikosov, A. A., Gorkov, L. P., Dzyaloshinski, I. E. & Silverman, R. A. *Methods of Quantum Field Theory in Statistical Physics*. *Dover Books on Physics* (Dover Publications, New York, 2012).
62. Galitskii, V. M. & Migdal, A. B. Application of quantum field theory methods to the many body problem. *Soviet Phys. J. Exp. Theor. Phys.* **7**, 96–104 (1958).
63. Boehnke, L., Hafermann, H., Ferrero, M., Lechermann, F. & Parcollet, O. Orthogonal polynomial representation of imaginary-time green's functions. *Phys. Rev. B* **84**, 075145 (2011).
64. Kaltak, M. *Merging GW with DMFT*. Ph.D. thesis, University of Vienna. http://othes.univie.ac.at/38099/ (2015).
65. Mostofi, A. A. et al. wannier90: a tool for obtaining maximally-localised Wannier functions. *Comput. Phys. Commun.* **178**, 685–699 (2008).
66. Medarde, M. L., Fernández-Daz, M. T. & Lacorre, P. Long-range charge order in the low-temperature insulating phase of $\mathrm{PrNiO_3}$. *Phys. Rev. B* **78**, 212101 (2008).

6

MECHANISM AND CONTROL PARAMETERS OF THE COUPLED TRANSITION

In this chapter I build a simplified model Hamiltonian, which elucidates the mechanism of the coupled electronic-structural MIT found in rare-earth nickelates. The work presented in this chapter is a collaboration with Oleg E. Peil, and Antoine Georges. Oleg E. Peil had the idea of the model description, which we discussed on from an early stage. Moreover, I supported the project by performing DFT+DMFT calculations of nickelate compounds to verify the model.

The following work was published as *"Mechanism and Control Parameters of the Coupled Structural and Metal-Insulator Transition in Nickelates"* in Physical Review B, see Ref. [51]. Copyright (2019) by the American Physical Society. The calculations for the model Hamiltonian were performed by Oleg E. Peil, as well as the construction of the Landau Theory. I performed the DFT+DMFT calculations, as well as the extraction of the parameters g and K from DFT.

6.1 MOTIVATION

In the last chapter I showed that an electronic instability is responsible for triggering the CDI state and furthermore, allows for a stable breathing mode distortion amplitude. Moreover, I demonstrated that by changing the octahedral rotation amplitude the tendency to the electronic instability is controlled. Eventually, leading to a loss of a stable finite breathing mode amplitude for $PrNiO_3$. In this chapter I use this empirical findings to build a simplified model Hamiltonian, which elucidates the exact electronic mechanism triggering the CDI state. Furthermore I identify the control parameters driving the transition, allowing to understand how certain structural changes, e.g. octahedral rotations, strain, or the breathing mode distortion affect the system. Moreover, this model Hamiltonian allows to determine the equilibrium R_1^+ amplitude without calculating the total energy. Finally, this leads to the formulation of a Landau theory, describing the paramagnetic coupled transition.

Since the joint publication [51] is presented in a rather compact format, I first give a more detailed introduction in the proposed model Hamiltonian. This is followed by a more detailed description on the realistic DFT+DMFT calculations which I performed. Moreover, I show how the parameters of the model can be extracted from DFT.

6.2 MODEL DESCRIPTION OF RARE-EARTH NICKELATES

We proposed a model Hamiltonian describing the nickelate series, only keeping the key low-energy degrees of freedom to produce the main features of the coupled electronic-structural transition. It consists of three parts, a purely electronic part, describing the hopping of electrons and the local Coulomb interaction, a lattice part describing the stiffness with respect to the breathing mode distortion, and importantly the electron-lattice coupling. The resulting Hamiltonian has the following form:

$$\hat{H} = \hat{H}_{\text{band}} + \hat{H}_{\text{int}} + \hat{H}_{\text{latt}}[Q] + \hat{H}_{\text{e-l}}[Q] \quad . \tag{130}$$

Here, I label the breathing mode distortion amplitude as Q instead of R_1^+ to be in line with the notation used in the corresponding paper Ref. [51].

We assume that the hoppings and the Coulomb interaction do not depend on Q. For the kinetic part, the band part, we construct a simplified tight-binding model with hopping amplitudes, t and t', limited to nearest and next-nearest neighbor sites:

$$\hat{H}_{\text{band}} = -\sum_{i,j,m,m',\sigma} t_{ij}^{mm'} c_{im\sigma}^{\dagger} c_{jm\sigma} \quad . \tag{131}$$

m corresponds to the two e_g orbitals, i, j indicate sites within a three dimensional cubic lattice, and σ is a spin index. The interaction term $\hat{H}_{\text{int}}$ is the Hubbard-Kanamori Hamiltonian, Eq. 52. The lattice response $\hat{H}_{\text{latt}}$ is described as:

$$\hat{H}_{\text{latt}}[Q] = \frac{K}{2} Q^2 \quad , \tag{132}$$

with K being the stiffness of the breathing mode distortion. The coupling between the breathing mode and the electronic degrees of freedom $\hat{H}_{\text{e-l}}$ is described as:

$$\hat{H}_{\text{e-l}}[Q] = \frac{1}{2} \sum_{m\sigma} \Delta_m^s[Q] \underbrace{\left[\sum_{i \in \text{SB}} \hat{n}_{im\sigma} - \sum_{i \in \text{LB}} \hat{n}_{im\sigma} \right]}_{\delta \hat{n}_m} \quad . \tag{133}$$

Here, we introduced $\Delta_m^s[Q]$, an on-site potential modulation due to the breathing mode distortion.

$\Delta_m^s[Q]$ can be obtained from DFT, and we find that it is linear in Q. This is shown for R =Lu, Sm, and Pr in Fig. 6 of Ref. [51]. Therefore, we expand Δ_m^s in Q and approximate it to be linear, introducing the electron-lattice coupling parameter g_m:

$$\Delta_m^s[Q] \approx g_m \, Q \quad . \tag{134}$$

Moreover, we neglect the orbital dependency m, because we observe in our DFT+DMFT calculations, that in the regime of $U - 3J \leqslant \Delta^s$ orbital polarization is greatly suppressed. Hence, $\hat{H}_{e\text{-}l}$ has the form:

$$\hat{H}_{e\text{-}l}[Q] = \frac{1}{2} g \, \delta\hat{n} \quad , \tag{135}$$

and the full model Hamiltonian becomes:

$$\hat{H} = \hat{H}_{band}[W] + \hat{H}_{int}[U, J] - \frac{1}{2} g \, \delta\hat{n} \, Q + \frac{K}{2} Q^2 \quad . \tag{136}$$

The band part depends on the bandwidth W, or the corresponding hopping amplitudes t, which have a one to one correspondence with the octahedral rotation strength (see Fig. 5 in Ref. [51]). The Coulomb interaction term depends on the interaction parameters U, and J. The last two terms, describing the electron-lattice coupling, and the breathing mode stiffness, are determined by the parameters g, and K.

Minimizing the total energy $E = \langle H \rangle$ with respect to Q, and using the Hellman-Feynman theorem gives:

$$\frac{2K}{g} \bar{Q} = \nu[\bar{Q}] \quad , \tag{137}$$

where $\nu[Q] = \langle \hat{n}_{LB} - \hat{n}_{SB} \rangle_Q$ is the average charge disproportionation for a given amplitude Q, and $\bar{Q}$ marks the equilibrium amplitude. This is the central equation allowing to determine the stable equilibrium breathing mode distortion by calculating $\nu[Q]$ curves, for a given set of parameters g and K, and finding intersection points of $\frac{2K}{g} Q$ and $\nu[Q]$.

The stability of the solution is determined by a renormalized stiffness:

$$\kappa = K - \frac{g^2}{2} \left(\frac{\partial \nu}{\partial \Delta^s} \right) \quad . \tag{138}$$

Therefore, for $\kappa < 0$ the breathing mode amplitude is unstable. At $Q = 0$, assuming no spontaneous charge disproportionation, we define the electronic susceptibility of the charge disproportionation with respect to the breathing mode distortion as:

$$\chi_e \equiv \left(\frac{\partial \nu}{\partial \Delta^s} \right)_{Q=0} \quad . \tag{139}$$

Hence, the stability of the high-temperature $Pbnm$ phase is controlled by the electronic response χ_e.

If the model captures the physics in rare-earth nickelates correctly, this allows to extract the stable equilibrium breathing mode amplitude also for realistic DFT+DMFT calculations. One can extract the parameters g, and K from DFT, and by calculating $\nu[Q]$ with DFT+DMFT, the stable breathing mode amplitude can be found from the intersection points. This has the advantage that one does not need to calculate total energies.

6.3 DFT+DMFT CALCULATIONS WITH INTER-SITE COULOMB INTERACTION

In Ref. [51], we perform OS DFT+DMFT calculations for the real material. The Wannier functions for the DMFT calculations are constructed via projections on local Ni e_g orbitals as described in chapter in 5. In order to mimic the effect of CSC, I included explicitly an inter-site interaction term in the Hamiltonian. Here, we follow the approach of Ref. [143] by including the inter-site interaction in Hartree approximation. Thus, the complete lattice Hamiltonian that serves as input for DMFT has the following form:

$$\hat{H} = \hat{H}^{C}_{kin} + \hat{H}_{int}[U, J] + \hat{H}_{V}. \tag{140}$$

where $\hat{H}_{kin}$ is obtained by DFT for various breathing mode distortion amplitudes Q, and $\hat{H}_V$ is the inter-site interaction. The inter-site interaction has the general form:

$$\hat{H}_V = \frac{1}{2}\sum_{i\neq j} V_{ij}\hat{n}_i\hat{n}_j \quad , \tag{141}$$

which is determined on a mean-field level as a Hartree potential shift in the DMFT self-energy. The shift depends on the relative occupation of the Ni_{LB} and Ni_{SB} sites, and can be thus defined as [143]:

$$\Sigma^{V}_{i} = z_{eff}V(n_j - n_i)/2 \quad . \tag{142}$$

Here, j designates the opposite sublattice relative to i, i.e. if $i = SB$ then $j = LB$ and vice versa. n_i is the e_g DMFT impurity occupancy of the corresponding site. z_{eff} denotes the effective lattice connectivity, which is obtained by summing all Ni site contribution to the inter-site interaction with the Madelung method. We set $z_{eff} \approx 1.747$ according to the value found in Ref. [143].

Since parts of both $\hat{H}_{int}$ and $\hat{H}_V$ are already taken into account on the DFT level, a DC correction must be included for both terms. For the calculations done here, I incorporate those contributions in the local self-energy Σ for each site i

$$\Sigma_i(i\omega_n) = \Sigma^{imp}_i - \Sigma^{imp}_{DC,i} + \Sigma^{V}_i - \Sigma^{V}_{DC,i} \quad . \tag{143}$$

The DC correction in Σ_i due to $\hat{H}_{int}$ is evaluated in the ANI parameterization for the e_g subspace as described in Eq. 123 with the DFT Wannier orbital occupations from DFT. Furthermore, the DC correction due to $\hat{H}_V$ is calculated as [143]:

$$\Sigma^{V}_{DC,i} = z_{eff}V(n^{DFT}_j - n^{DFT}_i)/2 \quad , \tag{144}$$

where n^{DFT}_i is the occupancy of the Wannier function in DFT. The energy correction due to the DC for the impurity part is thus:

$$E^{imp}_{DC,i} = \frac{\bar{U}}{2}n^{DFT}_i(n^{DFT}_i - 1) \, , \tag{145}$$

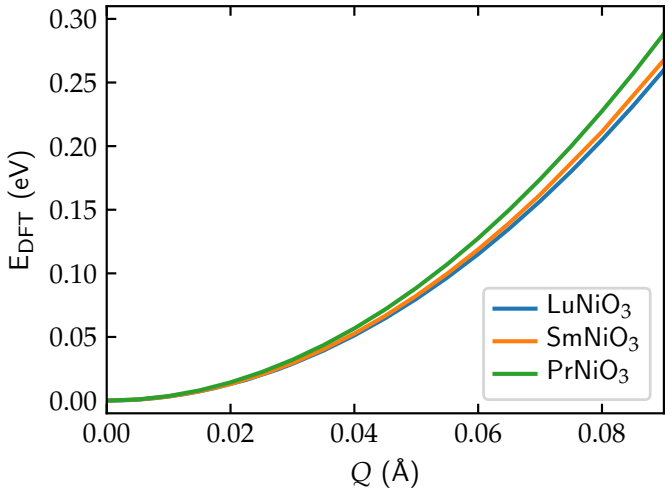

Figure 23: DFT total energies as functions of the breathing mode distortion amplitude Q for R =Lu, Sm, and Pr.

where $\bar{U}$ is the average Coulomb interaction (eq. 124). The energy contribution for the inter-site double-counting is per two Ni sites:

$$E^V_{DC} = \frac{1}{2}\left[\Sigma^V_{DC,LB} n_{LB} + \Sigma^V_{DC,SB} n_{SB}\right] \quad . \tag{146}$$

To better understand the effect of the DC correction on the energy one can rewrite the energy contributions of the DC terms using the fact that the sum over the two impurity occupations is constant ($n_{LB} + n_{SB} = 2$):

$$\begin{aligned} n_{LB} &= 1 + \frac{\nu}{2} \\ n_{SB} &= 1 - \frac{\nu}{2} \quad . \end{aligned} \tag{147}$$

Inserting this into the DC terms (145) and (146), the full DC contribution to the energy for 2 Ni sites reduces to

$$\begin{aligned} E_{DC} &= E^{imp}_{DC,LB} + E^{imp}_{DC,SB} + E^V_{DC} \\ &= \frac{\nu^2_{DFT}}{4}(\bar{U} - z_{eff} V) \quad . \end{aligned} \tag{148}$$

We then performed OS DFT+DMFT calculations for different members of the rare-earth nickelates with various breathing mode distortion amplitudes Q. In general, we find good qualitative agreement to the CSC DFT+DMFT calculations performed in Ref. [50].

6.4 DETERMINATION OF g AND K FROM DFT

To verify the model Hamiltonian, we extract the parameters g and K from DFT, to construct $2K/g \cdot Q$, which can be then compared with the $\nu[Q]$ curves from the DFT+DMFT calculations. The thereby found

stable equilibrium amplitudes can be compared with experiment and previous total energy results of DFT+DMFT [50].

We assume now that our DFT calculations represent the model in Eq. 136, if one sets the interaction parameters to zero in the model Hamiltonian, and subtracts interacting part already accounted for in DFT by subtracting the DC correction. Then, we perform calculations for R =Lu, Sm, and Pr for the Pbnm-relaxed nickelate structures as function of Q with DFT, from which the parameters g and K can be determined. To do so, we add on top of the relaxed Pbnm structures from DFT the R_1^+ breathing mode distortion. From these calculations, we obtain first the total energy, E_{DFT}, which is depicted in Fig. 23. Moreover, we can calculate $\nu_{DFT} \equiv \langle \delta n \rangle_{DFT}$ as function of Q by constructing Wannier functions for the e_g orbitals.

Next, we define λ as the charge-lattice response in DFT:

$$\nu_{DFT} = \lambda Q \quad , \tag{149}$$

which we calculate in Fig. 6 of Ref. [51]. From Fig. 23 it is observed that E_{DFT} appears to a good approximation quadratic in Q. Hence, we can perform a quadratic fitting to the DFT energy. Here, one needs to consider that DFT already accounts for certain interactions. Subtracting them via the DC correction Eq. 148 gives:

$$E_{DFT} - E_{DC} = \frac{c}{2} Q^2 \quad . \tag{150}$$

Next, one needs to connect the DFT parameters λ and c to the model parameters g and K. To do so, I can express the DFT energy (subtracting the DC correction) as expectation value of the model Hamiltonian with zero interaction strength

$$E_{DFT} - E_{DC} = \langle H_{band} \rangle - \frac{1}{2} g \, \nu_{DFT} \, Q + \frac{K}{2} Q^2 \quad , \tag{151}$$

where the expectation value of H_{band} depends implicitly on Q. To extract K, one takes the derivative with respect to Q:

$$\frac{\partial (E_{DFT} - E_{DC})}{\partial Q} = \left\langle \frac{\partial H}{\partial Q} \right\rangle = -\frac{1}{2} g \nu_{DFT} + KQ = cQ \tag{152}$$

and obtains K as:

$$K = c + \frac{1}{2} g \lambda \quad . \tag{153}$$

Finally, g needs to be extracted, which relates the energy level splitting between SB and LB sites Δ^s to Q:

$$\Delta^s = gQ \tag{154}$$

From the construction of the model Hamiltonian it is evident that Δ_s is the bare, without any interactions, level splitting between the

LB and SB site. Interaction effects are handled separately in $\hat{H}_{\text{int}}$. Therefore, one defines the DFT splitting as follows:

$$\Delta^{s}_{DFT} = \Delta^{s} + \Delta^{s}_{DC} + \Delta^{s}_{DC_V} \quad , \tag{155}$$

where Δ^{s}_{DC} is given by $\Sigma^{imp}_{DC,SB} - \Sigma^{imp}_{DC,LB}$, and $\Delta^{s}_{DC_V}$ is given by $\Sigma^{V}_{DC,SB} - \Sigma^{V}_{DC,LB}$. Using this, Eq. 155 can be now rewritten to extract the bare level splitting:

$$\Delta^{s} = g\ Q = \Delta^{s}_{DFT} - (z_{eff} V - \bar{U})\nu^{DFT} \quad , \tag{156}$$

which allows to determine g from DFT.

6.5 PROJECT SUMMARY

First, we perform DMFT calculations for the model Hamiltonian obtaining $\nu[Q]$ curves for various W,g, and K values. By finding intersection points with $2K/g \cdot Q$ we investigated solutions of Eq. 137. Thereby, we find a strong non-linear dependence of ν on Q, which is the key in determining the nature of the transition. We show that depending on g,K, and χ_e, there can be one, two, or three intersection points of $\nu[Q]$ with $2K/g \cdot Q$. By analyzing the stability criterion of the solutions we find coexistence of different $\bar{Q}$ values. This demonstrates that the nature of the coupled electronic-structural transition is of first order. Moreover, we find that the non-linear response occurs exactly while the system undergoes the MIT, similar to the findings of our work in Ref. [50], where the total energy curve shows a kink at the MIT. Additionally, we find a hysteresis for increasing and decreasing $\nu[Q]$ curves, due to the electronic transition itself.

From our model calculations we infer that the transition is controlled by the parameters g, K, and χ_e. We then extract these values from DFT and find that the ratio $2K/g$ is fairly constant across the nickelate series. Furthermore, we show that the renormalized stiffness κ, controlling the sensitivity to charge disproportionation at small Q, is dominated by the variation of χ_e across the series. χ_e extracted from DFT varies by almost a factor of two from R =Lu to Pr. Hence, we conclude that the transition is sensitively controlled by χ_e, which in turn is controlled by the bandwidth, respectively the octahedral rotations.

Next, we perform OS DFT+DMFT calculations for specific members of the series. Here, we find the same non-linear behavior of $\nu[Q]$ as in the model calculation. Moreover, we find a stable equilibrium breathing mode distortion, in quantitative agreement with experiment and CSC DFT+DMFT total energy calculations for $LuNiO_3$ and $SmNiO_3$. This verifies that the model incorporates the main ingredients determining the physics of the rare-earth nickelates series. For $PrNiO_3$ we find a stable breathing mode as well, in contrast to my

previous work [50]. However, $PrNiO_3$ seems to be very close to the transition, and here we used the same values U and J across the series. Using reduced U and J values for $PrNiO_3$, as obtained in our cRPA calculations, could lead to a destabilization of the breathing mode distortion, and thus agreement with the total energy calculation.

Finally, we rationalize these findings in a Landau theory involving the order parameters ν, and an additional parameter ϕ associated with the MIT. Both order parameters are then coupled as $\phi\nu^2$, which is the simplest coupling allowed by symmetry. From this Landau theory the non-linear behavior of $\nu[Q]$ is reproduced, showing the same features as the Model Hamiltonian. Furthermore, it is found that the coupling between electronic degrees and the structure $\phi\nu^2$ amplifies the charge disproportionation, critically determining the stability of a finite breathing mode amplitude.

6.6 CONCLUSION

In this chapter, we constructed a model Hamiltonian, which describes the coupled electronic-structural transition of rare-earth nickelates. We find a non-linear response of the charge disproportionation with respect to the breathing mode distortion, $\nu[Q]$, which leads to a coupled first-order transition within the model Hamiltonian in agreement with experiment. This shows, that only a explicit treatment of electronic and structural degrees of freedom on the same footing allows to correctly describe the coupled transition. Furthermore, we show that the trends across the nickelate series are driven by the susceptibility towards charge disproportionation, χ_e, which is sensitively controlled by the bandwidth.

We find that the constructed model agrees well with DFT+DMFT calculations performed for the nickelate series. This allows to extract the stable equilibrium breathing mode amplitude without calculating the total energy within DFT+DMFT. This is a severe advantage for practical calculations, since the calculation of total energies is numerically more demanding.

In the work of Mercy *et al.* [49] the mechanism of the MIT has also been investigated, showing that the octahedral rotations are sensitively connected to the MIT in agreement with the findings presented in this chapter. However, the model proposed by the authors of Ref. [49] contains only structural degrees of freedom and hence, the nature of the transition cannot be determined. Moreover, it is questionable how the performed magnetic DFT+U calculations relate to the paramagnetic insulating state in nickelates. Therefore, our work goes beyond the considerations of Ref. [49], by constructing a model that explicitly incorporates both, electronic, and structural degrees of freedom. In contrast, our work excludes a pure lattice effect of the transition by showing that it is the strong non-linear shape of

the electronic response which is critical in finding stable equilibrium breathing modes. All calculations are performed for the paramagnetic state, and render therefore for the first time a complete picture the paramagnetic coupled transition.

The idea of finding the stable equilibrium breathing mode distortion by intersection with $\nu[Q]$, can in principle also applied to other systems, thus allowing to determine structural trends or parameters without the need of performing total energy calculations. In a future step, one could incorporate the magnetic ordering into the model Hamiltonian, by allowing for magnetic ordering in the DMFT solution of the model, to investigate the differences of the paramagnetic and AFM insulating states. Moreover, the temperature dependence of the transition could also be analyzed.

6.7 PEER REVIEWED WORK

Mechanism and control parameters of the coupled structural and metal-insulator transition in nickelates

Oleg E. Peil,[1,2] Alexander Hampel,[3] Claude Ederer,[3] and Antoine Georges[2,4,5,6]
[1]*Materials Center Leoben Forschung GmbH, Roseggerstraße 12, 8700 Leoben, Austria*
[2]*DQMP, Université de Genève, 24 quai Ernest Ansermet, 1211 Genève, Switzerland*
[3]*Materials Theory, ETH Zürich, Wolfgang-Pauli-Strasse 27, 8093 Zürich, Switzerland*
[4]*Collège de France, 11 place Marcelin Berthelot, 75005 Paris, France*
[5]*Center for Computational Quantum Physics, Flatiron Institute, 162 Fifth Avenue, New York, New York 10010, USA*
[6]*CPHT, Ecole Polytechnique, CNRS, Université Paris-Saclay, 91128 Palaiseau, France*

(Received 19 September 2018; revised manuscript received 12 February 2019; published 12 June 2019)

Rare-earth nickelates exhibit a remarkable metal-insulator transition accompanied by a symmetry-lowering structural distortion. Using model considerations and first-principles calculations, we present a theory of this phase transition which reveals the key role of the coupling between electronic and lattice instabilities. We show that the transition is driven by the proximity to an instability towards electronic disproportionation which couples to a specific structural distortion mode, cooperatively driving the system into the insulating state. This allows us to identify two key control parameters of the transition: the susceptibility to electronic disproportionation and the stiffness of the lattice mode. We show that our findings can be rationalized in terms of a Landau theory involving two coupled order parameters, with general implications for transition-metal oxides.

DOI: 10.1103/PhysRevB.99.245127

I. INTRODUCTION

The coupling of electrons to lattice degrees of freedom provides a key opportunity to control the properties of strongly correlated materials as in, e.g., epitaxial heterostructures [1]. Such a coupling often leads to concomitant electronic and structural transitions, which have been observed in V_2O_3 [2], manganates [3], Ca_2RuO_4 [4,5], etc. Rare-earth nickelates (RNiO$_3$) [6–8] represent an ideal playground in this respect because their metal-insulator transition (MIT), tightly associated with a lattice mode, is easily tunable [9,10].

The MIT in RNiO$_3$ is accompanied by a bond disproportionation (BD), i.e., a coherent contraction of the NiO_6 octahedra on one sublattice [short-bond (SB) octahedra] and an expansion of the octahedra on the other sublattice [long-bond (LB) octahedra], also referred to as the "breathing mode" (BM) [7,11]. The resulting "bond-disproportionated insulator" (BDI) is also characterized by an electronic disproportionation (ED), whereby the local configuration of SB octahedra is close to $d^8\underline{L}^2$ and that of LB octahedra is close to d^8 [12–15], or, in terms of "frontier" e_g orbitals, to e_g^0 and e_g^2, respectively [16–19]. The electron localization on the LB sublattice is the result of a "site-selective Mott transition" [20], occurring irrespective of the (ground-state) magnetic ordering for all systems with R cations smaller than Nd, and lowering the energy of the insulating phase below that of the metallic phase [14,21–23]. Therefore, magnetic order seems to play only a secondary role for the smaller R cations from Lu to Sm, enhancing an already existing tendency towards the MIT [24–26].

The mechanism of the interplay between electronic and lattice degrees of freedom is not yet understood. This question is of key importance to identify the driving force responsible for the BD and for the first-order transition [27] into the paramagnetic insulating state. This transition was previously described either as a pure charge-order transition [28] or as a result of only the coupling between lattice modes [29]. Recently, the authors of Ref. [30] proposed that the transition corresponds to the gradual softening of the BM, associated with the opening of a Peierls gap at the Fermi level, where they used density functional theory (DFT) calculations including the $+U$ correction. This theory describes the transition as second order, contradicting the results of the differential scanning calorimetry which provide clear evidence of the first-order transition [27]. The theory also contradicts Raman-spectroscopy studies revealing no hint of the BM softening [31]. Furthermore, the obtained band structure is not compatible with observed optical spectra of nickelates [32,33]. In addition, it cannot describe the MIT into the paramagnetic state since DFT + U requires a magnetically ordered state to produce an insulating gap [34,35]. Crucially, in the absence of magnetic ordering, the Peierls gap does not open at the Fermi level [17,33] and cannot thus be responsible for the insulating nature of the paramagnetic phase.

Here, we present a theory describing specifically the interplay between the electronic and structural aspects of the paramagnetic MIT found for R = Lu to Sm. We show that the paramagnetic MIT is driven by the proximity to a spontaneous ED, which leads to a strongly nonlinear electronic response with respect to variations of the BM amplitude, resulting in a first-order phase transition. Furthermore, we show that this nonlinear behavior and the first-order nature is key for a correct description of the paramagnetic MIT and obtaining a finite, stable-equilibrium BM amplitude. Moreover, our

theory also identifies the BM stiffness and the electronic susceptibility at $\mathbf{q} = (\frac{1}{2}, \frac{1}{2}, \frac{1}{2})$ as key parameters controlling the transition. Experimentally, these parameters can be tuned by the choice of the R cation [6] or by epitaxial strain in thin films and heterostructures [9,10,36]. We validate our theory by performing combined DFT and dynamical mean-field theory (DMFT) [37,38] calculations, allowing us to explore the trends across the rare-earth series. We also rationalize the overall physical picture in terms of a Landau theory involving two coupled order parameters: the ED and an order parameter associated with the metallicity of the system.

The paper is organized as follows. First, in Sec. II we introduce the model description and analyze its behavior by identifying control parameters of the coupled transition. Next, in Sec. II we verify these findings with our realistic DFT + DMFT calculations. Finally, in Sec. IV, we present a Landau theory rationalizing our findings further, and in Sec. V, we summarize our main results.

II. MODEL DESCRIPTION

We start by constructing a simplified model which reproduces the main features of the MIT in $R\mathrm{NiO}_3$. The model retains only the key low-energy degrees of freedom: the interacting electrons in the two frontier e_g orbitals and the BM amplitude Q. The purely electronic part of the Hamiltonian, $H_{\mathrm{band}} + H_{\mathrm{int}}$, consists of a simplified tight-binding (TB) model, $H_{\mathrm{band}} = -\sum_{i,j,m,m',\sigma} t_{ij}^{mm'} d_{im\sigma}^{\dagger} d_{jm\sigma}$, and a local interaction term H_{int}. Here, i, j indicate sites within a simple cubic lattice, $m = 1, 2$ correspond to the $d_{x^2-y^2}$ and d_{z^2} orbitals on each site, and hopping matrices $t_{ij}^{mm'}$ are obtained using the Slater-Koster construction with two hopping amplitudes, t and t', limited to nearest-neighbor and next-nearest-neighbor sites, respectively [39]. The interaction term H_{int} involves two coupling constants, a repulsive interaction U and an intra-atomic (Hund's) exchange J, and takes the standard two-orbital Hubbard-Kanamori form [40]. The purely lattice part is described by an elastic term: $H_{\mathrm{latt}} = \frac{K}{2} Q^2$, with K being the stiffness of the BM. Finally, importantly, the coupling of the BM amplitude to the electrons is captured by the term

$$H_{\mathrm{e-l}} = \frac{1}{2} \sum_{m\sigma} \Delta_m^s[Q] \left[\sum_{i \in \mathrm{SB}} \hat{n}_{im\sigma} - \sum_{i \in \mathrm{LB}} \hat{n}_{im\sigma} \right], \tag{1}$$

where $\hat{n}_{im\sigma} = d_{im\sigma}^{\dagger} d_{im\sigma}$ is the electron occupation operator and $\Delta_m^s[Q]$ is a (Peierls-like) modulation of the on-site potential seen by orbital m due to the BM structural distortion parametrized by Q. It couples to the operator measuring the ED between the LB and SB octahedra. The total Hamiltonian thus reads

$$H = H_{\mathrm{band}} + H_{\mathrm{int}} + H_{\mathrm{e-l}} + H_{\mathrm{latt}}. \tag{2}$$

At this stage, we define the amplitude Q as the disproportionation in octahedral bond lengths, $b = b_0 + Q/2$ for LB and $b = b_0 - Q/2$ for SB octahedra. The modulation of the on-site potential $\Delta_m^s[Q]$ is given by the difference between the on-site energies of the SB and LB sites:

$$\begin{aligned} \Delta_m^s[Q] &= \varepsilon_m[b_0 - Q/2] - \varepsilon_m[b_0 + Q/2] \\ &\approx (d\varepsilon_m/db)_{b_0} Q \equiv g_m Q, \end{aligned} \tag{3}$$

where we have expanded in Q and introduced the electron-lattice coupling parameter g_m. Here, we assumed that $\Delta_m^s[Q]$ is linear in Q, which we checked by our DFT calculations for various representatives of the series (see Fig. 6 in Appendix A).

As emphasized in Refs. [17,18], an appropriate low-energy description of the negative-charge-transfer character of $R\mathrm{NiO}_3$ and of their tendency to form a BDI state is obtained with $U - 3J \lesssim \Delta_s$. In this regime, the orbital polarization is strongly suppressed, implying that the on-site energies are, to a good approximation, orbital independent: $\varepsilon_{z^2} \approx \varepsilon_{x^2-y^2}$. We thus assume that the e_g states are degenerate and omit the index m in one-electron quantities (i.e., $g_m = g$, $\Delta_m^s = \Delta_s$) [41].

Minimizing the total energy,

$$E = \langle H \rangle \equiv E_{\mathrm{el}}[\nu] - \frac{gQ\nu}{2} + \frac{KQ^2}{2}, \tag{4}$$

with respect to Q (using the Hellman-Feynman theorem) yields

$$\frac{2K}{g} \bar{Q} = \nu[\bar{Q}], \tag{5}$$

where $\nu[Q] = \langle \hat{n}_{\mathrm{LB}} - \hat{n}_{\mathrm{SB}} \rangle_Q$ is the average ED for a given amplitude Q, while $\bar{Q}$ denotes the equilibrium value of the amplitude corresponding to local energy minima (solutions corresponding to energy maxima are discarded). Equation (5) is the central equation of this paper: It enables one to determine the equilibrium BM amplitude from the knowledge of the electronic response encoded in $\nu[Q]$ for a given lattice stiffness K and electron-lattice coupling g. The stability of the solutions of this equation is determined by the renormalized stiffness

$$\kappa \equiv \frac{\partial^2 E}{\partial Q^2} = K - \frac{g^2}{2} \frac{\partial \nu}{\partial \Delta_s}. \tag{6}$$

Assuming no spontaneous ED ($\nu[Q = 0] = 0$), we obtain $\kappa = K - \chi_e g^2/2$, where $\chi_e \equiv (\partial \nu / \partial \Delta^s)_{Q=0}$ is the electronic susceptibility associated with a "charge" modulation at a wave vector $\mathbf{q} = (\frac{1}{2}, \frac{1}{2}, \frac{1}{2})$ (see Appendix A 3 for more information). Hence, the (linear) stability of the high-symmetry phase is controlled by the electronic response χ_e which must be compared to $2K/g^2$.

We investigate the solutions to Eq. (5) by performing DMFT calculations to obtain $\nu[Q]$ for various values of the bandwidth W (see Appendix A 4 for details). The results are shown in Fig. 1. The calculations were performed first for increasing values and then for decreasing values of Q, which resulted in a hysteresis. The most important feature of this plot is the strongly nonlinear dependence of ν on Q. Solutions of Eq. (5) are obtained by intersecting $\nu[Q]$ with the straight line $(2K/g)Q$.

This nonlinear shape of the $\nu[Q]$ curves plays an important role in determining the nature of the transition. For a given value of K/g and depending on W, there are either one, two, or three intersection points (disregarding symmetry-equivalent solutions for $Q < 0$). Consider $K/g = 5.3$ Å^{-1}. If W is large ($W \geqslant 2.07$ eV in Fig. 1), the straight line intersects the ED curve only at $Q = 0$, rendering it the only solution to Eq. (5). As W is decreased, it reaches a value below which there are

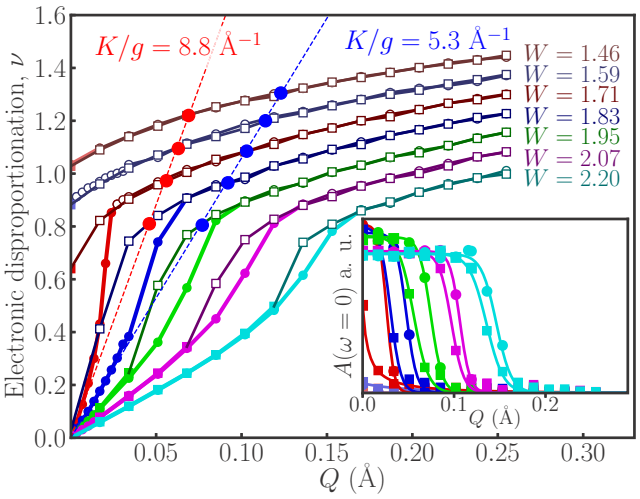

FIG. 1. Electronic disproportionation ν of the TB model as a function of bond disproportionation Q for various values of the bandwidth W (in eV). Open and solid symbols correspond to insulating and metallic branches, respectively. The dashed lines represent $(2K/g)Q$ for two values of K/g, with the intersection points giving the solutions to Eq. (5). Inset: Spectral weight as a function of Q.

three intersection points ($W = 1.95$ eV). The middle intersection point corresponds to an unstable solution ($\kappa < 0$). The two remaining stable solutions, $Q = 0$ and $Q = \bar{Q}[K, W] > 0$, mark the coexistence of two different phases. At even smaller values of W ($W \lesssim 1.8$) the solution at $Q = 0$ gets destabilized because $\kappa[Q = 0] < 0$. We are then left with only one solution, $Q = \bar{Q}[K, W] > 0$, telling us that only the BD phase is stable here. The behavior of the solutions of Eq. (5) as a function of W tells us that the BD transition is first order. Importantly, this is not directly related to the hysteretic behavior of $\nu[Q]$. Even if there were no such hysteresis, the particular nonlinear dependence of $\nu[Q]$ would imply that the BD transition is first order. The inset of Fig. 1 displays the spectral weight at the Fermi level as a function of Q. We see that the system undergoes a transition from metallic to insulating behavior as Q is increased and that the transition regime corresponds to the strongly nonlinear regime of $\nu[Q]$. Hence, it is the MIT which is responsible for the strong nonlinearity of $\nu[Q]$.

We can now discuss the control parameters of the combined BD/MIT, where Eq. (5) shows that the transition behavior depends on parameters g, K, and χ_e. We extract these parameters from our DFT calculations (see Appendix A 2 for details), and the obtained values for g, K, their ratios, χ_e, and the e_g bandwidth W are shown in Table I. To get a better feel for these numbers, one can estimate the maximum possible equilibrium BM amplitude by setting $\nu = 2$ in Eq. (1), which yields $\bar{Q}_{\max} = 2(g/2K) \approx 0.095$ Å, a value that sets the correct scale of distortions observed in experiment (e.g., $\bar{Q} = 0.075$ Å for $LuNiO_3$). This provides a strong argument in favor of the presented mechanism of the electron-lattice coupling as the dominant one in determining the structural transition.

The electron-lattice coupling g is found to vary by about 12% along the rare-earth series. Moreover, the stiffness K also varies by a similar amount and in the same direction (increasing from Lu to Sm). As a result, the ratio $2K/g$, which enters the equation of state, is fairly constant along the series. The renormalized stiffness controlling the sensitivity to disproportionation at small Q is proportional to $2K/g^2 - \chi_e$, with χ_e being the electronic susceptibility. From Table I it can be seen that the first term varies by about 10% along the series, but the electronic susceptibility varies by almost a factor of 2 from Pr to Lu. As a result, for the bulk materials, the transition is sensitively controlled by the electronic susceptibility (i.e., by the bandwidth and rotation and tilt angles [28]) and not by the stiffness K or electron-lattice coupling g. In heterostructures and under strain, the BM stiffness K varies, while g remains unaffected [36]. K is thus likely to be an important control parameter in those cases. This may shed light on the results of Ref. [42] and motivates the variation of K/g in our model calculations.

TABLE I. Values for g, K, $2K/g$, $2K/g^2$, the e_g bandwidth W, and the $d_{x^2-y^2}$ component of the electronic susceptibility $\chi_{1,1}$ for the three investigated compounds R = Lu, Sm, and Pr, extracted from DFT calculations.

R	g (eV/Å)	K (eV/Å^2)	$2K/g$ (1/Å)	$2K/g^2$ (1/eV)	W (eV)	$\chi_{1,1}$ (1/eV)
Lu	3.75	39.29	20.96	5.59	2.32	0.69
Sm	4.02	41.45	20.61	5.13	2.51	0.50
Pr	4.24	44.47	20.98	4.95	2.68	0.39

The effects of the two control parameters K and χ_e (tuned via K/g and W, respectively) are summarized in Fig. 2. The dashed curves indicate the boundaries (spinodals) of the BDI and metallic phases, with a narrow coexistence region in between. Solid lines show stable nonzero solutions $\bar{Q}[K, W]$. For fixed K, the bandwidth W (equivalently, χ_e) determines

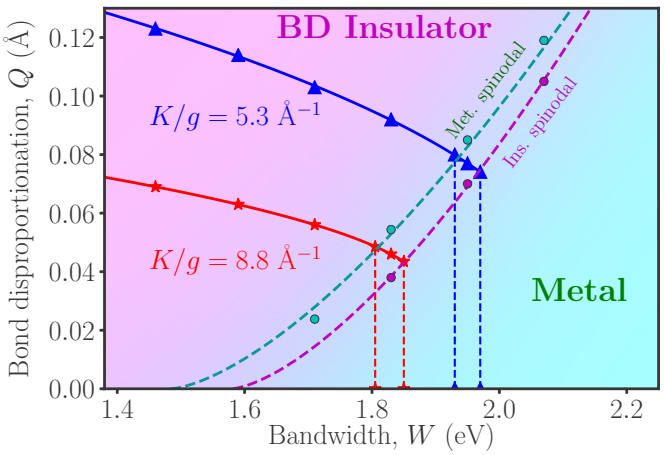

FIG. 2. Phase diagram of the TB model as a function of bandwidth W and BD Q. Circles are critical points for the metallic and insulating phases; dashed curves are spinodal lines obtained as fits to $\alpha(W - W_c)^{\frac{3}{2}}$ (see Sec. IV on the Landau theory). The solid lines with triangles and stars display the stable equilibrium values of Q for two values of K/g. Vertical dashed lines designate lower and upper critical values of W for the structural transition.

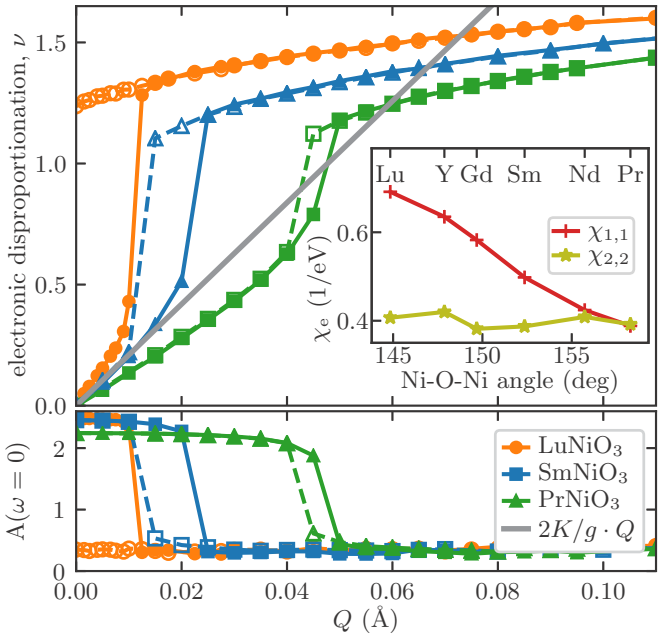

FIG. 3. Top: ED ν as a function of increasing Q (solid symbols) and decreasing Q (open symbols) for $R =$ Lu (red), Sm (blue), and Pr (green). The gray line represents $(2K/g)Q$ with values $g = 3.8$ eV/Å and $K = 39.3$ eV/Å^2 extracted from DFT. Inset: Electronic susceptibilities as a function of the Ni-O-Ni angle: $\chi_{1,1}$ is the $d_{x^2-y^2}$ component, and $\chi_{2,2}$ is the d_{z^2} component. Bottom: spectral weight at the Fermi level as a function of Q.

whether the paramagnetic ground state is a BDI phase. Moreover, the variation of K controls smoothly the position of the phase boundaries.

III. REALISTIC DFT + DMFT CALCULATIONS

We now perform *ab initio* DFT + DMFT calculations to confirm the physics found in the model calculations and assess materials trends quantitatively. The impurity model is constructed by projecting onto a low-energy e_g subspace following the scheme described in Refs. [17,18] (see Appendix A 4 for details).

Figure 3 shows the calculated $\nu(Q)$ for $R =$ Lu, Sm, and Pr (top panel). The overall nonlinear behavior of $\nu(Q)$ is very similar to that in the model calculations (Fig. 1), with the nonlinearity clearly related to the MIT (Fig. 3, bottom panel), also indicating a first-order character of the BD/MIT. This confirms that the model indeed incorporates the essential underlying physics. Furthermore, we obtain a strong decrease in the amplitude of the nonlinearity in $\nu(Q)$ from $R =$ Lu towards $R =$ Pr, consistent with the bandwidth variation in the model.

For the realistic calculations, we checked the change in bandwidth W for different R cations obtained by DFT. The corresponding values of W for $R =$ Lu, Sm, and Pr are shown in Table I (see also Fig. 5 in Appendix A). One can see that the bandwidth decreases by ∼13% from $R =$ Pr to $R =$ Lu. On the other hand, the $d_{x^2-y^2}$ component of the electronic susceptibility displayed in Fig. 3 (top, inset) increases steadily and almost doubles its value from Pr to Lu as the Ni-O-Ni bond angle is reduced. Together, this shows that the increased octahedral rotations for $R =$ Lu compared to $R =$ Pr have a much stronger impact on the electronic susceptibility χ_e than on the bandwidth W. This effect can be understood by realizing that the bandwidth is mainly determined by the nearest-neighbor hopping parameter t, while the susceptibility is also crucially dependent on the next-nearest-neighbor hopping parameter t' (more precisely, on the ratio t'/t), affecting the shape of the Fermi surface [28,39]. The bandwidth provides thus only an indirect measure of the changes in the true control parameter χ_e determining the proximity to the instability.

Finally, the values obtained for K and g from DFT (see Table I) lead to stable equilibrium BM amplitudes $\bar{Q}$ for all investigated compounds. This is shown in Fig. 3, where $\bar{Q}$ is obtained from the crossing points of $(2K/g)Q$ (gray line) with the $\nu[Q]$ curves. The value obtained for $\bar{Q}$ for $LuNiO_3$ of 0.073 Å is in very good agreement with available experimental data ($Q_{exp} = 0.075$ Å [27]). $PrNiO_3$ seems to be very close to the transition, as its $\bar{Q}$ value is very close to the MIT, and the stable BM would eventually be lost if a reduced U were used for $PrNiO_3$, as suggested by our constrained random-phase approximation calculations [22]. Moreover, previous studies find that the magnetic order appears to be crucial in stabilizing the BD phase in $PrNiO_3$ and $NdNiO_3$ [7,22,24,25]. The stability and influence of the magnetic order goes beyond the scope of our work and requires further investigation. However, the overall trend of an increase in Q and in the stability of the BM through the series for smaller R cations is consistent with experiments and in line with earlier studies [19,22,35]. Moreover, these results clearly show the capabilities of the method to correctly capture the coupled paramagnetic MIT and the resulting stability of the BM distortion compared to a DFT + U description.

IV. LANDAU THEORY

We finally show that the main qualitative features of the MIT found above can be rationalized in terms of a Landau theory, which involves two coupled scalar order parameters: the ED ν and an additional order parameter, ϕ, which distinguishes between metallic (conventionally associated with $\phi > 0$) and insulating behavior ($\phi < 0$). The reason why this second-order parameter is required is clear from the results above: a nonzero value of ν can correspond either to a metallic phase (at small values of the on-site modulation Δ_s or, equivalently, of Q) or to an insulating one. In other words, a metallic monoclinic phase with a nonzero value of the BM amplitude Q is, in principle, possible, in agreement with recent experimental findings [43]. Such an order parameter has been introduced to describe the Mott transition in the DMFT framework, in analogy with the liquid-gas transition [44,45]. Note that the present Landau theory aims at describing the MIT between the two paramagnetic phases, while the earlier Landau descriptions [24,39] aimed at the magnetic transition (see also Ref. [5] in relation to ruthenates.)

Assuming the simplest coupling allowed by symmetry, $\phi\nu^2$, the paramagnetic transitions can be described by the following energy functional:

$$F[\nu, \phi] = F_\nu + F_\phi + \lambda\phi\nu^2, \tag{7}$$

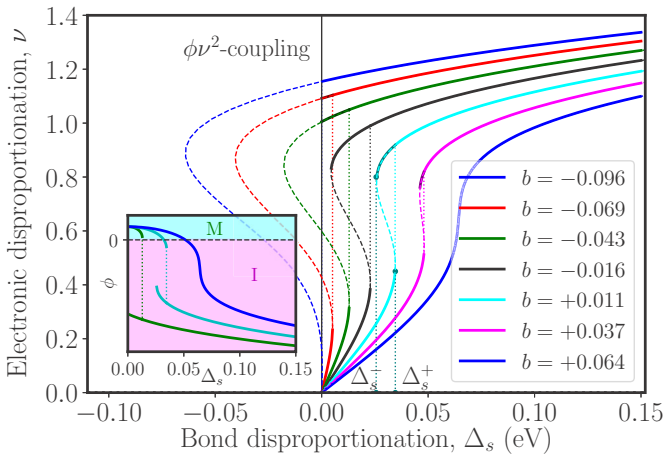

FIG. 4. ED ν as a function of Δ_s for various values of parameter b, as obtained within the Landau theory described in the text. Dashed lines display unstable solutions. Critical points Δ_s^-, Δ_s^+ are indicated for one of the cases. Inset: MI order parameter ϕ as a function of Δ_s for three selected cases ($b = -0.043$, 0.011, 0.064). The region marked M shows the metallic phase ($\phi > 0$); the region marked I shows the insulating phase ($\phi < 0$).

with

$$F_\nu = \tfrac{1}{2}b\nu^2 + \tfrac{1}{4}c\nu^4 - \Delta_s\nu + \tfrac{1}{2}\kappa\Delta_s^2,$$
$$F_\phi = \tfrac{1}{2}a\phi^2 + \tfrac{1}{4}u\phi^4 - h\phi, \tag{8}$$

where $u, c > 0$ and the coupling parameter $\lambda > 0$ is of order 1. The coupling to the lattice is represented by the linear term $\Delta_s\nu$, with Δ_s serving as a symmetry-breaking field (alternatively, the BM can be introduced with $Q = g\Delta_s$). In the absence of ED, the system is a metal, so that we must assume a and h are positive. Here, b is a key control parameter related to χ_e, and it depends critically on external parameters such as the bandwidth, $b = b_0(W - W_c)$.

Without loss of generality we can set $u = c = a = 1$. Minimizing $F[\nu, \phi]$ yields the following coupled equations of state:

$$b\nu + \nu^3 + 2\lambda\phi\nu = \Delta_s, \tag{9}$$

$$\phi + \phi^3 = h - \lambda\nu^2. \tag{10}$$

The numerical solution of these equations is displayed in Fig. 4 for various b. For $b > 0$, starting from a value $\phi = \phi_0 > 0$, typical for the metallic phase at $\nu = 0$, and increasing Δ_s lead to a strongly nonlinear dependence of ν on Δ_s, with ϕ continuously decreasing (because of the $-\lambda\nu^2$ term) and gradually reaching negative values (inset of Fig. 4). At a critical value of b, the $\nu[\Delta_s]$ curves acquire a vertical tangent, and beyond this value, an S shape with an unstable branch is found, typical of a first-order transition, with two vertical tangents delimiting the two spinodal values of Δ_s: Δ_s^- and Δ_s^+. When b is further decreased, a spontaneous instability is found, with a jump of ν to a finite value for an infinitesimal Δ_s. This general behavior is in excellent qualitative agreement with Fig. 1.

A more detailed analysis of the above equation can be carried out by considering two limits: small and large values of Δ_s. The small-Δ_s limit can be described in terms of the linear susceptibility at $\nu = 0$, $\chi_e = (b + 2\lambda\phi_0)^{-1}$, associated with the electronic disproportionation. Keeping terms up to $O(\Delta_s^2)$, we can get the nonlinear susceptibility (see Appendix B for details),

$$\frac{d\nu}{d\Delta_s} = \left[\chi_e^{-1} - S\chi_e^2\Delta_s^2\right]^{-1}, \tag{11}$$

where $S > 0$ is a constant enhancement factor proportional to λ^2. The equation emphasizes the role of the $\phi\nu^2$ coupling in amplifying the electronic disproportionation, driving it to the transition at $\Delta_s = \Delta_s^+ \equiv (b + 2\lambda\phi_0)^{\frac{3}{2}}/\sqrt{S} \sim (W - W^+)^{\frac{3}{2}}$. At this point $d\nu/d\Delta_s$ diverges, marking the spinodal of the metallic phase.

Analogously, the analysis of the large-Δ_s limit reveals that also for the spinodal of the insulating phase we get $\Delta_s^- \sim (W - W^-)^{\frac{3}{2}}$ (details are given in Appendix B). The similar behaviors of the metallic and insulating spinodals are confirmed by the DMFT results for the TB model displayed in Fig. 1, where one can see that the two boundaries are fairly parallel.

V. CONCLUSIONS

We have presented a theory of the combined structural and electronic metal-insulator transition in bulk RNiO$_3$. The driving force of this transition is the proximity to the electronic disproportionation instability, which is cooperatively reinforced by the coupling to the lattice breathing mode. The transition is thus controlled both by the electronic charge susceptibility and by the stiffness of this mode. The key nonlinearities associated with this cooperative effect can be rationalized in terms of a Landau theory. Our work provides a pathway to understanding the MIT in other geometries, such as ultrathin films and heterostructures, and is likely to have general applicability to other materials with a strong interplay between electronic correlations and lattice degrees of freedom.

ACKNOWLEDGMENTS

We are grateful to C. Ahn, D. Basov, J. Chakhalian, A. Georgescu, A. J. Millis, J. M. Triscone, and D. van der Marel for discussions. This work was supported by the European Research Council (Grant No. ERC-319286-'QMAC'), the Swiss National Science Foundation (NCCR MARVEL), and the Swiss National Supercomputing Centre (Projects No. s575, No. s624, No. mr17, and No. s820). The Flatiron Institute is a division of the Simons Foundation. O.E.P. gratefully acknowledges the financial support under the scope of the COMET program within the K2 Center "Integrated Computational Material, Process and Product Engineering (IC-MPPE)" (Project No. 859480). This program is supported by the Austrian Federal Ministry for Transport, Innovation and Technology (BMVIT) and Federal Ministry of Digital and Economic Affairs (BMDW), represented by the Austrian research funding association (FFG), and the federal states of Styria, Upper Austria, and Tyrol.

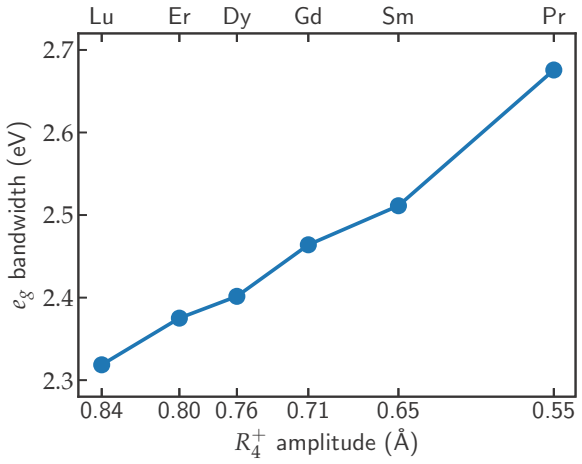

FIG. 5. Bandwidth W of the e_g bands as a function of rare-earth ion R obtained from DFT corresponding to the *Pbnm* structure ($Q = 0.0$ Å).

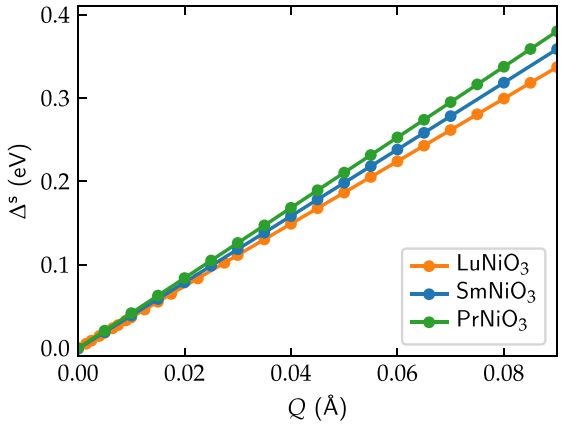

FIG. 6. $\Delta^s[Q]$ for R = Lu (red), Sm (blue), and Pr (green) as extracted from DFT. A clear linear dependency of $\Delta^s[Q]$ from Q can be observed for all three R cations.

APPENDIX A: CALCULATION DETAILS

1. DFT calculations

DFT calculations were performed using the projector augmented wave (PAW) method [46] implemented in the Vienna Ab initio Simulation Package (VASP) [47–49] and the exchange correlation functional according to Perdew, Burke, and Ernzerhof [50]. For Ni, the $3p$ semicore states were included as valence electrons in the PAW potential. For the rare-earth atoms, we used PAW potentials corresponding to a 3+ valence state with f electrons frozen into the core, and depending on the rare-earth cation, the corresponding $5p$ and $5s$ states were also included as valence electrons. A k-point mesh with $10 \times 10 \times 8$ grid points along the three reciprocal lattice directions was used, and a plane wave energy cutoff of 550 eV was chosen for the 20-atom *Pbnm* unit cell. The structures were fully relaxed, both internal parameters and lattice parameters, until the forces acting on all atoms were smaller than 10^{-4} eV/Å. Generally, our calculated lattice parameters agree very well with available experimental data across the whole series, with maximal deviations of the unit cell volume of a few percent or less. For example, for $LuNiO_3$ the nonmagnetic calculation results in a unit cell volume that deviates by -1.5% from the experimental high-temperature structure [27]. As can be seen from Ref. [35], all rotation and tilt angles are also in very good agreement with the experimental structure.

To check the influence of the different control parameters across the nickelate series, we extracted the bandwidth W of the e_g states from our DFT calculations for the relaxed *Pbnm* structures, which is depicted in Fig. 5. Here, W is plotted as function of the octahedral rotation distortion amplitude R_4^+, which is related to the Ni-O-Ni super-exchange angle [35].

2. Electron-lattice coupling

We use slightly different definitions of the BM amplitude Q in the model and in the realistic calculations. In the model, Q is defined as the difference in bond lengths (oxygen-atom displacement is $\sim Q/2$), while in DFT + DMFT calculations, the BM amplitude corresponds to a particular distortion mode (R_1^+) of a symmetry-based mode decomposition [35,51,52]. Since the amplitude of this mode is proportional to the displacement of oxygen atoms, its value is almost a factor of 2 smaller than the model value of Q. More specifically, an amplitude of $Q = 0.1$ Å would result in a displacement of 0.058 Å of each oxygen atom. The decomposition in distortion modes allows us to clearly separate the effect of the BM from other distortions and hence allows for a better comparison with the model. As experiments show [27,53], structural parameters besides the breathing mode distortion almost do not change during the MIT, and therefore, the use of our relaxed *Pbnm* structures is well justified.

In the model calculations, $Q = \Delta_s/g$ is controlled by varying the modulation parameter Δ_s. The length scale is set by setting $g = 1.7$ eV/Å, which is close to $g_{\mathrm{DFT}}/2$, with g_{DFT} being the value obtained in our DFT calculations for bulk $RNiO_3$ (see below). Model parameter K can be chosen rather arbitrarily, and we vary it in a range of values that results in equilibrium values of Q of the same order of magnitude as the experimentally observed values (and the ones resulting from DFT + DMFT calculations). Note that because of the difference in the definition of Q the model values of K would correspond to roughly four times larger values of the realistic BM stiffness.

In our realistic calculations, parameters g and K are determined from systematic DFT calculations for varying BM amplitude, where the modulation field Δ_s is extracted from the difference of the corresponding on-site terms of the Hamiltonian projected onto e_g states via Wannier construction as described in Refs. [54,55]. To this end, we use the TRIQS/DFTTOOLS software package [56,57]. The resulting values of Δ_s turn out to be linear in Q in the relevant range of BM amplitudes, as seen in Fig. 6, where we show several examples of such calculations. In the context of DFT + DMFT calculations, the value of Δ_s is corrected for the double-counting (DC) contributions as described in Ref. [18].

The obtained values of the parameters allow for an estimate of the relative strength of the electron-lattice coupling by considering a polaron binding energy $g^2/(2K)$, which is $E_p \approx 184$ meV for our obtained values g and K from DFT. The corresponding dimensionless coupling parameter is then equal

to $\lambda = E_p/W \approx 0.08 \ll 1$ for $LuNiO_3$ (it is even smaller for other compounds in the series), which tells us that electrons are coupled relatively weakly to the BM in nickelates. This emphasizes the key role that the electronic instability plays in effectively enhancing the coupling and destabilizing the BM.

3. Electronic susceptibility

Here, we show that the formula for the susceptibility given in the text is related to the usual definition of the charge susceptibility at a specific $\mathbf{q}$ point. If we consider an inhomogeneous perturbation potential of the form $H' = \sum_i \hat{n}_i \epsilon_i$ (again, assuming orbital degeneracy and omitting the orbital and spin indices), then the $\mathbf{q}$-dependent charge susceptibility is defined as

$$\chi(\mathbf{q}) = -\frac{\partial n(\mathbf{q})}{\partial \epsilon(\mathbf{q})}\Big|_{\epsilon\to 0}, \tag{A1}$$

with

$$n(\mathbf{q}) = \frac{1}{N}\sum_i \langle \hat{n}\rangle_i e^{i\mathbf{q}\mathbf{R}_i}, \quad \epsilon(\mathbf{q}) = \frac{1}{N}\sum_i \epsilon_i e^{i\mathbf{q}\mathbf{R}_i},$$

where $\mathbf{R}_i = m_i^1\mathbf{a}_1 + m_i^2\mathbf{a}_2 + m_i^3\mathbf{a}_3$ are the Bravais-lattice vectors, $\mathbf{a}_\alpha$ are the translation vectors of the pseudocubic unit cell, and $m_i^\alpha \in \mathbb{Z}$ ($\alpha = 1, 2, 3$).

Considering a modulated field ϵ_i equal to $\Delta_s/2$ on SB sites and to $-\Delta_s/2$ on LB sites, we have for a specific point $\mathbf{q}_R = \frac{2\pi}{a}(\frac{1}{2}, \frac{1}{2}, \frac{1}{2})$ in a pseudocubic structure

$$\begin{aligned} n(\mathbf{q}_R) &= \frac{1}{N}\sum_i \langle \hat{n}\rangle_i e^{i\pi(m_i^1+m_i^2+m_i^3)} \\ &= \frac{1}{N}\left(\sum_{i\in \mathrm{LB}}\langle \hat{n}\rangle_i - \sum_{i\in \mathrm{SB}}\langle \hat{n}\rangle_i\right) = \frac{1}{2}\nu \\ \epsilon(\mathbf{q}_R) &= \frac{1}{N}\sum_i \epsilon_i e^{i\pi(m_i^1+m_i^2+m_i^3)} \\ &= \frac{1}{N}\left(\sum_{i\in \mathrm{LB}}\epsilon_i - \sum_{i\in \mathrm{SB}}\epsilon_i\right) = -\frac{1}{2}\Delta_s, \end{aligned}$$

where we have associated LB and SB sites with the sites for which the values of $m_i = \sum_\alpha m_i^\alpha$ are even and odd, respectively.

Then, we get

$$\chi(\mathbf{q}_R) = \frac{\partial \nu}{\partial \Delta_s}\Big|_{\epsilon\to 0}, \tag{A2}$$

which is the definition of χ_e used in the main text.

4. DMFT calculations

DMFT calculations for the TB model Hamiltonian are performed in the paramagnetic state. The bandwidth is given by $W = 6.1t$, and the ratio, $t'/t = 0.13$, is fixed for all calculations. The interaction parameters are set to $U = 1.8$ eV, $J = 0.9$ eV, similar to what has been used for a realistic low-energy description of $RNiO_3$ [17,18]. The temperature is set to $T = 1/100$ eV $\simeq 120$ K. The DMFT calculations are performed using hybridization-expansion continuous-time quantum Monte Carlo [58], as implemented in the TRIQS package [57,59], with the rotationally invariant Kanamori-type interaction term.

Within the realistic DFT + DMFT framework, we solve the electronic problem defined by the lattice Hamiltonian, $\hat{H} = \hat{H}_{\mathrm{kin}} + \hat{H}_{\mathrm{int}} + \hat{H}_V$, utilizing the above-mentioned solver. Here, the first term in $\hat{H}$ corresponds to the full e_g bands extracted from DFT, including all off-diagonal hoppings and on-site terms; the second term is the local interaction Hamiltonian, where we use the rotationally invariant Kanamori form, and the last term describes the intersite Coulomb interaction V, as introduced in Ref. [18], which we include on a mean-field level as a Hartree shift in the local self-energy.

We perform one-shot DFT + DMFT calculations, but according to our test calculations (see also Ref. [22]), the incorporation of intersite interactions on a Hartree level within a one-shot DFT + DMFT scheme gives results that are very similar to fully charge self-consistent DFT + DMFT calculations using only the local interaction term.

To correct for the DC error, we employ the scheme described in Ref. [60], where we additionally perform a DC correction for the intersite interaction as described in Ref. [18]. For better comparability, we use the same interaction parameters, $U = 1.8$ eV, $J = 0.4$ eV, and $V = 0.6$ eV, for all compounds throughout the series. These values are close to the results of recent calculations using the constrained random-phase approximation [18,22]. All calculations are done for the paramagnetic phase, and the temperature was set to $T = 1/40$ eV $\simeq 290$ K.

APPENDIX B: LANDAU THEORY

Here, we elaborate on the derivation of the critical-point scaling mentioned in the main text. We start with the equations of state given by Eqs. (9) and (10) in the main text and consider separately metallic and insulating regimes.

Stability of the metallic phase. For the metallic regime, we perform derivation by expanding in the limit of small Δ_s. At $\nu = 0$, we set $\phi = \phi_0 > 0$ to make sure the system is metallic in the absence of BD.

The symmetry of the problem dictates that ν is an odd function and ϕ is an even function of Δ_s. To first order in Δ_s we get

$$\nu_0 \approx \chi_e \Delta_s, \tag{B1}$$

$$\chi_e = \frac{1}{b + 2\lambda\phi_0}, \quad b > -2\lambda\phi_0. \tag{B2}$$

This result is not very interesting because it implies a linear behavior of ν and a constant value of ϕ_0 as a function of Δ_s, with Δ_s having thus no effect on the metal-insulator order parameter. This excludes any transition induced by bond disproportionation, leaving only a simple externally driven transition when $b = 2\lambda\phi_0$.

To get the next leading order, let $\phi = \phi_0 + \phi_1$, which gives

$$\begin{aligned} (\phi_0 + \phi_1)^3 + (\phi_0 + \phi_1) &= h - \lambda\nu_0^2, \\ 3\phi_0^2\phi_1 + \phi_1 &\approx -\lambda\chi_e^2\Delta_s^2, \end{aligned}$$

where terms of order $o(\Delta_s^2)$ are dropped.

We obtain the following solution:

$$\phi_1 = -\frac{\lambda}{M}\chi_e^2\Delta_s^2, \quad M = 1 + 3\phi_e^2. \tag{B3}$$

Importantly, we see that $\phi_1 < 0$, and ϕ hence decreases quadratically with Δ_s (see the inset of Fig. 4). Moreover, the rate of the reduction is determined by the charge susceptibility χ_e and also by the strength ("conductivity") ϕ_0 of the metallic phase.

To estimate the dependence of the nonlinear susceptibility on Δ_s we take the derivatives of the equations of state, Eqs. (9) and (10), with respect to Δ_s. Denoting $\chi(\Delta_s) = \partial\nu/\partial\Delta_s$ and, again, keeping only terms up to $O(\Delta_s^2)$, we have

$$3\phi^2\frac{\partial\phi}{\partial\Delta_s} + \frac{\partial\phi}{\partial\Delta_s} = -2\lambda\nu\chi, \quad \frac{\partial\phi}{\partial\Delta_s} \approx -2\frac{\lambda}{M}\nu\chi, \tag{B4}$$

from which we have

$$\begin{aligned} 3\nu^2\chi + (b+2\lambda\phi)\chi + 2\lambda\nu\frac{\partial\phi}{\partial\Delta_s} &= 1, \\ \left(3\nu_0^2 + \chi_e^{-1} - 6\frac{\lambda^2}{M}\nu_0^2\right)\chi &= 1, \\ \chi_e^{-1} - 3\left(2\frac{\lambda^2}{M} - 1\right)\chi_e^2\Delta_s^2 &= \chi^{-1}, \end{aligned} \tag{B5}$$

where we have used Eqs. (B1), (B2), (B3), and (B4). The resulting equation is precisely our Eq. (11) in the main text, with $S = 3(2\lambda^2/M - 1)$.

The function $\chi(\Delta_s)$ is equal to χ_e at $\Delta_s = 0$, increases with Δ_s faster than $\chi_e\Delta_s$, and diverges when $\Delta_s = \Delta_s^+$, with

$$\Delta_s^+ = \frac{\chi_e^{-\frac{3}{2}}}{\sqrt{S}}. \tag{B6}$$

The important observation here is that

$$\Delta_s^+ \sim (b + 2\lambda\phi_0)^{\frac{3}{2}} \sim (W - W^+)^{\frac{3}{2}}, \tag{B7}$$

which is exactly the scaling employed in fitting the spinodal of the metallic phase in Fig. 2.

Stability of the insulating phase. The insulating phase can be analyzed in a similar fashion but starting from the asymptotic large-Δ_s solution:

$$\begin{aligned} \nu &\approx \Delta_s^{\frac{1}{3}} - (b+2\lambda\phi)\frac{1}{3\Delta_s^{\frac{1}{3}}}, \\ \nu^2 &\approx \Delta_s^{\frac{2}{3}} - \frac{2}{3}(b+2\lambda\phi) + \frac{(b+2\lambda\phi)^2}{9\Delta_s^{\frac{2}{3}}}. \end{aligned}$$

By substituting this back into Eq. (10), we get

$$\begin{aligned} \phi^3 + \phi &= h - \lambda\Delta_s^{\frac{2}{3}} + \lambda\frac{2}{3}(b+2\lambda\phi), \\ \phi^3 + \phi\left(1 - \frac{4}{3}\lambda^2\right) &= h + \lambda\frac{2}{3}b - \lambda\Delta_s^{\frac{2}{3}}, \\ \phi^3 - P\phi &= h + \lambda\frac{2}{3}b - \lambda\Delta_s^{\frac{2}{3}}, \end{aligned}$$

where we have neglected the terms containing inverse powers of Δ_s and introduced $P = 4\lambda^2/3 - 1$.

The insulating phase becomes unconditionally unstable when the right-hand side of the equation reaches the local maximum of the left-hand side. The location of the maximum ϕ_m is easily found from the left-hand side,

$$\phi_m = -\sqrt{\frac{P}{3}}.$$

This results in the following condition for the stability valid in the large Δ_s limit:

$$h + \lambda\frac{2}{3}b - \lambda\Delta_s^{\frac{2}{3}} = \frac{2}{3}\left(\frac{P}{3}\right)^{\frac{3}{2}},$$

from which we get the critical value of Δ_s,

$$\Delta_s^- = \left[\frac{2}{3}b + \frac{h}{\lambda} - \frac{2}{3\lambda}\left(\frac{P}{3}\right)\right]^{\frac{3}{2}}. \tag{B8}$$

Thus, in both the metallic and insulating cases, the scaling of the critical Δ_s is

$$\Delta_s^* \sim (b - b^*)^{\frac{3}{2}} \sim (W - W^*)^{\frac{3}{2}}, \tag{B9}$$

with $\Delta_s^* = \Delta_s^+, \Delta_s^-$ for the metallic and insulating spinodals, respectively. These scalings have been used to fit both boundaries in Fig. 2.

[1] P. Zubko, S. Gariglio, M. Gabay, P. Ghosez, and J.-M. Triscone, Annu. Rev. Condens. Matter Phys. **2**, 141 (2011).

[2] D. B. McWhan, T. M. Rice, and J. P. Remeika, Phys. Rev. Lett. **23**, 1384 (1969).

[3] Y. Tokura, Rep. Prog. Phys. **69**, 797 (2006).

[4] S. Nakatsuji, S. Ikeda, and Y. Maeno, J. Phys. Soc. Jpn. **66**, 1868 (1997).

[5] Q. Han and A. Millis, Phys. Rev. Lett. **121**, 067601 (2018).

[6] J. B. Torrance, P. Lacorre, A. I. Nazzal, E. J. Ansaldo, and C. Niedermayer, Phys. Rev. B **45**, 8209 (1992).

[7] M. L. Medarde, J. Phys.: Condens. Matter **9**, 1679 (1997).

[8] G. Catalan, Phase Transitions **81**, 729 (2008).

[9] S. Catalano, M. Gibert, J. Fowlie, J. Íñiguez, J.-M. Triscone, and J. Kreisel, Rep. Prog. Phys. **81**, 046501 (2018).

[10] S. Middey, J. Chakhalian, P. Mahadevan, J. W. Freeland, A. J. Millis, and D. D. Sarma, Annu. Rev. Mater. Res. **46**, 305 (2016).

[11] J. M. Rondinelli and N. A. Spaldin, Adv. Mater. **23**, 3363 (2011).

[12] A. Demourgues, F. Weill, B. Darriet, A. Wattiaux, J. Grenier, P. Gravereau, and M. Pouchard, J. Solid State Chem. **106**, 330 (1993).

[13] T. Mizokawa, D. I. Khomskii, and G. A. Sawatzky, Phys. Rev. B **61**, 11263 (2000).

[14] S. Johnston, A. Mukherjee, I. Elfimov, M. Berciu, and G. A. Sawatzky, Phys. Rev. Lett. **112**, 106404 (2014).

[15] B. Mandal, S. Sarkar, S. K. Pandey, P. Mahadevan, C. Franchini, A. J. Millis, and D. D. Sarma, arXiv:1701.06819.

[16] I. I. Mazin, D. I. Khomskii, R. Lengsdorf, J. A. Alonso, W. G. Marshall, R. M. Ibberson, A. Podlesnyak, M. J. Martínez-Lope, and M. M. Abd-Elmeguid, Phys. Rev. Lett. **98**, 176406 (2007).

[17] A. Subedi, O. E. Peil, and A. Georges, Phys. Rev. B **91**, 075128 (2015).

[18] P. Seth, O. E. Peil, L. Pourovskii, M. Betzinger, C. Friedrich, O. Parcollet, S. Biermann, F. Aryasetiawan, and A. Georges, Phys. Rev. B **96**, 205139 (2017).

[19] J. Varignon, M. N. Grisolia, J. Íñiguez, A. Barthélémy, and M. Bibes, npj Quantum Mater. **2**, 21 (2017).

[20] H. Park, A. J. Millis, and C. A. Marianetti, Phys. Rev. Lett. **109**, 156402 (2012).

[21] H. Park, A. J. Millis, and C. A. Marianetti, Phys. Rev. B **89**, 245133 (2014).

[22] A. Hampel, P. Liu, C. Franchini, and C. Ederer, npj Quantum Mater. **4**, 5 (2019).

[23] J. Varignon, M. Bibes, and A. Zunger, Nat. Commun. **10**, 1658 (2019).

[24] J. Ruppen, J. Teyssier, I. Ardizzone, O. E. Peil, S. Catalano, M. Gibert, J.-M. Triscone, A. Georges, and D. van der Marel, Phys. Rev. B **96**, 045120 (2017).

[25] K. Haule and G. L. Pascut, Sci. Rep. **7**, 10375 (2017).

[26] K. W. Post, A. S. McLeod, M. Hepting, M. Bluschke, Y. Wang, G. Cristiani, G. Logvenov, A. Charnukha, G. X. Ni, P. Radhakrishnan, M. Minola, A. Pasupathy, A. V. Boris, E. Benckiser, K. A. Dahmen, E. W. Carlson, B. Keimer, and D. N. Basov, Nat. Phys. **14**, 1056 (2018).

[27] J. A. Alonso, M. J. Martínez-Lope, M. T. Casais, J. L. García-Muñoz, M. T. Fernández-Díaz, and M. A. G. Aranda, Phys. Rev. B **64**, 094102 (2001).

[28] Y. Lu, Z. Zhong, M. W. Haverkort, and P. Hansmann, Phys. Rev. B **95**, 195117 (2017).

[29] G. G. Guzmán-Verri, R. T. Brierley, and P. B. Littlewood, arXiv:1701.02318.

[30] A. Mercy, J. Bieder, J. Íñiguez, and P. Ghosez, Nat. Commun. **8**, 1677 (2017).

[31] C. Girardot, J. Kreisel, S. Pignard, N. Caillault, and F. Weiss, Phys. Rev. B **78**, 104101 (2008).

[32] M. K. Stewart, J. Liu, M. Kareev, J. Chakhalian, and D. N. Basov, Phys. Rev. Lett. **107**, 176401 (2011).

[33] J. Ruppen, J. Teyssier, O. E. Peil, S. Catalano, M. Gibert, J. Mravlje, J.-M. Triscone, A. Georges, and D. van der Marel, Phys. Rev. B **92**, 155145 (2015).

[34] S. Prosandeev, L. Bellaiche, and J. Íñiguez, Phys. Rev. B **85**, 214431 (2012).

[35] A. Hampel and C. Ederer, Phys. Rev. B **96**, 165130 (2017).

[36] A. B. Georgescu, O. E. Peil, A. Disa, A. Georges, and A. J. Millis, arXiv:1810.00480.

[37] A. Georges, G. Kotliar, W. Krauth, and M. J. Rozenberg, Rev. Mod. Phys. **68**, 13 (1996).

[38] G. Kotliar, S. Y. Savrasov, K. Haule, V. S. Oudovenko, O. Parcollet, and C. A. Marianetti, Rev. Mod. Phys. **78**, 865 (2006).

[39] S. B. Lee, R. Chen, and L. Balents, Phys. Rev. B **84**, 165119 (2011); Phys. Rev. Lett. **106**, 016405 (2011).

[40] A. Georges, L. D. Medici, and J. Mravlje, Annu. Rev. Condens. Matter Phys. **4**, 137 (2013).

[41] We checked that in all our DMFT calculations the orbital occupation numbers always ended up being nearly equal.

[42] S. Catalano, M. Gibert, V. Bisogni, F. He, R. Sutarto, M. Viret, P. Zubko, R. Scherwitzl, G. A. Sawatzky, T. Schmitt, and J.-M. Triscone, APL Mater. **3**, 062506 (2015).

[43] S. Middey, D. Meyers, M. Kareev, Y. Cao, X. Liu, P. Shafer, J. W. Freeland, J.-W. Kim, P. J. Ryan, and J. Chakhalian, Phys. Rev. Lett. **120**, 156801 (2018).

[44] G. Kotliar, E. Lange, and M. J. Rozenberg, Phys. Rev. Lett. **84**, 5180 (2000).

[45] P. Limelette, A. Georges, D. Jérome, P. Wzietek, P. Metcalf, and J. M. Honig, Science **302**, 89 (2003).

[46] P. E. Blöchl, Phys. Rev. B **50**, 17953 (1994).

[47] G. Kresse and D. Joubert, Phys. Rev. B **59**, 1758 (1999).

[48] G. Kresse and J. Hafner, Phys. Rev. B **47**, 558 (1993).

[49] G. Kresse and J. Furthmüller, Phys. Rev. B **54**, 11169 (1996).

[50] J. P. Perdew, K. Burke, and M. Ernzerhof, Phys. Rev. Lett. **77**, 3865 (1996).

[51] B. J. Campbell, H. T. Stokes, D. E. Tanner, and D. M. Hatch, J. Appl. Crystallogr. **39**, 607 (2006).

[52] J. M. Perez-Mato, D. Orobengoa, and M. I. Aroyo, Acta Crystallogr. A **66**, 558 (2010).

[53] J. A. Alonso, M. J. Martínez-Lope, M. T. Casais, M. A. G. Aranda, and M. T. Fernández-Díaz, J. Am. Chem. Soc. **121**, 4754 (1999).

[54] M. Schüler, O. E. Peil, G. J. Kraberger, R. Pordzik, M. Marsman, G. Kresse, T. O. Wehling, and M. Aichhorn, J. Phys.: Condens. Matter **30**, 475901 (2018).

[55] B. Amadon, F. Lechermann, A. Georges, F. Jollet, T. O. Wehling, and A. I. Lichtenstein, Phys. Rev. B **77**, 205112 (2008).

[56] M. Aichhorn, L. Pourovskii, P. Seth, V. Vildosola, M. Zingl, O. E. Peil, X. Deng, J. Mravlje, G. J. Kraberger, C. Martins, M. Ferrero, and O. Parcollet, Comput. Phys. Commun. **204**, 200 (2016).

[57] O. Parcollet, M. Ferrero, T. Ayral, H. Hafermann, I. Krivenko, L. Messio, and P. Seth, Comput. Phys. Commun. **196**, 398 (2015).

[58] E. Gull, A. J. Millis, A. I. Lichtenstein, A. N. Rubtsov, M. Troyer, and P. Werner, Rev. Mod. Phys. **83**, 349 (2011).

[59] P. Seth, I. Krivenko, M. Ferrero, and O. Parcollet, Comput. Phys. Commun. **200**, 274 (2016).

[60] K. Held, Adv. Phys. **56**, 829 (2007).

7

INFLUENCE OF CHARGE SELF-CONSISTENCY AND DOUBLE-COUNTING IN DFT+DMFT

In chapter 5.2 I found that when performing DFT+DMFT calculations for the rare-earth nickelates, technical questions arise related to the effect of CSC and the DC correction. I found that performing CSC calculations reduced the required Hund's coupling strength to obtain a stable CDI state significantly. Moreover, I found that the DC correction influences the on-site potential shift between the Ni_{LB} and Ni_{SB} site, thus being also critical for the stability of the CDI phase. In the following chapter I elucidate the effect of CSC and also the connected DC correction effects, in the DFT+DMFT method.

The following work will be soon available as a preprint as *"Charge self-consistency and double-counting in DFT+DMFT calculations for complex transition metal oxides"* on arXiv, see Ref. [145]. All calculations for $CaVO_3$ have been performed by S. Beck, whereas all calculations for $LuNiO_3$ have been performed by myself. The manuscript was written together, and discussed and corrected by my supervisor C. Ederer.

7.1 MOTIVATION

Although, from a theoretical point of view (see section 3.7.5) full CSC calculations are necessary to fulfill the stationary conditions of the DFT+DMFT method, in practice OS calculations are often performed to reduce computational effort. These calculations often lead to reasonable results, close to the results of corresponding CSC calculations [146–148]. Also, for rare-earth nickelates, OS calculations led to qualitative correct physics [24, 43]. This raises the question, how relevant the CSC outer loop of DFT+DMFT is. Especially, if in general qualitative correct results can be obtained by performing OS calculations. Moreover, it is important to understand, when also quantitative results are obtained by OS DFT+DMFT calculations, and when a CSC treatment is necessary. For example, in Ref. [149] and [135] it is shown for $SrVO_3$ that the effect of orbital polarization under strain is reduced in CSC calculations compared to OS calculations. This suggests, that especially in systems where some kind of charge redistribution is occurring, the charge self-consistency can have an important effect on quantitative results.

In general, the DC correction depends on the chosen correlated subspace. During my work, I only investigate so-called frontier orbital models. In such models, the correlated subspace is built using

only the bands close to the Fermi level, that have dominant e_g or t_{2g} character (depending on the chosen compound). In this correlated subspace, the p-d energy splitting is determined completely on the DFT level and is not adjusted in DMFT by a DC correction. Therefore, the question of the d-p splitting in the context of DC, will not be addressed here. However, as shown in section 5.2, in the case of systems with multiple effective impurity problems, charge can be transferred between the impurities during the DMFT loop. This will change the local occupancy, and hence change the DC potential on each site. Therefore, the DC correction is not trivial in such systems, and can significantly influence the result of a DFT+DMFT calculation.

Most previous studies were focusing on the effect of CSC and DC in p-d models [52, 91, 131, 146–148]. However, the computational demands of frontier orbital models are significantly reduced compared to a p-d model, and therefore the application of such models is quite appealing. Especially, in cases with large systems including multiple effective impurity problems. However, there are currently very few studies available that provide a systematic quantitative comparison between CSC and OS calculations in frontier orbital models.

In this chapter, I discuss in more detail how CSC can influence quantitative results of DFT+DMFT calculations performed for frontier orbital models. This includes a discussion of the effects on spectral, as well as structural properties, where the latter is of special importance in the context of rare-earth nickelates. I discuss also the potential influence of the DC correction on DFT+DMFT calculations, and show that this question is in some cases entangled with the question of CSC.

In the following I present a collaborative research project, carried out together with Sophie Beck. We investigated the effect of CSC and the DC correction in two chosen prototypical systems. I investigated $LuNiO_3$ exhibiting charge ordering, whereas S. Beck investigated $CaVO_3$, a system showing strong orbital polarization under strain [150]. For both systems, we constructed the low-energy subspace from the frontier orbitals found at the Fermi level. For $CaVO_3$ this corresponds to three V t_{2g} orbitals, and for $LuNiO_3$ to the Ni e_g orbitals. The resulting systems were investigated within DFT+DMFT, by applying a Hubbard-Kanamori interaction.

7.2 PROJECT SUMMARY

In the first part of the project we investigate the effect of CSC on the orbital polarization in $CaVO_3$ with, and without epitaxial strain. To do so, we calculate the orbital-resolved occupation of the impurity and $A(\omega = 0)$ of the t_{2g} orbitals as function of U (see Fig. 1 in Ref. [145]). As U increases, the system undergoes a MIT at a critical value U_{MIT}, while the orbital polarization increases [151]. In our

calculations, the unstrained $CaVO_3$ system shows a moderate orbital polarization in the insulating phase, which is only weakly influenced by CSC. Under 4% epitaxial strain, the orbital polarization is strongly increased, emptying two of the three t_{2g} orbitals completely, in agreement with previous studies performing OS calculations [150]. Here, we find that CSC calculations reduce the orbital polarization significantly, by 30%, increasing U_{MIT} from 4.7 eV to 4.9 eV. The effect can be also observed in the calculated spectral functions in Fig. 2 of the presented paper [145].

In the second part of the project, we investigate $LuNiO_3$. First, we perform calculations for the structure exhibiting the experimental breathing mode distortion [29]. Here, we investigate, for a constant value of $U = 1.85$ eV, the influence of J on $\nu = \langle n_{LB} \rangle - \langle n_{SB} \rangle$. As shown in the previous chapters, J critically determines the occurrence of the CDI state, and hence the size of ν. In our calculations, we find that performing CSC calculations reduces ν by approximately 10% compared to OS calculations, and therefore the tendency to undergo the transition to the CDI state is slightly decreased (see Fig. 3 in Ref. [145]).

Furthermore, we investigate the influence of the DC correction in the calculations for $LuNiO_3$ with experimental breathing mode distortion amplitude. Here, we compare two different scenarios. In the first scenario, we determine the site occupations entering the DC potential by the DMFT impurity occupations, whereas in the other scenario they are determined by the DFT Wannier orbital occupations. Note, that in the first scenario the DC potential is updated each DMFT iteration. In our calculations, we find that using the DMFT impurity occupations greatly increases the tendency to the CDI state compared to using the DFT Wannier orbital occupations, no matter if OS or CSC calculations are performed. This results in a CDI state for $J \geqslant 0.2$ eV (see Fig. 3 in Ref. [145]). On the other hand, the calculations with DC occupations determined from the DFT Wannier orbitals undergo the MIT only at a larger value of $J \geqslant 1.0$ eV. Thereby, we demonstrate that for $LuNiO_3$ OS calculations and CSC calculations give qualitatively similar results if the DMFT impurity occupations are used for determining the DC correction.

It should be noted, that when performing CSC calculations the DFT Wannier orbital occupations have no physical meaning, because they do not correspond to the charge density used to evaluate the Kohn-Sham potential. Only the DMFT impurity occupations have a physical meaning in CSC calculations. Moreover, we obtain similar results if the DMFT impurity occupations are used, and hence we suggest that the use of DMFT impurity occupations also in OS calculations is conceptually more meaningful.

By analyzing the obtained results for $LuNiO_3$, we show that the on-site potential difference $\Delta_s = \Delta^s_{DFT} - \Delta^s_{DC}$ is greatly increased

due to the DC when the DMFT impurity occupations are used. This effectively reduces the required J value to obtain a stable CDI state, showing that the DC correction critically influences the obtained results.

Next, we perform an analysis of the influence of CSC and the DC correction on the breathing mode energetics (see Fig. 5 in Ref. [145]). We show that the OS calculations display a stronger response to the breathing mode distortion, which results in deeper energy minima. Moreover, we identify cases where this leads to a stable equilibrium breathing mode distortion in OS calculations, whereas no such stable distortion is found in corresponding CSC calculations. Thus, we conclude that for quantitative correct results, especially for total energy calculations, CSC calculations need to be performed in systems exhibiting strong charge redistribution when performing DMFT calculations.

7.3 CONCLUSION

In this chapter I presented a study on the effect of CSC and DC in frontier orbital DFT+DMFT calculations. In a joint research project with S. Beck, it is demonstrated that in systems with strong orbital polarization or charge ordering, CSC can have an important quantitative effect on the results. We find, that in such systems the CSC loop between DFT and DMFT reduces the effect of charge redistribution compared to OS calculations.

In frontier orbital models where the DC correction is not trivial with multiple effective impurity problems, it is shown that OS DFT+DMFT calculations give qualitative correct results compared with CSC DFT+DMFT calculations if the DMFT impurity occupations are used to determine the DC potential. In the case of rare-earth nickelates, or any other system possibly exhibiting charge transfer between impurities in DMFT this shows, that the DC correction can have a significant influence on obtained results, especially when evaluating total energies. However, we suggest that for qualitative insights on electronic or spectral properties, OS calculations are mostly sufficient, in agreement with previous results [24, 43, 146–149].

7.4 PREPRINT

Charge self-consistency and double-counting in DFT+DMFT calculations for complex transition metal oxides

Alexander Hampel,[1,*] Sophie Beck,[1,†] and Claude Ederer[1,‡]

[1] *Materials Theory, ETH Zürich, Wolfgang-Pauli-Strasse 27, 8093 Zürich, Switzerland*

(Dated: July 25, 2019)

We investigate the effect of charge self-consistency (CSC) in density functional theory plus dynamical mean-field theory (DFT+DMFT) calculations compared to simpler "one-shot" calculations for two instructive example materials. For the correlated metal $CaVO_3$, where epitaxial strain can induce a transition towards an orbitally polarized insulating state, we find that the computationally more costly CSC scheme has only a moderate, quantitative effect, reducing the orbital polarization compared to the one-shot case, and only slightly shifting the critical interaction strength for the metal-insulator transition under strain. In the rare-earth nickelate $LuNiO_3$, however, the CSC can strongly affect the charge redistribution between inequivalent Ni sites. Thereby, the main effect is related to the double-counting correction, which tends to enhance the charge disproportionation, whereas the feedback loop between DFT and DMFT then partially reverts this by favoring a more homogeneous charge distribution. The latter effect is analogous to reducing the orbital polarization in strained $CaVO_3$. The effect of CSC in $LuNiO_3$ can be mimicked to some extent by using DMFT occupations to evaluate the double-counting correction in the one-shot calculations.

I. INTRODUCTION

During recent years, the combination of density functional theory (DFT) and dynamical mean-field theory (DMFT) has become a widespread tool to calculate properties of so-called "correlated materials", i.e., materials where the strong Coulomb repulsion between electrons in partially filled d or f shells leads to effects that cannot easily be treated within effective non-interacting electron theories[1]. The basic idea in combining DFT and DMFT is the assumption that for the relevant materials the electronic degrees of freedom can be separated into a "weakly interacting" part, for which a standard DFT treatment is adequate, and a "correlated subspace", which requires a more elaborate treatment of the electron-electron interaction. The latter leads, in general, to a redistribution of electrons within the correlated subspace compared to the DFT result. This change should then enter, in a self-consistent way, the effective potential felt by the weakly interacting electrons, which is achieved by iterating between DFT and DMFT steps. However, such a charge self-consistent (CSC) DFT+DMFT calculation leads to a higher computational cost compared to simpler "one-shot" (OS) calculations, where the charge rearrangement within the correlated subspace is neglected in the DFT calculation.

While CSC DFT+DMFT calculations have become more common recently, the DFT+DMFT method also continues to be applied to larger and more complex systems, such as, e.g., oxide heterostructures,[2–5] defective systems,[6–8] or large molecules[9,10]. Thus, while DFT+DMFT develops towards a standard *ab initio*-based computational method for materials science[11,12], it becomes essential to be able to reduce the required computational effort whenever possible by using more approximate variants of the method, e.g., by neglecting charge self-consistency. Thus, a detailed understanding of the effect of charge self-consistency is desirable, in order to better judge in which cases a CSC calculation is crucial or, more importantly, under what circumstances a one-shot calculation is sufficient. Unfortunately, there are currently very few studies available that provide a systematic quantitative comparison between CSC and one-shot calculations. It can be assumed that charge self-consistency is particularly relevant for systems where correlation effects lead to a redistribution of electrons, e.g., for systems with charge-, and/or orbital-ordering. For example, existing studies of epitaxially strained $SrVO_3$ demonstrate a reduced orbital polarization in CSC calculations compared to OS[13,14].

Most previous work addressing the influence of charge self-consistency in DFT+DMFT calculations in transition metal (TM) oxides typically employed a so-called "p-d"-model to define the correlated subspace,[15–20] i.e., using a basis of rather localized, atomic-like orbitals constructed from a broad energy window that includes the TM d as well as all oxygen p bands. This appears conceptually appealing, since a wider energy window corresponds to a larger, and thus more complete, basis set, and since the use of rather localized orbitals provides better justification for the DMFT assumption of a purely local self-energy and Coulomb interaction[19]. On the other hand, this also increases the computational load compared to using a "minimal" correlated subspace corresponding to a narrow energy window. In transition metal oxides, the latter typically includes only either t_{2g} or e_g bands.

A crucial point arising in such DFT+DMFT calculations using a p-d-type orbital subspace, is that the physically very important charge transfer energy, $\Delta_{p\text{-}d}$, which describes the energy difference between oxygen p and transition metal d states, effectively becomes controlled by the double-counting correction[15,20]. The latter is required to account for the electron-electron interaction within the correlated subspace that is already included

on the DFT level, and is notoriously ill-defined[21]. Different expressions to account for the double counting (DC) have been suggested[20,22], but in some cases the double-counting needs to be adjusted manually, in order to obtain satisfactory results[15,16]. For such p-d-type calculations, it was shown that the CSC calculations produce essentially the same spectral properties as OS calculations, if one tunes the DC correction to yield the same d-state occupancy[15]. It is, however, not clear a priori, that more complex observables like the energy need to agree within both approaches.

In this work we focus on DFT+DMFT calculations that employ a minimal correlated subspace corresponding to only a small number of near-Fermi-surface bands, which are expressed in a localized basis through a suitable transformation in terms of Wannier functions[23]. This scheme requires a comparatively small computational cost, by including only the minimal number of orbitals needed to describe the dominant low-energy physics within DMFT. Furthermore, it often allows for an intuitive interpretation of Wannier occupations in terms of formal charge states, since the corresponding Wannier functions include the hybridization with the oxygen p states as "tails" located on the oxygen sites. The presence of these hybridization tails can also be viewed as inclusion of an "effective" p-d inter-site interaction[24], which is typically neglected in the p-d-model for simplicity. Finally, the use of a minimal correlated subspace avoids the problem that the DC correction critically affects the important charge transfer energy. However, as we show in the following, the DC correction can still have a strong effect for systems with multiple inequivalent correlated sites.

We focus on two specific cases, the strain-induced metal-insulator transition in $CaVO_3$, and the more complex case of $LuNiO_3$, which is representative for the whole series of rare earth nickelates that exhibit a metal-insulator transition involving charge disproportionation between the Ni sites. The charge disproportionation is also strongly coupled to a structural distortion. While for the case of $CaVO_3$ all TM sites are symmetry-equivalent, and thus the DC correction does not influence the results, this no longer holds for the rare earth nickelates, where the DC correction crucially affects the charge disproportionation between inequivalent Ni sites. The two cases will be discussed in Sec. III. However, first we will introduce the theoretical framework for our DFT+DMFT calculations (Sec. II).

II. THEORETICAL FRAMEWORK AND COMPUTATIONAL DETAILS

A. DFT calculations

The structural relaxations for $CaVO_3$ within the 20 atom unit cell in *Pbnm* space group symmetry are performed using the QUANTUM ESPRESSO package[25]. We employ scalar-relativistic ultrasoft pseudopotentials, with the $3s$ and $3p$ semicore states included in the valence for both V and Ca, together with the exchange-correlation functional according to Perdew, Burke, and Ernzerhof[26]. Cell parameters and internal coordinates are relaxed until all force components are smaller than 0.1 mRy/a_0 (a_0: Bohr radius) and all components of the stress tensor are smaller than 0.1 kbar. The plane-wave energy cutoff is set to 70 Ry for the wavefunctions and 840 Ry for the charge density. A $6\times6\times4$ Monkhorst-Pack k-point grid is used to sample the Brillouin zone, and the Methfessel-Paxton scheme with a smearing parameter of 0.02 Ry is used to broaden electron occupations. For the calculation of epitaxially strained $CaVO_3$, the in-plane lattice parameters are increased by 4% and kept fixed, while the c-component of the cell and all atomic positions are relaxed.

All DFT calculations for $LuNiO_3$ as well as the DFT parts of all our CSC DFT+DMFT calculations are performed using the projector augmented wave (PAW) method[27], implemented in the "Vienna Ab initio Simulation Package"(VASP)[28–30], and also using the exchange correlation functional according to Perdew, Burke, and Ernzerhof[26]. For Ni, we use the PAW potential where the $3p$ semi-core states are included as valence electrons, while for Lu, we use the PAW potential corresponding to a 3+ valence state with f-electrons frozen into the core. For the $CaVO_3$ calculations with VASP, we use the PAW potentials where the s and p semi-core states are included as valence electrons for both Ca and V. Furthermore, a k-point mesh with $9 \times 9 \times 7$ grid points along the three reciprocal lattice directions is used and a plane wave energy cut-off of 550 eV is chosen for $LuNiO_3$ and 600 eV for $CaVO_3$. The structure of $LuNiO_3$ is fully relaxed within *Pbnm* symmetry, both internal parameters and lattice parameters, until the forces acting on all atoms are smaller than 10^{-4} eV/Å.

B. DFT+DMFT calculations

a. Construction of the correlated subspace In the DFT+DMFT method, the Kohn-Sham (KS) Hamiltonian within the chosen energy window is mapped onto a basis of localized states, spanning the correlated subspace $\mathcal{C}$, then a local Coulomb interaction is added, and the resulting Hubbard-like lattice Hamiltonian is solved via the DMFT approximation. Without feedback to the DFT part, this corresponds to a OS calculation. To perform CSC calculations, one computes a correction to the charge density, $\Delta\rho = \rho^{\mathrm{DMFT}} - \rho^{\mathrm{DFT}}$, which is then passed back to the DFT code (here VASP) to calculate new KS wave-functions and hence, update the correlated subspace. In a fully CSC calculation, this is repeated until $\Delta\rho$ does not change compared to the previous iteration.

For the DMFT calculation, the electronic degrees of freedom within the chosen energy window are described

via the interacting lattice Green's function:

$$\hat{G}(\mathbf{k}, i\omega_n) = \left[(i\omega_n + \mu)\mathbb{1} - \hat{H}_{\mathrm{KS}}(\mathbf{k}) - \hat{\Sigma}(\mathbf{k}, i\omega_n)\right]^{-1} \quad (1)$$

where μ is the chemical potential and $\hat{H}_{\mathrm{KS}}(\mathbf{k})$ is the Kohn-Sham (KS) Hamiltonian. The lattice self-energy $\hat{\Sigma}(\mathbf{k}, i\omega_n)$ is obtained by solving the effective DMFT impurity problem (see next sub-section).

The lattice Green's function in Eq. (1) is expressed in the Kohn-Sham (Bloch) basis. To achieve the up/down-folding between the quantities defined within the correlated subspace and the Green's function in the KS basis,

$$\hat{G}^{\mathcal{C}}_{LL'}(i\omega_n) = \sum_{k,\nu\nu'} \hat{P}_{L\nu}(\mathbf{k})\ \hat{G}_{\nu\nu'}(\mathbf{k}, i\omega_n)\ \hat{P}^{\dagger}_{L\nu}(\mathbf{k})\ , \quad (2)$$

projector functions $\hat{P}_{L\nu}(\mathbf{k})$ are introduced. The projector functions are defined as projections of the KS eigenstates $|\Psi_{\nu\mathbf{k}}\rangle$ onto localized orbitals $|\chi_L\rangle$, $\hat{P}_{L\nu}(\mathbf{k}) \equiv \langle\chi_L|\Psi_{\nu\mathbf{k}}\rangle$. Here, L serves as compound index for all local quantum numbers (site, orbital, and spin-character).

Here, we use the recent implementation of projection to localized orbitals (PLOs)[31] in VASP[14], in combination with the TRIQS/DFTTools software package[32,33]. To construct an optimal projector function, we apply the scheme introduced in Ref. 14, choosing a linear combination of the PAW partial wave augmentation channels that maximizes the overlap between the projector and the KS state inside a chosen energy window, which matches that of the correlated subspace $\mathcal{C}$. In this work, we use projections on all five localized d states in VASP, while the subsequent orthonormalization within the TRIQS/DFTTools converter includes only the t_{2g}- or e_g-like orbitals within the energy window of the correlated subspace $\mathcal{C}$.

The strong octahedral rotations present within *Pbnm* symmetry lead to large off-diagonal crystal-field terms in the KS Hamiltonian, and the non-interacting Green's function for the effective impurity problem is no longer diagonal. Since this can induce severe numerical problems when solving the impurity problem, we perform a local unitary transformation of each impurity Green's function after the down- respectively before the up-folding, which diagonalizes the initial non-interacting local Hamiltonian on each site transforming the system into the crystal field basis. The DFT+DMFT code used for the calculations in this paper is publicly available on github[34].

For $CaVO_3$ we also perform OS DFT+DMFT calculations based on the electronic structure obtained with Quantum ESPRESSO. In this case the construction of the low-energy tight-binding Hamiltonian, used as input for the OS DMFT calculation, is performed using the Wannier90 code[35] and the wannier90 converter included in TRIQS/DFTTools.

b. Solving the impurity problem For both $CaVO_3$ (t_{2g} subspace) and $LuNiO_3$ (e_g subspace) the effective impurity problem within the DMFT cycle is solved with the TRIQS/cthyb continuous-time quantum Monte Carlo (QMC) hybridization-expansion solver[36]. For each impurity we add a local Coulomb interaction in the form of the Hubbard-Kanamori Hamiltonian[37],

$$\begin{aligned} H_{\mathrm{int}} \ =\ & U \sum_{m} \hat{n}_{m\uparrow}\hat{n}_{m\downarrow} \ +\ (U-2J) \sum_{m\neq m'} \hat{n}_{m\uparrow}\hat{n}_{m'\downarrow} \\ & + (U-3J) \sum_{m<m',\sigma} \hat{n}_{m\sigma}\hat{n}_{m'\sigma} \\ & + J \sum_{m\neq m'} c^{\dagger}_{m\uparrow}c^{\dagger}_{m\downarrow}c_{m'\downarrow}c_{m'\uparrow} - J \sum_{m\neq m'} c^{\dagger}_{m\uparrow}c_{m\downarrow}c^{\dagger}_{m'\downarrow}c_{m'\uparrow}\ , \end{aligned} \quad (3)$$

including all spin-flip and pair-hopping terms. Here, the operator $c^{\dagger}_{m\sigma}$ creates an electron in the atom-centered Wannier orbitals of type m and spin σ. The interaction parameters are given by the local intra-orbital Coulomb repulsion U, and the Hund's coupling J. To reduce the QMC noise in the high-frequency regime of the impurity self-energy Σ_{imp} and G_{imp}, we represent both quantities in the Legendre basis[38] and sample the Legendre coefficients G_l directly within the TRIQS/cthyb solver.

c. Double counting correction To correct the electron-electron interaction within the correlated subspace already accounted for within VASP, we use the fully-localized limit DC correction scheme[39]. Specifically, we use the parameterization given in Ref. 1 for the DC potential,

$$\Sigma^{\mathrm{imp}}_{dc,\alpha} = \bar{U}(n_\alpha - \frac{1}{2}) \quad , \quad (4)$$

where n_α is the occupation of impurity site α, and the averaged Coulomb interaction $\bar{U}$ is defined as[1]

$$\bar{U} = \frac{U + (M-1)(U-2J) + (M-1)(U-3J)}{2M-1}\ . \quad (5)$$

This potential shift is added to the impurity self-energy, and its form is directly tailored to the Hubbard-Kanamori interaction Hamiltonian in Eq. (3) for a t_{2g}- or e_g-model resulting from an octahedral crystal-field environment of M interacting orbitals ($M = 3$ for $CaVO_3$ and $M = 2$ for $LuNiO_3$).

In this work, we draw particular attention on how the occupations n_α used for the DC correction are evaluated, i.e., whether they correspond to: a) the occupations of the Wannier functions as obtained from DFT, or b) the occpations corresponding to the impurity Green's function G_{imp} calculated by the QMC solver within the DMFT step. It can be misleading to assume that these quantities are the same, even within a CSC calculation. Indeed, when the system is in a charge-ordered phase, such as, e.g., in heterostructures or nickelates, or in any other case with several inequivalent impurity problems, different impurities can exchange charge within the DMFT loop, potentially leading to drastic changes of the

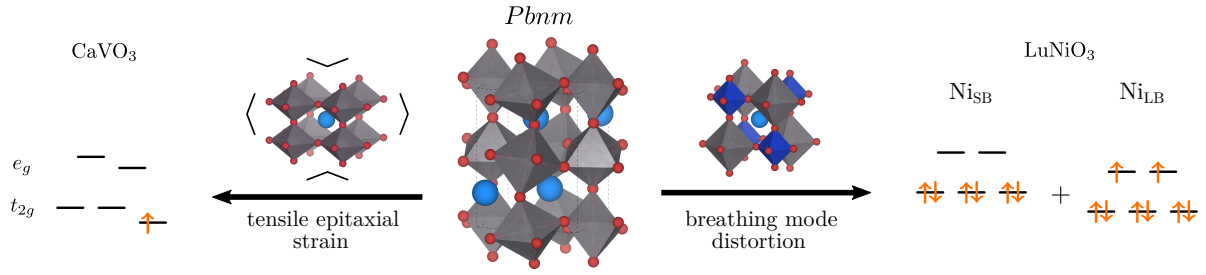

FIG. 1. Exemplary *Pbnm* crystal structure, as well as the main distortion modes relevant for the discussion of $CaVO_3$ and $LuNiO_3$, respectively, i.e., tetragonal strain (left) and octahedral breathing mode distortion (right). The d-orbital energy levels that result from these distortions and the occupations for each compound are also depicted. Note that for simplicity we omitted octahedral rotations in the simplified lattice structures and the corresponding d-level crystal-field splittings.

local occupations compared to the ones calculated within the DFT step. In principle, only the occupations evaluated for the impurity problem within DMFT that are used to define the charge density correction, have physical meaning within a CSC DFT+DMFT calculation. By contrast, the occupations obtained in the DFT part do not correspond to the charge density that is used to evaluate the Kohn-Sham potential. However, in the case of a OS DFT+DMFT calculation, the question of whether to use DFT or DMFT occupations for the DC correction is ambiguous. An informal (and perhaps unrepresentative) community survey conducted by us, has shown that both variants are currently used in different studies. Here, we show that in certain systems the question of how to extract n_α can have a strong influence on the results, and that one should be aware of this issue when evaluating the DC correction.

d. Calculation of observables From the imaginary-time Green's function, we calculate the spectral weight around the Fermi level, $\bar{A}(\omega=0) = -\frac{\beta}{\pi}\mathrm{Tr}\,\hat{G}^{\mathcal{C}}_{LL'}(\beta/2)$, which indicates whether the system is metallic ($\bar{A}(0) > 0$) or insulating ($\bar{A}(0) \approx 0$)[40]. For $T = 0$ ($\beta \to \infty$), $\bar{A}$ is identical to the spectral function at $\omega = 0$. For finite temperatures, it represents a weighted average around $\omega = 0$ with a width of $\sim k_\mathrm{B}T$[40].The full real-frequency spectral function $A(\omega)$ is obtained via analytic continuation using the maximum entropy method[41].

The on-site density matrix can be obtained directly from the local Matsubara Green's function as $n_{LL'} = \frac{1}{\beta}\sum_{\omega_n}\hat{G}^{\mathcal{C}}_{LL'}(i\omega_n)$. This quantity is also used to calculate the orbital polarization, i.e., the difference in orbital occupancies, after diagonalization of the on-site density matrix $n_{LL'}$[42].

To extract the total energy of the system we use the following formula[23]:

$$\begin{aligned} E_{\mathrm{DFT+DMFT}} = {} & E_{\mathrm{DFT}}[\rho] \\ & - \frac{1}{N_k}\sum_{\nu\in\mathcal{C},\mathbf{k}} \epsilon^{\mathrm{KS}}_{\nu,\mathbf{k}}\, f_{\nu\mathbf{k}} + \langle H_{\mathrm{KS}}\rangle_{\mathrm{DMFT}} \\ & + \langle H_{\mathrm{int}}\rangle_{\mathrm{DMFT}} - E^{\mathrm{imp}}_{\mathrm{DC}} \quad , \end{aligned} \tag{6}$$

where $\epsilon^{\mathrm{KS}}_{\nu,\mathbf{k}}$ are the KS eigenvalues with corresponding weights $f_{\nu\mathbf{k}}$ within the correlated subspace $\mathcal{C}$, and $\langle\cdot\rangle_{\mathrm{DMFT}}$ denotes quantities evaluated from the DMFT solution. The interaction energy $\langle H_{\mathrm{int}}\rangle_{\mathrm{DMFT}}$ is calculated using the Galitskii-Migdal formula[43,44], and the last term in Eq. (6) subtracts the DC energy. To ensure high accuracy, we sample the total energy over a minimum of additional 60 converged DMFT iterations after the CSC DFT+DMFT loop is already converged. Convergence is reached when the standard error of the site occupation during the last 10 DFT+DMFT loops is smaller than 1.5×10^{-3}. This way, we achieve an accuracy in the total energy of < 5 meV. All DMFT calculations are performed for $\beta = 40$ eV^{-1}, which corresponds to a temperature of 290 K.

III. MATERIALS & RESULTS

To analyze the effect of CSC within DFT+DMFT, we study two representative examples of TM oxides with different levels of complexity. First, we consider the case of unstrained and strained $CaVO_3$. While in the former case this material is a correlated metal[45,46], it has recently been demonstrated that tensile epitaxial strain leads to a transition towards the Mott insulating state within OS DFT+DMFT calculations[47]. An important aspect in this transition is the strain-induced crystal-field splitting between the partially filled t_{2g} orbitals, leading to a strong orbital polarization, and thus a local charge redistribution, which can potentially affect the result of a CSC compared to a OS DFT+DMFT calculation. However, in $CaVO_3$, all correlated sites are symmetry-equivalent and thus the DC correction is irrelevant when using a minimal "t_{2g}-only" correlated subspace.

Second, we consider the rare earth nickelate $LuNiO_3$, which exhibits a complex interplay between a specific structural distortion and an associated charge ordering leading to a metal-insulator transition[48]. Here, two symmetry-inequivalent types of Ni sites appear in the distorted insulating state, which allows also to analyze the effect of the site-dependent DC correction within a CSC DFT+DMFT calculation.

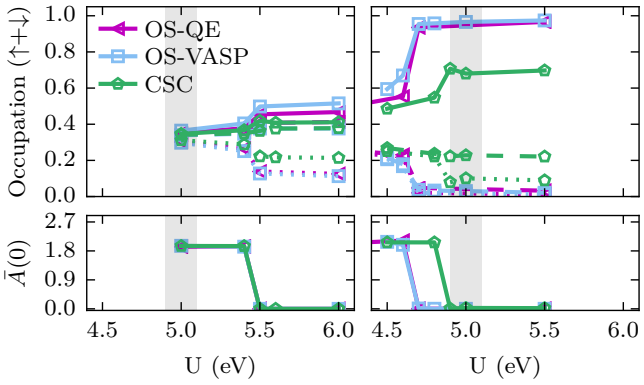

FIG. 2. Results obtained using OS and CSC DFT+DMFT employing the PLO basis in VASP, compared to OS calculations with Wannier functions and Quantum Espresso (QE), for bulk (left) and strained (right) $CaVO_3$. Top panels: Orbitally-resolved occupations as a function of the interaction parameter U. Bottom panels: averaged spectral weight at the Fermi level, $\bar{A}(0)$.

Both materials, $CaVO_3$ and $LuNiO_3$, exhibit a distorted perovskite structure with *Pbnm* space group (in the case of $LuNiO_3$ this corresponds to the high symmetry metallic phase). The corresponding unit cell contains four TM atoms surrounded by edge-connected oxygen octahedra, that are tilted and rotated around the Cartesian axes, corresponding to the so-called $GdFeO_3$-type distortion ($a^-a^-c^+$ tilt system in Glazer notation), as depicted in Fig. 1. The d-levels of the TM ions are split into e_g and t_{2g} manifolds by the octahedral crystal field, and the remaining degeneracies can be further lifted by additional distortions of the oxygen octahdra (also shown schematically in Fig. 1).

A. $CaVO_3$ - orbital polarization

As stated above, bulk $CaVO_3$ is a moderately correlated metal with weak orbital polarization that can undergo a transition to the Mott-insulating state under tensile epitaxial strain or in ultra-thin films[47,49,50]. As has been pointed out in Ref. 51, the orbital polarization resulting from the orthorhombic distortion of the perovskite structure is an important factor in the MIT. Several examples suggest that by an appropriate tuning of the bandwidth and the crystal-field splitting via, for example, strain or dimensional confinement, the resulting charge redistribution enhances the orbital polarization, eventually leading to a MIT[47,49,52]. For example, as depicted in Fig. 1, tensile epitaxial strain will lift the degeneracy of the t_{2g}-states, lowering the energy of one orbital compared to the other two. Since the orbital polarization in $CaVO_3$ can be seen as a measure for the likelihood of the Mott insulating state, it is clear that describing this quantity accurately is essential for the success of the chosen method.

As described in Sec. II, we perform DFT+DMFT calculations for the bulk structure of $CaVO_3$ using three different schemes, i.e., OS calculations using either maximally localized Wannier functions (magenta line in Fig. 2) or PLOs (blue lines in Fig. 2) to represent the correlated subspace, as well as CSC calculations using PLOs (green lines in Fig. 2). From this we obtain the orbital occupations and spectral weight at the Fermi level, shown in Fig. 2, as a function of the Coulomb interaction parameter U. In all cases, the spectral weight is finite for small values of U, where the system is metallic, and then becomes zero in the insulating phase for large U, with a rather sharp transition at $U_{\rm MIT}$. For the unstrained bulk system, all three approaches give identical results for the spectral weight as function of U, with a critical value of $U_{\rm MIT}$=5.5 eV. Thus, at $U \approx 5$ eV, which is typically considered as realistic value for $3d^1$ transition metal oxides[46], we find a finite weight corresponding to metallic behaviour, in agreement with experimental observations. This shows that the obtained results do not depend on details of the implementation, such as small differences in the basis used to represent the correlated sub-space.

From the occupations shown in Fig. 2 (top left), it can be seen that the orbital polarization is weak in the metallic regime, but is significantly enhanced above $U_{\rm MIT}$, where the occcupation of one orbital is decreased compared to the other two orbitals. This is in line with the bulk crystal-field splitting, where one orbital is energetically higher than the other two, with only a small difference between the latter[47]. Here, the two different OS calculations agree extremely well, while the orbital polarization is slightly reduced in the CSC calculation, however with no apparent effect on the predicted $U_{\rm MIT}$.

Under 4% tensile strain (right panels in Fig. 2), the MIT is shifted to lower U values, below the realistic value of $U \approx 5$ eV. Here, both the Wannier- and projector-type OS calculations agree within the accuracy of the method, and give exactly the same critical value of the critical interaction parameter of $U_{\rm MIT} = 4.7$ eV. The CSC calculation, however, places the MIT at a slightly higher value of $U = 4.9$ eV.

An even stronger difference between OS and CSC calculations can be seen in the orbital polarization, which is generally strongly enhanced compared to the unstrained case, due to a large strain-induced crystal-field splitting[47,52] (see Fig. 1). Within the OS calculations, both PLO and Wannier-based, we find that in the insulating regime two orbitals become completely empty, while the third one is essentially fully occupied by a single electron, i.e., the system exhibits full orbital polarization. In the CSC calculation this orbital polarization is significantly reduced, with a maximal occupation of ~ 0.7 in the preferential orbital. The crystal-field-induced orbital polarization, enhanced by electronic interaction effects, has previously been suggested to be an important factor supporting the insulating phase[46], since the resulting effective half-filling of only one orbital promotes the MIT as opposed to fractional occupation of three degen-

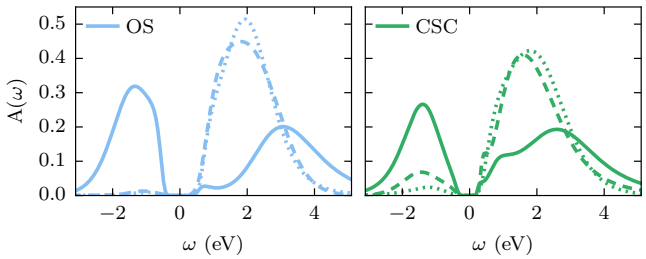

FIG. 3. Orbitally-resolved spectral functions for $CaVO_3$ under 4 % tensile epitaxial strain, obtained from OS (left) and CSC (right) DFT+DMFT calculations.

erate levels. This is consistent with our results, since the lower orbital polarization in the CSC calculation correlates with a higher U_{MIT} compared to the OS case. To illustrate the difference between OS and CSC calculations in the strained case, we plot the spectral function $A(\omega)$ at $U = 5.0\,\mathrm{eV}$ for both cases in Fig. 3. Here, the three different line-styles correspond to the three different t_{2g}-like orbitals. As discussed previously, in the OS calculation one of the orbitals is essentially completely occupied, while the remaining two are empty. In contrast to this, the CSC calculation shows a correlation-induced charge redistribution from the occupied orbital to the previously empty orbitals. Furthermore, comparing the gap sizes of both cases, it is clearly visible that in the CSC case the gap is reduced compared to OS, similar to what has been reported in earlier studies on $SrVO_3$[13].

Overall, we conclude that charge self-consistency only plays a minor role for systems with weak or vanishing orbital polarization, while for systems with largely different orbital occupations, the OS calculation can lead to an overestimation of the orbital polarization, which in turn can affect the tendency of the system to undergo a MIT. While the effect on U_{MIT} is not too strong in the present case, the corresponding differences in spectral properties can be more pronounced. Nevertheless, it appears that for the present case, OS calculations can at least give reliable qualitative information about the overall system behavior, such as, e.g., the effect of tensile epitaxial strain on U_{MIT}, favoring the insulating state.

Furthermore, we note that in our calculations using frontier orbitals, we find very good agreement between the PLO and Wannier-based method, both in the spectral properties and for the orbital occupations. This is in contrast to previous studies, reporting that projector-based methods require a larger U in *p-d* models due to larger hybridization effects[16].

B. $LuNiO_3$ — charge-ordering and structural energetics

The second case that we analyze is the rare earth nickelate $LuNiO_3$. This material belongs to the family of rare-earth nickelates, $RNiO_3$, where R can be any rare-earth ion ranging from Lu to Pr, including Y. All members of the series exhibit a MIT, which is accompanied by a structural transition, lowering the space group symmetry from $Pbnm$ to $P2_1/n$. The corresponding structural distortion results in a three dimensional checkerboard-like arrangement of long bond (LB) and short bond (SB) NiO_6 octahedra, referred to as breathing mode distortion[53], and schematically shown on the right side of Fig. 1. Recent theoretical work indicates that this transition is related to an electronic instability towards spontaneous charge disproportionation on the Ni sites, which couples to the breathing mode, leading to a first-order coupled structural-electronic transition into a charge-disproportionated insulator (CDI)[54,55]. Furthermore, the choice of the R site cation determines the degree of octahedral rotations in the corresponding high symmetry $Pbnm$ structure, and thus the bandwidth. The latter then controls how close the system is to the electronic instability, driving trends across the series[54–58].

Here, we use the case of $LuNiO_3$ to analyze if, and how, the charge disproportionation, as a specific example for charge-ordering phenomena in general, is affected by the inclusion of charge self-consistency in DFT+DMFT. Earlier studies by Park *et al.*[59] also investigated the effect of CSC and DC for $LuNiO_3$ using a *p-d*-type subspace. They found only a small effect due to CSC on total energy calculations, but had to adjust the DC correction to obtain a stable finite equilibrium breathing mode distortion. Here, we use a minimal correlated subspace of two "frontier" e_g-like orbitals per Ni site for our DFT+DMFT calculations. As shown in Ref. 60, the electronic instability towards charge disproportionation and the resulting *site-selective Mott transition*[61] is well described within DFT+DMFT using such a minimal subspace.

To isolate the effect of the structural breathing mode distortion on the electronic charge disproportionation and the total energy of the system, we employ a symmetry-based mode decomposition[62], as outlined in Refs. 55, 58, and 63, and using the software ISODISTORT[64]. This allows to add the breathing mode distortion, with symmetry label R_1^+, on top of the relaxed $Pbnm$ structure, and systematically vary its amplitude without changing any other parameter of the unit cell.

a. Results for fixed structure First, we calculate the properties of $LuNiO_3$ for a fixed structure, using the experimentally observed breathing mode amplitude, $R_1^+ = 0.075$ Å[65], and for varying Hund's coupling J. As shown in Ref. 60, the charge disproportionation and the resulting MIT depend sensitively on J, which thus allows us to critically examine the influence of CSC on the most crucial system properties. We use a fixed U value of 1.85 eV, which corresponds to the value calculated for $LuNiO_3$ using the constrained random phase approximation (cRPA)[55,66]. The results are depicted in Fig. 4, where in the top panel the charge disproportionation, $\nu \equiv \langle n_{\mathrm{LB}} \rangle - \langle n_{\mathrm{SB}} \rangle$, i.e. the difference of the e_g occupation between the LB and SB Ni sites, is shown as function of J. The bottom panel shows the corresponding value

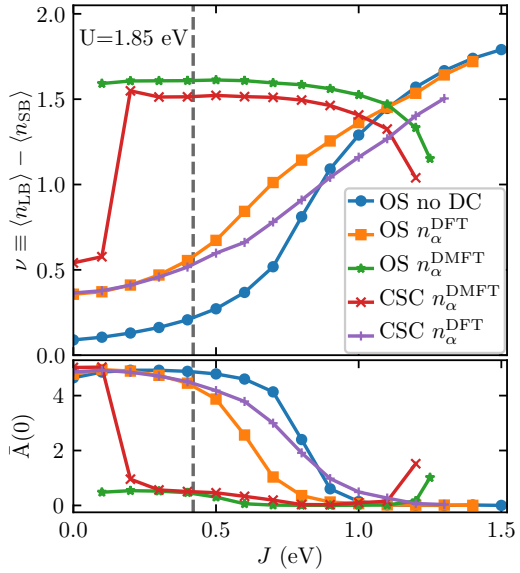

FIG. 4. Results of different DFT+DMFT calculations for $LuNiO_3$ using the experimental R_1^+ amplitude, $U = 1.85\,\mathrm{eV}$, and varying J. CSC and OS calculations are labeled accordingly. For calculations labeled n_α^{DFT} (n_α^{DMFT}) the DFT (DMFT) occupations have been used to evaluate the DC corcetion. The dashed vertical line marks the cRPA value of J[55]. Top: charge disproportionation ν; bottom: corresponding spectral weight at the Fermi level.

for $\bar{A}(0)$, indicating whether the system is metallic or insulating. The dashed vertical line corresponds to the J value obtained within cRPA[55,66]. Different data-sets in Fig. 4 correspond to DFT+DMFT calculations with different treatments of the DC correction, both OS and CSC, which we discuss in the following.

We first focus on the data-set labeled "CSC n_α^{DMFT}" (shown in red), which corresponds to the CSC calculation where the occupations entering the DC correction are calculated from the impurity occupations, and are updated in each DMFT iteration. This can be considered as the correct way to perform such CSC DFT+DMFT calculations, since the converged n_α^{DMFT} correspond to the corrected charge density from which the KS potential is constructed within the DFT step. In this case, the transition to the CDI occurs at $J = 0.2$ eV, indicated by clear jumps in ν and $\bar{A}(0)$. Note that the jump in ν leads to a drastic change in the DC potential difference between the Ni sites. For not too large J (see also below), the DC correction tends to increase the charge disproportionation by further lowering the e_g states on the more occupied LB site compared to the less occupied SB site. For further increasing J, ν stays almost constant until $J \approx 0.8$ eV, where ν decreases again. Finally, at around $J = 1.2$ eV, the system becomes metallic again. This can be explained by the fact that for increasing J, the DC potential, proportional to $\bar{U} = U - \frac{5}{3}J$, decreases, and eventually changes sign for $J = 1.11$ eV where $\bar{U} = 0$. Thus, above $J = 1.11\,\mathrm{eV}$ the DC correction opposes the charge disproportionaton by lowering the e_g levels of the SB sites relative to the LB sites.

Comparing the CSC calculation with the OS calculation where also n_α^{DMFT} has been used to evaluate the DC correction (shown in green), it can be observed that in the OS calculation the system is already in the CDI state even for $J = 0.2$ eV. In addition, a small shift to larger ν can be observed compared to the CSC case. Thus, the tendency towards the CDI state is slightly stronger than in the CSC calculation. In contrast, the OS calculation using n_α^{DFT} (shown in orange) leads to a significantly reduced ν, which increases slowly with increasing J. Moreover, for small $J < 0.5$ eV, clear metallic behavior is observed, while from $J = 0.5$ to 1.0 eV, the system undergoes the MIT, where eventually at $J = 1.0$ eV the system is completely in the CDI state with $\nu > 1.0$. The occupations obtained in the initial DFT step are $n_{\mathrm{LB}}^{\mathrm{DFT}} \approx 1.15$ and $n_{\mathrm{SB}}^{\mathrm{DFT}} \approx 0.85$.

For comparison, we also perform a CSC calculation where the DFT ocupations are used for the DC correction (shown in purple). However, one should note, that these calculations are somewhat artificial, since the DFT Wannier orbital occupations loose their physical meaning in a CSC calculation, and are used here just to allow for a more systematic comparison between OS and CSC calculations. One can see that overall the results of these calculations show similar behavior than the corresponding OS calculation using n_α^{DFT}, albeit with a small further reduction of ν.

The fixed structure calculations for $LuNiO_3$, show that performing CSC calculations leads to a small reduction of ν compared to OS calculations, if in both calculations the DMFT impurity occupations are used to determine the DC potential. Moreover, we find that the DC has a very strong effect, so that a OS calculation with DFT occupations significantly underestimates the tendency towards charge disproportionation compared to the "correct" CSC calculation.

To compare our calculations with Ref. 60 we also performed OS calculations without a DC correction (shown in blue). These calculations exhibit overall smaller ν values, clearly showing that the DC correction supports the CDI state (for positive $\bar{U}$). Furthermore, at $J = 1.1$ eV, where $\bar{U} \approx 0$, the DC vanishes and all OS calculations give the same result, while in the CSC calculations a shift to slightly smaller ν can be observed.

The complex behavior found in our calculations can be explained, as first proposed by Mazin *et al.*[67], by the fact that the Hund's coupling J is the critical ingredient of the CDI state. They showed in an atomic picture that when $U - 3J$ becomes small and is overcome by the energy difference between the Ni sites, Δ_s, which results from the breathing mode distortion and the charge disproportionation, the CDI state is favored. This regime is accessible in systems with small or negative charge-transfer gap, which results in a strong screening of the Coulomb interaction in the effective d bands, whereas the Hund's coupling is less sensitive to screening[67]. A strong

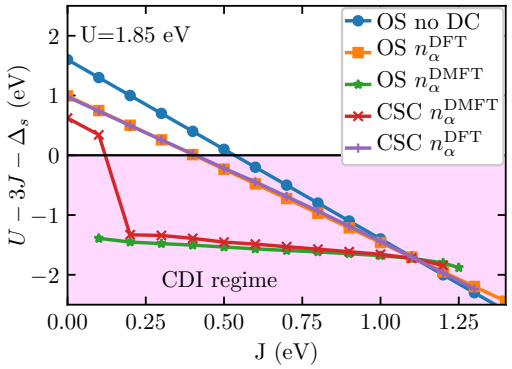

FIG. 5. $U-3J-\Delta_s$ as function of J for $LuNiO_3$ with the experimental R_1^+ amplitude[65], corresponding to the calculations shown in Fig. 4. $U-3J-\Delta_s$ is shown for the different flavors of DC (n_α^{DFT} vs. n_α^{DMFT}) and for OS and CSC calculations. If $U-3J-\Delta_s<0$ the CDI state is favored (magenta shaded area).

screening of U has been confirmed in recent cRPA studies of nickelates[24,55]. Moreover, in Ref. 68 it is shown, that such a CDI regime for small or negative $U-3J$ is also accessible in a general three orbital Hubbard model, and is thus not limited to nickelate systems.

Subedi *et al.*[60] found that the CDI state emerges in the frontier e_g model for nickelates when the following inequality is satisfied (derived from the the atomic limit):

$$U-3J \lesssim \Delta_s \quad . \tag{7}$$

Here, Δ_s is the "bare" site splitting between the SB and LB Ni sites and is given as:

$$\Delta_s = \Delta_s^{\mathrm{DFT}} - \Delta_s^{\mathrm{DC}} \quad , \tag{8}$$

where the first term, Δ_s^{DFT}, denotes the corresponding splitting obtained within DFT from the on-site energies of the Wannier functions, and is found to be ≈ 0.25 eV for $R_1^+ = 0.075$ Å. The second term, Δ_s^{DC}, arises from the difference in the DC potential between the Ni_{SB} and Ni_{LB} sites:

$$\Delta_s^{\mathrm{DC}} = \Sigma_{\mathrm{dc,SB}} - \Sigma_{\mathrm{dc,LB}} \quad . \tag{9}$$

The behavior of $U-3J-\Delta_s$ is depicted in Fig. 5 for the different flavors of DC, and for OS and CSC calculations at fixed $U=1.85$ eV and $\Delta_s^{\mathrm{DFT}}=0.25$ eV. The parameter regime which corresponds to the CDI in the atomic limit is highlighted in magenta.

For the OS calculation without DC, $\Delta_s^{\mathrm{DC}}=0$ eV, (blue circles) $U-3J-\Delta_s$ becomes negative for $J=0.53$ eV, which fits nicely with the enhancement of ν and the onset of the MIT for $J>0.55$ eV in Fig. 4. Then, for the calculations with DC from DFT occupations (OS: orange squares and CSC: purple crosses) the crossing happens at a slightly smaller J values, in perfect agreement with the $\nu(J)$ curves in Fig. 4, where ν is slightly increased compared to the calculations without DC corrections. The strong tendency to form the CDI state in the calculations with n_α^{DMFT} can be explained as well. It can be seen that for CSC calculations (red crosses), the CDI regime is entered already at $J=0.2$ eV, and for OS calculations (green stars) even for smaller J. Importantly, it can be seen that in this case the DC potential jumps at the MIT, strongly favoring the CDI state. Of course the atomic limit consideration neglects the importance of bandwidth, but nevertheless gives a qualitative explanation of the underlying physics.

Therefore, we conclude that CSC has a small, but certainly not negligible influence on the DFT+DMFT calculations for $LuNiO_3$, reducing ν by approx. 10%. However, this only holds if DMFT occupations are used in the OS calculation to evaluate the DC correction. If DFT occupations are used in the OS calculation, then the tendency towards the CDI state is significantly weakened, indicated by the much smaller ν, which is clearly related to the smaller Δ_s^{DC}. However, compared to a hypothetical CSC calculation also using n_α^{DFT} for the DC correction, ν is again slightly enhanced in the OS calculation. Thus, one can clearly distinguish between the effect of the DC correction, and the effect of the charge density correction in the CSC calculation. The latter tends to reduce the charge disproportionation, independently of the chosen DC scheme, and analogous to reducing the orbital polarization in the case of $CaVO_3$ discussed in Sec. III A. Moreover, we observe that the flavor of the DC correction in the OS calculation crucially determines the stability of the CDI state.

Finally, our results also indicate that the OS calculations using DMFT occupations for the DC correction already provide a good approximation for the CSC calculation, even though they slightly overestimate the SB/LB splitting and thus the tendency towards the CDI state.

b. Influence on energetics Another important aspect is the influence of charge self-consistency in total energy calculations for different R_1^+ amplitudes. As the R_1^+ amplitude, and thus ν, changes, the DC potential and energy correction changes accordingly. In addition, within the CSC calculation, the Hartree energy and other DFT energy contributions are evaluated from the corrected, self-consistent charge density. To analyze the resulting effects, we again use $U=1.85$ eV and two different values for J, 0.42 eV (the cRPA value) and 1.1 eV (where $\bar{U}\approx 0$ and thus the DC correction vanishes). For both cases, we compare OS with CSC calculations with different treatments of the DC correction, as introduced above. The results are shown in Fig. 6, where the top panels show the total energy as function of the R_1^+ amplitude, and the bottom panels show the corresponding $\bar{A}(0)$.

For the smaller value, $J=0.42$ eV, both the OS (green) and CSC (red) result in an energy minimum at a finite R_1^+ amplitude close to the experimental value (indicated by the vertical line). However, the OS calculation exhibits a much stronger response on the R_1^+ amplitude,

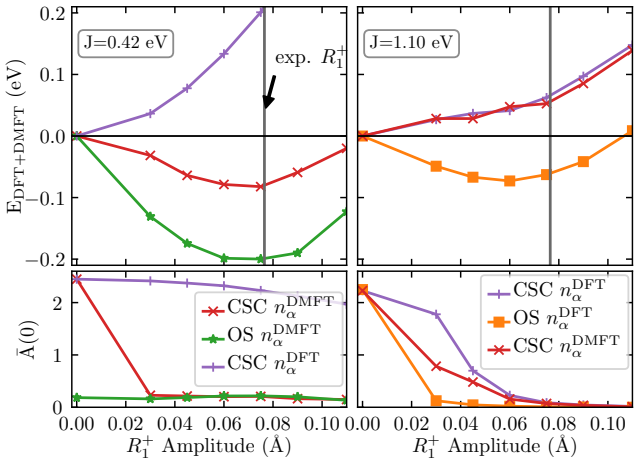

FIG. 6. Comparison of energetics from DFT+DMFT for $LuNiO_3$ as function of the R_1^+ amplitude. Calculations without CSC are labeled OS, both in combination with DC occupations obtained from DFT (n_α^{DFT}) or with occupations obtained from each DMFT step (n_α^{DMFT}). The left panels show results for small $J = 0.42$ eV and the right panels for large $J = 1.1$ eV, where the upper panel shows the energy as function of the R_1^+ amplitude and the panels at the bottom the corresponding spectral weight at the Fermi level.

and hence shows a significantly deeper energy minimum. In contrast, the "artificial" CSC calculation using n_α^{DFT} for the DC correction (purple), exhibits no energy minimum for $R_1^+ > 0$. Furthermore, the "correct" CSC calculation using n_α^{DMFT} undergoes a MIT to the CDI between $R_1^+ = 0$ and $R_1^+ = 0.03$ Å, while the corresponding OS calculation is already insulating without structural distortion and the CSC calculation with n_α^{DFT} remains metallic for any calculated R_1^+ amplitude.

For $J = 1.1$ eV, both CSC calculations, done either with DFT (purple) or DMFT occupations (red), agree very well (due to $\bar{U} \approx 0$ in the DC) and do not result in a stable finite breathing mode amplitude, even though both undergo a MIT at around $R_1^+ = 0.03$ Å and exhibit a large charge disproportionation ν in the insulating state. In contrast, the OS calculation (orange), shows a stronger response, and predicts a breathing mode amplitude of $R_1^+ = 0.06$ Å. Note that here we used n_α^{DFT} for the DC correction, but the same result would be obtained using n_α^{DMFT}, due to $\bar{U} \approx 0$. These results show that, even though the effect of charge self-consistency on ν for fixed crystal structure seems to be relatively minor, the effect on the energetics can be quite drastic, such that one can obtain a finite breathing mode distortion within a OS calculation, while the CSC calculation does not exhibit an energy minimum for $R_1^+ > 0$.

IV. SUMMARY

We have studied the effect of charge self-consistency and the role of the DC in two representative examples of transition metal oxides, using only a minimal correlated subspace corresponding to few "frontier" bands around the Fermi level. Our goal is to better understand in which cases charge self-consistency is really required in order to obtain accurate results, and in which cases a computationally much cheaper OS calculation might be sufficient.

For $CaVO_3$, we find that the strong orbital polarization in the insulating phase under tensile strain is significantly overestimated by about 30 % in OS compared to CSC calculations, in agreement with similar calculations for $SrVO_3$ in Ref. 13 and 14. This has a small but noticeable effect on U_{MIT}, the critical U for the MIT, which is slightly underestimated in the OS calculations. In contrast, for the unstrained system, where the orbital polarization is much smaller, the difference between CSC and OS calculations is nearly negligible, even though also in this case the orbital polarization is slightly overestimated in OS calculations. Furthermore, we also compared OS calculations using projector-based and Wannier-based schemes for constructing the correlated subspace, and found very good agreement between the two methods.

While for $CaVO_3$ all TM sites are symmetry-equivalent, and thus the site-dependent but orbitally-independent DC correction does not affect the results, for the second example investigated in this work, $LuNiO_3$, the DC correction becomes rather important. Here, we find that if DMFT occupations are used to evaluate the DC correction in the OS calculation, one can obtain results that are in rather good agreement with the CSC calculation, even though the charge disproportionation ν is overestimated by ~ 10 %. Thus, similar to reducing the orbital polarization for strained $CaVO_3$, including charge self-consistency leads to a somewhat more homogeneous charge distribution compared to a OS calculation. Nevertheless, it appears that in order to obtain qualitative insights or general trends, OS calculations can be a reasonable approximation, even in charge ordered systems, if the DMFT occupations are used for the DC. However, our analysis of the energetics of the breathing mode distortion shows that for certain observables, such as the total energy and resulting structural distortions, charge self-consistency can be crucial. For example in the case of $LuNiO_3$, OS calculations overestimate the response on the R_1^+ mode, in the most extreme case leading to a stable finite breathing mode amplitude, which is absent in the CSC calculation. In this case it is is inevitable to perform a full CSC calculation to obtain reliable results.

In summary, the effect of charge self-consistency is mainly to reduce a potential site or orbital polarization by favoring a more "homogeneous" distribution of electrons over all sites and/or orbitals. For the cases studied in this work, this results in a weak to moderate charge redistribution, which can be quantitatively relevant, de-

pending on the specific application. In particular for total energy calculations, which depend on a subtle balance between different contributions, charge self-consistency can be crucial to obtain quantitatively and even qualitatively correct results. Nevertheless, it appears that cheaper OS calculations are often sufficient to gain insight into the system properties on a qualitative level, even though the, in principle ambiguous, choice of DFT or DMFT occupations to evaluate the DC correction in the OS calculations can become crucial. In the present examples, the use of DMFT occupations provided better agreement with the full CSC calculation, but in other cases this approach might also severely overestimate the electron transfer between inequivalent sites.

We hope that our detailed analysis of two specifically selected cases, provides useful insights for future DFT+DMFT studies of related material systems, thus allowing the treatment of larger and more complex materials systems by avoiding the higher computational cost of a CSC calculation when possible.

ACKNOWLEDGMENTS

This work was supported by ETH Zurich and the Swiss National Science Foundation through NCCR-MARVEL. Calculations have been performed on the cluster "Piz Daint" hosted by the Swiss National Supercomputing Centre.

* alexander.hampel@mat.ethz.ch
† sophie.beck@mat.ethz.ch
‡ claude.ederer@mat.ethz.ch

[1] K. Held, Advances in Physics **56**, 829 (2007).
[2] H. Ishida and A. Liebsch, Physical Review B **79**, 045130 (2009).
[3] Z. Zhong, M. Wallerberger, J. M. Tomczak, C. Taranto, N. Parragh, A. Toschi, G. Sangiovanni, and K. Held, Physical Review Letters **114**, 246401 (2015).
[4] F. Lechermann, in *Handbook of Materials Modeling* (Springer International Publishing, 2018) pp. 1–20.
[5] S. Beck and C. Ederer, arXiv:1905.00290 (2019).
[6] S. Backes, T. C. Rödel, F. Fortuna, E. Frantzeskakis, P. Le Fèvre, F. Bertran, M. Kobayashi, R. Yukawa, T. Mitsuhashi, M. Kitamura, K. Horiba, H. Kumigashira, R. Saint-Martin, A. Fouchet, B. Berini, Y. Dumont, A. J. Kim, F. Lechermann, H. O. Jeschke, M. J. Rozenberg, R. Valentí, and A. F. Santander-Syro, Physical Review B **94**, 241110 (2016).
[7] M. Sing, H. O. Jeschke, F. Lechermann, R. Valentí, and R. Claessen, The European Physical Journal Special Topics **226**, 2457 (2017).
[8] J. Souto-Casares, N. A. Spaldin, and C. Ederer, arXiv:1901.01884 (2019).
[9] D. Jacob, K. Haule, and G. Kotliar, Physical Review B **82**, 195115 (2010).
[10] V. Turkowski, A. Kabir, N. Nayyar, and T. S. Rahman, The Journal of Chemical Physics **136**, 114108 (2012).
[11] D. Grieger, C. Piefke, O. E. Peil, and F. Lechermann, Physical Review B **86**, 155121 (2012).
[12] R. Adler, C.-J. Kang, C.-H. Yee, and G. Kotliar, Reports on Progress in Physics **82**, 012504 (2019).
[13] S. Bhandary, E. Assmann, M. Aichhorn, and K. Held, Physical Review B **94**, 155131 (2016).
[14] M. Schüler, O. E. Peil, G. J. Kraberger, R. Pordzik, M. Marsman, G. Kresse, T. O. Wehling, and M. Aichhorn, Journal of Physics: Condensed Matter **30**, 475901 (2018).
[15] X. Wang, M. J. Han, L. de' Medici, H. Park, C. A. Marianetti, and A. J. Millis, Physical Review B **86**, 195136 (2012).
[16] H. T. Dang, X. Ai, A. J. Millis, and C. A. Marianetti, Physical Review B **90**, 125114 (2014).
[17] H. Park, A. J. Millis, and C. A. Marianetti, Physical Review B **90**, 235103 (2014).
[18] M. Aichhorn, L. Pourovskii, V. Vildosola, M. Ferrero, O. Parcollet, T. Miyake, A. Georges, and S. Biermann, Physical Review B **80**, 085101 (2009).
[19] M. Aichhorn, L. Pourovskii, and A. Georges, Physical Review B **84**, 054529 (2011).
[20] M. Karolak, G. Ulm, T. Wehling, V. Mazurenko, A. Poteryaev, and A. Lichtenstein, Journal of Electron Spectroscopy and Related Phenomena **181**, 11 (2010), proceedings of International Workshop on Strong Correlations and Angle-Resolved Photoemission Spectroscopy 2009.
[21] G. Kotliar, S. Y. Savrasov, K. Haule, V. S. Oudovenko, O. Parcollet, and C. A. Marianetti, Reviews of Modern Physics **78**, 865 (2006).
[22] K. Haule, Physical Review Letters **115**, 196403 (2015).
[23] F. Lechermann, A. Georges, A. Poteryaev, S. Biermann, M. Posternak, A. Yamasaki, and O. K. Andersen, Physical Review B **74**, 125120 (2006).
[24] P. Seth, P. Hansmann, A. van Roekeghem, L. Vaugier, and S. Biermann, Physical Review Letters **119**, 056401 (2017).
[25] P. Giannozzi, S. Baroni, N. Bonini, M. Calandra, R. Car, C. Cavazzoni, D. Ceresoli, G. L. Chiarotti, M. Cococcioni, I. Dabo, A. D. Corso, S. de Gironcoli, S. Fabris, G. Fratesi, R. Gebauer, U. Gerstmann, C. Gougoussis, A. Kokalj, M. Lazzeri, L. Martin-Samos, N. Marzari, F. Mauri, R. Mazzarello, S. Paolini, A. Pasquarello, L. Paulatto, C. Sbraccia, S. Scandalo, G. Sclauzero, A. P. Seitsonen, A. Smogunov, P. Umari, and R. Wentzcovitch, Journal of Physics: Condensed Matter **21**, 395502 (2009).
[26] J. P. Perdew, K. Burke, and M. Ernzerhof, Physical Review Letters **77**, 3865 (1996).
[27] P. E. Blöchl, Physical Review B **50**, 17953 (1994).
[28] G. Kresse and J. Hafner, Physical Review B **47**, 558 (1993).
[29] G. Kresse and J. Furthmüller, Physical Review B **54**, 11169 (1996).
[30] G. Kresse and D. Joubert, Physical Review B **59**, 1758 (1999).
[31] B. Amadon, F. Lechermann, A. Georges, F. Jollet, T. O. Wehling, and A. I. Lichtenstein, Physical Review B **77**, 205112 (2008).
[32] M. Aichhorn, L. Pourovskii, P. Seth, V. Vildosola,

M. Zingl, O. Peil, X. Deng, J. Mravlje, G. Kraberger, C. Martins, M. Ferrero, and O. Parcollet, Computer Physics Communications **204**, 200 (2016).
[33] O. Parcollet, M. Ferrero, T. Ayral, H. Hafermann, I. Krivenko, L. Messio, and P. Seth, Computer Physics Communications **196**, 398 (2015).
[34] A. Hampel, S. Beck, and C. Ederer, "soliDMFT," `https://github.com/materialstheory/soliDMFT` (2019).
[35] A. A. Mostofi, J. R. Yates, G. Pizzi, Y.-S. Lee, I. Souza, D. Vanderbilt, and N. Marzari, Computer Physics Communications **185**, 2309 (2014).
[36] P. Seth, I. Krivenko, M. Ferrero, and O. Parcollet, Computer Physics Communications **200**, 274 (2016).
[37] L. Vaugier, H. Jiang, and S. Biermann, Physical Review B **86**, 165105 (2012).
[38] L. Boehnke, H. Hafermann, M. Ferrero, F. Lechermann, and O. Parcollet, Physical Review B **84**, 075145 (2011).
[39] V. I. Anisimov, F. Aryasetiawan, and A. I. Lichtenstein, Journal of Physics: Condensed Matter **9**, 767 (1997).
[40] S. Fuchs, E. Gull, M. Troyer, M. Jarrell, and T. Pruschke, Physical Review B **83**, 235113 (2011).
[41] M. Jarrell and J. Gubernatis, Physics Reports **269**, 133 (1996).
[42] E. Pavarini and E. Koch, Physical Review Letters **104**, 086402 (2010).
[43] A. A. Abrikosov, Gorkov, L.P., I. E. Dzyaloshinski, and R. A. Silverman, *Methods of Quantum Field Theory in Statistical Physics*, Dover Books on Physics (Dover Publications, 2012).
[44] V. Galitskii and A. Migdal, Soviet Physics Journal of Experimental and Theoretical Physics **7**, 96 (1958).
[45] I. A. Nekrasov, G. Keller, D. E. Kondakov, A. V. Kozhevnikov, T. Pruschke, K. Held, D. Vollhardt, and V. I. Anisimov, Physical Review B **72**, 155106 (2005).
[46] E. Pavarini, S. Biermann, A. Poteryaev, A. I. Lichtenstein, A. Georges, and O. K. Andersen, Physical Review Letters **92**, 176403 (2004).
[47] S. Beck, G. Sclauzero, U. Chopra, and C. Ederer, Physical Review B **97**, 075107 (2018).
[48] S. Catalano, M. Gibert, J. Fowlie, J. Íñiguez, J.-M. Triscone, and J. Kreisel, Reports on Progress in Physics **81**, 046501 (2018).
[49] M. Gu, J. Laverock, B. Chen, K. E. Smith, S. A. Wolf, and J. Lu, Journal of Applied Physics **113**, 133704 (2013).
[50] D. E. McNally, X. Lu, J. Pelliciari, S. Beck, M. Dantz, M. Naamneh, T. Shang, M. Medarde, C. W. Schneider, V. N. Strocov, *et al.*, npj Quantum Materials **4**, 6 (2019).
[51] E. Pavarini, A. Yamasaki, J. Nuss, and O. K. Andersen, New Journal of Physics **7**, 188 (2005).
[52] G. Sclauzero, K. Dymkowski, and C. Ederer, Physical Review B **94**, 245109 (2016).
[53] M. Medarde, M. T. Fernández-Díaz, and P. Lacorre, Physical Review B **78**, 212101 (2008).
[54] O. E. Peil, A. Hampel, C. Ederer, and A. Georges, Physical Review B **99**, 245127 (2019).
[55] A. Hampel, P. Liu, C. Franchini, and C. Ederer, npj Quantum Materials **4**, 5 (2019).
[56] A. Mercy, J. Bieder, J. Íñiguez, and P. Ghosez, Nature Communications **8**, 1677 (2017).
[57] J. Varignon, M. N. Grisolia, J. Íñiguez, A. Barthélémy, and M. Bibes, Nature Partner Journals Quantum Materials **2**, 21 (2017).
[58] A. Hampel and C. Ederer, Physical Review B **96**, 165130 (2017).
[59] H. Park, A. J. Millis, and C. A. Marianetti, Physical Review B **89**, 245133 (2014).
[60] A. Subedi, O. E. Peil, and A. Georges, Physical Review B **91**, 075128 (2015).
[61] H. Park, A. J. Millis, and C. A. Marianetti, Physical Review Letters **109**, 156402 (2012).
[62] J. M. Perez-Mato, D. Orobengoa, and M. I. Aroyo, Acta Crystallographica A **66**, 558 (2010).
[63] P. V. Balachandran and J. M. Rondinelli, Physical Review B **88**, 054101 (2013).
[64] B. J. Campbell, H. T. Stokes, D. E. Tanner, and D. M. Hatch, Journal of Applied Crystallography **39**, 607 (2006).
[65] J. A. Alonso, M. J. Martínez-Lope, M. T. Casais, J. L. García-Muñoz, M. T. Fernández-Díaz, and M. A. G. Aranda, Physical Review B **64**, 094102 (2001).
[66] P. Seth, O. E. Peil, L. Pourovskii, M. Betzinger, C. Friedrich, O. Parcollet, S. Biermann, F. Aryasetiawan, and A. Georges, Physical Review B **96**, 205139 (2017).
[67] I. I. Mazin, D. I. Khomskii, R. Lengsdorf, J. A. Alonso, W. G. Marshall, R. M. Ibberson, A. Podlesnyak, M. J. Martínez-Lope, and M. M. Abd-Elmeguid, Physical Review Letters **98**, 176406 (2007).
[68] A. Isidori, M. Berović, L. Fanfarillo, L. de' Medici, M. Fabrizio, and M. Capone, Physical Review Letters **122**, 186401 (2019).

8

DESCRIBING THE MAGNETIC PHASE WITHIN DFT+DMFT

In this chapter I investigate the possibilities to model the magnetically ordered phase of rare-earth nickelates using the DFT+DMFT method. In particular, I address the question of whether the complex AFM ordering found in nickelates can in principle be captured by a frontier orbital model, containing only the Ni e_g states. Moreover, I investigate the influence of temperature, variation of the R site cation, and of the breathing mode distortion amplitude.

In chapter 5 and 6, I presented a detailed study about structural parameters obtained in the paramagnetic phase, and the related MIT, of rare-earth nickelates by using DFT+DMFT. Consistent with experiments, the breathing mode distortion in $PrNiO_3$ could not be stabilized within the paramagnetic phase. Note, that for the compounds with R=Lu to Sm, $T_N \neq T_{MIT}$, whereas for R=Nd, and Pr both transition occur at the same temperatures, $T_N = T_{MIT}$ [19]. Furthermore, I analyzed the structural parameters in the magnetically ordered state, by performing a detailed DFT+U study in chapter 4. I also compared the structural trends obtained from the two different studies, demonstrating that DFT+DMFT gives a stronger reduction of the R_1^+ amplitude across the series in the paramagnetic insulating state. However, to compare the results of DFT+U and DFT+DMFT quantitatively, it is necessary to perform DFT+DMFT calculations for the magnetically ordered state.

In principle DFT should correctly describe the magnetically ordered ground state at $T \approx 0$ correctly, and hence DFT should be sufficient to describe magnetically ordered phases at low-temperatures. However, at temperatures above zero, correlation effects can in principle play an important role. Conceptually, performing magnetic DMFT calculations is straightforward, by removing the symmetry of the spin up and down channels in the self-energy and Green's function. Yet, there exist only very few studies using DFT+DMFT to investigate magnetic properties. For example, in iron-based compounds it was shown that electron correlations play an important role in the correct description of the magnetically ordered state [148, 152–154]. An investigation of how structural parameters are influenced by correlation effects in the magnetically ordered phase has only been performed in Ref. [16, 144, 154] for iron based compounds.

From a technical point of view, it becomes apparent from these studies that the magnetic transition temperature obtained from DFT+DMFT calculations can deviate drastically from experiment.

Moreover, the transition temperature depends on the chosen interaction parameters and the chosen correlated subspace. Note, that the temperature in the QMC solver of DMFT is just an electronic temperature, not including any thermal fluctuations of the lattice. Moreover, the conceptual question of whether one should use spin-polarized DFT calculations in favor of non-magnetic DFT calculations during the CSC cycle is still under debate (compare [152] with [144]).

Performing DFT+DMFT calculations for the magnetically ordered state in nickelates will test the capabilities of the method to capture the complete phase diagram, by stabilizing a finite R_1^+ amplitude also for compounds with $T_N = T_{MIT}$. Moreover, this allows to elucidate whether electron correlation effects, responsible for the insulating behavior above T_N, influence the magnetically ordered state. As described in section 2.5, Raman scattering experiments for $SmNiO_3$ found that at the magnetic transition temperature, T_N, the structural properties of the system change [59]. Hence, it becomes evident, that a full description within DFT+DMFT is desirable to also understand the paramagnetic insulating to antiferromagnetic insulating transition.

In a recent study of Haule & Pascut [144], it was demonstrated for $NdNiO_3$, that the correct magnetic order can indeed be obtained from DFT+DMFT calculations. Haule & Pascut [144] find that for $NdNiO_3$, the breathing mode distortion stabilizes only if magnetic order is allowed, in agreement with experiment. Moreover, they obtain structural parameters in good agreement with experiment Ref. [60]. However, this is demonstrated only for a single compound, where $T_N = T_{MIT}$. The question whether structural parameters change at T_N from the paramagnetic insulating to magnetically insulating state remains for compounds with $T_N \neq T_{MIT}$.

8.1 T-AFM ORDER IN THE NI e_g ONLY MODEL

I start by performing magnetic OS DFT+DMFT calculations for $PrNiO_3$. Here, technical questions related to CSC do not arise, and I perform these calculations using the DFT Wannier orbital occupancies for the DC correction. The underlying DFT calculations are performed without considering spin-polarization. The low-energy subspace is built for the Ni e_g states only, using the PLO formalism. Hence, a large J value is required to obtain the CDI electronic state (see section 5.3). I use a value of $U = 1.8$ eV and $J = 0.9$ eV as parameters for the Hubbard-Kanamori Hamiltonian.

The calculations are performed in the same 80 atom unit cell as the DFT+U calculations in chapter 4, allowing for the $k = (1/4\ 1/4\ 1/4)_{pc}$ AFM ordering found in experiment [61]. I first fix the structure by using the Pbnm-relaxed GGA structure from Ref. [140], and adding the R_1^+ breathing mode distortion with an amplitude of 0.04 Å. This

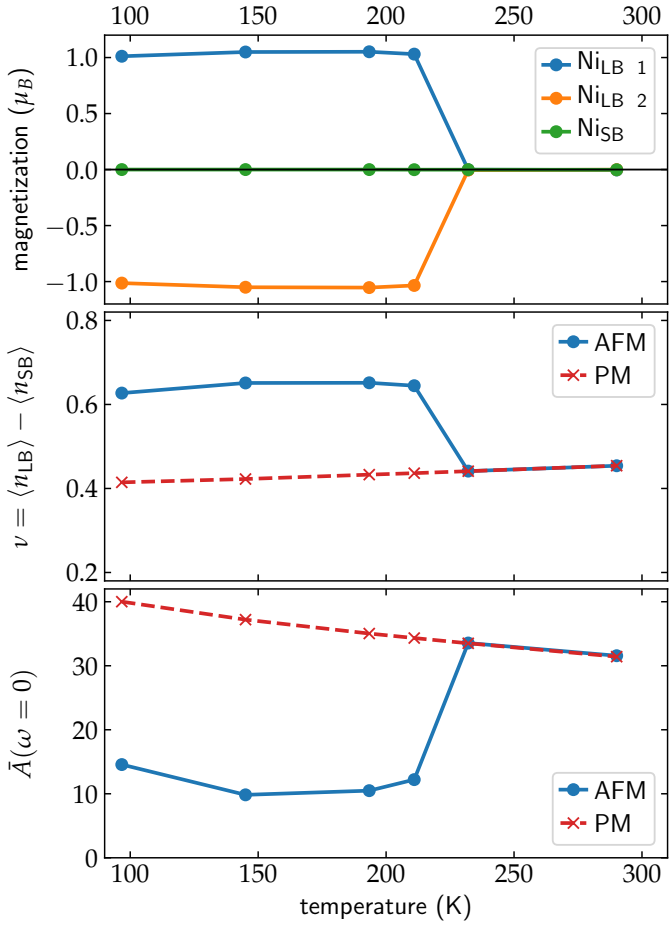

Figure 24: Results of the magnetic OS DFT+DMFT calculations for $PrNiO_3$ with $R_1^+ = 0.04$ Å. $U = 1.8$ eV and $J = 0.9$ eV are used as interaction parameters. Top: magnetization of the different Ni sites as function of temperature. The $Ni_{LB}1$ site (blue), the $Ni_{LB}2$ site (orange), and the Ni_{SB} site are shown. At $T \approx 220$ K the Ni_{LB} moments order antiferromagnetically. Middle: charge disproportionation, ν, as function of temperature for the AFM (blue), and paramagnetic (red) calculations. Bottom: corresponding spectral weights at the Fermi level, $\bar{A}(\omega = 0)$.

corresponds to the value found in experiment [61]. The resulting unit cell contains 16 Ni sites, i.e. 16 impurity problems. When considering the experimentally observed AFM order, one ends up with 2 inequivalent Ni_{LB} and 2 inequivalent Ni_{SB} sites. The 2 Ni_{LB}, and the 2 Ni_{SB} sites order antiferromagnetically with respect to each other. Therefore, one has to solve 4 effective impurity problems. However, the impurity problem of one of the Ni_{LB} sites can be solved by copying the resulting self-energy of the other Ni_{LB} site and exchanging up and down spin channel.

The results, obtained for various temperatures, are shown in Fig. 24. At $T \approx 290$ K ($\beta = 40$ eV^{-1}), at which all previous DFT+DMFT calculations have been performed, no magnetic order is found and the

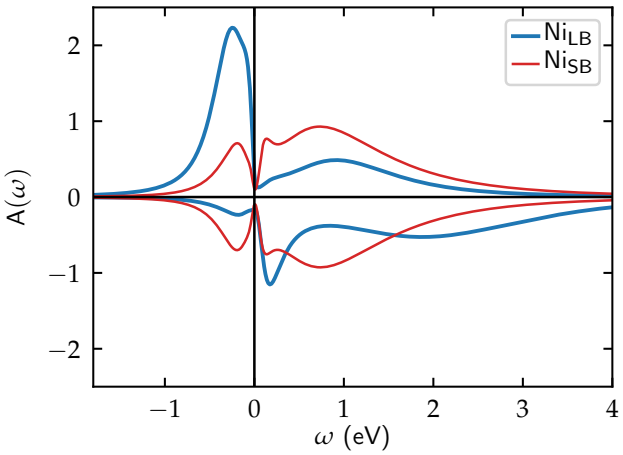

Figure 25: Spectral functions for $PrNiO_3$ with $R_1^+ = 0.04$ Å at $\beta = 80$ eV^{-1} ($T \approx 145$ K), $U = 1.8$ eV, and $J = 0.9$ eV. The Ni_{LB} site (blue) and Ni_{SB} site (red) are shown, separated in spin up (positive) and spin down (negative) channels respectively.

system is in a paramagnetic metallic state. While the temperature is lowered, the system undergoes a magnetic transition at $T \approx 220$ K to an AFM ordered state. I performed also calculations without using the symmetry between "up" and "down" between Ni sites, and without initializing magnetic moments, obtaining the same magnetic order. This AFM order is identical to the one found in DFT+U calculations in chapter 4. Hence, the Ni_{SB} moment is found to be zero. The magnetic moments as function of temperature are shown in the top panel of Fig. 24.

Furthermore, a jump is observed in the charge disproportionation between the Ni sites $\nu = \langle n_{LB} \rangle - \langle n_{SB} \rangle$ at T_N from 0.4 to 0.6 (middle panel of Fig. 24), going along with a reduction in $\bar{A}(\omega = 0)$ (bottom panel). I performed also calculations constrained to the paramagnetic solution, denoted by red dashed lines, which show no jump in ν nor $\bar{A}(\omega = 0)$, but a small decrease of ν in temperature. This jump in ν indicates a positive coupling mechanism between AFM order and charge disproportionation, which allows the system to undergo a MIT at T_N.

To confirm the insulating character of the magnetic state, I perform an analytical continuation of the the impurity Green's functions to the real frequency axis at $\beta = 80$ eV^{-1} ($T \approx 145$ K), utilizing the *triqs/maxent* software [142]. The resulting spectral functions are depicted in Fig. 25 for the Ni_{LB} (blue) and Ni_{SB} (red) site. Positive values correspond to "spin up" and negative values to "spin down" contributions. A very small gap is visible at the Fermi level, and the Ni_{LB} site shows strong spin splitting with almost vanishing spin down occupation. The Ni_{SB} site spectral function shows no formation of a magnetic moment.

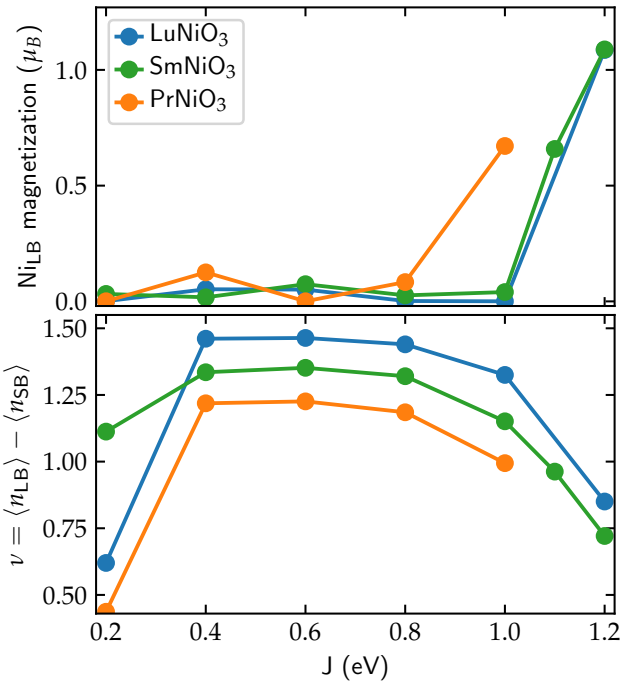

Figure 26: Results of magnetic CSC DFT+DMFT calculations for R=Lu, Sm, and Pr. All calculations are performed with $R_1^+ = 0.06$ Å, at $\beta = 100$ eV^{-1} (T $\approx$ 116 K), using $\mathcal{U} = 1.8$ eV, and DMFT impurity occupations for the determination of the DC correction. Top: Ni_{LB} magnetization as function of $\mathcal{J}$. Bottom: corresponding charge disproportionation ν.

These results demonstrate, that DFT+DMFT is able to capture the complex AFM ordering found in rare-earth nickelates in agreement with Ref. [144]. Moreover, the system undergoes a MIT at T_N as the charge disproportionation increases. The resulting gap is very small, which is further discussed in section 8.3. Since I always obtained the same AFM ordering, I will from now on only show the magnetic moments of one Ni_{LB} site.

8.2 MAGNETIC CSC DFT+DMFT: INFLUENCE OF $\mathcal{J}$

After demonstrating that the magnetic order is obtained within my DFT+DMFT setup, I check whether the same can be obtained in CSC calculations, which then allows also to address interplay with structural properties. Ideally, I find a consistent setting of interaction parameters that can be used for all phases across the series, e.g. the obtained cRPA values in chapter 5. Then, this should allow to find a finite equilibrium R_1^+ amplitude for compounds with R=Nd, and Pr in the AFM ordered state. Here, the CSC steps are performed by averaging the up and down spin-channels of the obtained charge density correction from DMFT, and performing non spin-polarized DFT calculations with the spin-averaged charge density.

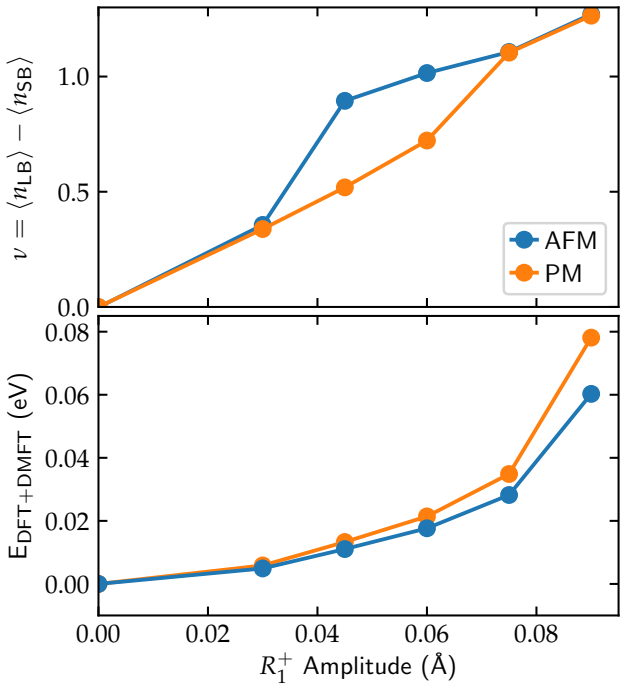

Figure 27: CSC DFT+DMFT calculations as function of the R_1^+ amplitude for $PrNiO_3$, performed at $\beta = 150$ eV^{-1} ($T \approx 77$ K), using $U = 1.8$ eV and $J = 0.8$ eV. The AFM result (blue), and the paramagnetic (orange) result are shown. top: charge disproportionation as function of the R_1^+ amplitude, demonstrating a stronger non-linear response in the magnetically ordered phase. Note, the system is only antiferromagnetically ordered for 0.03 Å$\leqslant R_1^+ \leqslant$ 0.075 Å. bottom: corresponding DFT+DMFT total energy per Ni site.

First tests for $PrNiO_3$ using the experimental R_1^+ amplitude did not display any magnetic ordering down to $T \approx 58$ K, when using the cRPA obtained interaction parameters, and the same computational setup as described in chapter 5. Also for different R_1^+ amplitudes no AFM order could be stabilized. Eventually, the system should order magnetically at low temperatures. However, such low temperatures where not accessible due to the computational limitations of the QMC method. For further studies, it may be advisable to use another impurity solver that is better at handling low temperatures.

To check the reason for this drastic reduction of T_N, I decided to perform a J scan at fixed $U = 1.8$ eV for R=Lu, Sm, and Pr. For all three compounds, I use a R_1^+ amplitude of 0.06 Å, and a fixed temperature of $T \approx 116$ K. The results are shown in Fig. 26. It can be observed that for $LuNiO_3$ and $SmNiO_3$ only for large values $J > 1.0$ eV magnetic order is obtained. Also for $PrNiO_3$, the magnetic order is only obtained for $J > 0.8$ eV. This shows, that for stabilizing the AFM order in $PrNiO_3$ using CSC calculations, a considerably larger value of J is needed, than the obtained cRPA value of $J = 0.39$ eV. Moreover,

I found that the calculations are very hard to converge compared to the OS calculations.

In the bottom panel of Fig. 26, the charge disproportionation, ν, as function of J for the three compounds is shown. One can observe, that the magnetic ordering is only stabilized if ν is not too large. Comparing the results of $PrNiO_3$ with the other two compounds, the value of $J = 1,0$ eV, which gives a AFM result, produces roughly the same value of ν as $J = 1.1$ eV in $SmNiO_3$, and $J = 1.2$ eV in $LuNiO_3$ resulting in an AFM ordered state. This could be a hint that ν is an important indicator determining whether the system can undergo the magnetic transition. In Addition, such large Hund's coupling also favors the formation of local moments.

Next, I perform CSC DFT+DMFT calculations as function of the R_1^+ amplitude for $PrNiO_3$ using $U = 1.8$ eV and $J = 0.8$ eV. This is of course not in accordance with the values used in chapter 5, but the aim was to see whether a stable finite equilibrium R_1^+ amplitude can be obtained at all. Here, I choose a temperature corresponding to $\beta = 150$ eV^{-1} ($T \approx 77$ K), which is well below T_N obtained from the OS calculations. The result is depicted in Fig. 27 for the AFM state as well as the paramagnetic constrained calculations. From the charge disproportionation, ν, shown in the top panel, it becomes evident that the AFM state couples stronger to the R_1^+ amplitude than the PM state, which manifests in the stronger non-linear enhancement of ν around $R_1^+ = 0.05$ Å. As discussed in chapter 6, this non-linearity is essential to obtain a stable equilibrium R_1^+ amplitude. From the corresponding total energies in the bottom panel it can be also seen, that the AFM state is always lower in energy than the paramagnetic state. However, there is no global, or even local minima, observed in $E(R_1^+)$ for finite R_1^+ amplitudes.

These results are a bit puzzling. To some extent they seem to be in agreement with experiment, giving larger ν values when AFM ordered, and the AFM state being lower in energy than the paramagnetic state. However, the large J value required in CSC calculations is not in agreement with my previous results, and moreover no stable finite equilibrium R_1^+ amplitude is obtained. Therefore, I limit myself in the following to OS calculations, in order to first get a better understanding of the overall behavior of the system. The OS calculations are considerably faster, and easier to converge. Hence, the following results should be seen more like an investigation of a model system.

8.3 INFLUENCE OF TEMPERATURE AND BREATHING MODE DISTORTION

To better understand the behavior the system better I perform OS calculations similar to the ones presented in Fig. 24 for $SmNiO_3$ and $PrNiO_3$ at various R_1^+ amplitudes and temperatures. Results are

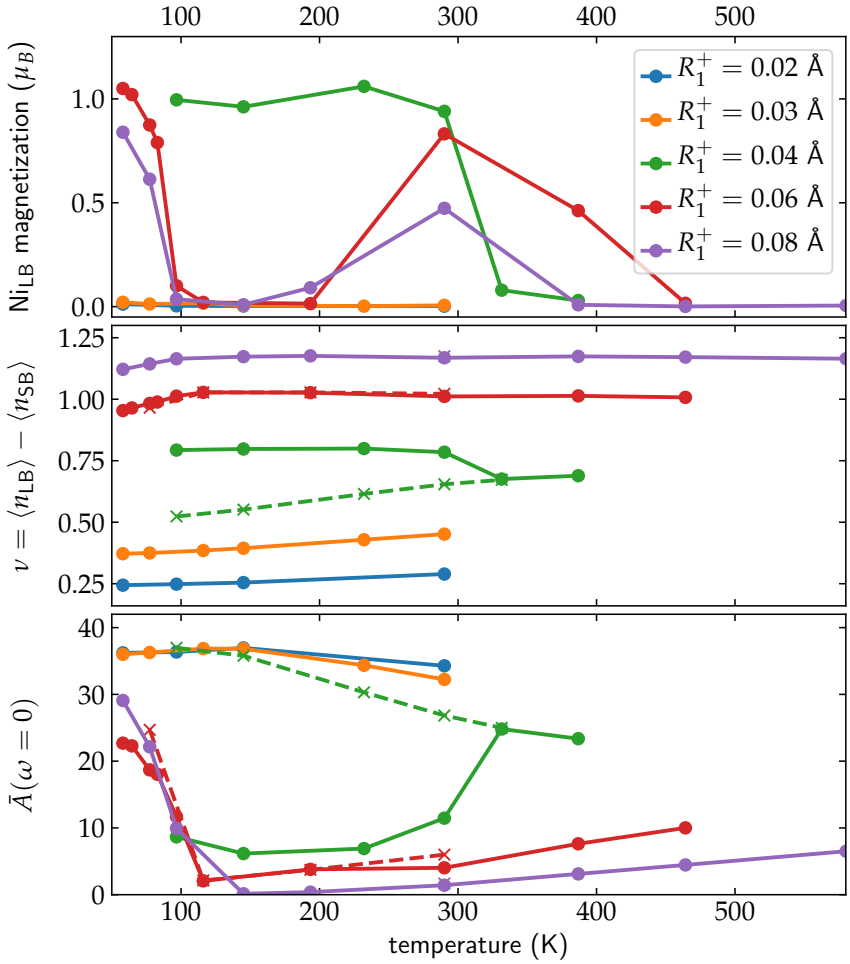

Figure 28: Results of the magnetic OS DFT+DMFT calculations for $SmNiO_3$ with various R_1^+ amplitudes. $U = 1.8$ eV and $J = 0.9$ eV are used as interaction parameters. Top: magnetization of the Ni_{LB} site as function of temperature. Middle: charge disproportionation ν as function of temperature for the AFM (solid lines), and paramagnetic (dashed lines) calculations. Bottom: corresponding spectral weights at the Fermi level, $\bar{A}(\omega = 0)$.

shown in Fig. 28 for $SmNiO_3$ and in Fig. 30 for $PrNiO_3$. I perform AFM calculations, which are presented by solid lines, and paramagnetic calculations, presented by dashed lines.

First, I discuss the results of $SmNiO_3$. From $\bar{A}(\omega = 0)$ as function of temperature (bottom panel of Fig. 28) it can be observed, that for $R_1^+ = 0.04$ Å the system undergoes a MIT at $T_N \approx 300$ K, similar to results obtained for $PrNiO_3$ in Fig. 24. For very small amplitudes $R_1^+ \leqslant 0.03$ Å no magnetic order is observed down to ~ 58 K, showing clearly a positive coupling mechanism between the breathing mode distortion and the magnetic order. For larger R_1^+ amplitudes, $\geqslant 0.06$ Å, the system is at higher temperatures in the paramagnetic CDI state, indicated by $\nu > 1.0$ in the middle panel of Fig. 28. For these large R_1^+ amplitudes the magnetic ordering appears at very

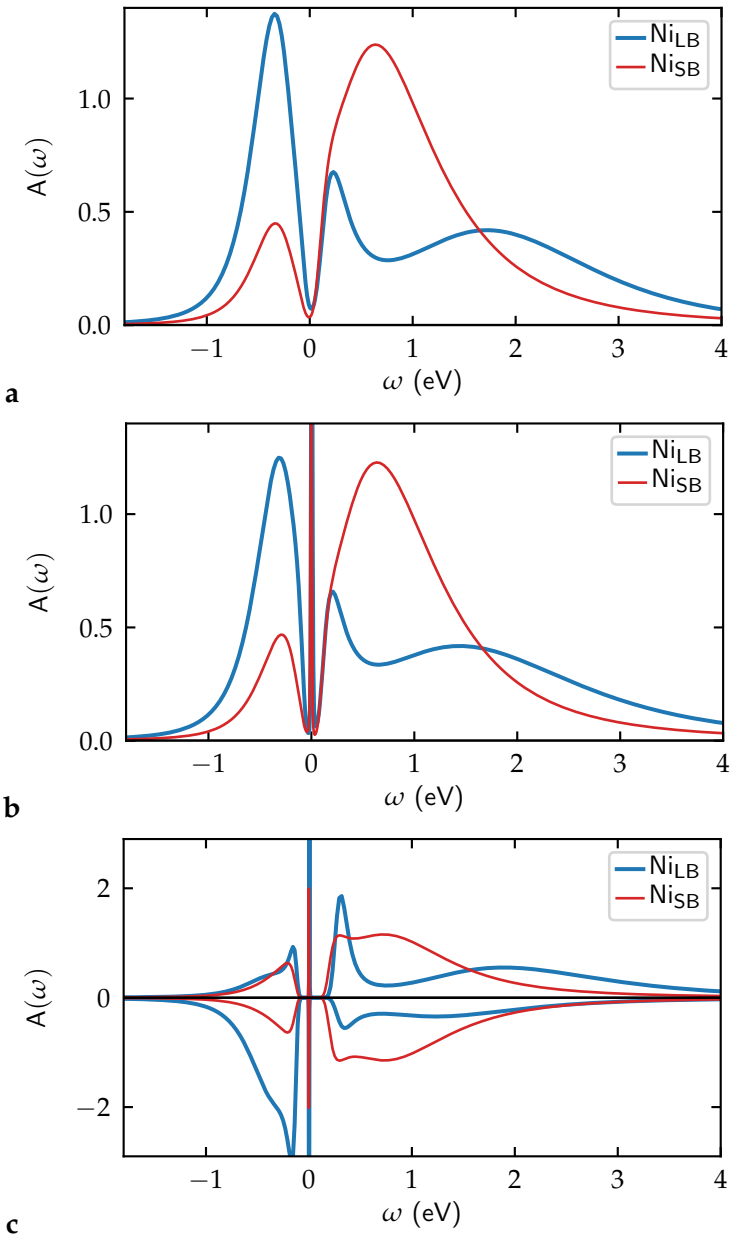

Figure 29: Spectral functions for $SmNiO_3$ with $R_1^+ = 0.06$ Å, and interaction parameters $U = 1.8$ eV and $J = 0.9$ eV. The Ni_{LB} site (blue) and Ni_{SB} site (red) are shown. **a** Paramagnetic calculation at $\beta = 40$ eV^{-1} ($T \approx 290$ K) **b** Paramagnetic calculation at $\beta = 150$ eV^{-1} ($T \approx 77$ K), where a strong peak appears at $\omega = 0$ eV. **c** AFM calculation at $\beta = 150$ eV^{-1} ($T \approx 77$ K) with a clear gap at $\omega = 0$ eV, separated in spin-up (positive) and spin-down (negative) channels, and showing also a very sharp peak at $\omega = 0$ eV.

low temperatures below 100 K, which could explain why I previously did not obtained any AFM ordered state for $SmNiO_3$. Note, that $R_1^+ = 0.06$ Å corresponds to the equilibrium breathing mode amplitude value found in chapter 5 in the paramagnetic CDI state. Furthermore, for the larger R_1^+ amplitudes, ν decreases as function

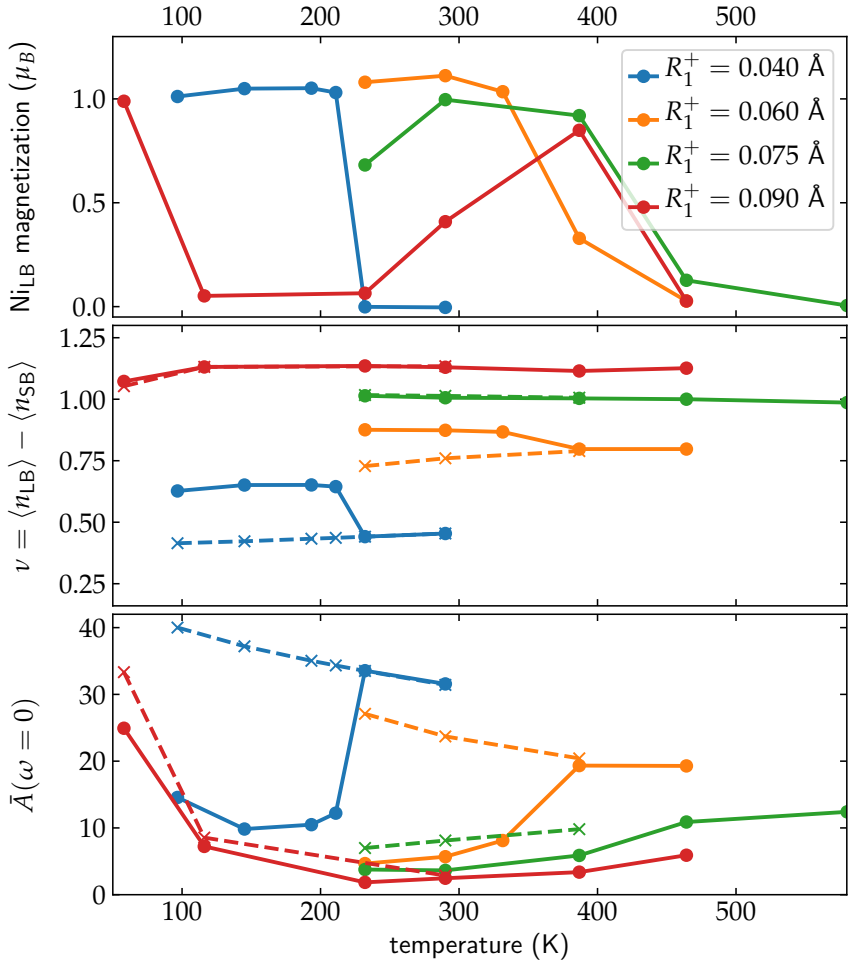

Figure 30: Results of the magnetic OS DFT+DMFT calculations for $PrNiO_3$ with various R_1^+ amplitudes. $R_1^+0.04$ Å corresponds to the experimental value [61]. $U = 1.8$ eV and $J = 0.9$ eV are used as interaction parameters. Top: magnetization of the Ni_{LB} site as function of temperature. Middle: charge disproportionation ν as function of temperature for the AFM (solid lines), and paramagnetic (dashed lines) calculations. Bottom: corresponding spectral weights at the Fermi level, $\bar{A}(\omega = 0)$.

of temperature within the AFM phase. Therefore, it seems that the coupling to the R_1^+ mode is only positive if the system is not yet in a paramagnetic CDI state. Then, the system undergoes a MIT at T_N, and ν increases. If the R_1^+ amplitude becomes larger than $\geqslant 0.06$ Å, T_N is considerably lowered.

For $R_1^+ \geqslant 0.06$ Å the AFM order appears to be stable again at high temperatures between 200 K and 450 K. This behavior seems not physically reasonable and it is not clear, if this indicates a problem of the model, or maybe the AFM order can be stabilized in these calculations, but is energetically not favored compared to the paramagnetic state. Hence, the occurrence would be a local minima in energy. This needs to be further investigated. However, I note that the calculations

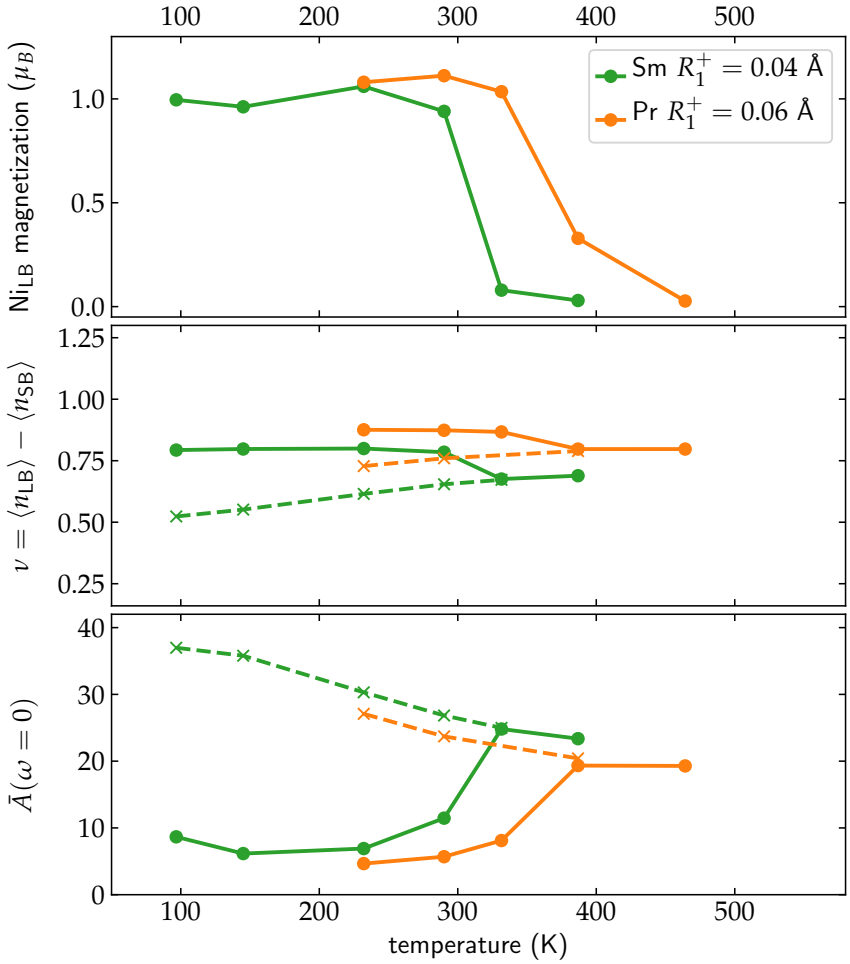

Figure 31: Comparison of results for $PrNiO_3$ ($R_1^+ = 0.06$ Å) with $SmNiO_3$ ($R_1^+ = 0.04$ Å). $U = 1.8$ eV and $J = 0.9$ eV are used as interaction parameters. Top: magnetization of the Ni_{LB} site as function of temperature. Middle: charge disproportionation ν as function of temperature for the AFM (solid lines), and paramagnetic (dashed lines) calculations. Bottom: corresponding spectral weights at the Fermi level, $\bar{A}(\omega = 0)$.

with this magnetic ordering at higher temperatures are harder to converge, which could be an indication that the solution is not stable.

It can also observed that $\bar{A}(\omega = 0)$ increases drastically below 100 K for all calculations in an insulating state, also the paramagnetic ones. To further analyze this behavior I calculate spectral functions at different temperatures for $R_1^+ = 0.06$ Å, which are presented in Fig. 29. In the top panel $A(\omega)$ of the Ni_{LB} (blue) and Ni_{SB} (red) are shown for $\beta = 40$ eV^{-1} ($T \approx 290$ K) in the paramagnetic state. A very small gap is visible at $\omega = 0$ eV, and the Ni_{LB} site has a higher occupancy than the Ni_{SB} site. In the middle and bottom panel, $A(\omega)$ for the AFM and paramagnetic state at $\beta = 150$ eV^{-1} ($T \approx 77$ K) are shown. The paramagnetic spectral functions show only marginal differences compared to the one at higher temperature, but at $\omega = 0$ eV a very sharp peak

appears for $\beta = 150$ eV^{-1}, in agreement with the higher $\bar{A}(\omega = 0)$ in Fig. 28. Interestingly, the AFM spectral functions shows a gap of ~ 0.25 eV, also with a sharp peak appearing at $\omega = 0$ eV, which explains the high value of $\bar{A}(\omega = 0)$. Such a sharp peak appears to be unphysical, and could be a numerical artefact. However, let me note that those calculations are very well converged with respect to QMC cycles, and also the Legendre cut-off is chosen and checked carefully. A comparison with a calculation using tail-fitting instead of Legendre sampling still needs to be done to exclude numerical problems.

For $PrNiO_3$, I also perform analogous calculations at varying R_1^+ amplitudes. The results are shown in Fig. 30, and display similar behavior as for $SmNiO_3$. Also here, a cooperative coupling between magnetic order and R_1^+ mode can be observed up to $R_1^+ = 0.09$ Å, resulting in a drastically lower T_N for larger R_1^+ amplitudes. The spurious occurrence of AFM order at higher temperatures can be found as well for $R_1^+ \geqslant 0.075$ Å. The results for $R_1^+ = 0.04$ Å (blue) are identical to the ones shown in Fig. 24.

In contrast to $SmNiO_3$, the coupling of the charge disproportionation, ν, to the R_1^+ mode is not as pronounced as in $PrNiO_3$. This is due to the reduced octahedral rotations as explained in chapter 5 and 6. Meaning, that using the same R_1^+ amplitude in $PrNiO_3$ leads to a smaller value of ν compared to $SmNiO_3$. I find that if a R_1^+ amplitude is chosen that leads to the same ν in both systems, it will lead to a very similar temperature behavior regarding the magnetization, ν, and $\bar{A}(\omega = 0)$. This is demonstrated in Fig. 31. Here, calculations for $PrNiO_3$, with $R_1^+ = 0.06$ Å, are compared with calculations for $SmNiO_3$, with $R_1^+ = 0.04$ Å. Both systems exhibit a comparable value of ν at high temperatures. It can be observed that both system behave very similar when the temperature is lowered with respect to ν, magnetic order, and $\bar{A}(\omega = 0)$.

8.4 CONCLUSION

So far, no complete coherent picture can be drawn from the results obtained here. However, I demonstrated that DFT+DMFT, using only the Ni e_g states for the construction of the correlated subspace, is in principle able to describe the AFM ordering found in experiment. Here, the same magnetic order can be stabilized as found in DFT+U calculations. Moreover, $PrNiO_3$ becomes insulating while undergoing the magnetic transition for suitably chosen values of U, J, and R_1^+. These results are in agreement with experiment [61]. In the context of this thesis, these are important findings, demonstrating that DFT+DMFT can potentially be used to describe the full phase diagram of rare-earth nickelates. Interestingly, it is found that the charge-disproportionation, ν, decreases as function of temperature in the paramagnetic state for all performed calculations.

However, performing CSC calculations using the same interaction parameters as used in chapter 5 to describe the paramagnetic phase, did not result in any magnetic ordering down to $T \approx 58$ K. Only for large values of $\mathcal{J}$, magnetic order was obtained, and even if such large value of $\mathcal{J}$ is used to perform DFT+DMFT total energy calculations, no stable finite equilibrium R_1^+ amplitude is obtained.

The results obtained from the less demanding OS calculations show, that the charge disproportionation ν seems to critically determine the stability of the magnetic phase. By comparing results for $SmNiO_3$ and $PrNiO_3$ it is found that similar values of ν yield similar behavior. For $\nu > 1.0$ a CDI state is obtained at high temperatures, which seems to suppress the magnetic order down to very low temperatures. Only for moderate values of $0.4 < \nu < 1.0$, T_N is found to be above 100 K, going along with an increase of ν at T_N and a decrease of $\bar{A}(\omega = 0)$. If ν is smaller than $\leqslant 0.4$ no magnetic order occurs. Importantly, this is observed for both OS and CSC calculations, indicating that it is not the CSC treatment disfavoring the magnetic order. However, it is not yet clear, if the magnetic ordering can also be found for smaller values of $\mathcal{J}$, or if a large value of $\mathcal{J}$ is essential. This could be resolved by performing DFT+DMFT calculations with another impurity solver, which allows calculations at lower temperatures.

The large values of ν obtained in the Ni e_g only model could be problematic, since they result in almost empty Ni_{SB} sites. If one assumes that a certain amount of electrons is needed on all sites to mediate the magnetic coupling, a too large charge disproportionation could destabilize the magnetic ordering. Even though, I found a positive coupling between magnetic order and the R_1+ mode in some cases, this could explain why the AFM order suddenly disappears for large R_1^+ amplitudes. However, it is not clear if this is a problem of the chosen minimal correlated subspace, or whether it represents the actual physics of the system.

In general, the strong temperature dependence of T_N makes a systematic parameter variation difficult. It is not clear, if this strong temperature dependence is an artefact of using only the Ni e_g states. The study of Haule & Pascut [144] was performed by constructing a low-energy subspace for a large energy window containing all Ni d and all oxygen p states. Therefore, a comparison with DFT+DMFT calculations using all Ni d states as well as all oxygen p states would give important insights.

Before any further conclusion can be drawn, also in the context of the whole phase diagram, more calculations are necessary. Mainly, the reappearing of magnetic order at higher temperatures for certain R_1^+ amplitudes is spurious, as well as the sharp peak in $A(\omega)$ at the Fermi level below 100 K. Moreover, the need of different interaction parameters for the paramagnetic and AFM phase should be further investigated.

9 SUMMARY & OUTLOOK

In this thesis, I demonstrated that DFT++ methods can be used to gain insights into the complex phase-diagram of the rare-earth nickelates series completely *ab initio*. These compounds exhibit a rich phase diagram, in which electronic correlations, magnetic ordering, and structural properties are coupled. Previous theoretical studies demonstrated that capturing all of these effects is extremely challenging [22, 23, 26]. In order to obtain a complete and coherent picture of the phase diagram, it is necessary to model structural and electronic degrees of freedom on equal footing. Moreover, experimental data on bulk samples is sparse due to a challenging synthesis, making theoretical insights extremely valuable [19–21].

The first goal of this thesis, presented in chapter 1, was to test the possibilities of the DFT method to obtain structural parameters for the nickelate series. Thus, I performed a detailed DFT+U study across the whole series, which is described in chapter 4. The results obtained from plain DFT calculations correctly captured all structural properties that seem to be decoupled from the strong electronic correlations. Moreover, I found that DFT+U yields an appropriate description of the magnetically ordered phase of the series. However, this study also revealed the deficiencies of the effective single-particle picture in DFT to model the insulating paramagnetic state of nickelates driven by electronic correlations, and the necessity to use more advanced methods.

By utilizing the more sophisticated DFT+DMFT method, with interaction parameters obtained by cRPA, I then successfully described structural parameters across the series for the paramagnetic insulating state on a quantitative level, another goal formulated in chapter 1. This demonstrated the predictive power of DFT+DMFT to obtain not only spectral, but also structural parameters correctly. Additionally, a detailed analysis of the breathing mode distortion energetics within DFT+DMFT revealed the first-order nature of the coupled MIT. These findings were then transferred and generalized to a model Hamiltonian, which allowed to identify the mechanism of the MIT, and the control parameters that drive the trends across the series. These results allow to understand the underlying physics of the nickelates phase diagram to a large extent, and are therefore highly valuable to the community. Moreover, the applied methodology can be used to investigate other materials in which structural and electronic degrees of freedom are coupled. Thereby, I achieved another goal, which was

to make the theoretical investigation of systems with coupled structural and electronic degrees of freedom more feasible.

In addition, I conducted a detailed analysis of the DFT+DMFT approach to illustrate the impact of CSC and the DC correction to better understand unclear technical aspects and current limitations of the approach. Such technical analysis and its documentation, i.e. to identify the limitations and to understand which technical aspects need to be improved, is of special importance for future work predicting materials properties on a quantitative level. In this respect, the "GW+DMFT" method is an interesting development, eliminating the DC problem [155]. Moreover, the explicit treatment of non-local correlation and interaction effects could play an important role in improving existing *ab initio* approaches [156, 157].

A last missing piece is the understanding of the AFM order in rare-earth nickelates. Although the magnetic order obtained in DFT+U agrees well with experimental data, the origin of the complex order is not understood up to now. Performing DFT+DMFT calculations in the magnetically ordered phase, seems to be a promising route to shine light on these aspects [144]. I showed that the strong electronic correlations that are responsible for the insulating nature in the paramagnetic regime, seem to play a crucial role in understanding also the AFM phase transition. However, results presented in this thesis do not yet allow, for a conclusive understanding across the series. Moreover, it remains an open question whether the frontier orbital model is sufficient for a full quantitative description of the magnetic order. Here, more research is necessary.

The understanding of correlated materials using *ab initio* methods remains an extremely challenging and complex problem, in particular if multiple degrees of freedom couple. However, progress in recent years has made the use of methods such as DFT+DMFT more and more practical for calculating structural properties in realistic correlated systems [18]. This development will enable the prediction of structural properties on an unprecedented level completely *ab inito*, leading also to better, more fundamental, understanding of how structural and electronic degrees of freedom couple, which in turn will allow to design better performing functional materials. Thus, the research presented in this thesis is an important advance showing that modern *ab initio* methods correctly describe materials with coupled degrees of freedom, pushing the boundaries of DFT++ methods, and improving their predictive power.

A

CALCULATION OF THE IMPURITY ENERGY

In this appendix I will give a detailed derivation of the interaction energy formula Eq. 120. The goal is to find a closed expression of the following expectation value:

$$\langle H^{\text{int}}_{\alpha\beta\gamma\delta}\rangle = \frac{1}{2}\sum_{\alpha\beta\gamma\delta} V_{\alpha\beta\gamma\delta}\,\langle\Psi_0|\,c^\dagger_\alpha c^\dagger_\beta c_\delta c_\gamma\,|\Psi_0\rangle\ , \tag{157}$$

where $|\Psi_0\rangle$ is the ground state of the system. The derivation is based on Ref. [127] and Ref. [113]. I will start with the equation of motion for the Green's functions:

$$i\frac{\partial}{\partial t}G_{\alpha\beta}(t,t') = \frac{\partial}{\partial t}\,\langle\Psi_0|\,T[c_\alpha(t)c^\dagger_\beta(t')]\,|\Psi_0\rangle\ . \tag{158}$$

For this derivation it is necessary to write the time ordered product in the following form:

$$T[c_\alpha(t)c^\dagger_\beta(t')] = \theta(t-t')c_\alpha(t)c^\dagger_\beta(t') - \theta(t'-t)c^\dagger_\beta(t')c_\alpha(t)\ . \tag{159}$$

where,

$$\theta(t) = \begin{cases} 1 \text{ for } t > 0 \\ 0 \text{ for } t < 0\ . \end{cases} \tag{160}$$

Therefore I get by using the product rule and

$$\frac{\partial}{\partial t}\theta(t-t') = \delta(t-t')\ , \tag{161}$$

for the equation of motion:

$$\begin{aligned} i\frac{\partial}{\partial t}G_{\alpha\beta}(t,t') = \langle\Psi_0|\,\theta(t-t')\frac{\partial c_\alpha(t)}{\partial t}c^\dagger_\beta(t') - \theta(t'-t)c^\dagger_\beta(t')\frac{\partial c_\alpha(t)}{\partial t} \\ + \delta(t-t')\left(c_\alpha(t)c^\dagger_\beta(t) + c^\dagger_\beta(t)c_\alpha(t)\right)|\Psi_0\rangle\ . \end{aligned} \tag{162}$$

The second line contains the anti-commutator, and the first line is the time ordered product of derivations of annihilation operators:

$$i\frac{\partial}{\partial t}G_{\alpha\beta}(t,t') = \langle\Psi_0|\,T[\frac{\partial c_\alpha(t)}{\partial t}c^\dagger_\beta(t')]\,|\Psi_0\rangle + \delta(t-t')\delta_{\alpha\beta}\ . \tag{163}$$

Using now the Heisenberg equation of motion gives:

$$i\frac{\partial c_\alpha(t)}{\partial t} = e^{i\hat{H}t}[c_\alpha,\hat{H}]e^{-i\hat{H}t}\quad , \tag{164}$$

and one finds:

$$\begin{aligned} i\frac{\partial}{\partial t}G_{\alpha\beta}(t,t') = -i\ \langle\Psi_0|\,T[e^{i\hat{H}t}[c_\alpha,\hat{H}]e^{-i\hat{H}t}c^\dagger_\beta(t')]\,|\Psi_0\rangle \\ + \delta(t-t')\delta_{\alpha\beta}\ . \end{aligned} \tag{165}$$

Note, that the time evolution is determined by the full Hamiltonian of the system. Here, I will use a generic Hubbard Hamiltonian, consisting of a one-particle kinetic term and the above Coulomb interaction.

As one can see it boils down to the calculation of the anti-commutator $[c_\alpha,\hat{H}]$. Fortunately, the time dependence is outside of the commutator and I can now split the commutator according to:

$$[c_\alpha,\hat{H}] = \underbrace{[c_\alpha,\hat{H}_{kin}]}_{(1)} + \underbrace{[c_\alpha,\hat{H}_{int}]}_{(2)} \tag{166}$$

Starting with anti-commutator (1), I will change the indices of $\hat{H}$ to not mix with the original indices:

$$[c_\alpha,\hat{H}_{kin}] = \sum_{\alpha'\beta'} t_{\alpha'\beta'}[c_\alpha,c^\dagger_{\alpha'}c_{\beta'}]\ . \tag{167}$$

Now, I switch to the momentum basis, where the kinetic hamiltonian is diagonal:

$$[c_\alpha,\hat{H}_{kin}] = \sum_{\alpha'} t_{\alpha'\alpha'}[c_\alpha,c^\dagger_{\alpha'}c_{\alpha'}]\ . \tag{168}$$

Next, I use the identity:

$$[A,BC] = [A,B]C - B[C,A] \tag{169}$$

to obtain:

$$\begin{aligned} [c_\alpha,\hat{H}_{kin}] &= \sum_{\alpha'} t_{\alpha'\alpha'}\left(\underbrace{[c_\alpha,c^\dagger_{\alpha'}]}_{\delta_{\alpha\alpha'}}c_{\alpha'} - c^\dagger_{\alpha'}\underbrace{[c_{\alpha'},c_\alpha]}_{0}\right) \\ &= \sum_{\alpha'} t_{\alpha'\alpha'}\delta_{\alpha\alpha'}c_{\alpha'} \\ &= \epsilon_\alpha c_\alpha\ . \end{aligned} \tag{170}$$

Therefore, I have for the full anti-commutator:

$$[c_\alpha,\hat{H}] = \epsilon_\alpha c_\alpha + \underbrace{[c_\alpha,\hat{H}_{int}]}_{(2)}\ . \tag{171}$$

Note, I chose a basis of α and β where $\hat{H}_{kin}$ is diagonal.

For anti-commutator (2) I get:

$$[c_\alpha,\hat{H}_{int}] = \frac{1}{2}\sum_{\beta\beta'\gamma\gamma'} V_{\beta\beta',\gamma\gamma'}[c_\alpha,c^\dagger_\beta c^\dagger_\gamma c_{\gamma'}c_{\beta'}] \tag{172}$$

For the anti-commutator of the creation and annihilation operators I get:

$$\begin{aligned}
[\underbrace{c_\alpha}_{A}, \underbrace{c^\dagger_\beta c^\dagger_\gamma}_{B} \underbrace{c_{\gamma'} c_{\beta'}}_{C}] &= [c_\alpha, c^\dagger_\beta c^\dagger_\gamma] c_{\gamma'} c_{\beta'} - c^\dagger_\beta c^\dagger_\gamma \underbrace{[c_{\gamma'} c_{\beta'}, c_\alpha]}_{0} \\
&= [\underbrace{c_\alpha}_{A}, \underbrace{c^\dagger_\beta}_{B} \underbrace{c^\dagger_\gamma}_{C}] c_{\gamma'} c_{\beta'} \\
&= \underbrace{[c_\alpha, c^\dagger_\beta]}_{\delta_{\alpha\beta}} c^\dagger_\gamma c_{\gamma'} c_{\beta'} - c^\dagger_\beta \underbrace{[c^\dagger_\gamma, c_\alpha]}_{\delta_{\alpha\gamma}} c_{\gamma'} c_{\beta'} \\
&= \delta_{\alpha\beta} c^\dagger_\gamma c_{\gamma'} c_{\beta'} - \delta_{\alpha\gamma} c^\dagger_\beta c_{\gamma'} c_{\beta'} ,
\end{aligned} \tag{173}$$

which can now inserted back, to obtain:

$$\begin{aligned}
[c_\alpha, \hat{H}_{\text{int}}] &= \frac{1}{2} \sum_{\beta\beta'\gamma\gamma'} V_{\beta\beta',\gamma\gamma'} \left(\delta_{\alpha\beta} c^\dagger_\gamma c_{\gamma'} c_{\beta'} - \delta_{\alpha\gamma} c^\dagger_\beta c_{\gamma'} c_{\beta'} \right) \\
&= \frac{1}{2} \sum_{\beta'\gamma\gamma'} V_{\alpha\beta',\gamma\gamma'}\, c^\dagger_\gamma c_{\gamma'} c_{\beta'} - \frac{1}{2} \sum_{\beta\beta'\gamma'} V_{\beta\beta',\alpha\gamma'}\, c^\dagger_\beta c_{\gamma'} c_{\beta'} .
\end{aligned} \tag{174}$$

In the last term I change $\beta \to \gamma$, $\beta' \to \gamma'$ and $\gamma' \to \beta'$:

$$[c_\alpha, \hat{H}_{\text{int}}] = \frac{1}{2} \sum_{\beta'\gamma\gamma'} V_{\alpha\beta',\gamma\gamma'}\, c^\dagger_\gamma c_{\gamma'} c_{\beta'} - \frac{1}{2} \sum_{\gamma\gamma'\beta'} V_{\gamma\gamma',\alpha\beta'}\, c^\dagger_\gamma c_{\beta'} c_{\gamma'} . \tag{175}$$

Now, I use $V_{\alpha\alpha',\beta\beta'} = V_{\beta\beta',\alpha\alpha'}$, and exchange $c_{\beta'} c_{\gamma'}$ by picking up a minus sign:

$$[c_\alpha, \hat{H}_{\text{int}}] = \frac{1}{2} \sum_{\beta'\gamma\gamma'} V_{\alpha\beta',\gamma\gamma'}\, c^\dagger_\gamma c_{\gamma'} c_{\beta'} + \frac{1}{2} \sum_{\gamma\gamma'\beta'} V_{\alpha\beta',\gamma\gamma'}\, c^\dagger_\gamma c_{\gamma'} c_{\beta'} , \tag{176}$$

which finally gives:

$$[c_\alpha, \hat{H}_{\text{int}}] = \sum_{\beta'\gamma\gamma'} V_{\alpha\beta',\gamma\gamma'}\, c^\dagger_\gamma c_{\gamma'} c_{\beta'} . \tag{177}$$

Putting all together I get for the whole anti-commutator:

$$[c_\alpha, \hat{H}] = \epsilon_\alpha c_\alpha + \sum_{\gamma\gamma'\beta'} V_{\alpha\beta',\gamma\gamma'}\, c^\dagger_\gamma c_{\gamma'} c_{\beta'} . \tag{178}$$

Putting everything back into the equation of motion in Eq. 165:

$$\begin{aligned}
&i \frac{\partial}{\partial t} G_{\alpha\beta}(t, t') \\
&= -i\, \langle \Psi_0 | T[e^{i\hat{H}t} \left(\epsilon_\alpha c_\alpha + \sum_{\gamma\gamma'\beta'} V_{\alpha\beta',\gamma\gamma'}\, c^\dagger_\gamma c_{\gamma'} c_{\beta'} \right) e^{-i\hat{H}t} c^\dagger_\beta(t')] | \Psi_0 \rangle \\
&+ \delta(t - t') \delta'_{\alpha\beta} .
\end{aligned} \tag{179}$$

Now lets introduce the time evolution operators carefully:

$$
\begin{aligned}
& i\frac{\partial}{\partial t}G_{\alpha\beta}(t,t') \\
& = -i\ \langle\Psi_0|\,T[\ \Big(\ \epsilon_\alpha e^{i\hat{H}t}c_\alpha e^{-i\hat{H}t} \\
& + \sum_{\gamma\gamma'\beta'} V_{\alpha\beta',\gamma\gamma'}\ e^{i\hat{H}t}c^\dagger_\gamma c_{\gamma'}c_{\beta'}e^{-i\hat{H}t}\ \Big)\ c^\dagger_\beta(t')]\,|\Psi_0\rangle \\
& + \delta(t-t')\delta_{\alpha\beta} \\
& = -i\ \langle\Psi_0|\,T[\ \Big(\ \epsilon_\alpha c_\alpha(t) \\
& + \sum_{\gamma\gamma'\beta'} V_{\alpha\beta',\gamma\gamma'}\ e^{i\hat{H}t}c^\dagger_\gamma e^{-i\hat{H}t}e^{i\hat{H}t}c_{\gamma'}e^{-i\hat{H}t}e^{i\hat{H}t}c_{\beta'}e^{-i\hat{H}t}\ \Big)\ c^\dagger_\beta(t')]\,|\Psi_0\rangle \\
& + \delta(t-t')\delta_{\alpha\beta} \\
& = -i\ \langle\Psi_0|\,T[\left(\epsilon_\alpha c_\alpha(t) + \sum_{\gamma\gamma'\beta'} V_{\alpha\beta',\gamma\gamma'}\ c^\dagger_\gamma(t)c_{\gamma'}(t)c_{\beta'}(t)\right) c^\dagger_\beta(t')]\,|\Psi_0\rangle \\
& + \delta(t-t')\delta_{\alpha\beta}\ .
\end{aligned}
\tag{180}
$$

Introducing a limes on both sites:

$$
\begin{aligned}
& \lim_{t'\to t^+} i\frac{\partial}{\partial t}G_{\alpha\beta}(t,t') \\
& = -i\ \lim_{t'\to t^+}\langle\Psi_0|\,T[\left(\epsilon_\alpha c_\alpha(t) + \sum_{\gamma\gamma'\beta'} V_{\alpha\beta',\gamma\gamma'}\ c^\dagger_\gamma(t)c_{\gamma'}(t)c_{\beta'}(t)\right) c^\dagger_\beta(t')]\,|\Psi_0\rangle \\
& + \lim_{t'\to t^+}\delta(t-t')\delta_{\alpha\beta}\ .
\end{aligned}
\tag{181}
$$

Derivative and limes exchange and I obtain:

$$
\begin{aligned}
& i\frac{\partial}{\partial t}G_{\alpha\beta}(t,t^+) \\
& = -i\ \langle\Psi_0|\,\epsilon_\alpha c^\dagger_\beta(t^+)c_\alpha(t) \\
& - i\ \sum_{\gamma\gamma'\beta'} V_{\alpha\beta',\gamma\gamma'}\ c^\dagger_\beta(t^+)c^\dagger_\gamma(t)c_{\gamma'}(t)c_{\beta'}(t)\,|\Psi_0\rangle + \delta_{\alpha\beta}\ .
\end{aligned}
\tag{182}
$$

After rearranging one obtains:

$$
\begin{aligned}
& i\frac{\partial}{\partial t}G_{\alpha\beta}(t,t^+) + i\ \epsilon_\alpha\,\langle\Psi_0|\,c^\dagger_\beta(t^+)c_\alpha(t)\,|\Psi_0\rangle - \delta_{\alpha\beta} \\
& = -i\ \sum_{\gamma\gamma'\beta'} V_{\alpha\beta',\gamma\gamma'}\ \langle\Psi_0|\,c^\dagger_\beta(t^+)c^\dagger_\gamma(t)c_{\gamma'}(t)c_{\beta'}(t)\,|\Psi_0\rangle\ .
\end{aligned}
\tag{183}
$$

The second term on the left side is $-\epsilon_\alpha G_{\alpha\beta}(t,t^+)$, if I write the term with a time ordering operator and pick up the minus sign from particle exchange. Therefore I get:

$$\begin{aligned}&\left(i\frac{\partial}{\partial t}-\epsilon_\alpha\right)G_{\alpha\beta}(t,t^+)-\delta_{\alpha\beta}\\&=-i\sum_{\gamma\gamma'\beta'}V_{\alpha\beta',\gamma\gamma'}\ \langle\Psi_0|\,c^\dagger_\beta(t^+)c^\dagger_\gamma(t)c_{\gamma'}(t)c_{\beta'}(t)\,|\Psi_0\rangle\ .\end{aligned}\tag{184}$$

if I now use the definition of the free one-particle Green's function:

$$G^0_{\alpha\beta}(t,t')=\frac{\delta(t-t')\delta_{\alpha\beta}}{i\frac{\partial}{\partial t}-\epsilon_\alpha}\ ,\tag{185}$$

I can rewrite the left side of the equation in the following way:

$$\begin{aligned}&\left(i\frac{\partial}{\partial t}-\epsilon_\alpha\right)\left[G_{\alpha\beta}(t,t^+)-G^0_{\alpha\beta}(t,t^+)\right]\\&=-i\sum_{\beta'\gamma\gamma'}V_{\alpha\beta',\gamma\gamma'}\ \langle\Psi_0|\,c^\dagger_\beta(t^+)c^\dagger_\gamma(t)c_{\gamma'}(t)c_{\beta'}(t)\,|\Psi_0\rangle\ .\end{aligned}\tag{186}$$

Remember that we chose $\hat{H}_{kin}$ to be diagonal. Therefore $G^0_{\alpha\beta}(t,t^+)$ is diagonal by definition as well.

On the right side of the equation one has almost two times $\langle H_{int}\rangle$. Now, I introduce the sum over α on both sites:

$$\begin{aligned}&\sum_\alpha\left(i\frac{\partial}{\partial t}-\epsilon_\alpha\right)\left[G_{\alpha\alpha}(t,t^+)-G^0_{\alpha\alpha}(t,t^+)\right]\\&=-i\sum_{\alpha\beta'\gamma\gamma'}V_{\alpha\beta',\gamma\gamma'}\ \langle\Psi_0|\,c^\dagger_\alpha(t^+)c^\dagger_\gamma(t)c_{\gamma'}(t)c_{\beta'}(t)\,|\Psi_0\rangle\ .\end{aligned}\tag{187}$$

If one now compares the right side of the equation with equation 157, one has two times the expectation value of H_{int} on the right side of the equation:

$$\sum_\alpha\left(i\frac{\partial}{\partial t}-\epsilon_\alpha\right)\left[G_{\alpha\alpha}(t,t^+)-G^0_{\alpha\alpha}(t,t^+)\right]=-i\,2\langle H_{int}\rangle\ .\tag{188}$$

This shows that one can describe the expectation value of the two-particle Coulomb interaction by one-particle Green's functions. Since $\alpha=\beta$ the definition of the free one-particle Green's function reduces to $G^0_{\alpha\alpha}(t,t^+)=\left(i\frac{\partial}{\partial t}-\epsilon_\alpha\right)^{-1}$, and I obtain:

$$\sum_\alpha G^0_{\alpha\alpha}(t,t^+)^{-1}\left[G_{\alpha\alpha}(t,t^+)-G^0_{\alpha\alpha}(t,t^+)\right]=-i\,2\langle H_{int}\rangle\ .\tag{189}$$

In the main text, $\langle H_{int}\rangle$ is defined by $\frac{1}{2}tr[\Sigma G]$. To get to this result I will use the Dyson equation:

$$\Sigma=G_0^{-1}-G^{-1}\ ,\tag{190}$$

and multiply from the right by G:

$$\begin{aligned}\Sigma G &= G_0^{-1} G - G^{-1} G \\ &= G_0^{-1} G - 1 \\ &= G_0^{-1}[G - G_0]\end{aligned} \tag{191}$$

However, although the last line looks more or less the same as the left side of equation 189, we encounter a problem. The Dyson equation is made for matrices, and equation 189 is only for the diagonal parts of G.

Assuming now that one is only interested in the diagonal parts of the matrix product ΣG:

$$(\Sigma G)_{\alpha\alpha} = \sum_{\beta} \Sigma_{\alpha\beta} G_{\beta\alpha} \, . \tag{192}$$

Now we use equation 191 to rewrite this to:

$$\sum_{\beta} \Sigma_{\alpha\beta} G_{\beta\alpha} = \sum_{\beta} (G^0_{\alpha\beta})^{-1} [G_{\beta\alpha} - G^0_{\beta\alpha}] \, . \tag{193}$$

Now I can use the fact, that $G^0_{\alpha\beta}$ is diagonal and insert a $\delta_{\alpha\beta}$:

$$\sum_{\beta} \Sigma_{\alpha\beta} G_{\beta\alpha} = \sum_{\beta} (G^0_{\alpha\beta})^{-1} \delta_{\alpha\beta} [G_{\beta\alpha} - G^0_{\beta\alpha}] \tag{194}$$

if one does the summation over β the result is:

$$\sum_{\beta} \Sigma_{\alpha\beta} G_{\beta\alpha} = (G^0_{\alpha\alpha})^{-1} [G_{\alpha\alpha} - G^0_{\alpha\alpha}] \tag{195}$$

which is exactly what is written on the left side of equation 189 in case of a diagonal G^0. Therefore the result reduces to:

$$\sum_{\alpha} \sum_{\beta} \Sigma_{\alpha\beta}(t, t^+) G_{\beta\alpha}(t, t^+) = -i \, 2 \langle H_{\text{int}} \rangle \tag{196}$$

$$\Leftrightarrow \langle H_{\text{int}} \rangle = -\frac{i}{2} \sum_{\alpha\beta} \Sigma_{\alpha\beta}(t, t^+) G_{\beta\alpha}(t, t^+) \, . \tag{197}$$

This is of course:

$$\langle H_{\text{int}} \rangle = -\frac{i}{2} \text{tr} \left[\Sigma(t, t^+) G(t, t^+) \right] \tag{198}$$

which is exactly the result that is given in the paper from [127], or in the book from [113].

Since G and Σ act only at the same time t (t^+), one can transform the result easily to the frequency domain or Matsubara functions. The result in the Matsubara frequency domain is:

$$\langle H_{\text{int}} \rangle = \frac{1}{2} \sum_{n} \text{tr} \left[\Sigma(i\omega_n) G(i\omega_n) \right] \, . \tag{199}$$

B

LIST OF PUBLICATIONS

Here, I list the publications that resulted from the work carried out during my PhD. The four publications [50, 51, 140, 145] form the main part of my thesis.

1. Hampel, A. & Ederer, C. Interplay between breathing mode distortion and magnetic order in rare-earth nickelates $RNiO_3$ within DFT + U. *Phys. Rev. B* **96,** 165130 (16 2017).
2. Hampel, A., Liu, P., Franchini, C. & Ederer, C. Energetics of the coupled electronic-structural transition in the rare-earth nickelates. *npj Quantum Materials* **4,** 5 (2019).
3. Peil, O. E., Hampel, A., Ederer, C. & Georges, A. Mechanism and control parameters of the coupled structural and metal-insulator transition in nickelates. *Phys. Rev. B* **99,** 245127 (24 2019).
4. Hampel, A., Beck, S. & Ederer, C. Charge self-consistency and double-counting in DFT+DMFT calculations for complex transition metal oxides. *ArXiv e-prints.* arXiv: 1907.10339 (2019).

BIBLIOGRAPHY

1. Heber, J. Enter the oxides. *Nature* **459** (2009) (cit. on p. 1).
2. Takagi, H. & Hwang, H. Y. An emergent change of phase for electronics. *Science* **327** (2010) (cit. on p. 1).
3. Z., Y. & R., S. Correlated Electron Materials and Field Effect Transistors for Logic: A Review. *Crit. Rev. Solid State Mater. Sci.* **38,** 286–317 (2013) (cit. on p. 1).
4. Khomskii, D. Trend: Classifying multiferroics: Mechanisms and effects. *Physics* **2** (2009) (cit. on p. 1).
5. Stewart, G. R. Non-Fermi-liquid behavior in d- and f-electron metals. *Rev. Mod. Phys.* **73,** 797–855 (4 2001) (cit. on p. 1).
6. Dagotto, E. Correlated electrons in high-temperature superconductors. *Rev. Mod. Phys.* **66,** 763–840 (3 1994) (cit. on p. 1).
7. Imada, M., Fujimori, A. & Tokura, Y. Metal-insulator transitions. *Rev. Mod. Phys.* **70,** 1039–1263 (4 1998) (cit. on pp. 1, 2, 13).
8. Ramesh, R. & Schlom, D. G. Whither Oxide Electronics? *MRS Bull.* **33** (2008) (cit. on p. 1).
9. Granozio, F. M., Koster, G. & Rijnders, G. Functional oxide interfaces. *MRS Bull.* **38** (2013) (cit. on p. 1).
10. Dagotto, E. Complexity in Strongly Correlated Electronic Systems. *Science* **309,** 257–262 (2005) (cit. on p. 1).
11. Mannhart, J. & Schlom, D. G. Oxide Interfaces—An Opportunity for Electronics. *Science* **327,** 1607–1611 (2010) (cit. on p. 1).
12. Sawa, A. Resistive switching in transition metal oxides. *Mater. Today* **11,** 28 –36 (2008) (cit. on p. 1).
13. Basov, D. N., Averitt, R. D. & Hsieh, D. Towards properties on demand in quantum materials. *Nat. Mater.* **16.** Review Article, 1077 EP – (2017) (cit. on p. 2).
14. Kotliar, G. *et al.* Electronic structure calculations with dynamical mean-field theory. *Reviews of Modern Physics* **78,** 865–951 (3 2006) (cit. on pp. 2, 52).
15. Held, K. Electronic structure calculations using dynamical mean field theory. *Adv. Phys.* **56,** 829–926 (2007) (cit. on pp. 2, 42, 57).
16. Haule, K. & Pascut, G. L. Forces for structural optimizations in correlated materials within a DFT+embedded DMFT functional approach. *Phys. Rev. B* **94,** 195146 (19 2016) (cit. on pp. 2, 131).

17. Leonov, I., Anisimov, V. I. & Vollhardt, D. First-Principles Calculation of Atomic Forces and Structural Distortions in Strongly Correlated Materials. *Phys. Rev. Lett.* **112,** 146401 (14 2014) (cit. on p. 2).

18. Haule, K. Structural predictions for Correlated Electron Materials Using the Functional Dynamical Mean Field Theory Approach. *J. Phys. Soc. Jpn.* **87,** 041005 (2018) (cit. on pp. 2, 4, 146).

19. Catalano, S. *et al.* Rare-earth nickelates $RNiO_3$: thin films and heterostructures. *Rep. Prog. Phys.* **81,** 046501 (2018) (cit. on pp. 2, 8, 9, 15–17, 20, 88, 131, 145).

20. Medarde, M. L. Structural, magnetic and electronic properties of $RNiO_3$ perovskites (R = rare earth). *J. Phys.: Condens. Matter* **9,** 1679–1707 (Feb. 1997) (cit. on pp. 2, 9, 145).

21. Catalan, G. Progress in perovskite nickelate research. *Phase Transitions* **81** (July 2008) (cit. on pp. 2, 9, 14, 145).

22. Mazin, I. I. *et al.* Charge Ordering as Alternative to Jahn-Teller Distortion. *Phys. Rev. Lett.* **98,** 176406 (17 2007) (cit. on pp. 2, 14, 15, 84, 145).

23. Park, H., Millis, A. J. & Marianetti, C. A. Site-Selective Mott Transition in Rare-Earth-Element Nickelates. *Phys. Rev. Lett.* **109,** 156402 (15 2012) (cit. on pp. 2, 14–16, 64, 83, 145).

24. Park, H., Millis, A. J. & Marianetti, C. A. Total energy calculations using DFT+DMFT: Computing the pressure phase diagram of the rare earth nickelates. *Phys. Rev. B* **89,** 245133 (24 2014) (cit. on pp. 3, 16, 64, 66, 83, 84, 115, 118).

25. Giovannetti, G. *et al.* Multiferroicity in rare-earth nickelates $RNiO_3$. *Phys. Rev. Lett.* **103** (Oct. 2009) (cit. on pp. 3, 9, 17).

26. Prosandeev, S., Bellaiche, L. & Íñiguez, J. Ab initio study of the factors affecting the ground state of rare-earth nickelates. *Phys. Rev. B* **85,** 214431 (21 2012) (cit. on pp. 3, 64, 66, 145).

27. Alonso, J. A., Martınez-Lope, M. J. & Rasines, I. Preparation, crystal structure, and metal-to-insulator transition of EuNiO3. *J. Solid State Chem.* **120** (1995) (cit. on p. 9).

28. Alonso, J. A. *et al.* Room-temperature monoclinic distortion due to charge disproportionation in $RNiO_3$ perovskites with small rare-earth cations (R=Ho, Y, Er, Tm, Yb, and Lu): A neutron diffraction study. *Phys. Rev. B* **61,** 1756–1763 (3 2000) (cit. on pp. 9, 10, 63).

29. Alonso, J. A. *et al.* High-temperature structural evolution of $RNiO_3$ (R= Ho, Y , Er, Lu) perovskites: Charge disproportionation and electronic localization. *Phys. Rev. B* **64,** 094102 (9 2001) (cit. on pp. 9, 10, 18, 63–65, 81, 83, 117).

30. Alonso, J. A. *et al.* Charge Disproportionation in $RNiO_3$ Perovskites: Simultaneous Metal-Insulator and Structural Transition in $YNiO_3$. *Phys. Rev. Lett.* **82,** 3871–3874 (19 1999) (cit. on pp. 9, 10).

31. Muñoz, A, Alonso, J. A., Martínez-Lope, M. J. & Fernández-Díaz, M. T. On the magnetic structure of DyNiO3. *J. Solid State Chem.* **182** (July 2009) (cit. on pp. 9, 15, 17, 18, 63).

32. Alonso, J. A. *et al.* Charge disproportionation in $RNiO_3$ (R = Tm, Yb) perovskites observed in situ by neutron diffraction and ^{57}Fe probe Mössbauer spectroscopy. *Phys. Rev. B* **87,** 184111 (18 2013) (cit. on p. 9).

33. Momma, K. & Izumi, F. VESTA3 for three-dimensional visualization of crystal, volumetric and morphology data. *J. Appl. Crystallogr.* **44,** 1272–1276 (2011) (cit. on p. 10).

34. He, Z. & Millis, A. J. Strain control of electronic phase in rare-earth nickelates. *Phys. Rev. B* **91,** 195138 (19 2015) (cit. on pp. 9, 64).

35. Scherwitzl, R. *et al.* Electric-Field Control of the Metal-Insulator Transition in Ultrathin $NdNiO_3$ Films. *Adv. Mater.* **22,** 5517–5520. ISSN: 1521-4095 (2010) (cit. on p. 9).

36. Middey, S. *et al.* Physics of Ultrathin Films and Heterostructures of Rare-Earth Nickelates. *Annu. Rev. Mater. Res.* **46,** 305–334 (2016) (cit. on p. 9).

37. Guo, H. *et al.* Antiferromagnetic correlations in the metallic strongly correlated transition metal oxide $LaNiO_3$. *Nat. Commun.* **9,** 43. ISSN: 2041-1723 (2018) (cit. on p. 9).

38. Subedi, A. Breathing distortions in the metallic, antiferromagnetic phase of $LaNiO_3$. *SciPost Phys.* **5,** 20 (3 2018) (cit. on p. 9).

39. Demazeau, G., Marbeuf, A., Pouchard, M. & Hagenmuller, P. Sur une série de composés oxygènes du nickel trivalent derivés de la perovskite. *J. Solid State Chem.* **3,** 582 –589. ISSN: 0022-4596 (1971) (cit. on p. 10).

40. Zaanen, J., Sawatzky, G. A. & Allen, J. W. Band gaps and electronic structure of transition-metal compounds. *Phys. Rev. Lett.* **55,** 418–421 (4 1985) (cit. on p. 13).

41. Coey, J. M. D., Viret, M., Ranno, L. & Ounadjela, K. Electron Localization in Mixed-Valence Manganites. *Phys. Rev. Lett.* **75,** 3910–3913 (21 1995) (cit. on p. 14).

42. Johnston, S. *et al.* Charge Disproportionation without Charge Transfer in the Rare-Earth-Element Nickelates as a Possible Mechanism for the Metal-Insulator Transition. *Phys. Rev. Lett.* **112,** 106404 (10 2014) (cit. on p. 15).

43. Subedi, A., Peil, O. E. & Georges, A. Low-energy description of the metal-insulator transition in the rare-earth nickelates. *Phys. Rev. B* **91** (Feb. 2015) (cit. on pp. 15, 16, 83–86, 115, 118).

44. Varignon, J. *et al.* Complete phase diagram of rare-earth nickelates from first-principles. *npj Quantum Materials* (Apr. 2017) (cit. on pp. 15, 64, 66, 84).

45. Mizokawa, T., Khomskii, D. I. & Sawatzky, G. A. Spin and charge ordering in self-doped Mott insulators. *Phys. Rev. B* **61,** 11263–11266 (17 2000) (cit. on p. 15).

46. Mizokawa, T. *et al.* Electronic structure of the local-singlet insulator $NaCuO_2$. *Phys. Rev. B* **49,** 7193–7204 (11 1994) (cit. on pp. 15, 16).

47. Fernández-Díaz, M. T. *et al.* Magnetic structure of the $HoNiO_3$ perovskite. *Phys. Rev. B* **64,** 144417 (14 2001) (cit. on pp. 15, 17).

48. Vobornik, I. *et al.* Electronic-structure evolution through the metal-insulator transition in $RNiO_3$. *Phys. Rev. B* **60,** R8426–R8429 (12 1999) (cit. on p. 15).

49. Mercy, A., Bieder, J., Íñiguez, J. & Ghosez, P. Structurally triggered metal-insulator transition in rare-earth nickelates. *Nat. Commun.* **8,** 1677 (2017) (cit. on pp. 15, 64, 66, 67, 89, 104).

50. Hampel, A., Liu, P., Franchini, C. & Ederer, C. Energetics of the coupled electronic-structural transition in the rare-earth nickelates. *npj Quantum Materials* **4,** 5 (2019) (cit. on pp. 15, 81, 86, 88, 101–104, 153).

51. Peil, O. E., Hampel, A., Ederer, C. & Georges, A. Mechanism and control parameters of the coupled structural and metal-insulator transition in nickelates. *Phys. Rev. B* **99,** 245127 (24 2019) (cit. on pp. 15, 97–100, 102, 153).

52. Park, H., Millis, A. J. & Marianetti, C. A. Computing total energies in complex materials using charge self-consistent DFT+DMFT. *Phys. Rev. B* **90,** 235103 (23 2014) (cit. on pp. 16, 83, 84, 116).

53. Woodward, P. M. *et al.* Structural studies of charge disproportionation and magnetic order in $CaFeO_3$. *Phys. Rev. B* **62,** 844–855 (2 2000) (cit. on p. 16).

54. García-Muñoz, J. L., Rodríguez-Carvajal, J., Lacorre, P. & Torrance, J. B. Neutron-diffraction study of $RNiO_3$ (R=La,Pr,Nd,Sm): Electronically induced structural changes across the metal-insulator transition. *Phys. Rev. B* **46,** 4414–4425 (8 1992) (cit. on p. 16).

55. García-Muñoz, J. L., Rodríguez-Carvajal, J. & Lacorre, P. Neutron-diffraction study of the magnetic ordering in the insulating regime of the perovskites $RNiO_3$ (R=Pr and Nd). *Phys. Rev. B* **50,** 978–992 (2 1994) (cit. on p. 16).

56. García-Muñoz, J. L., Rodríguez-Carvajal, J. & Lacorre, P. Sudden Appearance of an Unusual Spin Density Wave At the Metal-Insulator Transition in the Perovskites $RNiO_3$ (R = Pr, Nd). *Europhys. Lett.* **20** (1992) (cit. on p. 16).

57. Lu, Y. *et al.* Site-Selective Probe of Magnetic Excitations in Rare-Earth Nickelates Using Resonant Inelastic X-ray Scattering. *Phys. Rev. X* **8,** 031014 (3 2018) (cit. on p. 17).

58. Ruppen, J. *et al.* Impact of antiferromagnetism on the optical properties of rare-earth nickelates. *Phys. Rev. B* **96** (4 2017) (cit. on p. 17).

59. Girardot, C. *et al.* Raman scattering investigation across the magnetic and metal-insulator transition in rare earth nickelate $RNiO_3$ (R = Sm, Nd) thin films. *Phys. Rev. B* **78,** 104101 (10 2008) (cit. on pp. 17, 132).

60. García-Muñoz, J. L., Aranda, M. A. G., Alonso, J. A. & Martínez-Lope, M. J. Structure and charge order in the antiferromagnetic band-insulating phase of $NdNiO_3$. *Phys. Rev. B* **79,** 134432 (13 2009) (cit. on pp. 18, 88, 132).

61. Medarde, M. L., Fernández-Díaz, M. T. & Lacorre, P. Long-range charge order in the low-temperature insulating phase of $PrNiO_3$. *Phys. Rev. B* **78,** 212101 (21 2008) (cit. on pp. 18, 88, 132, 133, 140, 142).

62. Perez-Mato, J. M., Orobengoa, D & Aroyo, M. I. Mode crystallography of distorted structures. *Acta Crystallographica A* **66** (July 2010) (cit. on p. 18).

63. Balachandran, P. V. & Rondinelli, J. M. Interplay of octahedral rotations and breathing distortions in charge-ordering perovskite oxides. *Phys. Rev. B* **88,** 054101 (5 2013) (cit. on pp. 18, 19, 63).

64. Campbell, B. J., Stokes, H. T., Tanner, D. E. & Hatch, D. M. ISODISPLACE: a web-based tool for exploring structural distortions. *J. Appl. Crystallogr.* **39** (July 2006) (cit. on p. 20).

65. Scherwitzl, R. *Metal-insulator transitions in nickelate heterostructures* eng. ID: unige:21740. PhD thesis (Université de Genève, 2012). https://nbn-resolving.org/urn:nbn:ch:unige-217406 (cit. on p. 20).

66. Hohenberg, P. & Kohn, W. Inhomogeneous Electron Gas. *Phys. Rev.* **136** (Nov. 1964) (cit. on p. 22).

67. Kohn, W. & Sham, L. J. Self-Consistent Equations Including Exchange and Correlation Effects. *Phys. Rev.* **140** (Nov. 1965) (cit. on pp. 22–24).

68. Von Barth, U. & Hedin, L. A local exchange-correlation potential for the spin polarized case. i. *J. Phys. C: Solid State Phys.* **5,** 1629–1642 (1972) (cit. on p. 24).

69. Ceperley, D. M. & Alder, B. J. Ground State of the Electron Gas by a Stochastic Method. *Phys. Rev. Lett.* **45,** 566–569 (7 1980) (cit. on p. 24).

70. Gunnarsson, O. & Lundqvist, B. I. Exchange and correlation in atoms, molecules, and solids by the spin-density-functional formalism. *Phys. Rev. B* **13,** 4274–4298 (10 1976) (cit. on p. 24).

71. Perdew, J. P. & Zunger, A. Self-interaction correction to density-functional approximations for many-electron systems. *Phys. Rev. B* **23,** 5048–5079 (10 1981) (cit. on p. 24).

72. Perdew, J. P. *et al.* Atoms, molecules, solids, and surfaces: Applications of the generalized gradient approximation for exchange and correlation. *Phys. Rev. B* **46** (Sept. 1992) (cit. on p. 24).

73. Perdew, J. P., Burke, K. & Ernzerhof, M. Generalized Gradient Approximation Made Simple. *Phys. Rev. Lett.* **77,** 3865–3868 (18 1996) (cit. on p. 25).

74. Martin, R. *Electronic Structure: Basic Theory and Practical Methods* ISBN: 9781139643658 (Cambridge University Press, 2004) (cit. on p. 25).

75. Bloch, F. Über die Quantenmechanik der Elektronen in Kristallgittern. *Zeitschrift für physik* **52** (1929) (cit. on p. 25).

76. Blöchl, P. E. Projector augmented-wave method. *Phys. Rev. B* **50** (Dec. 1994) (cit. on p. 26).

77. Kresse, G. & Hafner, J. Ab initio molecular dynamics for liquid metals. *Phys. Rev. B* **47,** 558–561 (1 1993) (cit. on p. 26).

78. Kresse, G. & Furthmüller, J. Efficient iterative schemes for ab initio total-energy calculations using a plane-wave basis set. *Phys. Rev. B* **54,** 11169–11186 (16 1996) (cit. on p. 26).

79. Kresse, G. & Joubert, D. From ultrasoft pseudopotentials to the projector augmented-wave method. *Phys. Rev. B* **59,** 1758–1775 (3 1999) (cit. on pp. 26, 27).

80. E., B. P. in (eds Pavarini, E., Koch, E., Lichtenstein, A. & Vollhardt, D. E.) pp. 2.1 –2.44 (Schriften des Forschungszentrums Jülich, 2011). http://juser.fz-juelich.de/record/17645 (cit. on p. 27).

81. Vanderbilt, D. Soft self-consistent pseudopotentials in a generalized eigenvalue formalism. *Phys. Rev. B* **41,** 7892–7895 (11 1990) (cit. on p. 28).

82. Varignon, J., Bibes, M. & Zunger, A. Origin of band gaps in 3d perovskite oxides. *Nat. Commun.* **10,** 1658. ISSN: 2041-1723 (2019) (cit. on p. 28).

83. Lichtenstein, A. I. & Katsnelson, M. I. Ab initio calculations of quasiparticle band structure in correlated systems: LDA++ approach. *Phys. Rev. B* **57,** 6884–6895 (12 1998) (cit. on p. 29).

84. Anisimov, V. I., Zaanen, J. & Andersen, O. K. Band theory and Mott insulators: Hubbard *U* instead of Stoner *I*. *Phys. Rev. B* **44** (3 1991) (cit. on pp. 29, 39, 57).

85. Anisimov, V. I. *et al.* Density-functional theory and NiO photoemission spectra. *Phys. Rev. B* **48,** 16929–16934 (23 1993) (cit. on p. 29).

86. Lechermann, F. *et al.* Dynamical mean-field theory using Wannier functions: A flexible route to electronic structure calculations of strongly correlated materials. *Phys. Rev. B* **74,** 125120 (12 2006) (cit. on p. 29).

87. Marzari, N. *et al.* Maximally localized Wannier functions: Theory and applications. *Rev. Mod. Phys.* **84,** 1419–1475 (4 2012) (cit. on pp. 30, 84).

88. Mostofi, A. A. *et al.* wannier90: A tool for obtaining maximally-localised Wannier functions. *Comput. Phys. Commun.* **178,** 685 –699 (2008) (cit. on pp. 30, 84).

89. Mostofi, A. A. *et al.* An updated version of wannier90: A tool for obtaining maximally-localised Wannier functions. *Comput. Phys. Commun.* **185,** 2309 –2310 (2014) (cit. on p. 30).

90. Amadon, B. *et al.* Plane-wave based electronic structure calculations for correlated materials using dynamical mean-field theory and projected local orbitals. *Phys. Rev. B* **77,** 205112 (20 2008) (cit. on pp. 31, 58).

91. Aichhorn, M. *et al.* Dynamical mean-field theory within an augmented plane-wave framework: Assessing electronic correlations in the iron pnictide LaFeAsO. *Phys. Rev. B* **80,** 085101 (8 2009) (cit. on pp. 31, 33, 39, 116).

92. Karolak, M. *Electronic Correlation Effects in Transition Metal Systems: From Bulk Crystals to Nanostructures* PhD thesis (University of Hamburg, 2013). https://www.physnet.uni-hamburg.de/services/biblio/dissertation/dissfbPhysik/___Volltexte/Michael___Karolak/Michael___Karolak.pdf (cit. on p. 32).

93. Pavarini, E., Koch, E., Lichtenstein, A. & Vollhardt, D. E. *The LDA+DMFT approach to strongly correlated materials* Record converted from VDB: 12.11.2012. http://juser.fz-juelich.de/record/17645 (Schriften des Forschungszentrums Jülich, 2011) (cit. on pp. 32, 33, 36, 42).

94. Slater, L. J. *Confluent hypergeometric functions* (Cambridge Univ. Press, 1960) (cit. on p. 33).

95. Sugano, S. *Multiplets of Transition-Metal Ions in Crystals* ISBN: 9780323154796 (Elsevier Science, 1970) (cit. on p. 33).

96. Vaugier, L., Jiang, H. & Biermann, S. Hubbard U and Hund exchange J in transition metal oxides: Screening versus localization trends from constrained random phase approximation. *Phys. Rev. B* **86,** 165105 (16 2012) (cit. on pp. 34, 39).

97. Tanabe, Y. & Sugano, S. On the Absorption Spectra of Complex Ions. I. *J. Phys. Soc. Jpn.* **9,** 753–766 (1954) (cit. on p. 34).

98. De Groot, F. M. F., Fuggle, J. C., Thole, B. T. & Sawatzky, G. A. 2p X-ray absorption of 3d transition-metal compounds: An atomic multiplet description including the crystal field. *Phys. Rev. B* **42,** 5459–5468 (9 1990) (cit. on p. 34).

99. Castellani, C., Natoli, C. R. & Ranninger, J. Magnetic structure of V_2O_3 in the insulating phase. *Phys. Rev. B* **18,** 4945–4966 (9 1978) (cit. on pp. 34, 36).

100. Kanamori, J. Electron Correlation and Ferromagnetism of Transition Metals. *Progress of Theoretical Physics* **30,** 275–289 (Sept. 1963) (cit. on p. 34).

101. Ribic, T., Assmann, E., Tóth, A. & Held, K. Cubic interaction parameters for t_{2g} Wannier orbitals. *Phys. Rev. B* **90,** 165105 (16 2014) (cit. on p. 36).

102. Aryasetiawan, F. *et al.* Frequency-dependent local interactions and low-energy effective models from electronic structure calculations. *Phys. Rev. B* **70,** 195104 (19 2004) (cit. on pp. 37, 38).

103. Kaltak, M. *Merging GW with DMFT* PhD thesis (University of Vienna http://othes.univie.ac.at/38099/, 2015). http://othes.univie.ac.at/38099/ (cit. on pp. 37, 39, 86).

104. Aryasetiawan, F., Miyake, T. & Sakuma, R. in (eds Pavarini, E., Koch, E., Lichtenstein, A. & Vollhardt, D. E.) pp. 7.1 –7.26 (Schriften des Forschungszentrums Jülich, 2011). http://juser.fz-juelich.de/record/17645 (cit. on p. 37).

105. Casula, M. *et al.* Low-Energy Models for Correlated Materials: Bandwidth Renormalization from Coulombic Screening. *Phys. Rev. Lett.* **109,** 126408 (12 2012) (cit. on p. 39).

106. Anisimov, V. I. & Gunnarsson, O. Density-functional calculation of effective Coulomb interactions in metals. *Phys. Rev. B* **43,** 7570–7574 (10 1991) (cit. on p. 39).

107. Honerkamp, C., Shinaoka, H., Assaad, F. F. & Werner, P. Limitations of constrained random phase approximation downfolding. *Phys. Rev. B* **98,** 235151 (23 2018) (cit. on pp. 39, 41).

108. Himmetoglu, B., Floris, A., de Gironcoli, S. & Cococcioni, M. Hubbard-corrected DFT energy functionals: The LDA+U description of correlated systems. *Int. J. Quantum Chem.* **114,** 14–49 (2014) (cit. on p. 39).

109. Liechtenstein, A. I., Anisimov, V. I. & Zaanen, J. Density-functional theory and strong interactions: Orbital ordering in Mott-Hubbard insulators. *Phys. Rev. B* **52** (Aug. 1995) (cit. on p. 40).

110. Hubbard, J. Electron Correlations in Narrow Energy Bands. *Proceedings of the Royal Society of London A: Mathematical, Physical and Engineering Sciences* **276** (1963) (cit. on p. 41).

111. Beck, S. private communication. 2018 (cit. on p. 42).

112. Lechermann, F. in (eds Pavarini, E., Koch, E., Lichtenstein, A. & Vollhardt, D.) 6.1 –6.27 (Forschungszentrum Jülich GmbH Zentralbibliothek, Velag, Jülich, Sept. 17, 2018). ISBN: 978-3-95806-313-6. http://hdl.handle.net/2128/19720 (cit. on pp. 42, 52).

113. Fetter, A. L. & Walecka, J. D. *Quantum theory of many-particle systems to I w* 2003 (cit. on pp. 42, 147, 152).

114. Boehnke, L. *et al.* Orthogonal polynomial representation of imaginary-time Green's functions. *Phys. Rev. B* **84,** 075145 (7 2011) (cit. on pp. 44, 51).

115. Metzner, W. & Vollhardt, D. Correlated Lattice Fermions in $d = \infty$ Dimensions. *Phys. Rev. Lett.* **62,** 324–327 (3 1989) (cit. on p. 45).

116. Georges, A., Kotliar, G., Krauth, W. & Rozenberg, M. J. Dynamical mean-field theory of strongly correlated fermion systems and the limit of infinite dimensions. *Rev. Mod. Phys.* **68,** 13–125 (1 1996) (cit. on pp. 45, 46).

117. Georges, A. & Kotliar, G. Hubbard model in infinite dimensions. *Phys. Rev. B* **45,** 6479–6483 (12 1992) (cit. on pp. 45, 46).

118. Gull, E. *et al.* Continuous-time Monte Carlo methods for quantum impurity models. *Rev. Mod. Phys.* **83,** 349–404 (2 2011) (cit. on pp. 47–49).

119. Rubtsov, A. & Lichtenstein, A. Continuous-time quantum monte carlo method for fermions: Beyond auxiliary field framework. *Journal of Experimental and Theoretical Physics Letters* **80** (2004) (cit. on pp. 47, 48).

120. Werner, P. *et al.* Continuous-Time Solver for Quantum Impurity Models. *Phys. Rev. Lett.* **97,** 076405 (7 2006) (cit. on pp. 47, 48).

121. Loh, E. Y. *et al.* Sign problem in the numerical simulation of many-electron systems. *Phys. Rev. B* **41,** 9301–9307 (13 1990) (cit. on p. 48).

122. Seth, P., Krivenko, I., Ferrero, M. & Parcollet, O. TRIQS/CTHYB: A continuous-time quantum Monte Carlo hybridisation expansion solver for quantum impurity problems. *Comput. Phys. Commun.* **200,** 274 –284 (2016) (cit. on pp. 49, 52, 60).

123. Gull, E., Werner, P., Millis, A. & Troyer, M. Performance analysis of continuous-time solvers for quantum impurity models. *Phys. Rev. B* **76,** 235123 (23 2007) (cit. on p. 50).

124. Savrasov, S. Y. & Kotliar, G. Spectral density functionals for electronic structure calculations. *Phys. Rev. B* **69,** 245101 (24 2004) (cit. on pp. 52, 53, 56).

125. Baym, G. & Kadanoff, L. P. Conservation Laws and Correlation Functions. *Phys. Rev.* **124,** 287–299 (2 1961) (cit. on p. 52).

126. Haule, K. & Birol, T. Free Energy from Stationary Implementation of the DFT + DMFT Functional. *Phys. Rev. Lett.* **115,** 256402 (25 2015) (cit. on pp. 54–56).

127. Galitskii, V. M. & Migdal, A. B. *Application of quantum field theory methods to the many body problem* (Zhur. Eksptl'. i Teoret. Fiz., 1958) (cit. on pp. 56, 147, 152).

128. Czyzyk, M. T. & Sawatzky, G. A. Local-density functional and on-site correlations: The electronic structure of La_2CuO_4 and $LaCuO_3$. *Phys. Rev. B* **49,** 14211–14228 (20 1994) (cit. on p. 57).

129. Petukhov, A. G., Mazin, I. I., Chioncel, L & Lichtenstein, A. I. Correlated metals and the LDA+Umethod. *Phys. Rev. B* **67** (Apr. 2003) (cit. on p. 57).

130. Anisimov, V. I., Aryasetiawan, F. & Lichtenstein, A. I. First-principles calculations of the electronic structure and spectra of strongly correlated systems: the LDA+U method. *J. Phys.: Condens. Matter* **9,** 767 (1997) (cit. on p. 57).

131. Karolak, M. *et al.* Double counting in LDA+DMFT - The example of NiO. *J. Electron Spectrosc. Relat. Phenom.* **181.** Proceedings of International Workshop on Strong Correlations and Angle-Resolved Photoemission Spectroscopy 2009, 11 –15 (2010) (cit. on pp. 57, 89, 116).

132. Savrasov, S. Y., Kotliar, G. & Abrahams, E. Correlated electrons in d-plutonium within a dynamical mean-field picture. *Nature* **410,** 793–795. ISSN: 1476-4687 (2001) (cit. on p. 58).

133. Pourovskii, L. V., Amadon, B., Biermann, S. & Georges, A. Self-consistency over the charge density in dynamical mean-field theory: A linear muffin-tin implementation and some physical implications. *Phys. Rev. B* **76,** 235101 (23 2007) (cit. on p. 58).

134. Amadon, B, Biermann, S, Georges, A & Aryasetiawan, F. The α-γTransition of Cerium Is Entropy Driven. *Phys. Rev. Lett.* **96** (Feb. 2006) (cit. on p. 58).

135. Schüler, M. *et al.* Charge self-consistent many-body corrections using optimized projected localized orbitals. *J. Phys.: Condens. Matter* **30** (Nov. 2018) (cit. on pp. 58, 59, 115).

136. Karolak, M, Wehling, T. O., Lechermann, F & Lichtenstein, A. I. General DFT++ method implemented with projector augmented waves: electronic structure of $SrVO_3$ and the Mott transition in $Ca_{2-x}Sr_xRuO_4$. *J. Phys.: Condens. Matter* **23,** 085601 (2011) (cit. on p. 58).

137. Aichhorn, M. *et al.* TRIQS/DFTTools: A TRIQS application for ab initio calculations of correlated materials. *Comput. Phys. Commun.* **204** (Apr. 2016) (cit. on p. 59).

138. Parcollet, O. *et al.* TRIQS: A toolbox for research on interacting quantum systems. *Comput. Phys. Commun.* **196,** 398 –415 (2015) (cit. on pp. 59, 60).

139. Hampel, A., Beck, S. & Ederer, C. *soliDMFT* `https://github.com/materialstheory/soliDMFT`. 2019 (cit. on p. 61).

140. Hampel, A. & Ederer, C. Interplay between breathing mode distortion and magnetic order in rare-earth nickelates $RNiO_3$ within DFT + U. *Phys. Rev. B* **96,** 165130 (16 2017) (cit. on pp. 63–65, 132, 153).

141. Jarrell, M. & Gubernatis, J. Bayesian inference and the analytic continuation of imaginary-time quantum Monte Carlo data. *Phys. Rep.* **269,** 133 –195 (1996) (cit. on p. 85).

142. Kraberger, G. J., Triebl, R., Zingl, M. & Aichhorn, M. Maximum entropy formalism for the analytic continuation of matrix-valued Green's functions. *Phys. Rev. B* **96,** 155128 (15 2017) (cit. on pp. 85, 134).

143. Seth, P. *et al.* Renormalization of effective interactions in a negative charge transfer insulator. *Phys. Rev. B* **96,** 205139 (20 2017) (cit. on pp. 86, 100).

144. Haule, K. & Pascut, G. L. Mott Transition and Magnetism in Rare Earth Nickelates and its Fingerprint on the X-ray Scattering. *Sci. Rep.* **7,** 10375 (2017) (cit. on pp. 88, 131, 132, 135, 143, 146).

145. Hampel, A., Beck, S. & Ederer, C. Charge self-consistency and double-counting in DFT+DMFT calculations for complex transition metal oxides. *in preperation* (2019) (cit. on pp. 115–118, 153).

146. Wang, X. *et al.* Covalency, double-counting, and the metal-insulator phase diagram in transition metal oxides. *Phys. Rev. B* **86,** 195136 (19 2012) (cit. on pp. 115, 116, 118).

147. Dang, H. T., Ai, X., Millis, A. J. & Marianetti, C. A. Density functional plus dynamical mean-field theory of the metal-insulator transition in early transition-metal oxides. *Phys. Rev. B* **90,** 125114 (12 2014) (cit. on pp. 115, 116, 118).

148. Aichhorn, M., Pourovskii, L. & Georges, A. Importance of electronic correlations for structural and magnetic properties of the iron pnictide superconductor LaFeAsO. *Phys. Rev. B* **84,** 054529 (5 2011) (cit. on pp. 115, 116, 118, 131).

149. Bhandary, S., Assmann, E., Aichhorn, M. & Held, K. Charge self-consistency in density functional theory combined with dynamical mean field theory: k-space reoccupation and orbital order. *Phys. Rev. B* **94,** 155131 (15 2016) (cit. on pp. 115, 118).

150. Sclauzero, G., Dymkowski, K. & Ederer, C. Tuning the metal-insulator transition in d^1 and d^2 perovskites by epitaxial strain: A first-principles-based study. *Phys. Rev. B* **94,** 245109 (24 2016) (cit. on pp. 116, 117).

151. Pavarini, E. *et al.* Mott Transition and Suppression of Orbital Fluctuations in Orthorhombic $3d^1$ Perovskites. *Phys. Rev. Lett.* **92,** 176403 (17 2004) (cit. on p. 116).

152. Kvashnin, Y. O. *et al.* Microscopic Origin of Heisenberg and Non-Heisenberg Exchange Interactions in Ferromagnetic bcc Fe. *Phys. Rev. Lett.* **116,** 217202 (21 2016) (cit. on pp. 131, 132).

153. Mandal, S., Cohen, R. E. & Haule, K. Pressure suppression of electron correlation in the collapsed tetragonal phase of $CaFe_2As_2$: A DFT-DMFT investigation. *Phys. Rev. B* **90,** 060501 (6 2014) (cit. on p. 131).

154. Leonov, I., Poteryaev, A. I., Anisimov, V. I. & Vollhardt, D. Electronic Correlations at the α–γ Structural Phase Transition in Paramagnetic Iron. *Phys. Rev. Lett.* **106,** 106405 (10 2011) (cit. on p. 131).

155. Tomczak, J. M. *et al.* Merging GW with DMFT and non-local correlations beyond. *The European Physical Journal Special Topics* **226,** 2565–2590. ISSN: 1951-6401 (2017) (cit. on p. 146).

156. Ayral, T. & Parcollet, O. Mott physics and spin fluctuations: A unified framework. *Phys. Rev. B* **92,** 115109 (11 2015) (cit. on p. 146).

157. Galler, A. *et al.* Towards ab initio Calculations with the Dynamical Vertex Approximation. *Journal of the Physical Society of Japan* **87,** 041004 (2018) (cit. on p. 146).